

**Dynamics of Electromagnetic Particles and
Its Application for Mitigation and Utilization Technologies of
Regolith on Moon, Mars, and Asteroids**

February 2017

Masato ADACHI

**Dynamics of Electromagnetic Particles and
Its Application for Mitigation and Utilization Technologies of
Regolith on Moon, Mars, and Asteroids**

February 2017

Waseda University

Graduate School of Fundamental Science and Engineering

Department of Applied Mechanics

Research on Precision Engineering

Masato ADACHI

Table of Contents

1 Introduction

1.1 Background.....	1
1.1.1 Space Exploration Missions.....	1
1.1.2 Regolith Particles on the Moon, Mars, and Asteroids.....	1
1.1.3 Problems Caused by Lunar and Martian Dust in Space Exploration Missions.....	6
1.1.4 Utilization of Lunar and Martian Regolith Particles.....	7
1.2 Previous Studies about Handling Technology of Particles.....	8
1.2.1 Mechanical and Pneumatic Methods.....	8
1.2.2 Electrostatic and Magnetic Methods.....	11
1.3 Objective of Research.....	17
1.3.1 Position of Research.....	17
1.3.2 Development of Dust Shield System for Lunar and Mars Explorations.....	19
1.3.3 Development of Size-Sorting System for ISRU Missions.....	21
1.3.4 Development of Sampling System for Sample Return Missions.....	23
1.3.5 Development of Regolith Transport System in Space Environment.....	25
1.4 Structure of Dissertation.....	27

2 Dynamics of Electromagnetic Particles

2.1 Introduction.....	31
2.2 Basic Equations.....	31
2.3 External Forces Acting on Particles.....	32
2.3.1 Coulomb Force.....	32
2.3.2 Dielectrophoresis Force and Magnetic Force.....	33
2.3.3 Adhesion Force.....	36
2.3.4 Gravitational Force and Air Drag.....	37
2.4 Numerical Calculations of Electrostatic and Magnetic Fields.....	39
2.4.1 Numerical Calculation of Electrostatic Field.....	39
2.4.2 Numerical Calculation of Magnetic Field.....	40
2.5 Measurement of Parameters.....	42

2.5.1	Measurement of Adhesion Force.....	42
2.5.2	Measurement of Particle Charge.....	44
2.5.3	Measurement of Dielectrophoresis Force.....	47
2.6	<i>Comparison of External Forces.....</i>	48
2.6.1	Effect of Electrostatic Force.....	48
2.6.2	Effect of Magnetic Force.....	50
2.6.3	Disturbance of Air Drag.....	52
2.7	<i>Numerical Calculation of Particle Motion.....</i>	53
2.7.1	Distinct Element Method.....	53
2.7.2	Soft Sphere Model.....	54
2.7.3	Hard Sphere Model.....	55
2.7.4	Modified Hard Sphere Model.....	59
2.7.5	Accuracy of Modified Hard Sphere Model.....	61
2.7.6	Electrostatic and Magnetic Interactions between Particles.....	64
2.7.7	Cyclic Boundary Conditions and Detection Method for Particle Collisions.....	66
2.8	<i>Summary.....</i>	67

3 Electrostatic Dust Shield System Used for Lunar and Mars Exploration Equipment

3.1	<i>Introduction.....</i>	69
3.2	<i>Experiment.....</i>	69
3.2.1	System Configuration.....	69
3.2.2	Experimental Setup.....	72
3.2.3	Control of Particle Charge.....	73
3.3	<i>Numerical Calculation.....</i>	77
3.4	<i>Results and Discussion.....</i>	78
3.4.1	Basic Characteristic of Electrostatic Dust Shield System on Earth.....	78
3.4.2	Shield Performance in Space Environments.....	81
3.4.3	Power Consumption.....	83
3.5	<i>Summary.....</i>	85

4 Particle Size-Sorting System for Lunar Regolith Using Electrostatic Traveling Wave

4.1 Introduction.....	86
4.2 System Configuration.....	87
4.3 Measurement of particle charge.....	88
4.3.1 Free-Fall Method.....	88
4.3.2 Effect of Tribocharging on Conveyor.....	89
4.4 Numerical Calculation.....	91
4.5 Experiment in Vacuum.....	92
4.6 Results and Discussions.....	93
4.6.1 Size Sorting in Vacuum.....	93
4.6.2 Size Sorting in Moon Environment.....	97
4.7 Summary.....	98

5 Sampling of Regolith on Asteroids Using Electrostatic Force

5.1 Introduction.....	99
5.2 System Configuration.....	100
5.3 Particle Dynamics under Operation of Electrostatic Sampling System.....	102
5.4 Effect of Dielectrophoresis Force on Large Particles.....	103
5.5 Numerical Calculation.....	106
5.6 Experiment in Low-Gravity Environment.....	106
5.7 Results and Discussions.....	107
5.7.1 Sampling of Small Particles.....	107
5.7.2 Sampling of Large Particles.....	112
5.8 Summary.....	120

6 Sampling of Regolith on the Moon, Mars, and Asteroids Utilizing Magnetic Force

6.1 Introduction.....	122
6.2 System Configuration.....	122
6.3 Calculation of Particle Motion in Simple Model.....	124
6.3.1 Calculation Methodology.....	124
6.3.2 Calculated Motion of Single Particle.....	124
6.4 Experimental Procedure.....	127
6.5 Numerical Calculation.....	128
6.6 Results and Discussions.....	129
6.6.1 Basic Characteristic of Magnetic Sampler.....	129
6.6.2 Sampler Performance in Vacuum Environment.....	132
6.6.3 Sampler Performance in Low-Gravity Environment.....	134
6.7 Summary.....	135

7 Vibration Transport of Regolith and its Application in Combination with Electrostatic and Magnetic Samplers

7.1 Introduction.....	137
7.2 Calculation of Particle Motion under Operation of Vibration Transport System.....	138
7.2.1 Mechanism of Vibration Transport.....	138
7.2.2 Calculation Model of Transported Particle.....	139
7.2.3 Calculated Particle Motions in Earth and Space Environments.....	141
7.3 Vibration Transport System Using Dielectric Elastomer Actuator.....	147
7.3.1 Driving Mechanism of Dielectric Elastomer Actuator.....	147
7.3.2 System Configuration of Vibration Transport System Using Dielectric Elastomer Actuator.....	148
7.3.3 Performance of Vibration Transport System Using Dielectric Elastomer Actuator.....	152
7.4 Vibration Sampling System Using Electromagnetic Actuator.....	156
7.4.1 System Configuration.....	156
7.4.2 Performance of Vibration Sampling and Transport System Using Electromagnetic Vibra-	

tor.....	158
7.5 Combination of Vibration Sampling with Electrostatic and Magnetic Samplers.....	161
7.5.1 Configuration of Experimental Setup.....	161
7.5.2 Sampling and Transport Performance of Vibration System Combined with Electrostatic Sampler.....	162
7.5.3 Sampling and Transport Performance of Vibration System Combined with Magnetic Sampler.....	163
7.6 Summary.....	164
8 Conclusion	
8.1 Discussion of Particle Dynamics in Space Environments.....	166
8.1.1 Effect of Gravitational Acceleration to Large Particles.....	166
8.1.2 Dynamics of Small Particles in Vacuum.....	169
8.2 Summary of Dissertation.....	170
8.3 Future Works.....	173
Acknowledgements.....	175
References.....	179
Research Achievements.....	191

Nomenclature

A	vector potential	H·A/m
A_{plate}	amplitude of vibration	m
AT	unit for magneto-motive force (product of ampere and wire turns)	–
B	magnetic flux density	T
b	position vector from rotating shaft to particle	m
C	capacitance	F
C_C	Cunningham correction factor	–
C_D	drag coefficient	–
c_n, c_t	damping constant	–
D	electric flux density	C/m ²
d	small distance in dipole moment	m
E	electrostatic field	V/m
F	external force	N
f	frequency of applied voltage	Hz
G_v	coefficient for vibration acceleration	1-G _v = 9.8 m/s ²
G	coefficient for gravitational acceleration	1-G = 9.8 m/s ²
g	gravitational acceleration	m/s ²
H	Hamaker constant	–
h	gap between particle surfaces	m
Δh	mesh length of one side of grid	m
I	particle inertia	kg·m ²
i	subscript quantity	–
I_S	electric current	A
J	impulsive force	N
J	electric current density	A/m ²
j	subscript quantity	–
K	Knudsen number	–
k_n, k_t	spring constants	–
k	subscript quantity	–
L	modulus of rigidity	Pa
M	Mean value	–
M	external torque	N·m

m	particle mass	kg
N	repulsive force from the vibrating plate	N
N	number of particles	–
\mathbf{n}	normal unit vector	–
\mathbf{p}_{ele}	electrostatic dipole moment	C·m
\mathbf{p}_{mag}	magnetic dipole moment	Wb·m
Q	total charge of bulk particles	C
q	particle charge	C
P	pressure of atmosphere	Pa
R	particle radius	m
R_S	shunt resistance	Ω
Re	Reynolds number	–
\mathbf{r}	position vector between particles	m
S	Sutherland's constant	–
SD	standard deviation	–
T	temperature of atmosphere	$^{\circ}\text{C}$
\mathbf{t}	tangential unit vector	–
t	time	s
U_{ele}	electrostatic energy	J
U_{mag}	magnetic energy	J
V	voltage	V
V_p	particle volume	m^3
\mathbf{v}	relative velocity of particle	m/s
W	power consumption	W
$\mathbf{x}, \mathbf{y}, \mathbf{z}$	positional coordinate	m
y	coefficient of restitution in the tangential direction	–
Z	correction coefficient depending on object permittivity	–
α	correction coefficient of adhesion force	–
α_{plate}	acceleration of vibrating plate	m/s^2
β	Young's modulus	Pa
δ	diameter of molecule	m
δ_n, δ_t	overlap of particles	m
ϵ_0	permittivity of free space	$= 8.85 \times 10^{-12} \text{ F/m}$
ϵ_r	relative permittivity	–
ϕ	electric potential	V

γ	coefficient of restitution	–
η	viscosity of air	$= 1.82 \times 10^{-5} \text{ Pa}\cdot\text{s}$
φ	particle position in system of rotating axes	m
λ	mean free path of the atmosphere	m
μ_0	magnetic permeability of free space	$= 1.25 \times 10^{-6} \text{ H/m}$
μ_r	relative magnetic permeability	–
μ_d	friction coefficient	–
μ_f	rotational friction coefficient	–
μ_d'	dynamic coefficient of particle friction	–
ν	Poisson's ratio	–
π	circular constant	$= 3.14$
θ	inclination of vibrating plate	rad
$\theta_x, \theta_y, \theta_z$	rotational coordinate	rad
θ_c	contact angle of liquid	rad
ρ	atmospheric density	kg/m^3
ρ_s	specific gravity of particle	kg/m^3
ρ_c	charge density of particle	C/m^3
σ	surface tension	N/m
σ_p	conductivity	$\text{A/V}\cdot\text{m}$
ω_c	angular velocity	rad/s
ω	angular frequency of vibrating plate	rad/s
ψ	inclination of vibration	rad
ζ	particle position in system of rotating axes	m

Chapter 1 Introduction

1.1 Background

1.1.1 Space Exploration Missions

Space exploration missions, such as those to the Moon [1-6], Mars [7-10], asteroids [11-13], and comets [14-16], have been conducted by space agencies and research institutions worldwide to reveal more about the history of the solar system as well as the origin of life. There is important evidence that reveals the actual properties of material, such as gas, soil, and rocks, which cannot be precisely measured by observation from the Earth. In addition, this evidence has yielded information that shows traces of the history of these materials. By directly analyzing the evidence, the formation process of the solar system can be deduced. In addition, the revealed conditions on planets can be used to determine whether life can exist on planets other than the Earth. Moreover, the information can be used to help determine how to construct exploration bases on another planet, which will enable deeper exploration of space. The possibility of future migration of humans from the Earth depends on the success of future exploration missions. In light of the success of previous missions, additional exploration missions have been undertaken and planned [17-19] not only by space agencies, but also by other enterprises as well. The increase in participation and cooperation by the private sector will lead to further development of space science.

1.1.2 Regolith Particles on the Moon, Mars, and Asteroids

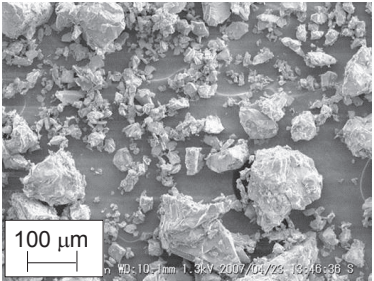
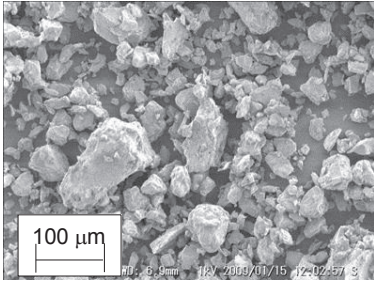
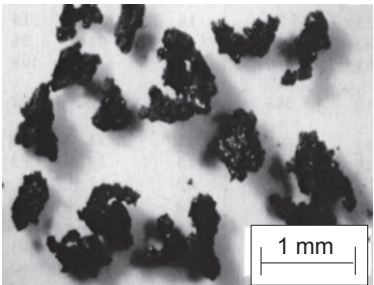
Planets and small celestial bodies are covered with regolith, a layer of unconsolidated rocks, pebbles, and soil particles. In space exploration missions, the analysis of regolith is crucial to the advancement of our knowledge of space science. Regolith is affected by meteoroid bombardments, solar wind, and cosmic rays, and it is important to investigate its mechanical, electromagnetic, and chemical properties, which vary depending on the history of the planets and small celestial bodies under scrutiny. In previous exploration missions, 321 g and 115 kg of lunar regolith particles were brought back to the Earth in the Luna and Apollo missions, respectively [20], and the samples were analyzed to determine the conditions of the lunar surface [21]. Martian regolith has never been brought to the Earth; however, its regolith has been investigated in situ by landers and rovers operated by the National Aeronautics and Space Administration (NASA) [7-10]. Particles of the asteroid Itokawa, returned by the Hayabusa spacecraft operated by the Japan Aerospace Exploration Agency (JAXA), were the only asteroid samples that humans have succeeded in bringing back to the Earth [22-24]. In addition, the Philae lander, which separated from the Rosetta spacecraft operated by the European Space Agency (ESA), tried to analyze a sample of comet 67P/Churyumov–Gerasimenko in situ [15].

Regolith particles smaller than 1 cm in diameter have been classified as lunar “soil” [21], whereas

particles smaller than 1 mm in diameter have been classified as “fines,” and particles smaller than 100 μm in diameter have been classified as “dust”, historically [20]. The “dust” has occasionally been redefined with an upper limit less than 10 or 20 μm . Based on previous investigations of lunar and Martian regolith, simulants of particles have been developed for use as research objects because the use of actual regolith particles is limited, owing to the small amounts available. Simulants such as FJS-1, JSC-1A, and JSC Mars-1 approximate the mechanical, electrostatic, and magnetic properties of regolith. The properties of lunar regolith and the simulants, FJS-1 and JSC-1A, are listed in Table 1.1, and those of Martian regolith and the simulant, JSC Mars-1, are listed in Table 1.2. In addition, the size distribution of FJS-1 is shown in Figure 1.1. As listed in Table 1.1, the lunar regolith and simulants contain few magnetic materials, such as FeO, and the simulants contain oxidized materials, such as Fe₂O₃, because they are exposed to air that includes oxygen on the Earth. The main components of the particles are silica; therefore, the relative permittivities of the particles, ranging from approximately 3.0 to 4.0, are also similar to that of silica. The lunar regolith and simulants appear sharp, and the regolith looks more distorted because it contains agglutinates that are aggregates of smaller lunar regolith. These aggregates probably bonded during a sublimation process caused by micrometeoroid impacts and quenching. The agglutinate particles are usually smaller than 1 mm, and the particles hold many fine-grained Fe metals called nanophase irons (np-Fe⁰), as shown in Figure 1.2. The np-Fe⁰ has probably been formed at the rim of the agglutinate during the reduction process of the iron droplets, caused by micrometeoroid impact and by solar wind irradiation and sputter deposition. The relative magnetic permeability of the lunar regolith is larger than that of the simulant owing to the larger amount of FeO and np-Fe⁰. In addition, the lunar regolith and the simulant contain large amounts of small particles; approximately 50 wt% of the regolith consists of particles that are less than 70 μm , as shown in Figure 1.1.

The properties of Martian regolith have not been determined in detail because the amount of samples has been limited. Comparing Tables 1.1 and 1.2, the compositions of Martian regolith, simulant, as well as lunar regolith are similar; therefore, the properties of Martian regolith can be assumed to be similar to the lunar regolith. In addition, because the Martian regolith could be captured by a magnet mounted on rovers [37], as shown in Figure 1.3, the regolith has magnetic properties as well. Although the size distribution of Martian regolith has not been determined, the simulant contains over 75 wt% of large particle above 150 μm , as shown in Table 1.2. The shapes of the Martian regolith and the simulant appear more rounded than the lunar regolith because they are probably not affected by micrometeoroid impacts, owing to the properties of the Martian atmosphere; moreover, the particles do not contain agglutinates. Although the simulants and regolith have slightly different properties, they are almost similar. Therefore, the simulants can be reasonably used for experiments as alternatives. In addition, because the main components of the particles are silica and the maximum sizes of the particles are approximately 1mm, the use of pure glass particles is a convenient option if particles larger than 1 mm are necessary for the experiment.

Table 1.1 Properties of FJS-1 and JSC-1A lunar regolith simulants, and actual lunar regolith.

Types	Parameters	Measured Values	Remarks	
Lunar regolith simulant FJS-1 	Specific gravity	2.7 [25]	g/cm ³	
	Bulk Density	1.4–1.7 [25]	g/cm ³	
	Angle of internal friction	33 [25]	°	
	Major composition		wt %	
		SiO ₂	49.4 [25]	
		Al ₂ O ₃	10.0 [25]	
		CaO	9.3 [25]	
	FeO	8.0 [25]		
	MgO	5.2 [25]		
	Fe ₂ O ₃	4.4 [25]		
	Relative magnetic permeability			
	overall*	1.073		
	magnetic**	1.193		
	nonmagnetic***	1.004		
	Relative permittivity	3.8–4.5 [26]		
Lunar regolith simulant JSC-1A 	Specific gravity	2.87 [27]	g/cm ³	
	Bulk Density	1.5–2.03 [27]	g/cm ³	
	Peak angle of internal friction	41–56 [28]	°	
	Major composition		wt %	
		SiO ₂	45.7 [29]	
		Al ₂ O ₃	16.2 [29]	
		Fe ₂ O ₃	12.4 [29] ****	
	CaO	10.0 [29]		
	MgO	8.7 [29]		
	Relative magnetic permeability			
	overall*	1.085		
	magnetic**	1.092		
	nonmagnetic***	1.007		
	Relative permittivity	3.9–4.2 [30]		
Lunar Regolith [21]  (Apollo 11 sample 10084; Source: NASA Photo S69-54827)	Specific gravity	2.3–3.2 [31]	g/cm ³	
	Bulk Density	1.5–1.74 [31]	g/cm ³	
	Angle of internal friction	30–50 [31]	°	
	Major composition *****		wt %	
		SiO ₂	45.1 [32]	
		FeO	19.8 [32]	
		MgO	10.9 [32]	
	Al ₂ O ₃	10.2 [32]		
	CaO	9.9 [32]		
	Relative magnetic permeability	1.311 [33]		
	Relative permittivity (effective value)	3.0 [31]		

* overall: particles without classification

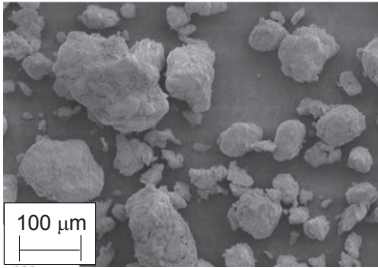
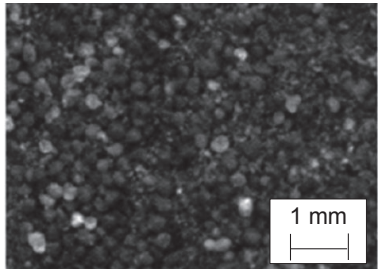
** magnetic: particles adhered to a permanent magnet. (400 mT magnetic flux density at the surface)

*** nonmagnetic: particles that did not adhere to a permanent magnet (400 mT magnetic flux density at the surface)

**** No separate determination was made for FeO, and the total iron oxide content was reported as Fe₂O₃ [28].

***** element composition of Apollo sample 15601

Table 1.2 Properties of JSC Mars-1 Martian regolith simulant, and actual Martian regolith.

Types	Parameters	Measured Values	Remarks	
Martian regolith simulant JSC Mars-1 	Bulk Density	0.87–1.07 [34]	g/cm^3	
	Size distribution	μm	wt %	
		<5 5–52 53–149 150–249 250–449 450–1,000	1 [34] 5 [34] 19 [34] 24 [34] 30 [34] 21 [34]	
	Major composition		wt %	
		SiO_2 Al_2O_3 Fe_2O_3 CaO MgO	43.5 [34] 23.3 [34] 15.6 [34] 6.2 [34] 3.4 [34]	
Martian regolith [38]  (sand in Gusev crater, Source: sol 710, NASA/JPL/Cornell/USGS)	Bulk Density	1.52 [35]	g/cm^3	
	Major composition		wt %	
		SiO_2 Fe_2O_3 Al_2O_3 MgO CaO	44.0 [36] 16.5 [36] 7.5 [36] 7.0 [36] 5.6 [36]	

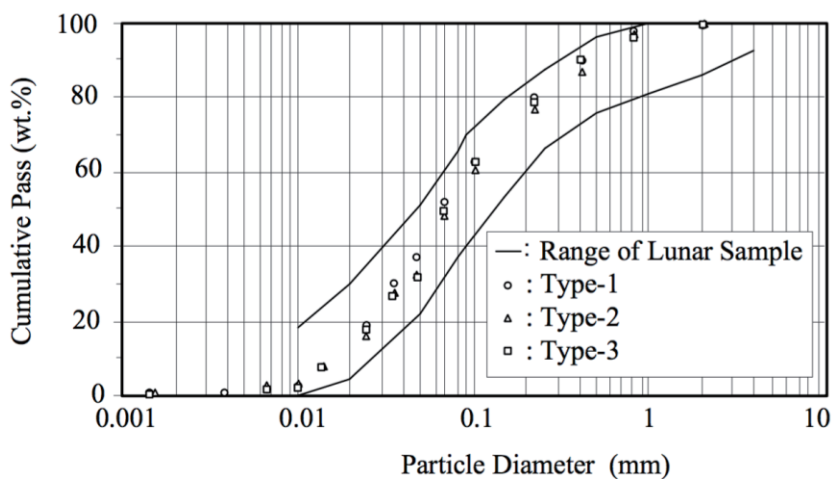


Figure 1.1 Size distributions of lunar regolith and FJS-1 simulant; obtained from literature [26].

The Hayabusa spacecraft took at least 1,534 particles from Itokawa, and these grains were less than a few hundred micrometers in diameter [24]. Because the sample amount was very small, the entire composition of the Itokawa particles has not been determined. One of the remarkable features was that the asteroid could have magnetic properties. As shown in Figure 1.4, the particle of Itokawa contains Fe^0 -bearing rims, and the formation process of np-Fe^0 would be similar to that of the lunar regolith [22].

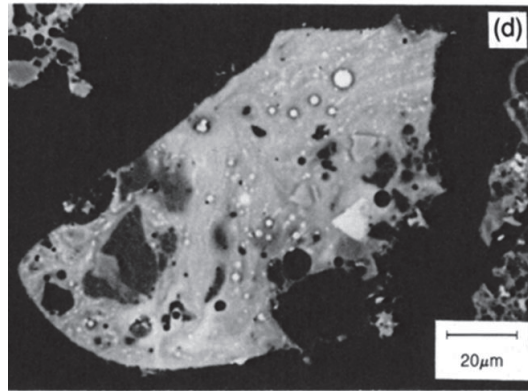


Figure 1.2 Image of a thin polished section of lunar regolith agglutinate using back-scattered electrons obtained from literature [21]. The bright circles are np-Fe^0 particles, which are not confined to surfaces, but are present throughout the volume of most agglutinates (Source: NASA Photo S87-38816).

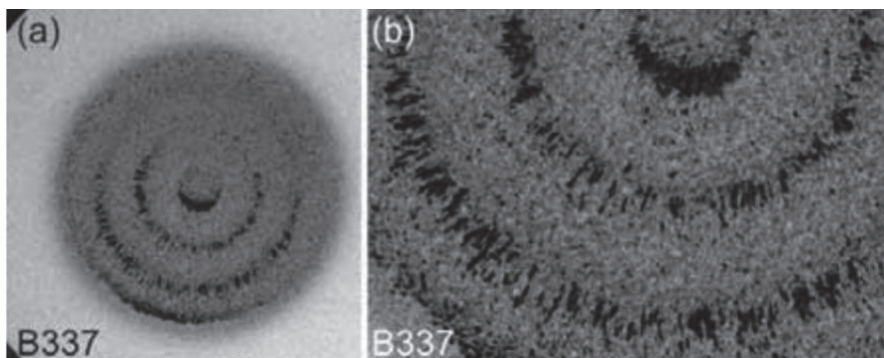


Figure 1.3 Observed magnetic chains of Martian regolith on a magnet mounted on the MER-B rover; obtained from literature [37]: (a) area of image: 30 mm^2 , and (b) enlarged view of lower part of (a).

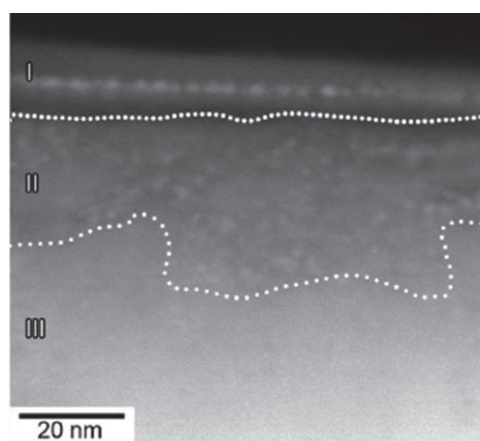


Figure 1.4 High-angle annular dark-field STEM image of pyroxene at the edge of an Itokawa particle (sample: RA-QD02-0042); obtained from literature [22]. Zones I, II, and III show amorphous surface layers containing np-Fe^0 , partially amorphized area, and crystalline substrate minerals, respectively. The bright dots are np-Fe^0 enclosed in darker material.

1.1.3 Problems Caused by Lunar and Martian Dust in Space Exploration Missions

During the Apollo missions, the astronauts often reported that lunar dust significantly hampered their extravehicular activities [39]. In the lunar environment, owing to the absence of air drag and the presence of a small gravitational force, lunar dust particles were easily lifted by manned and unmanned extravehicular activities [40], rocket exhaust [41], and meteoroid bombardments [42]. Moreover, the lunar surface is electrostatically charged owing to a number of complex processes, including the collection of electrons and ions, photoemission, and secondary electrons [43, 44], and the resultant electrostatic field created above the lunar surface naturally lifts lunar regolith particles to high altitudes [45-47]. Although concentrations of atmospheric gases, which can cause light scattering, are extremely low on the Moon, the solar corona/zodiacal light glow was observed by Apollo crew members; therefore, the scattering of solar light was due to a significant amount of lunar dust that floated owing to the electrostatic field. The electrostatically charged floating particles had a strong tendency of adhering to spacesuits and equipment because of the relatively large electrostatic and non-electrostatic adhesion forces. This caused several problems in the Apollo missions, such as obscuration of astronauts' vision during landing, clogging of equipment mechanisms, spacesuit abrasions as shown in Figure 1.5, instrument surface scratches, radiator performance degradation, seal malfunctions, and irritation of astronauts' eyes and lungs [48-50]. After the Apollo missions, the toxicity of lunar dust was also be considered. The Apollo crew reported that the dust was transferred to the command module during the Apollo 12 flight and dust inhalation occurred. The dust gave off a distinctive, pungent odor, similar to gunpowder, suggesting that there are reactive volatiles on the dust particles [49].

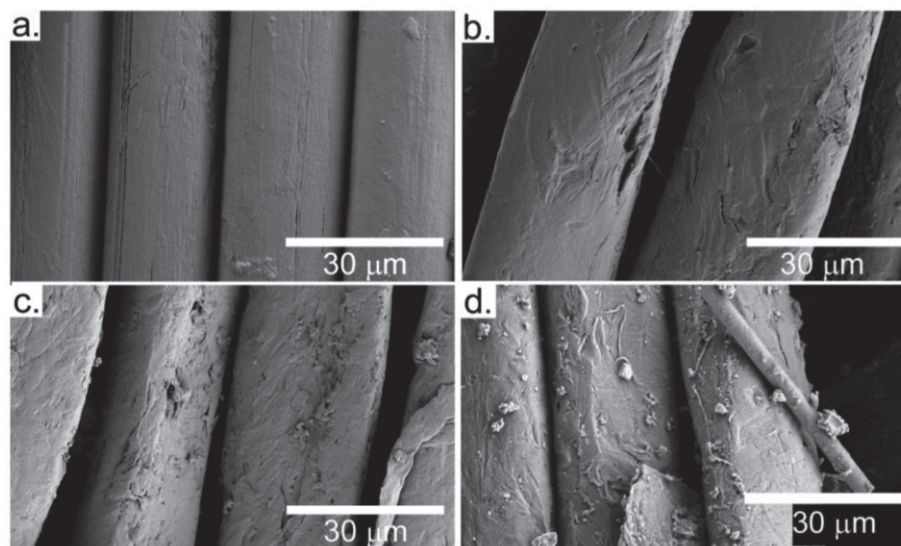


Figure 1.5 SEM images from literature [50] showing progressive fabric wear and damage of T-164 Teflon fabric from the Apollo 12 integrated thermal micrometeorite garment: (a) unused fabric in Apollo era, (b) unexposed fabric, (c) exposed fabric from shoulder area, and (d) exposed fabric from left knee area with particulate and glass fibers.

In addition, similar dust-related problems may be experienced in the Martian environment, where frequent dust devils occur and whirlwinds lift Martian regolith particles into the atmosphere [51, 52]. The particles are electrostatically charged owing to collisions among them and with other objects [53, 54]. The floating Martian dust deposited on exploration rovers, as shown in Figure 1.6, and deposited particles caused some problems. The deposited dust on the solar panels of the Spirit rover resulted in power degradation [55]. The Phoenix spacecraft collected Martian regolith samples by using the robotic arm scoop; however, the regolith particles were dumped onto the inlet screen of the Thermal Evolved Gas Analyzer, and that disturbed a normal operation of the equipment [56]. Lunar and Martian regolith will cause serious problems in future exploration missions, unless effective countermeasures are undertaken to address this issue in future missions.

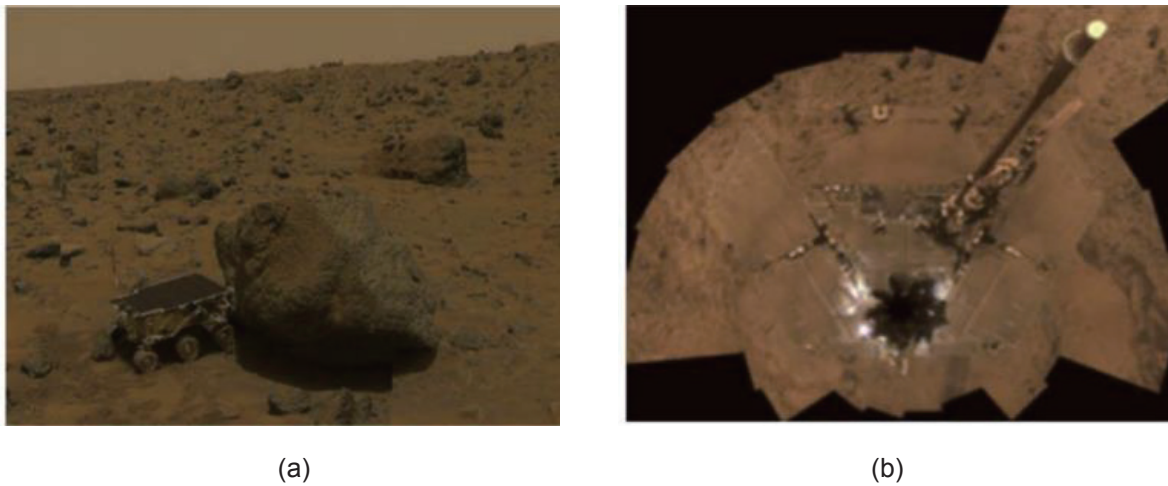


Figure 1.6 Photographs obtained from literature [56] (Source: NASA/JPL/Caltech/Cornell); (a) Sojourner rover displaying build-up of fine-grained material in wheel (Sojourner is approximately $65 \times 48 \times 30 \text{ cm}^3$), and (b) Circular projection showing Spirit rover with solar panels almost coated with dust (Spirit is approximately $2.3 \times 1.6 \times 1.5 \text{ m}^3$).

1.1.4 Utilization of Lunar and Martian Regolith Particles

Lunar and Martian regolith particles have many characteristics that are not detrimental to exploration missions as well. These characteristics demonstrate that the particles can potentially serve as resources that can be used in manned and unmanned exploration missions. To reduce launch mass, costs, and mission risks for the purpose of advanced future exploration missions, as well as the colonization of space beyond the Earth, In-Situ Resource Utilization (ISRU) has been proposed. This effort will harness natural and discarded resources at exploration sites to create fuel propellant and life support consumables for astronauts, and also to prepare repair tools and parts for robotic equipment in situ [57-59]. If ISRU is not conducted, astronauts must continue to bring everything from the Earth for their exploration missions, such as significant amounts of oxygen, water, and fuel, and the equipment must not malfunction. The primary goals of ISRU are the ex-

traction or production of critical consumables from liquid, gas, and regolith present on site. The goals are roughly separated into five areas [59]:

- Resource characterization and mapping
- Mission consumable production (propellants, fuel, life support consumables, and feedstock for manufacturing and construction)
- Civil engineering and surface construction (radiation shields, landing pads, habitats)
- Energy generation, storage, and transfer using in-situ resources (solar, electrical, thermal)
- Manufacturing and repair using in-situ resources (spare parts, wires, trusses, systems)

In an environment where there is no gas or liquid, similar to the lunar environment, the resources are expected to combine with and remain in regolith particles. Utilization technologies for these particles must be developed in order to achieve the five goals listed above in future missions. In particular, the handling technology of the regolith is fundamental in achieving these goals, and the technology must be able to address the dust problems described in section 1.1.3.

The use of lunar regolith is interesting not only because of the ISRU in exploration missions, but also for the importation of these resources to the Earth where they can contribute to the global economy [60, 61]. In fact, several private companies were established with the aim of exploiting extraterrestrial resources, considering the possibility of utilizing these resources for economic activities. Considerable interest has been focused on the light isotope of helium, ^3He . ^3He could be fused with deuterium to yield large amount of energy by nuclear reaction. ^3He is very rare on the Earth, but it is abundant on the Moon; hence, ^3He can be mined there and transported to the Earth where the resource could be used to generate electrical power [61]. In addition, rare earth elements, such as Ti, Au, and Ag, which are precious metals that have commercially-valuable optical, electrical, magnetic and catalytic properties, have also been proposed to be imported from the Moon [60, 61].

1.2 Previous Studies about Handling Technology of Particles

1.2.1 Mechanical and Pneumatic Methods

To mitigate and utilize regolith particles in space environments, mechanical and pneumatic handling technologies have been used. In Apollo missions, the astronauts sampled the lunar surface by using a scoop, tong, and rake, as shown in Figure 1.7 (a) and (b) [1, 62]. The astronauts used a battery-powered drill and core tube sampler to sample deeper layers of the regolith as shown in Figure 1.7 (c) and (d) [1, 62].

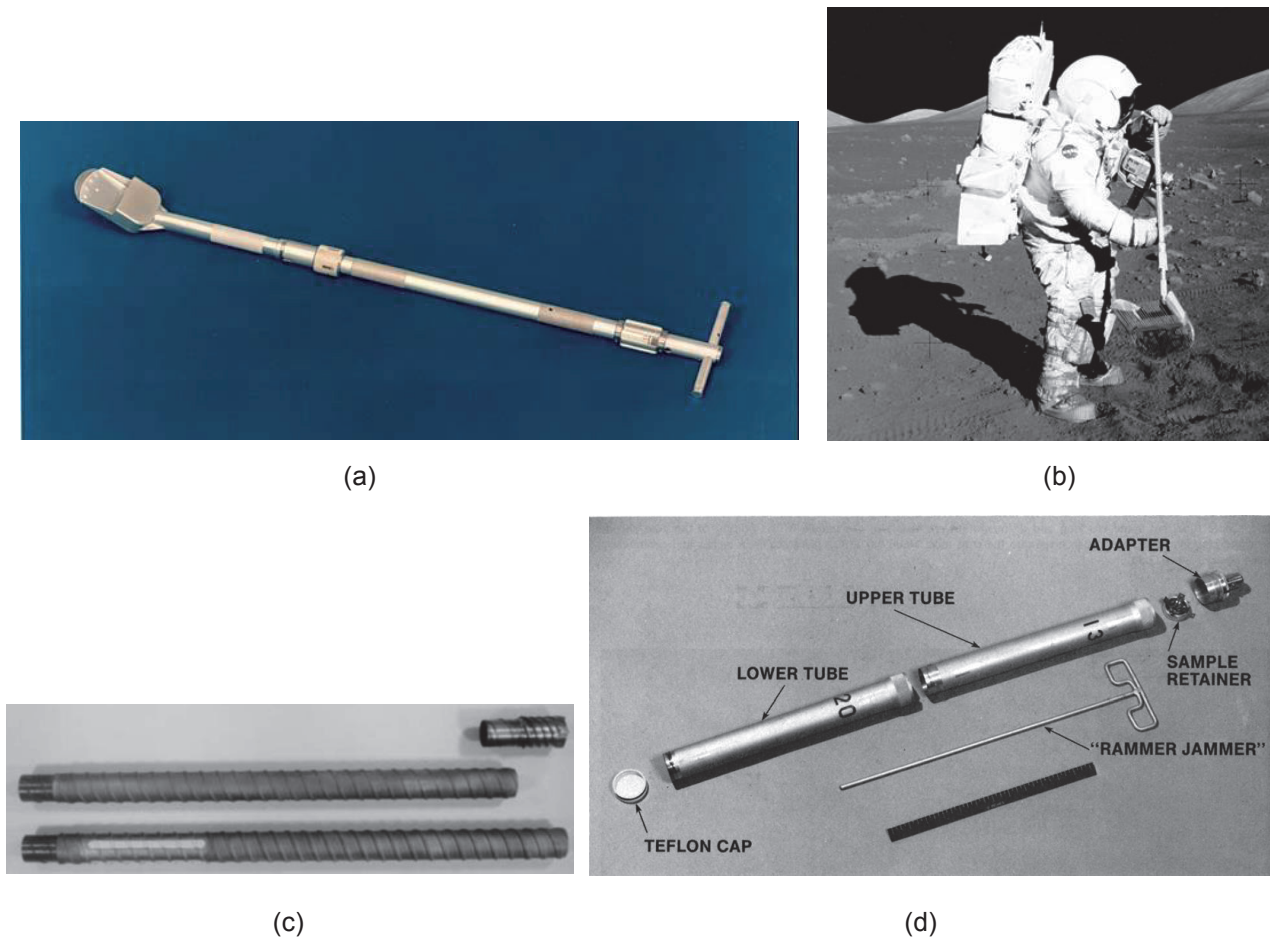


Figure 1.7 Images of (a) scoop for Apollo 12 and 14 missions, (b) rake for Apollo 15–17 missions, (c) drill core of rotary-percussive drill for Apollo 15–17 missions, and (d) core tube sampler used in Apollo 15–16 missions (modified photographs from literature [1, 62]).

The mechanical means that astronauts used have also been utilized in robotic systems. For example, regolith sampling was conducted using scoops with Viking lander 1 and 2 on the Mars [63], and the Phoenix lander was equipped with the Icy Soil Acquisition Device, which is composed of a scoop with passive cutting blades and a small motor-driven drill to sample hard frozen soil from the Martian polar region [64]. The Curiosity rover was equipped with the Sample Acquisition, Processing, and Handling subsystem to obtain interior rock and regolith samples from Martian surface materials using a scoop and drill, as shown in Figure 1.8. The Philae lander was equipped with a sampling drill, named the Sampling, Drilling, and Distribution (SD2) subsystem, to investigate the surface of comet 67P/Churyumov–Gerasimenko [66], as shown in Figure 1.9. The mechanical handling systems were mainly mounted at the ends of the robotic arm or at the extended boom of the rovers and landers. The particles collected by rovers and landers were analyzed by on-board instruments. In addition, it has been planned that the collected regolith will be transported by a rover delivery system toward a site where ISRU processing will be performed [67]. As with other mechanical systems, some type of bucket ladder, hopper, conveyor belt, auger, impeller, and scraper have been proposed and prototypes were developed for lunar excavation [68]. The advantages of mechanical systems are their

ability to grind hard surfaces and rock, collect samples at the subsurface level and at deep layers, and deal with large amounts of regolith and large particles. Moreover, there have been many experiences on the development and operation of these systems for terrestrial applications in civil engineering and in granular processing. On the other hand, some problems with the mechanical systems have not been resolved including dust contamination, short equipment lifetime owing to mechanical abrasion, and high-power consumption. In addition, these systems have large and complex configuration. As a conventional technology, the Apollo crew tried to remove dust attached to the extravehicular equipment by using brushes [49]. For the Curiosity rover, the Dust Removal Tool was mounted on the turret of the robotic arm to clear off the loose material that has been deposited from the observation tray, as shown in Figure 1.8 [65].

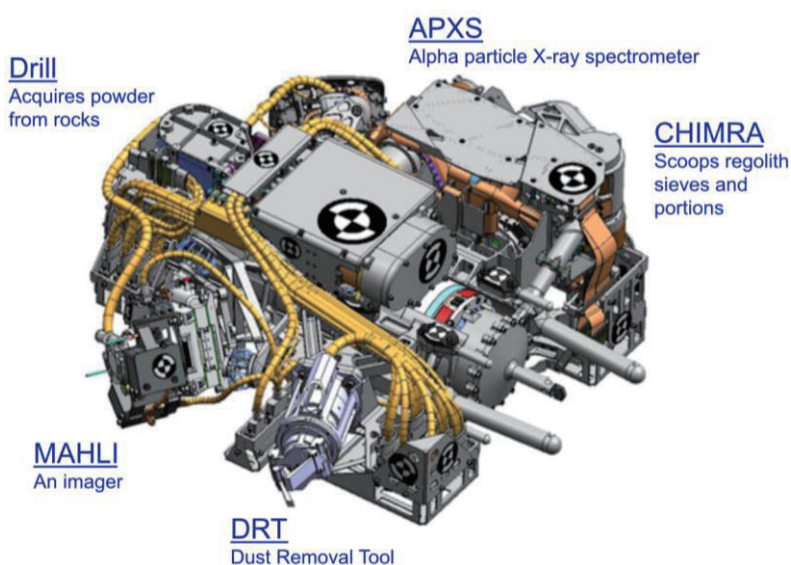


Figure 1.8 Image of the turret structure, approximately 60 cm in diameter, composed of a drill and scoop mounted at the end of the robotic arm of the Curiosity rover; obtained from literature [65].

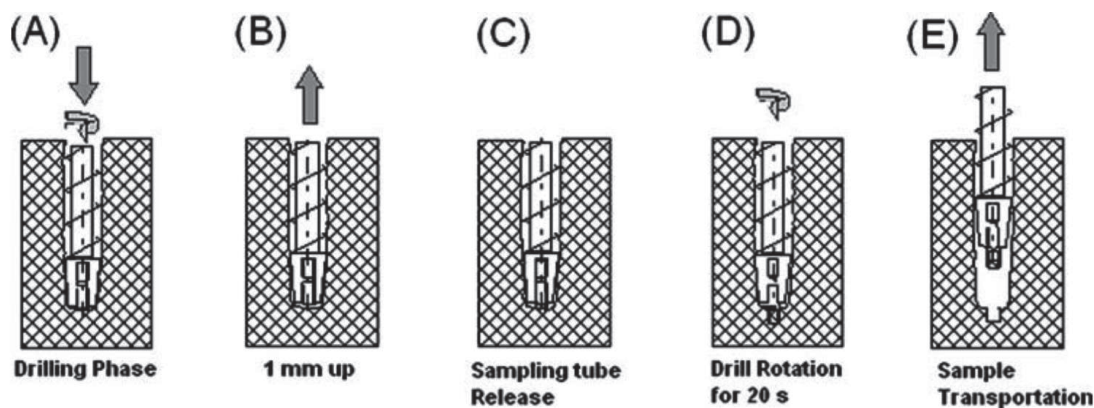


Figure 1.9 Diagram of the sample acquisition mechanism of SD2; obtained from literature [66]. Once the sampling depth has been reached, the sampling tube is pushed to collect samples as a coring device.

Pneumatic handling technology has been used in terrestrial applications for moving fines and coarse particulates. The technology has some advantages, such as no moving parts that would cause clogging and jamming, ease of guiding the dusty gas stream across long distances and in variable directions, and low probability of dust contact that would cause large abrasion to mechanical equipment. This measure has been considered for use in space environments. Several types of pneumatic systems have been developed for feeding regolith particles into devices that perform chemical processing in ISRU, and the performance in a vacuum and at lunar gravity during parabolic flights have been investigated [69-71]. Recently, a pneumatic system was mounted on the OSIRIS-REx spacecraft to sample asteroid particles, as shown in Figure 1.10[19]. The main disadvantage of pneumatic systems is that all the required gas must be transported from the Earth because extracting gas in situ is difficult; thus, it is not suitable for long-term operation. Even if gas production is feasible, the system may require a pump with mechanical drives in order to sustain the gas flow for long-term operation. In addition, the gas must be handled with the utmost care to prevent leakage.

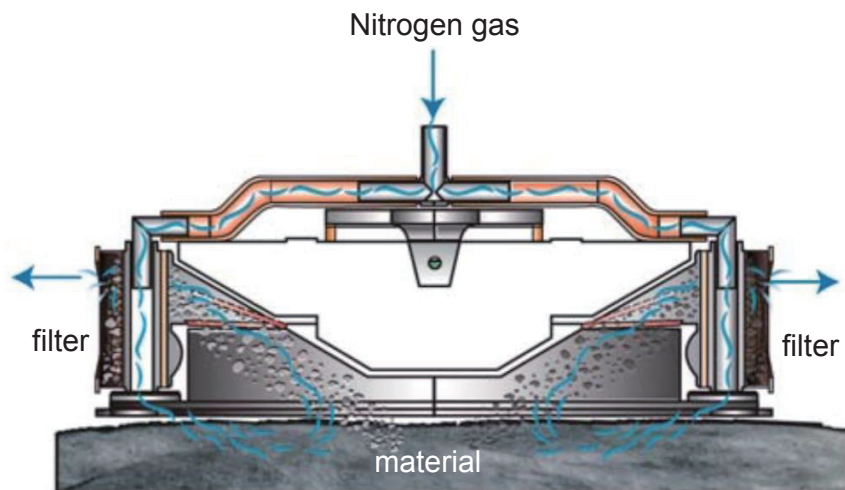


Figure 1.10 Image of the Touch-and-Go Sample Acquisition Mechanism (TAGSAM) mounted on the OSIRIS-REx; obtained from literature [19]. Nitrogen gas injected into the interior of the annulus entrains material and forces it through a filter, where it is captured.

1.2.2 Electrostatic and Magnetic Methods

As an alternative to mechanical and pneumatic systems, electrostatic handling technology for particles has been considered because these systems do not need mechanical drives, gas, or liquid. Because the electrostatic force is relatively small, the systems have been utilized in limited areas of terrestrial applications, such as in electrostatic precipitators and electrophotography [72].

The electrostatic precipitator consists of a grounded electrode outer frame and wire electrode. Dust-laden gas is passed through the outer frame and the wire located at the centerline of the gas flow. When

a high voltage is applied to the wire, a corona discharge near the wire of the discharge electrode causes ions to traverse between the outer frame and the wire, and the particles obtain an electric charge of the same polarity as the voltage of the discharge electrode. The charged particles move toward the outer frame of the collecting electrode and are deposited there, owing to the electrostatic field between the outer frame and wire. The captured particles are removed from the collecting electrode by rapping mechanisms to clean the electrode. The technology is mainly utilized in industrial applications to capture particles that are equal to or less than a micron in size, such as in the diesel engine exhaust gas and plant emissions, because the technology has several advantages, such as low-pressure drop, low power consumption, and high-collection efficiency [72]. Considering its advantages, the electrostatic precipitator has been considered for use in ISRU for the production of oxygen in the Martian environment [73, 74]. The Martian atmosphere contains large amounts of carbon dioxide, as well as dust lifted into the air by frequent dust devils [51, 52]. The electrostatic precipitator is expected to make the atmospheric gas clean and usable for oxygen extraction. Some prototypes of the electrostatic precipitator for the Martian environment have been developed, as shown in Figure 1.11 [73, 74].

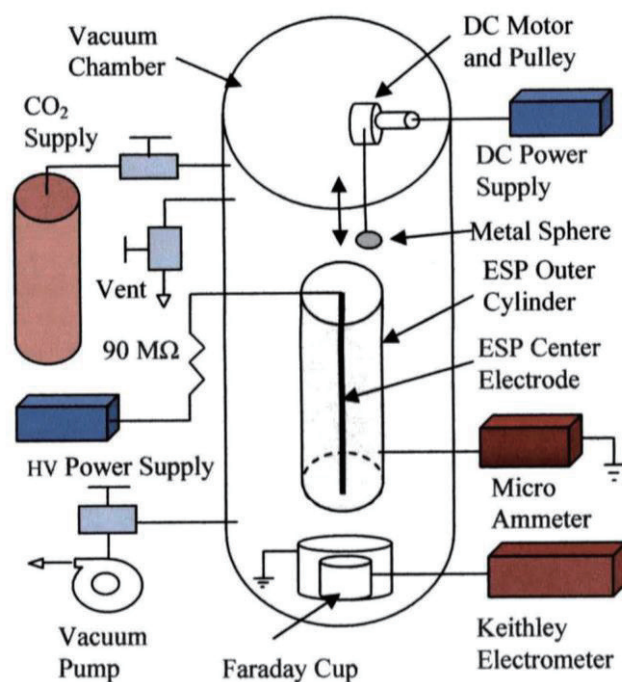


Figure 1.11 Schematic of the experimental setup of an electrostatic precipitator for the Martian environment; obtained from literature [73].

Electrophotography is another process that utilizes electrostatic force. It is used only in terrestrial applications, such as in copiers and laser printers. Although the technology does not relate to space applications, it has contributed toward building the theory of particle dynamics in an electromagnetic field. For this reason, a summarized description is included here. The technology mainly consists of six distinct steps

[75-78]: charging, exposure, development, transfer, fusing, and cleaning. These steps are shown in Figure 1.12. In electrophotography, the motions of pigmented toner particles on the photoreceptor are controlled using electrostatic and magnetic forces and the image of these toner particles are formed during the development process. The toner images formed are transferred and fixed on a paper surface, and then the paper is delivered outside the printer. For the development process, the two-component magnetic brush development system is widely used. As shown in Figure 1.12, magnetic carrier particles with electrostatically attached toner particles are introduced into the vicinity of a rotatory sleeve, inside of which is a stationary multipolar magnetic roller. The diameter of the carrier particle is several tens of micrometers, and that of the toner particle is several micrometers. In the magnetic field created by the stationary magnetic roller, the carrier particles form their chain brushes by interacting magnetically with each other. The magnetic brushes are transported with toner particles by the rotating sleeve and contact the photoreceptor surface at the smallest gap between the two rollers. The toner particles then separate from the brushes and move toward the electrostatic latent images created on the photoreceptor by the electrostatic force to form real images. This technology utilizes the balance of forces acting on particles to control their motions. For example, the electrostatic force acting on the toner must exceed the adhesion force required to separate the toner particles from the magnetic brushes, and the magnetic force acting on the carrier particles should be set as the dominant force to create their brushes. The dynamics of electromagnetic particles, whose sizes range from a few to dozens of micrometers in diameter, in the environment on the Earth has been widely investigated in the field of electrophotography [75-78].

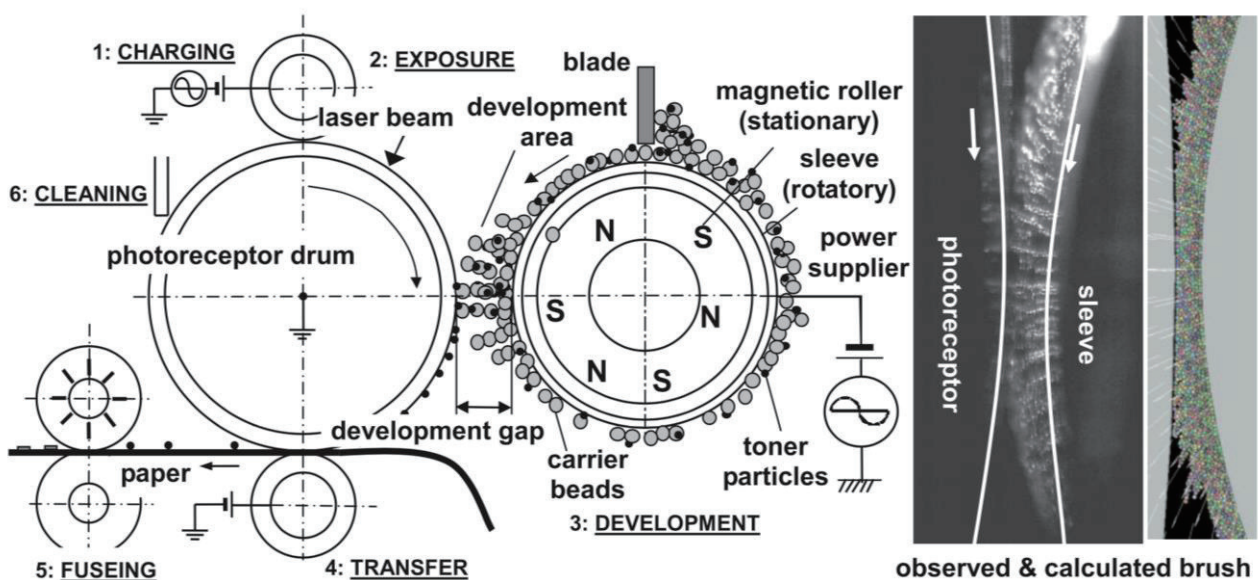


Figure 1.12 Schematic of a two-component magnetic brush development system in electrophotography; obtained from literature [77]. The picture on the right shows the observed and calculated magnetic particles in the development area (The diameter of electromagnetic particles ranges from a few to dozens of micrometers in diameter).

Related to electrophotography, the electrostatic curtain and electrostatic traveling wave were developed [79, 80] to transport toner particles [81, 82]. The electrostatic curtain is generated on the surface of insulating materials in which the parallel electrodes are embedded separately from one another when the AC high voltage of a standing wave is applied to the electrodes. The resultant electrostatic curtain creates an electrostatic force that can move small particles on the insulator. If the traveling wave is applied to the electrodes, the resultant electrostatic field moves in one direction, and the particles can be transported in the direction, as shown in Figure 1.13. Recently, electrostatic systems have also been utilized for cleaning dust particles deposited on the surfaces of solar panels, as shown in Figure 1.14 [83-85]. Sand storms often occur in desert areas, and the storm lifts up and blows the sand in the atmosphere. The floating particles are deposited on solar panels, causing degradation of power generation from mega solar plants [86, 87]. Electrostatic systems are expected as effective countermeasures to dust related problems. Studies on electrostatic curtain and electrostatic traveling wave have shown the applicability of the electrostatic force to particles that are not industrially produced, exist in nature, and have non-uniform properties.

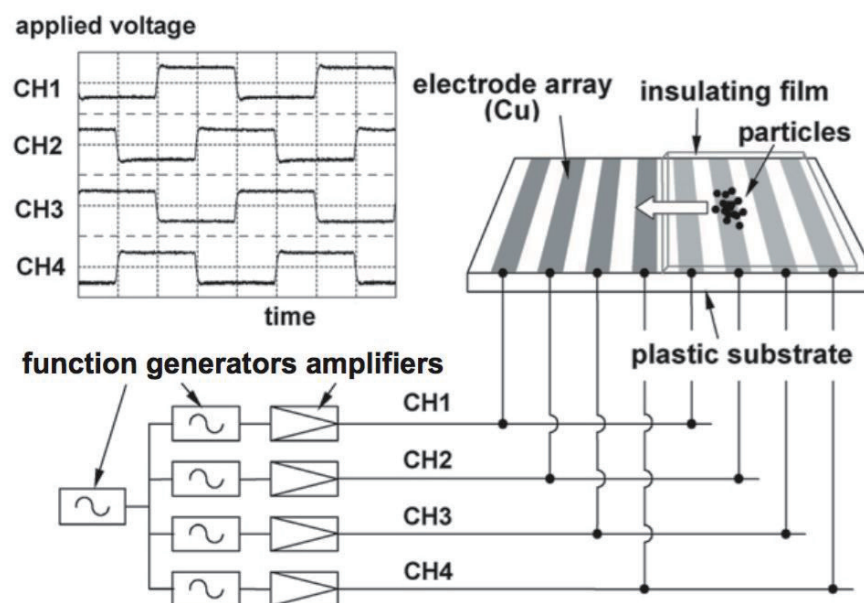


Figure 1.13 Schematic of an electrostatic traveling wave that transports particles to the left on a plastic substrate; obtained from literature [82].



(a) before cleaning operation

(b) after cleaning operation

Figure 1.14 Demonstration of an electrostatic cleaning system on a solar panel: (a) before and (b) after cleaning; obtained from literature [85] and modified. The cleaning operation was applied only to the left half of the solar panel for three minutes.

The Electrodynamic Dust Shield System, which utilizes the same mechanisms of an electrostatic curtain and electrostatic traveling wave has been planned for space applications [88] and developed as cleaning equipment for optical lenses, solar panels, and thermal radiators [89-93]. For space applications, transparent indium tin oxide (ITO) is used for the electrode material because ITO is transparent in the visible region of the electromagnetic spectrum, and does not disturb the operation of optical equipment and solar panels. Electrostatic cleaning systems could clean most of the deposited lunar regolith simulant, JSC-1A [89, 91], FJS-1 [93], and Martian regolith simulant [91] in air and at 1-G ($G = 9.8 \text{ m/s}^2$). In addition, cleaning in vacuum environments had been performed against the simulants [89, 91] as well as against the actual lunar regolith [93]. Moreover, cleaning in a vacuum and reduced gravity environments against the lunar regolith simulant JSC-1AF and actual regolith had been performed [90]. Numerical calculations were used to predict cleaning performance in the lunar environment [93]. The experimental and calculated results show high cleaning performance in reproduced space environments, and it is expected that performances in actual lunar and Martian environments are better than that in the Earth environment owing to the low gravitational force and absence of air drag that degrade the particle mobility. However, it should be noted that gas discharge occurs easily on the Mars owing to the low density of air; therefore, preventive measures must be taken.

For other electrostatic mitigation technologies in space applications, the concepts of electrostatic lunar dust collector and electrostatic lunar dust repeller have been proposed for use at the site between the light side and the dark side of the Moon. At this location, a large electrostatic field is created, owing to the effect of cosmic rays and solar winds, and lunar dust could be lifted by the resultant electrostatic field [94, 95]. The electrostatic lunar dust collector and the electrostatic lunar dust repeller are composed of vertical plates and wire electrodes, respectively, above the lunar instrument. When a high DC voltage is applied to some electrodes and the others are grounded, the resultant electrostatic force could attract the floating dust to

the plates or repel them from the wires. The performance was predicted using numerical calculations, and the results showed high mitigation against particles that are charged with the same polarity [94, 95]. In addition, electrostatic and magnetic cleaning systems for removing lunar dust adhering to spacesuits have been developed [96, 97]. Although the cleaning mechanism of the electrostatic system is almost the same as that of the Electrodynamic Dust Shield, the system was adapted for spacesuit fabric consisting of insulated wire electrodes stitched into the outer layer of the fabric [96]. When an alternating high voltage is applied to the electrodes, most of the lunar regolith simulant, FJS-1, deposited on the fabric could be removed. The magnetic system consists of a shaft, stationary multipolar magnetic roller, rotating sleeve, collection bag, and back-up magnet. The magnet was similar to the stationary magnetic roller used in electrophotography to attract and transport carrier particles [75]. The sleeve is pushed against the fabric surface and pulled in a lateral direction by hand. Because lunar dust contains magnetic materials, the particles are attracted to the stationary magnetic roller and transported on the rotating sleeve by means of magnetic and frictional forces. The magnetic roller is designed such that a repulsive force acts on the particles at a particular position where the particles separate from the sleeve and the separated particles are gathered in the collection bag [97].

In addition to particle mitigation, a utilization technology using the electrostatic force has been developed, such as electrostatic beneficiation systems for the ISRU process [98, 99]. Refinement or enrichment of specific minerals in the regolith into feedstock for ISRU before the chemical processing to extract oxygen, water, and construction materials is more desirable as it can reduce the size and energy requirements of the equipment and simplify the process. In the electrostatic beneficiation system, the regolith is tribocharged by passing it through a static mixer, allowing it to fall through a high-electrostatic field that is produced by a pair of high-voltage parallel plates. From there, the regolith falls into a series of seven collection bins that collect the separated regolith. The beneficiation mechanism ensures that different minerals will be tribocharged differently, depending on the difference of the work function between the specific mineral and the static charger. Electrostatic beneficiation was demonstrated to enhance the desired mineral concentrates, such as iron oxides and ilmenite, in the lunar regolith simulant KSC-1 [98] and NU-LHT-2M [99], although the beneficiation using JSC-1A was not successful because of its lack of ilmenite [99].

As for particle utilization technologies, a magnetic conveyor that utilizes the mechanism of the magnetic coil gun to transport particles has been developed for terrestrial applications [100-103]. The magnetic coil gun has been conventionally used for firing a bullet that is larger than the particles, and the basic characteristic of the control of the bullet motion has been widely investigated [104-106]. Based on studies concerning the bullet, the mechanism has been also utilized for the manufacturing and processing of small particles ranging from several tens to several hundreds of micrometers. The magnetic system does not have mechanical parts; thus, it is not necessary to consider mechanical malfunctions. Although space application is expected, the studies focused only on industrial processing, and the application was limited to ferromagnetic particles that can be easily handled using a magnetic force [101, 102].

1.3 Objective of Research

According to the previous studies mentioned above, the electrostatic and magnetic handling technologies of regolith particles have several advantages that are suitable in space environments. The technologies have been developed for dealing with particles ranging from submicron sizes to sizes of several hundred micrometers, because the balance of forces acting on particles corresponds to the particle size and the electrostatic and magnetic force would be the dominant forces in that range. Although the balance of forces in the Earth environment has been investigated in previous studies, the balance is expected to change in the space environment owing to the low gravity and low air drag, and the effect of these factors has not been investigated in detail. Researchers studying the Electrodynamic Dust Shield and electrostatic beneficiation systems have performed experiments in a vacuum and at low gravity; however, the experiments focused only on showing the feasibility of the system in the space environment. This is because frequent tests cannot be conducted owing to the long preparation time and large expense; thus, the change in the force balance has not been investigated thoroughly. On the other hand, although the numerical calculation is a suitable method of investigating the force balance, the previous studies performed the calculations independently, and there are still some doubtful points regarding their accuracy. Numerical calculation needs to be developed and evaluated by mutually interacting with experimental results on the Earth as well as on reproduced space environments. Regarding the lack of insight on particle dynamics in space environments, the application of electrostatic and magnetic forces to handle particle motion has been few; in particular, the magnetic system has not been developed efficiently. Although there are still issues related to regolith particles, electrostatic and magnetic systems can be used for a specific application for future exploration missions.

1.3.1 Position of Research

Following the summary of the previous research shown above, the objective of this study is to build a fundamental theory on the dynamics of electromagnetic particles in space environments. This theory is applied to develop particle-handling technologies that utilize electrostatic and magnetic forces, which are suitable for use in space environments. The position of this research is shown in Figure 1.15. A variation in the balance of external forces acting on a particle, corresponding to its size, is crucial for understanding the dynamics of the particle. In addition, particle dynamics in the space environment is investigated in this research by theoretical calculations using actual properties of particles that exist in space. Based on the calculation results, some electrostatic and magnetic systems are developed, focusing on specific issues relating to regolith particles on the Moon, Mars, and asteroids, where the gravitational force and vacuum rate are different from those on the Earth. In particular, an electrostatic dust shield system for manned and unmanned exploration on the Moon and Mars, an electrostatic size-sorting system for the lunar ISRU, an electrostatic and magnetic samplers used for sample return missions on asteroids, and an vibration transport system for ISRU as well as for sample return, are developed for future space missions. The explanations for each system are described in

later sections. The performances of the systems have been evaluated by conducting not only experiments in terrestrial environment, but also demonstrations in a vacuum and low-gravity and numerical calculations.

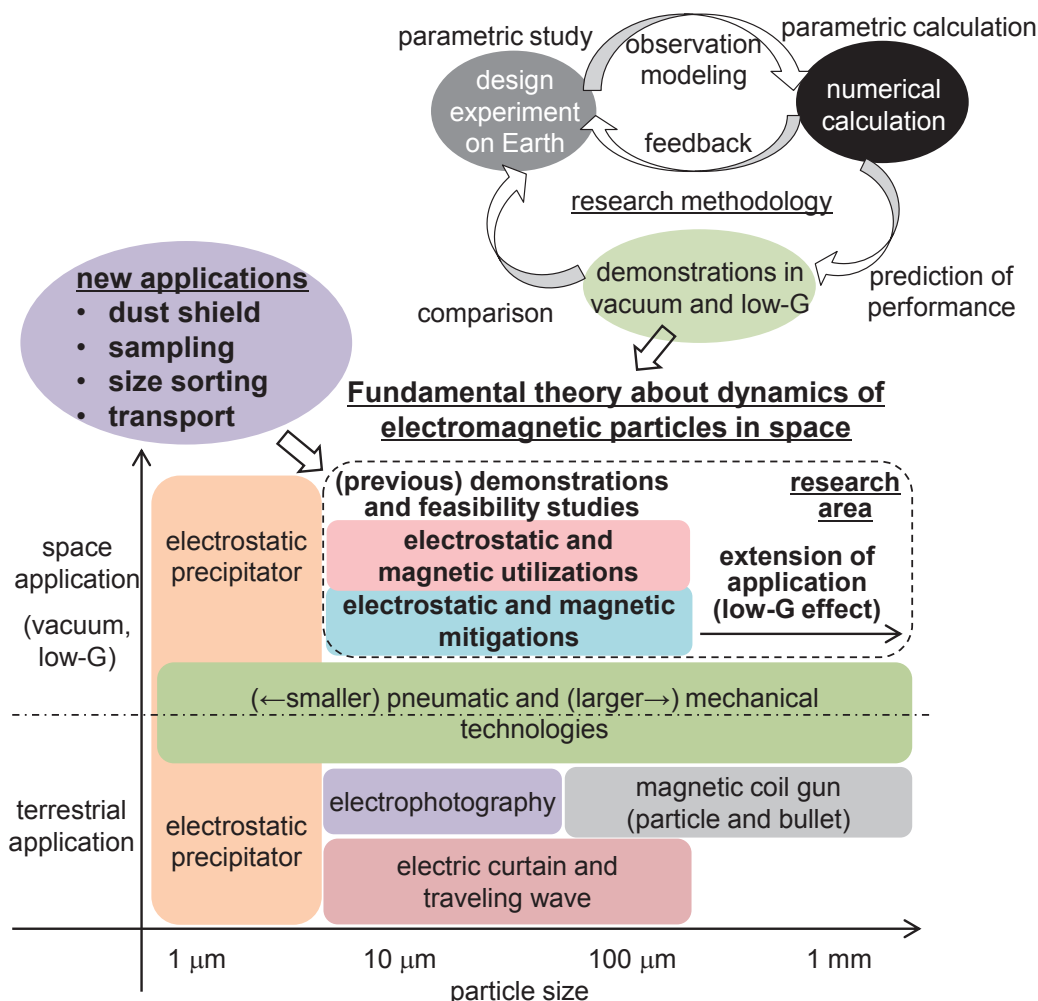


Figure 1.15 Diagram of the position of this research.

The distinct element method (DEM) is utilized [107] as the calculation method. The method has been used in several areas related to granular and particle dynamics, such as in electrophotography [75-78], fluidized bed [108-110], and geographical engineering [111-112]. Although the method is suitable for simulating the distinct motion of each particle and the mechanical and electromagnetic interactions of particles with one another, the large calculation load is an issue. To reduce the calculation load and reproduce more actual conditions of particle dynamics, the calculation model needs to be modified. The fundamental theory on the dynamics of electromagnetic particles in space is constructed by conducting a combined process of parametric study in experiments, actual demonstrations, and numerical calculations. Because the dynamics of particles smaller than several micrometers have been considered in the field of electrostatic precipitators, this research focuses on particles ranging from several micrometers to several millimeters in size, as shown in

Figure 1.15. Although the electrostatic force has been utilized to manipulate particles smaller than 1 mm in previous research [89-93, 98, 99], the use of this force for particles larger than 1 mm is attempted in this research, while considering the smaller gravitational forces present in space.

1.3.2 Development of Dust Shield System for Lunar and Mars Explorations

As described in section 1.1.3, one of the problems caused by lunar dust particles during the Apollo missions was their intrusion into the gaps of the mechanical drives installed on the equipment used for extravehicular activities [49]. In the lunar environment, lunar dust particles are easily lifted by exterior influences, and these floating particles adhere to the extravehicular systems and spacesuits. The adhered particles easily enter into the gaps of the equipment, resulting in serious mechanical problems, such as mechanical malfunction, excessive leakage of air from the spacesuits, and the abrasion of mechanical drives [49]. Furthermore, when electrical connectors are mated and de-mated repeatedly, and the surfaces are contaminated by dust, the adhered dust can clog the gaps and cause electrical malfunctions [48]. Based on the lessons learned from the Apollo missions, the problem of dust intrusion into the gaps of mechanical and electrical systems has been considered to be priority issue for future lunar explorations by space agencies worldwide. In addition, in Martian environment, frequently occurring dust devils lift Martian regolith particles into the atmosphere [51, 52], and it can be assumed that the floating particles cause the same problems as lunar dust. In the lunar and Martian environments, the repair and maintenance of equipment is difficult owing to the lack of tools and parts. Therefore, a dust shield system for mechanical gaps is required to prevent regolith contamination over a long exploration period. The sealing system, consisting of a brush seal made of fluorine resin and a labyrinth seal made of aluminum and SUS304, has been developed by JAXA [113, 114], as shown in Figure 1.16. JAXA has also considered the utilization of mechanical seals, such as Varilip[®] and Variseal[®], as shown in Figure 1.17 [115]. NASA has considered the application of a spring-loaded Teflon seal, such as Bal Seal[®] [116], as shown Figure 1.18. The performances of the systems in air and vacuum environments have been investigated, and the high-shield performance for dust intrusion were confirmed experimentally [114]. However, because the mechanical shields had to contact the rotating shaft, casing, and particles, abrasion of the shield was unavoidable. The life cycles of the mechanical shields have to be improved by decreasing the probability of contact with dust. As a mitigation technology for electrical malfunction caused by dust, the Dust-Tolerant Connector was developed by Honeybee Robotics [117], as shown in Figure 1.19. When the connectors are mated, permeable membranes are connected initially, and the membranes trap dust particles. After the dust is trapped, electrical pins stored in membranes are pushed through the membranes and mated. Although small amounts of dust could intrude into the membranes, no dust could reach the pins during the dozens of mate and de-mate cycles. To further extend the life cycle of the connection, dust must be kept away from the gaps of the connectors, and the intrusion of dust particles into the membranes should be prevented before mating and de-mating.

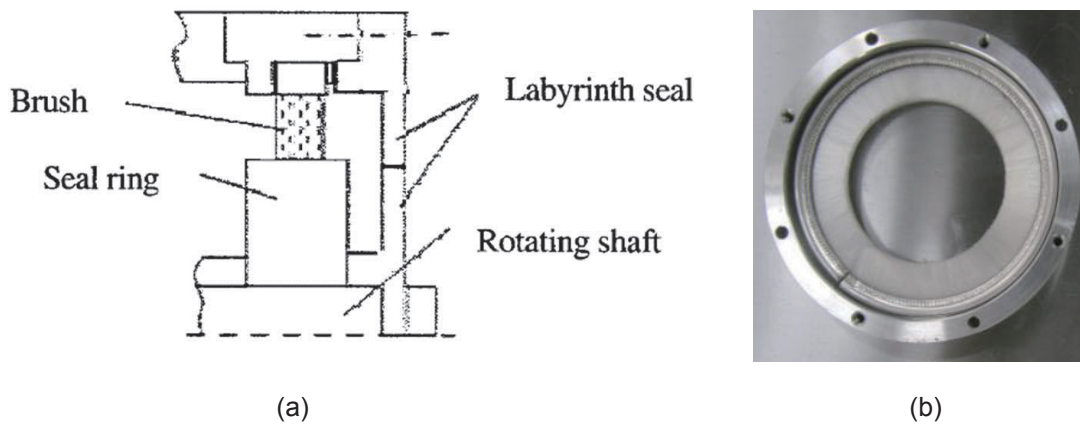


Figure 1.16 (a) Diagram of sealing system consisting of a labyrinth seal and a brush seal, and (b) photograph of a brush seal; obtained from literature [113, 114] and modified.

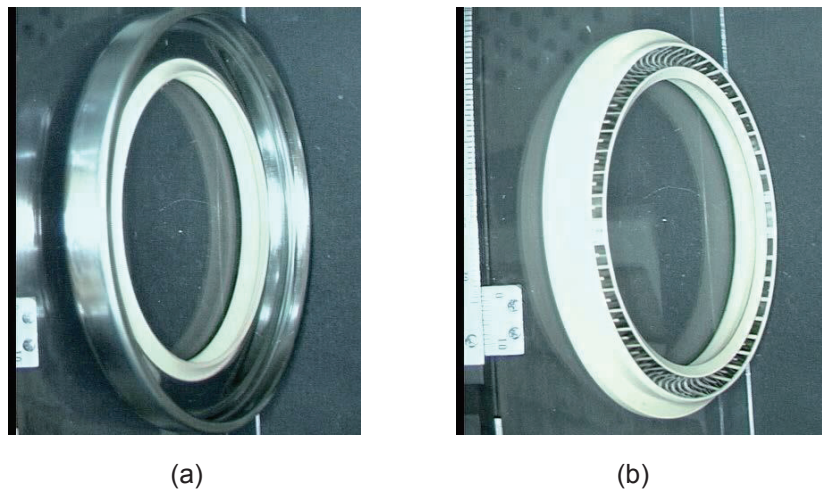


Figure 1.17 Photographs of (a) Varilip[®] and (b) Variseal[®]; obtained from literature [115] and modified.

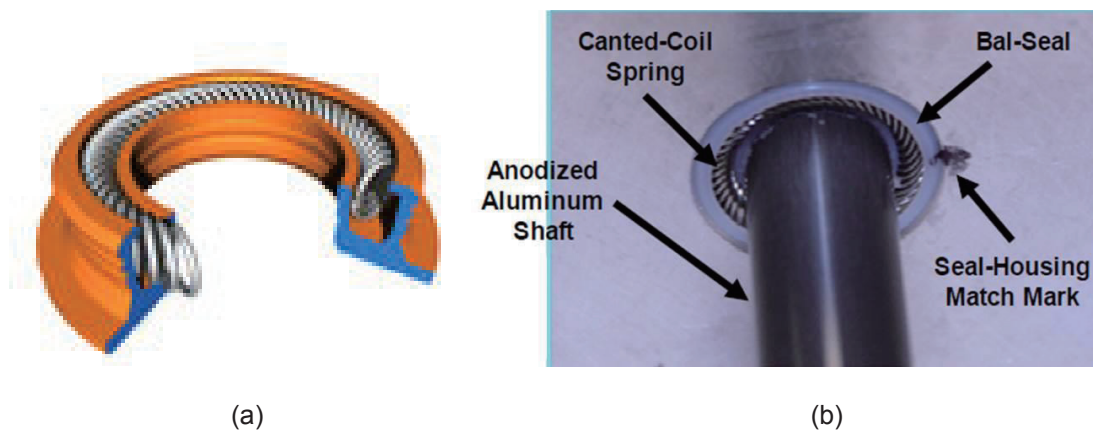


Figure 1.18 (a) Schematic of a Bal Seal[®] and (b) rotary shaft of approximately 19 mm in diameter equipped with the Bal Seal[®]; obtained from literature [116] and modified.

To support the mechanical shields and connectors and extend their lifetimes, new technology is needed to prevent the dust from coming in to contact with the mechanical systems. To achieve this, the electrostatic shield system is developed in this study. The electrostatic system utilizes the Coulomb force and the dielectrophoresis force to remove the particles that may intrude into the mechanical gaps. The electrostatic system has some advantages, such as no mechanical drives, easy control, low-power consumption, and adaptability to mechanical systems. It is expected that the electrostatic system can increase the lifetime of the mechanical shields and connectors for long-term exploration missions on the Moon and Mars.

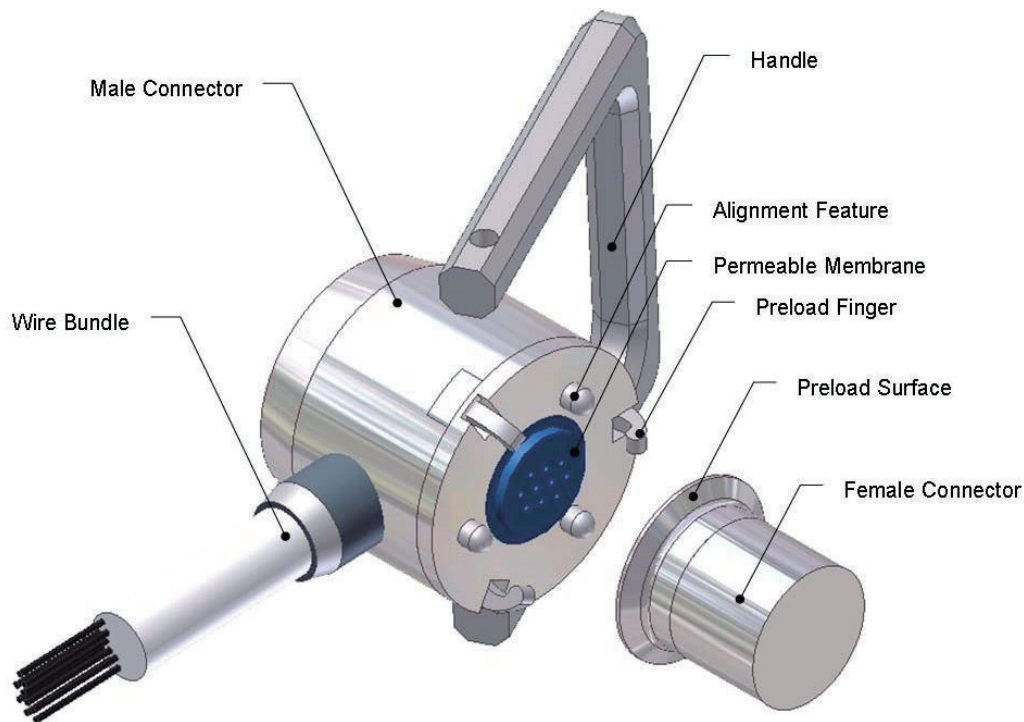


Figure 1.19 Concept of the Dust-Tolerant Connector developed by Honeybee Robotics; obtained from literature [117].

1.3.3 Development of Size-Sorting System for ISRU Missions

Before conducting ISRU processes, a particle size-sorting system will play an important role in improving ISRU performance [59]. The required particle size depends on the objective of the ISRU missions, because the components and properties of the lunar regolith changes with the diameter of the particle [118], as shown in Figure 1.20. In addition, to improve the efficiency of chemical processing in ISRU and to stabilize performance, particles in a particular size range have to be supplied continuously. Although the size sorting of particles by size in any range is acceptable, that of small particles is significant for ISRU. Lunar regolith particles smaller than $10\ \mu\text{m}$ in diameter contain relatively rich amounts of np-Fe^0 , as shown in Figure 1.20. Owing to the existence of np-Fe^0 , lunar regolith is expected to be a strong microwave absorber. It is expected to shape and form a brick from the regolith by sintering it using “hot pressing” [119, 120]. The microwave

can easily melt np-Fe^0 and quickly fuse the particles with each other, thereby creating aggregates with high strength, as shown in Figure 1.21. The aggregates can be used as a lunar construction material for landing pads, paved roads, and habitats on the Moon. During hot pressing, the extraction of small particles containing rich amounts of np-Fe^0 from the bulk of the lunar regolith is crucial. Furthermore, using small particles is important for improving chemical processing in ISRU, because the surface area of a particle is large compared with its mass, and the reaction rate of the process is high [59, 121]. For the purpose of ISRU as well as for scientific surveying, it is necessary to prepare a large amount of small particles to be used for toxicity tests on astronauts for future manned explorations.

For the above reasons, the development of a size-sorting system for small particles used in the lunar environment is one of the most important challenges, as the system must be adaptable to the harsh environment, such as dust contamination of equipment, limited power source, and non-existence of gas and liquid. To this end, a unique size-sorting system that utilizes the electrostatic traveling wave is developed to extract small particles. The electrostatic traveling wave was developed mainly in the industrial field of electrophotography to transport toner particles as described in section 1.2.2, and this study will introduce size-sorting as a new function of the technology.

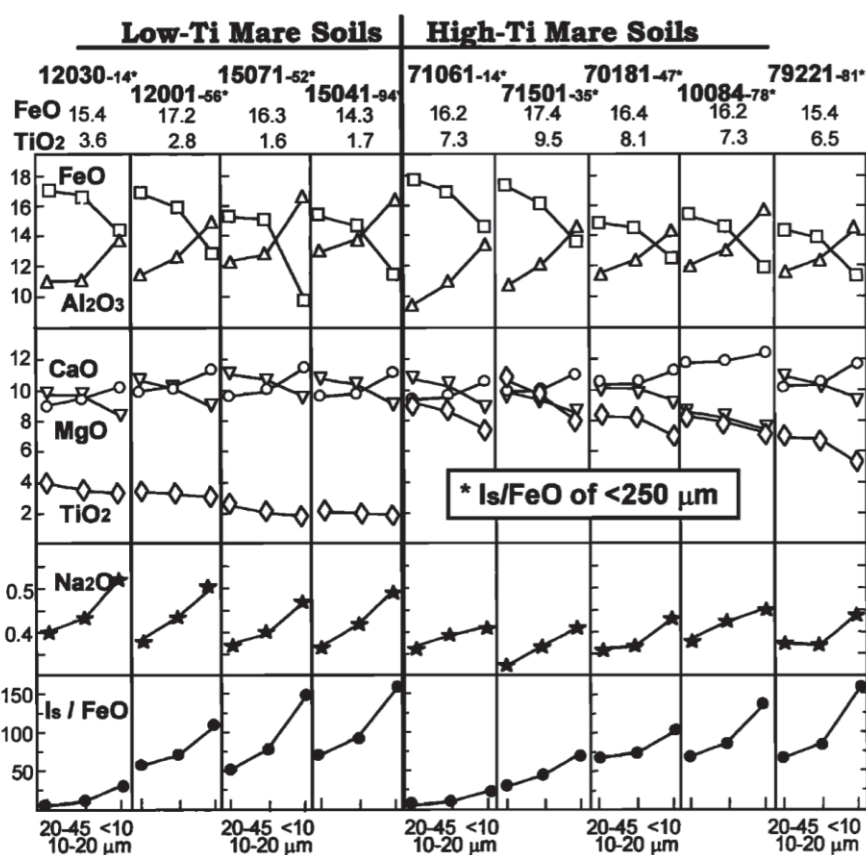


Figure 1.20 Chemistry of fine size fractions of lunar mare regolith; obtained from literature [118]. Regolith is divided into high-Ti and low-Ti types. Relative abundance of np-Fe^0 is expressed as Is, and FeO expresses total iron content of regolith size fraction.

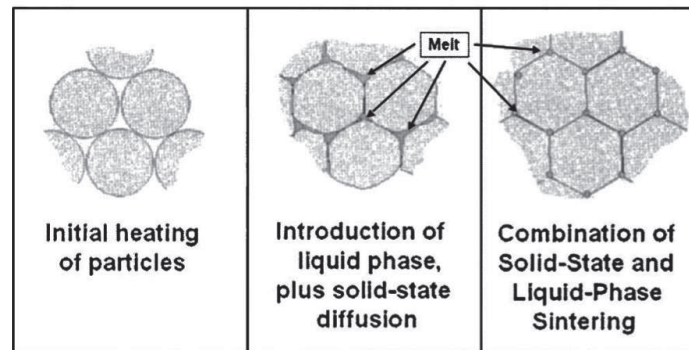


Figure 1.21 Diagram of the sintering process of lunar regolith; obtained from literature [120]. Development of transient liquid phase is caused by $np\text{-Fe}^0$.

1.3.4 Development of Sampling System for Sample Return Missions

To obtain information about the formative history of asteroids and the solar system, as well as the origin of life, it is necessary to collect samples from asteroids and return them to the Earth, as described in section 1.1.1. The development of a sampling system that works effectively on the surface of an asteroid is critical to the success of a sample return mission. In the Hayabusa mission, the Hayabusa spacecraft was equipped with an impact-sampling system for sample collection [122]. This system was intended to fire a small bullet at the surface of an asteroid and capture the resulting regolith spray, using its deployable collection horn, as shown in Figure 1.22. This system is adaptable to any surface condition, such as hard bedrock and regolith; therefore, the sampling system was appropriate for use in Hayabusa, because asteroid Itokawa's surface condition was unclear from Earth-based observation. However, this system is very challenging because it requires a series of accurate and autonomous operations (i.e., landing on the asteroid, firing the bullet, and collecting samples) to be accomplished within a short duration without delay. In reality, the bullet was not fired at all owing to a slight error, and only a few floating particles were collected (possibly as a result of the Hayabusa touchdown operation). The bullet firing system mounted on Hayabusa was also used for Hayabusa-2. Although its design is similar to that of Hayabusa, a new component was installed in the Hayabusa-2 [124]. Hayabusa-2 was designed to create an artificial crater on the surface of asteroid 1999 JU3 by using a small explosive and metal liner as a projectile, before collecting the samples to expose the internal materials and structures, as shown in Figure 1.23. The samples of exposed regolith were collected in a capsule. The Small Carry-on Impactor system also requires precise autonomous control. As with other sampling systems, some mechanical and pneumatic sampling methods used during touchdown have been developed, such as tethered sampling [125, 126], adhesive-based sampling [123], brush wheel sampler [127], bucket drum regolith excavator [128], and the touch-and-go sample acquisition mechanism (TAGSAM) that was installed in OSIRIS-REx [19].

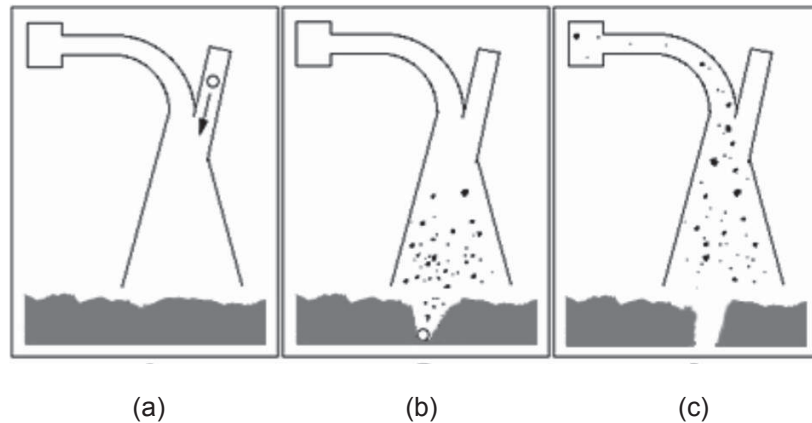


Figure 1.22 Diagram of the sampling method mounted on the Hayabusa spacecraft; obtained from literature [123]: (a) firing projectile, (b) breaking surface, and (c) collecting surface spray.

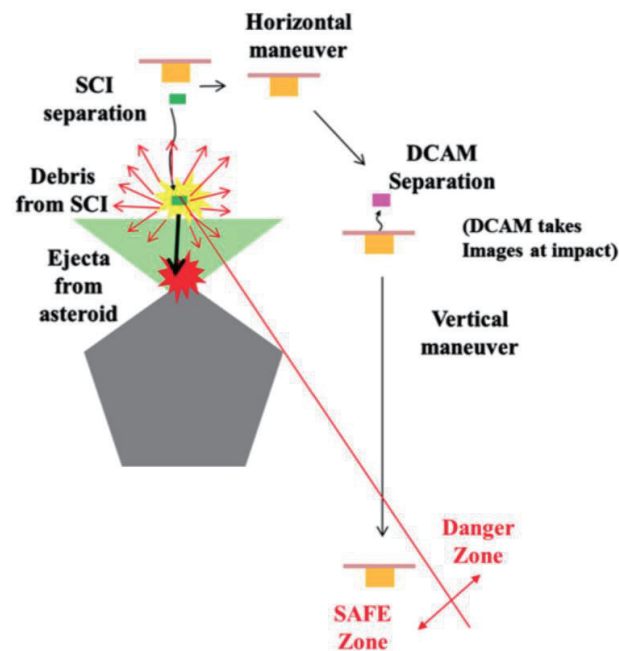


Figure 1.23 Outline of impact operation of Small Carry-on Impactor System in Hayabusa-2; obtained from literature [124]. Mother spacecraft escapes to avoid fractions ejected from asteroid 1999 JU2.

Instead of a sampling system used during touchdown, when a spacecraft lands on the asteroid surface, scooping [129] and drilling [130, 131] methods can be used efficiently in long-term operations because they can collect a large amount of samples from the surface and subsurface of an asteroid, and can be adapted to any surface condition, including ice and hard surfaces. For example, in the Rosetta mission [15], the Philae lander was equipped with a drilling for collecting nucleus samples of a comet [66], as described in section 1.2.1. Although these methods require a successful landing on the asteroid surface, they are most suitable when the target surface condition is well-known, as would be the case, for example, on the Moon

and Mars. As discussed above, each sampling system has some advantages and disadvantages, and a selecting an appropriate system that is adaptable to the target surface conditions is necessary for a successful sample return mission. However, in space missions, it is difficult to predict incidents that may occur and prevent normal sampling operations. It is also difficult to prepare for them in advance, as in the case of the Hayabusa mission. In addition to selecting an appropriate sampling method for an objective surface condition, a reliable method with simple configuration and easy control configuration is necessary for ensuring sample collection under any condition.

In this study, an electrostatic sampler and a magnetic sampler are developed as sampling systems with high reliability in the space environment. Because the regolith particles on asteroids are expected to be electrostatically charged by solar wind and cosmic rays, the electrostatic sampler uses the Coulomb and dielectrophoresis forces to capture the particles and transport them to a collection capsule. On the other hand, the magnetic sampler utilizes the mechanism of the magnetic coil gun to collect samples [104-106]. Although a powder processing system that utilizes the magnetic force has been used on the Earth in previous studies [100-103], a magnetic sampling system of particles has not been developed yet. It was confirmed that magnetic particles exist on the surface of asteroids and planets, such as on Itokawa, the Moon, and Mars [21-22, 38], and the magnetic sampler is expected to work effectively in these environments. The mechanisms of electrostatic and magnetic samplers are simple, and the samplers do not require mechanical drives and complicated controls, which make them highly reliable in space missions.

1.3.5 Development of Regolith Transport System in Space Environment

In lunar and Mars exploration missions, ISRU, and sample return missions, the transport of regolith particles from one place to another is a fundamental process; however, the amount of the particles and the transport distance depends on the objective of using the particles. For example, in the construction of a lunar base, a large amount of particles are collected from an excavation site and transported to a silo near the construction site; then, the stored particles are used as the construction materials. In addition, to synthesize regolith particles and extract precious resources during ISRU, the regolith particles must be transported to the location where chemical processing is conducted. Moreover, collected asteroid samples have to be transported from the sampler to the container to keep the particles from being contamination with impurities. For these requirements, mechanical and pneumatic transport systems have been considered, including bucket ladders, conveyer belts, augers, and gas transfer systems, as described in section 1.2.1 [68-71]. Although these mechanical systems can transfer large amount of regolith, the system must be equipped with mechanical drives, and malfunctions caused by small dust particles have been a concern. The gas transfer system can fluidize the regolith by using pressurized gas nozzles, and can transfer heat to or from the regolith. Therefore, the system is compatible with chemical processing in ISRU to improve the performance. In addition, the system does not require mechanical drives, and the gas purified using a filter can be reused. However, the gas must

be handled carefully to prevent leakage, and the system should be equipped with a pump, which requires a mechanical drive to maintain the gas flow for long-term operation. In addition, a magnetic transport system has been proposed for space missions, as shown in Figure 1.24 [132]. Although the transport systems do not require mechanical drives and the systems have high reliability in space, the magnetic force cannot be applied to non-magnetic materials.

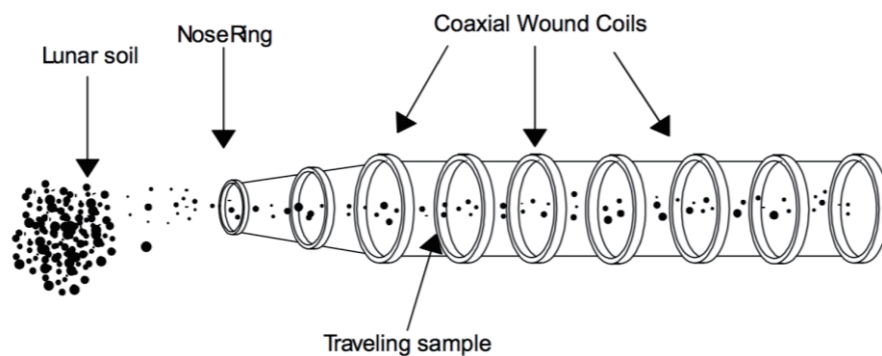


Figure 1.24 Schematic of magnetic transport system, obtained from literature [132]. Coaxial rings are sequentially powered up and down to transport magnetic particles.

Although the transport systems described above have some advantages and can be used in a specific area where the advantages of the system can be utilized efficiently, it is necessary to develop a new transport system that can be used for a wide range of space applications for long durations without serious problems. The requirements of the new system include high tolerance to dust contamination, simple configuration, and the ability to transport large amount of particles regardless of type. In this study, a reliable transport technology, which utilizes the mechanism of vibration transport, is developed. The mechanism of vibration transport is simple. The solid parts that contact particles, such as the plate and tube, are vibrated using actuators, and the vibration pushes the particles in one direction repeatedly. Although this mechanism has been utilized in industries, such as food processing and drug development, because it can carry a large amount of particles regardless of the particle type, the system has not been sufficiently investigated for space applications. In a previous study [71], a spiral elevator using a vibration mechanism was developed by NASA, as shown in Figure 1.25. This device uses vibration to toss a material in a forward direction up an inclined spiral ramp without damaging the material. Although the spiral elevator could feasibly transport the JSC-1A lunar regolith simulant, the system was too massive and oversized, and detailed research has not been conducted. Moreover, the system was equipped with shaker motors to produce the vibration; thus, mechanical malfunctions have to be considered. In this study, a simple vibration transport system equipped with actuators, which have no mechanical drives and has a high tolerance for dust contamination, is developed for space applications, and the transport performance is investigated in detail.



Figure 1.25 Photograph of particle layers transported by the outlet of a spiral elevator; obtained from literature [71].

1.4 Structure of Dissertation

This research centers on the dynamics of electromagnetic particles in space environments, and this dissertation consists of eight chapters, as shown in Figure 1.26. The first chapter includes the introduction that has already explained the objective and position of the research.

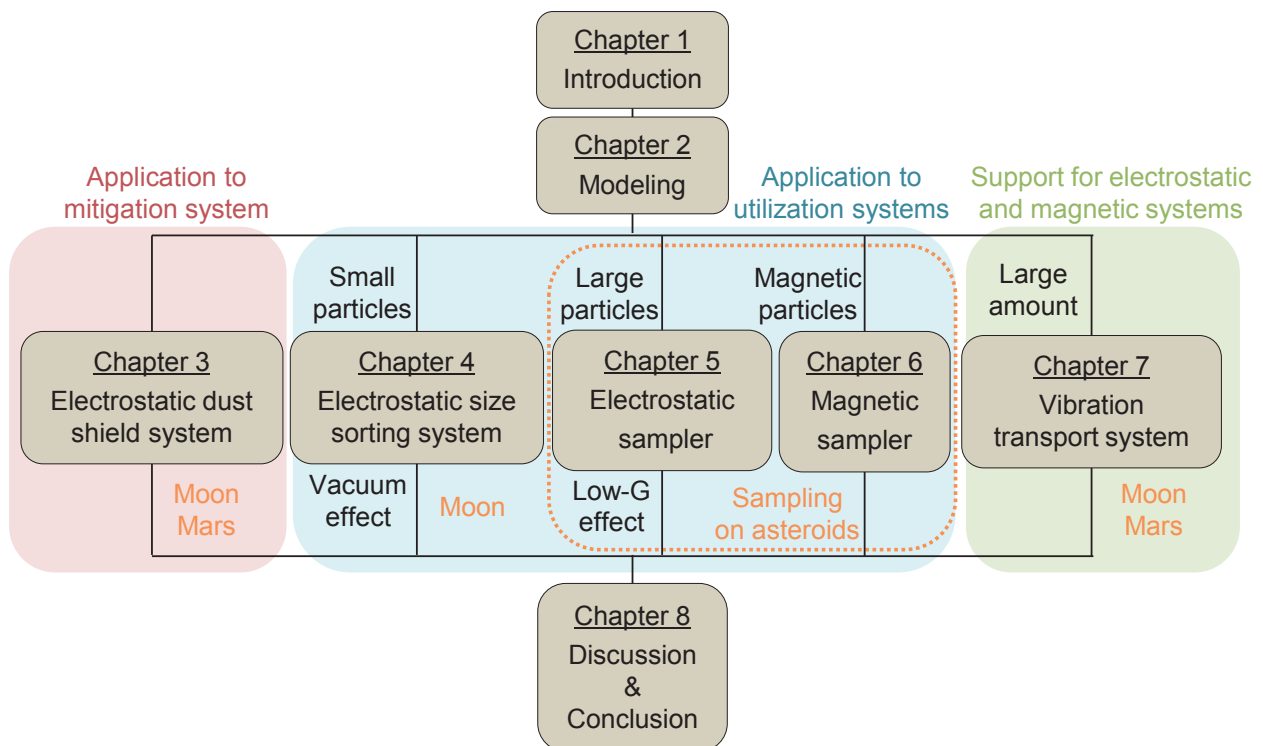


Figure 1.26 Diagram of dissertation structure.

In the second chapter, the theoretical equations for the external forces acting on the electromagnetic particle, and the theoretical model of the particle motion, are summarized. To consider the characteristics of actual particles in the equations, such as mechanical, electrostatic, and magnetic properties of the lunar regolith particle, model experiments were conducted to obtain the properties. Then, the balance of the forces acting on a single particle in a resting state was calculated. The calculation result could reveal the dominant factors that control the dynamics of the particle. A numerical calculation using the DEM, which is important for the completion of this research, is developed based on the theoretical model, and the algorithm and procedure are described here. A new calculation model for the mechanical interaction between particles is developed to reduce the calculation load. The calculation result of the theoretical model and numerical calculation method are used in later chapters of this dissertation. The main achievement of this chapter is that the fundamental theory of electromagnetic particle dynamics in the space environment has been constructed for the first time. In addition, the new calculation model of the DEM modified for this research can contribute to the field of numerical calculation for particle dynamics.

Application technologies for handling electromagnetic particles are described in chapters three through seven. This dissertation focuses on lunar, Martian, and asteroid regolith, whose properties are summarized in section 1.1.2, and the handling technologies that are applied to those particles. In the third chapter, an electrostatic dust shield system is developed to prevent lunar and Martian dust particles from intruding into the mechanical gaps of extravehicular equipment. In addition, the terrestrial performance of the lunar regolith simulant is investigated experimentally to clarify fundamental effects of electrostatic parameters, including the effect of charge density of the particle on the motion. The accuracy of the calculation method is confirmed by comparing the experimental results and numerical calculations. The calculation predicted the performance of the system in the lunar and Martian environments. A unique and unprecedented point in the third chapter is that the electrostatic force is used as the dust shield system.

In the fourth chapter, an electrostatic size-sorting system is developed to extract small particles of lunar regolith for future ISRU missions. During the development process, the effect of air drag on particle dynamics is investigated because air drag has a major effect on small particles. The difference between size-sorting performance in air and in a vacuum is calculated numerically, and an experiment is conducted in a vacuum. From the results of the experiments and calculations, the effect of vacuum environment on the motion of electromagnetic particles is confirmed. Finally, size-sorting performance and the feasibility of its application on the Moon are described.

The descriptions of an electrostatic sampler and a magnetic sampler are provided in the fifth and sixth chapters, respectively. These devices were developed to achieve a reliable sampling of regolith particles from an asteroid surface for future sample return missions. The electrostatic sampler utilizes the Coulomb force and dielectrophoresis force. The performance in a low-gravity environment is investigated using numerical calculations and model experiments in 0.01-G, reproduced by the parabolic flight of an aircraft. In the development process, several particle types with different sizes are sampled, and the effect of gravity on

particle size is clarified. In addition, the dielectrophoresis force becomes larger with respect to the particle size; therefore, the effect of particle conductivity on the dielectrophoresis force applied to large particles is also investigated. Finally, in the fifth chapter, the feasibility of the electrostatic sampler in negligible gravity on asteroid surfaces is explored. In the sixth chapter, the development of a magnetic sampler employing a coil gun mechanism is explained. A sampling is experimentally performed in air and in a vacuum by using the magnetic system, and sampling in low gravity is predicted using numerical calculations. From the results, the magnetic interaction of magnetically polarized particles is clarified and the fundamental characteristics of the sampling on the Earth and in space environments are confirmed.

In the seventh chapter, two types of vibration transport systems are developed to transport large quantities of particles in space environments. First, the feasibility of vibration transport is investigated by a simple calculation involving a model of single particle on a vibrating plate. The calculation results indicate the fundamental characteristics of particle dynamics on a vibrating plate, and the potential for transporting large amounts of particles in both the horizontal and oblique directions. Based on the calculation results, a unique vibration transport system that utilizes a dielectric elastomer actuator (DEA) as the excitation device is developed. The actuator is excited only by the electrostatic force with no mechanical drives, and the transport performance in the horizontal direction is experimentally investigated. In addition, another vibration transport system using electromagnetic force as an excitation actuator is developed; this actuator also does not require the use of mechanical drives. In the development of this transport system, the transport performance in the oblique direction is clarified. Moreover, as an extension of the vibration transport system, the combinations of the electrostatic sampler and magnetic sampler are considered.

The range of potential applications for the handling technologies described in Chapters 3–7 are summarized in Table 1.3. The lunar and Martian simulants are mainly used for convenience in this dissertation, and the basic properties are described in section 1.1.2. In the eighth chapter, the effect of vacuum and small gravity on the particle dynamics is discussed, considering the experimental and calculation results achieved in Chapters 3–7. Finally, the conclusion of this research and the future plan are described here.

Table 1.3 Range of applications for the handling technologies described in Chapters 3–7.

Handling technologies	Particle properties	Usages	Research Objective
Electrostatic dust shield system (Chapter 3)	<ul style="list-style-type: none"> • lunar and Martian regolith • dust size 1–100 μm • relative permittivity: 3.0–4.5 	<ul style="list-style-type: none"> • Moon (1/6-G, high vacuum) • Mars (1/3-G, high vacuum) • mitigation of regolith 	<ul style="list-style-type: none"> • effect of particle charge density • basic characteristic of electrical parameters
Electrostatic size-sorting system (Chapter 4)	<ul style="list-style-type: none"> • lunar and Martian regolith • dust size 1–100 μm in particular, < $\sim 10 \mu\text{m}$ • relative permittivity: 3.0–4.5 	<ul style="list-style-type: none"> • Moon (1/6-G, high vacuum) • utilization of regolith 	<ul style="list-style-type: none"> • effect of vacuum on small particle
Electrostatic sampler (Chapter 5)	<ul style="list-style-type: none"> • lunar and Martian regolith • particles 1–10 mm • relative permittivity: 3.0–4.5 • conductive and insulative 	<ul style="list-style-type: none"> • Asteroid ($\mu\text{-G}$, high vacuum) • utilization of regolith 	<ul style="list-style-type: none"> • effect of low-G on large particle • effect of particle conductivity on dielectrophoresis force
Magnetic sampler (Chapter 6)	<ul style="list-style-type: none"> • magnetic particles • relative permeability: ~ 4 • several tens micrometers 	<ul style="list-style-type: none"> • Asteroid ($\mu\text{-G}$, high vacuum) • utilization of regolith 	<ul style="list-style-type: none"> • basic characteristic of magnetic parameters • effect of magnetic interaction between particles
Vibration transport system (Chapter 7)	<ul style="list-style-type: none"> • lunar and Martian regolith • size 1 μm to 1 mm • regardless of particle composition 	<ul style="list-style-type: none"> • Moon (1/6-G, high vacuum) • Mars (1/3-G, high vacuum) • support for electrostatic and magnetic systems 	<ul style="list-style-type: none"> • basic characteristic of vibration • combination with electrostatic and magnetic samplers

Chapter 2 Dynamics of Electromagnetic Particles

2.1 Introduction

In this chapter, the theoretical equations for the external forces acting on a particle in an electromagnetic field are described, and the particle motions affected by the forces in the Earth and space environments are predicted. After conducting several model experiments to obtain the parameters of lunar regolith, the balance of forces acting on a particle in a resting state is calculated by considering the characteristics of the actual particle in the equations. In subsequent chapters, several electrostatic and magnetic handling technologies for particles are developed based on insights obtained from these calculations. In addition, a numerical calculation using the DEM is developed based on theoretical equations. This is critical to the development of the handling technologies and for the prediction of the performance in space environments. The calculation methodology and algorithm are described here. Because the conventional algorithm of the DEM requires a large calculation load, a new calculation model for the mechanical interaction between particles is proposed to reduce the calculation load.

2.2 Basic Equations

The motion equations of the i -th particle with six degrees of freedom, including rotations are represented as Equations (2.1) and (2.2).

$$m_i \ddot{\mathbf{x}}_i = \sum_j \mathbf{F}_{ij} \quad (2.1)$$

$$I_i \ddot{\boldsymbol{\theta}}_i = \sum_j \mathbf{M}_{ij} \quad (2.2)$$

where m , \mathbf{x} , I , $\boldsymbol{\theta}$, \mathbf{F} , and \mathbf{M} are the particle mass, positional coordinate (x , y , z), particle inertia, rotational coordinate ($\boldsymbol{\theta}_x$, $\boldsymbol{\theta}_y$, $\boldsymbol{\theta}_z$), external force, and external torque, respectively. The subscript j represents the type of force applied to i -th particle. The equations show that particle motion is affected by the summation of the external forces \mathbf{F} and torques \mathbf{M} . The Coulomb force, dielectrophoresis force, magnetic force, adhesion force, gravitational force, air drag, and mechanical interaction forces generated during contacts with other objects mainly affect particle dynamics in the electrostatic and magnetic fields. Balancing the external forces acting on a particle in the electrostatic and magnetic fields is crucial for the handling of particles using electrostatic and magnetic forces. Therefore, as a first step, the forces acting on the particle are calculated by assuming the property of the lunar regolith, and also by assuming the effects of the space environments, such as vacuum and low gravity. Then, an evaluation of the balance of the forces is performed. Assuming simple particle dynamics as shown in Figure 2.1, when the electrostatic and magnetic forces, which consist of the Coulomb

force, dielectrophoresis force, and magnetic force, exceed the adhesion and gravitational forces toward the ground, the particles start to float perpendicularly to the ground if the mechanical force is neglected. The floating particles move along the direction of the electrostatic and magnetic forces, disturbed by the gravitational force and air drag. If the particle touches the ground, the adhesion force is produced again between the particle and the ground. Therefore, it is important to understand the balance of forces to control particle motion, and the utilization of estimated balance is important for developing handling technologies for particles.

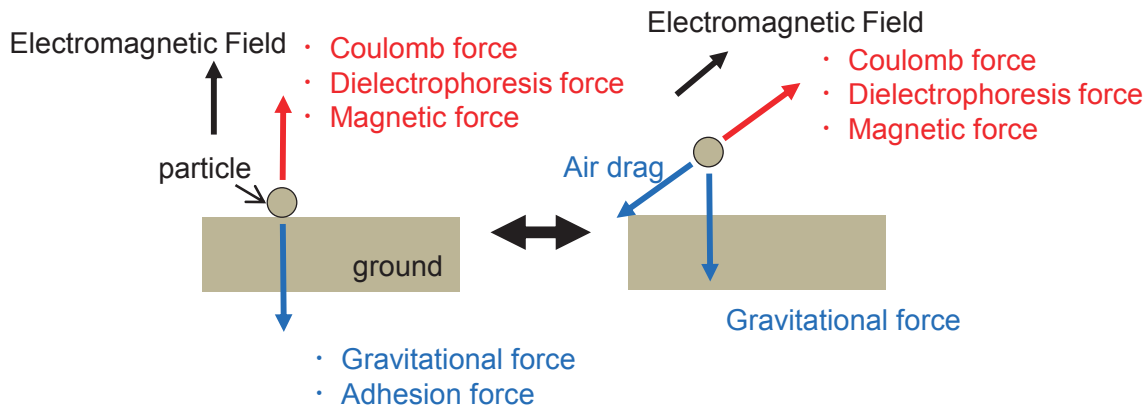


Figure 2.1 Simplified particle dynamics in electrostatic and magnetic fields.

2.3 External Forces Acting on Particles

2.3.1 Coulomb Force

The Coulomb force acting on the i -th particle is represented by Equation (2.3) [1].

$$\mathbf{F} = q_i \mathbf{E} \quad (2.3)$$

Here, q and \mathbf{E} are the particle charge and electrostatic field, respectively. A particle can be electrostatically charged by tribocharging during contact with other objects, and by using an electron gun and corona discharge on the Earth. In space environments, particles are charged through irradiation by positive and negative ions, electrons, and protons, which are included in the cosmic ray and solar wind [2, 3]. In addition, a particle is exposed to solar light and electrons are ejected from the particle, resulting in a positively charged. When electrons collide with a particle, the secondary electrons are ejected from the particle, and the ejected electrons affect other particles electrostatically. Lunar and Martian regolith contains many components, and each particle has its own specific tendency for electrification [4]. Thus, it is assumed that the particles are charged by several factors in space. However, the particle surface is not charged uniformly and it has been assumed that the charges are heterogeneously distributed on the particle surface [5]. Considering that the particle size is substantially small compared to the non-uniformity of the electrostatic field \mathbf{E} , the particle charge q can be assumed to represent the total charges distributed on the particle surface. In this research, the charge q is as-

sumed to be the total charge, and its position is assumed to be at the center of the particle. Moreover, the torque of the Coulomb force can be neglected.

The electrostatic field \mathbf{E} is generated by applying a voltage to electrodes and by the electrostatic charge q . The field \mathbf{E} is determined by the gradient of the electric potential ϕ of voltage V , as represented by Equation (2.4) [6].

$$\mathbf{E} = -\nabla\phi \quad (2.4)$$

The potential ϕ can be calculated by the Poisson equation or Laplace equation, as shown by Equations (2.5) or (2.6), respectively.

$$\nabla \cdot (\varepsilon_r \varepsilon_0 \nabla \phi) = q \quad (2.5)$$

$$\nabla \cdot (\varepsilon_r \varepsilon_0 \nabla \phi) = 0 \quad (2.6)$$

where ε_r and ε_0 , are the relative permittivity and permittivity of free space (8.85×10^{-12} F/m), respectively. If the charge q exists, the Poisson equation is applied; otherwise, the Laplace equation is applied. If the geometry of the experimental setup is simple, the electrostatic field can be calculated using Equations (2.5) and (2.6) analytically. In case of a complex experimental setup, the field \mathbf{E} can be calculated numerically assuming the boundary conditions of the setup.

2.3.2 Dielectrophoresis Force and Magnetic Force

Because the mechanism of the dielectrophoresis force is similar to that of magnetic force acting on the particle [7], the theories are explained in this section. If a particle exists in the electrostatic field \mathbf{E} or in the field of the magnetic flux density \mathbf{B} , the electrostatic or magnetic dipole moments are generated in the particle, respectively, as shown in Figure 2.2. The dielectrophoresis force and the magnetic force are produced by the dipole moments in the particle [7].

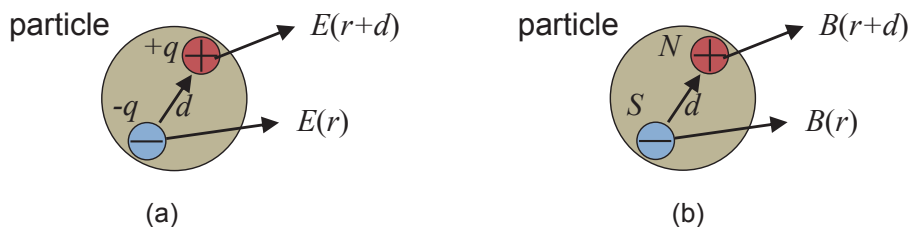


Figure 2.2 Dipole moments of a particle, which are generated in (a) electrostatic and (b) magnetic fields.

If the electrostatic field \mathbf{E} is non-uniform, it can be assumed that the dipole, which consists of two charges with an equal and opposite polarity over a small distance d , is created as shown in Figure 2.2 (a). Using Equation (2.3), the Coulomb force acting on the dipole moment of the particle can be represented by

Equation (2.7).

$$\mathbf{F} = q\mathbf{E}(\mathbf{r} + \mathbf{d}) - q\mathbf{E}(\mathbf{r}) \quad (2.7)$$

Here, \mathbf{r} is the position vector of the negative part of the dipole. Because the distance \mathbf{d} is much smaller than the non-uniformity of the electrostatic field \mathbf{E} , the field \mathbf{E} at the position of $\mathbf{r} + \mathbf{d}$ can be modified using the Taylor expansion. The higher orders can be neglected over the second order, and Equation (2.7) can be arranged as Equation (2.8).

$$\mathbf{F} = (q\mathbf{d} \cdot \nabla)\mathbf{E}(\mathbf{r}) \quad (2.8)$$

Assuming the dipole moment $\mathbf{p}_{ele} = q\mathbf{d}$, Equation (2.8) is modified as Equation (2.9).

$$\mathbf{F} = (\mathbf{p}_{ele} \cdot \nabla)\mathbf{E} \quad (2.9)$$

The force in Equation (2.9) is the dielectrophoresis force. Assuming that torque is exerted by the electrostatic field and the dipole moment, the torque is expressed by Equation (2.10).

$$\mathbf{M} = \frac{\mathbf{d}}{2} \times q\mathbf{E} + \frac{-\mathbf{d}}{2} \times (-q\mathbf{E}) \quad (2.10)$$

Substituting the dipole moment \mathbf{p}_{ele} , Equation (2.10) is modified as Equation (2.11).

$$\mathbf{M} = \mathbf{p}_{ele} \times \mathbf{E} \quad (2.11)$$

The dipole moment \mathbf{p}_{ele} is also represented by Equation (2.12) [7], and the dielectrophoresis force is expressed as Equation (2.13) conventionally by substituting Equation (2.12) into Equation (2.9).

$$\mathbf{p}_{ele} = 4\pi\epsilon_0 \frac{\epsilon_r - 1}{\epsilon_r + 2} R^3 \mathbf{E} \quad (2.12)$$

$$\mathbf{F} = \left(4\pi\epsilon_0 \frac{\epsilon_r - 1}{\epsilon_r + 2} R^3 \mathbf{E} \cdot \nabla \right) \mathbf{E} \quad (2.13)$$

where R is the particle radius. Considering Equation (2.4), (2.14), and (2.15), Equation (2.13) is simplified as Equation (2.16).

$$(\mathbf{E} \cdot \nabla)\mathbf{E} = (\nabla \times \mathbf{E}) \times \mathbf{E} + \frac{1}{2}(\nabla E^2) \quad (2.14)$$

$$\nabla \times (-\nabla \phi) = 0 \quad (2.15)$$

$$\mathbf{F} = 2\pi\epsilon_0 \frac{\epsilon_r - 1}{\epsilon_r + 2} R^3 \nabla E^2 \quad (2.16)$$

By similarity, the magnetic force and torque can be represented by Equations (2.17) and (2.18), respectively.

$$\mathbf{F} = (\mathbf{p}_{mag} \cdot \nabla) \mathbf{B} \quad (2.17)$$

$$\mathbf{M} = \mathbf{p}_{mag} \times \mathbf{B} \quad (2.18)$$

The magnetic dipole moment \mathbf{p}_{mag} is represented by Equation (2.19), and the magnetic force is expressed as Equation (2.20) conventionally by substituting Equation (2.19) into Equation (2.17).

$$\mathbf{p}_{mag} = \frac{4\pi}{\mu_0} \frac{\mu_r - 1}{\mu_r + 2} R^3 \mathbf{B} \quad (2.19)$$

$$\mathbf{F} = \left(\frac{4\pi}{\mu_0} \frac{\mu_r - 1}{\mu_r + 2} R^3 \mathbf{B} \cdot \nabla \right) \mathbf{B} \quad (2.20)$$

where μ_r and μ_0 are the relative magnetic permeability of the particle and the magnetic permeability of free space (1.25×10^{-6} H/m), respectively. The magnetic flux density \mathbf{B} can be calculated assuming the vector potential \mathbf{A} , as in Equation (2.21).

$$\mathbf{B} = \nabla \times \mathbf{A} \quad (2.21)$$

In addition, the derivative system of Ampere's law is shown as Equation (2.22).

$$\nabla \times \mathbf{B} = \mu_0 \mathbf{j} \quad (2.22)$$

Here, \mathbf{j} is the electric current density. By combining Equations (2.21) and (2.22), Equation (2.23) is derived.

$$\nabla \times (\nabla \times \mathbf{A}) = \mu_0 \mathbf{j} \quad (2.23)$$

Equation (2.23) is rearranged by substituting Equations (2.24) and (2.25), and then Equation (2.26) can be derived.

$$\nabla \times (\nabla \times \mathbf{A}) = \nabla (\nabla \cdot \mathbf{A}) - \nabla^2 \mathbf{A} \quad (2.24)$$

$$\nabla \cdot \mathbf{A} = 0 \quad (2.25)$$

$$\nabla^2 \mathbf{A} = -\mu_0 \mathbf{j} \quad (2.26)$$

Equation (2.26) is the Poisson equation about the vector potential \mathbf{A} . After calculating vector potential \mathbf{A} , the field of the magnetic flux density \mathbf{B} can be determined by calculating the rotation of the potential \mathbf{A} . The magnetic field is calculated conventionally using numerical calculations.

2.3.3 Adhesion Force

The adhesion force mainly consists of the non-electrostatic adhesion force and the electrostatic adhesion force. For the non-electrostatic adhesion force, the Van der Waals force and the liquid bridge force are well known, and studies on these forces have been widely conducted in the field of electrophotography. The Van der Waals force occurs between atoms, ions, and molecules as an attractive force, and it is applied when any material comes into contact with another object. The Van der Waals force between the i -th particle and k -th object is expressed by Equation (2.27) [8].

$$\mathbf{F} = \frac{H}{6h^2} \left(\frac{R_i R_k}{R_i + R_k} \right) \mathbf{n}_{ik} \quad (2.27)$$

where H , h and \mathbf{n} are the Hamaker constant, and the gap between particle surfaces, and the unit normal vector from the i -th particle to the k -th object, respectively. In addition, the liquid bridge force occurs at the point where the liquid bridge is generated between two objects in a highly humid environment. If there is no moisture or liquid, as in the space environment, the force does not exist. The liquid bridge force between the k -th object to the i -th particle is expressed using Equation (2.28) [8].

$$\mathbf{F} = 4\pi\sigma R_i \cos\theta_c \mathbf{n}_{ik} \quad (2.28)$$

Here, σ and θ_c are the surface tension and contact angle of liquid, respectively. The forces easily vary when the particle has an irregular surface or the contact conditions between the particle and object vary. Although some models that consider the influence of these factors have been developed, it has been confirmed that the measured adhesion force is significantly different from the theoretical calculation models.

The image force is often considered to be the electrostatic adhesion force. If a charged particle is close to conductive and insulative objects, the particle evokes a charge that has an equal and opposite value of the polarity of the contacting objects, and an attractive force occurs between the particle charge and the induced charge. The image force between the i -th particle, which has charge q , and the k -th object is expressed using Equation (2.29) [8].

$$\mathbf{F} = -\frac{Zq^2}{16\pi\epsilon_0 R_i^2} \left(\frac{\epsilon_0 - 1}{\epsilon_0 + 1} \right) \mathbf{n}_{ik} \quad (2.29)$$

Here, Z and ϵ_0 are the correction coefficient depending on the permittivity of the objects, and the relative permittivity of the k -th object, respectively. Although Equation (2.29) deems that the particle is charged uniformly, the electrification process is complex and the charges are distributed on the particle surface as stated in section 2.3.1. Therefore, it has been confirmed that the measured adhesion force is significantly different from the theoretical calculation. Recently, the charge patch model that takes into account the distributed charges has been developed, and the model can reproduce the experimentally measured value fairly well [8]. However, the adhesion force is easily altered by changes in contact type and electrification conditions.

Therefore, the adhesion force is affected by many factors. It is not stable and is easily altered. For simplicity, the adhesion force is assumed as Equation (2.30) in this research, which is Equation (2.27) modified to incorporate the correction coefficient of the adhesion force α .

$$\mathbf{F} = \alpha \left(\frac{R_i R_k}{R_i + R_k} \right) \mathbf{n}_{ik} \quad (2.30)$$

Equation (2.30) means that the force is proportional to the particle diameter. If the adhesion force is measured experimentally, the correction coefficient of the adhesion force α is deduced from the results and the adhesion force can be determined.

2.3.4 Gravitational Force and Air Drag

The gravitational force is expressed as Equation (2.31).

$$\mathbf{F} = m\mathbf{g} \quad (2.31)$$

The gravitational acceleration \mathbf{g} is 9.8 m/s^2 on the Earth. The specific gravitational acceleration on the Moon, Mars, and or an asteroid should be considered.

Conventionally, air drag can be calculated using Equation (2.32) from Stokes equation [9].

$$\mathbf{F} = 6\pi\eta R_i \dot{\mathbf{x}} \quad (2.32)$$

The viscosity of air η is $1.82 \times 10^{-5} \text{ Pa}\cdot\text{s}$ at 1 atm, and it is determined by the compositions and condition of the atmosphere. The viscosity is calculated by Equation (2.33) from Sutherland's formula [10].

$$\eta_2 = \eta_1 \left(\frac{T_1 + S}{T_2 + S} \right) \left(\frac{T_2}{T_1} \right)^{\frac{3}{2}} \quad (2.33)$$

Here, T and S are the temperature of the atmosphere and Sutherland's constant, respectively. The value with subscript 2 is calculated using the given value with subscript 1. When the Reynolds number of the moving particle is large, the air drag equation (2.32) is modified as Equation (2.34) [9].

$$\mathbf{F} = C_D \left(\pi R^2 \right) \left(\frac{\rho \dot{\mathbf{x}}^2}{2} \right) \quad (2.34)$$

where ρ and C_D are the atmospheric density and drag coefficient, respectively. The drag coefficient is determined by the Reynolds number Re as shown in Equation (2.35).

$$C_D = \begin{cases} 24Re^{-1} & (Re < 2) \\ 10Re^{-\frac{1}{2}} & (2 < Re < 500) \\ 0.44 & (500 < Re) \end{cases} \quad (2.35)$$

$$Re = \frac{2\rho\dot{x}R}{\eta} \quad (2.36)$$

If the Reynolds number is less than 2, Equation (2.34) becomes Equation (2.32). In addition, if the atmospheric pressure is low, Stokes equation is modified using the Cunningham correction factor C_C , as shown in Equation (2.37) [11].

$$F = \frac{6\pi\eta R_t \dot{x}}{C_C} \quad (2.37)$$

There are some models for calculating the Cunningham correction factor C_C , which were determined from experiments. In this research, Davis's model is used. The Cunningham correction factor C_C is determined using Equation (2.38) [12].

$$C_C = 1 + K \left(0.882 + 0.281 \times \exp\left(-\frac{1.57}{K}\right) \right) \quad (2.38)$$

where K is the Knudsen number which is calculated using Equation (2.39).

$$K = \frac{\lambda}{2R} \quad (2.39)$$

The mean free path of the atmosphere λ is affected by the composition and condition of the atmosphere. The equation used to calculate the mean free path of the atmosphere is described by Equation (2.40) [13].

$$\lambda = 3.11 \times 10^{-24} \frac{T}{\delta^2 P} \quad (2.40)$$

where δ and P are the diameter of the molecule and the pressure of the atmosphere, respectively. The appropriate equation for calculating air drag has to be selected to simulate specific environmental effects, such as the low pressure and variable temperature on the Mars, if the air drag significantly affects the particle dynamics.

2.4 Numerical Calculations of Electrostatic and Magnetic Fields

2.4.1 Numerical Calculation of Electrostatic Field

The Poisson's equation for electric potential ϕ can be calculated using the finite difference method [6]. To calculate Equation (2.5) using the finite difference method, a square-shaped computational mesh is used as shown in Figure 2.3. The boundary conditions are fixed as the potential ϕ of the voltage V and the charge q at the node and as the relative permittivity ϵ_r at the element. Δh is the mesh length of one side of the grid. The control volume is assumed around the node ij . The subscripts i and j express the number of the grids in the x - and y - directions, respectively.

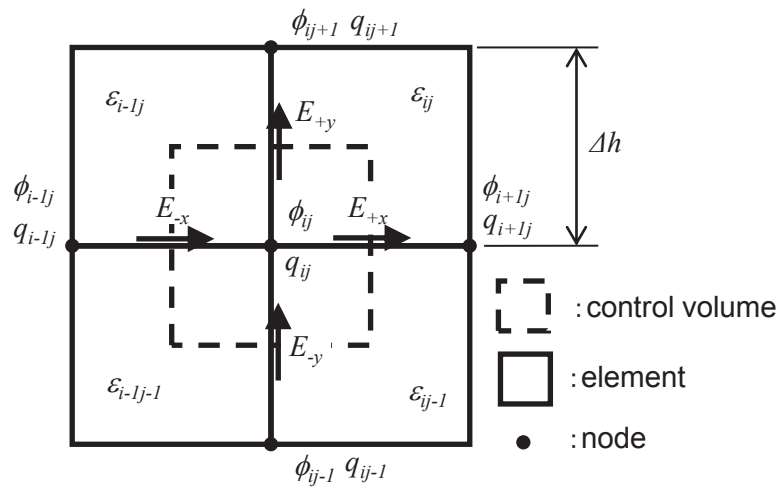


Figure 2.3 Computational mesh for calculating the electrostatic field using the finite difference method.

For the finite difference method, the integration system is convenient; therefore, Equation (2.5) is expressed as the integration system of the electric flux density \mathbf{D} as Equation (2.41).

$$\int_S \mathbf{D} \cdot d\mathbf{s} = q \quad (2.41)$$

The electric flux density is calculated by Equation (2.42).

$$\mathbf{D} = \epsilon_0 \epsilon_r \mathbf{E} \quad (2.42)$$

Equation (2.41) indicates that the electric flux density flowing in and out of the control volume is equal to the charges in the volume. \mathbf{E}_{+x} in Figure 2.3 is expressed as Equation (2.43).

$$\mathbf{E}_{+x} = -\frac{\phi_{i+1j} - \phi_{ij}}{\Delta h} \quad (2.43)$$

E_{-x} , E_{+y} , and E_{-y} are expressed similarly to Equation (2.43). Using E_{+x} and Equation (2.42), D_{+x} is expressed by Equation (2.44), and the average relative permittivity is used in the equation.

$$D_{+x} = \frac{\varepsilon_{ij} + \varepsilon_{ij-1}}{2} E_{+x} \quad (2.44)$$

D_{-x} , D_{+y} , and D_{-y} are expressed similarly to Equation (2.44). The balance of the inflow and outflow of the electric flux density D and the charge q in Equation (2.41) can be expressed by Equation (2.45).

$$(D_{+x} - D_{-x} - D_{+y} + D_{-y})\Delta h = q \quad (2.45)$$

Using Equations (2.43) and (2.44), Equation (2.45) is arranged for ϕ_{ij} , as shown in Equation (2.46).

$$\phi_{ij} = \frac{(\varepsilon_{i-1j} + \varepsilon_{ij})\phi_{ij+1} + (\varepsilon_{i-1j-1} + \varepsilon_{ij-1})\phi_{ij-1} + (\varepsilon_{i-1j} + \varepsilon_{i-1j-1})\phi_{i-1j} + (\varepsilon_{ij} + \varepsilon_{ij-1})\phi_{i+1j} - 2\Delta h q}{2(\varepsilon_{i-1j} + \varepsilon_{i-1j-1} + \varepsilon_{ij} + \varepsilon_{ij-1})} \quad (2.46)$$

If the charge q is neglected, Equation (2.46) is modified as Equation (2.47).

$$\phi_{ij} = \frac{(\varepsilon_{i-1j} + \varepsilon_{ij})\phi_{ij+1} + (\varepsilon_{i-1j-1} + \varepsilon_{ij-1})\phi_{ij-1} + (\varepsilon_{i-1j} + \varepsilon_{i-1j-1})\phi_{i-1j} + (\varepsilon_{ij} + \varepsilon_{ij-1})\phi_{i+1j}}{2(\varepsilon_{i-1j} + \varepsilon_{i-1j-1} + \varepsilon_{ij} + \varepsilon_{ij-1})} \quad (2.47)$$

If there is no charge, Equation (2.47) is calculated about the potential ϕ at all nodes repeatedly until the calculation residual is stabilized at less than a substantially small value. Then, the distribution of the potential ϕ is calculated. Finally, the distribution of the electrostatic field E is calculated by solving Equation (2.4). If the specific boundary conditions are reproduced in the same way as with the actual experimental setup, such as the potential ϕ at the electrode, the charge q at particles, and the relative permittivity ε_r at the insulating tape, the complex electrostatic field can be calculated. Although the explained procedure focuses on two dimensions, the procedure can be expanded to three dimensions.

2.4.2 Numerical Calculation of Magnetic Field

The magnetic flux density B can also be calculated by the finite difference method. Because a solenoid coil is used to generate the magnetic field B in this research, as shown in Figure 2.4, the cylindrical coordinate system is convenient for calculating the magnetic field.

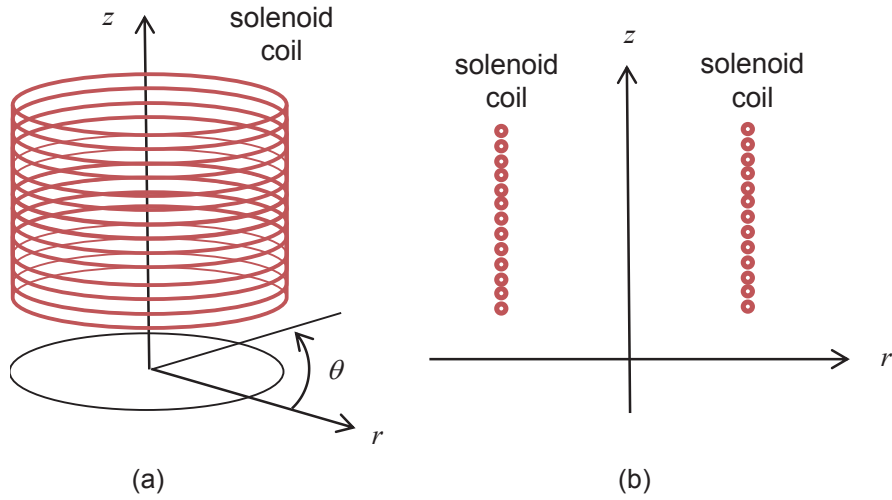


Figure 2.4 (a) Solenoid coil in cylindrical coordinate and (b) cross-sectional view of the coil.

Regarding axial symmetry, the calculation area can be simplified into two dimensions as shown in Figure 2.4 (b). The rotational operation in the cylindrical coordinates system is expressed as Equation (2.48)

$$\nabla \times \mathbf{A} = \left[\frac{1}{r} \frac{\partial A_z}{\partial \theta} - \frac{\partial A_\theta}{\partial z} \right]_r + \left[\frac{\partial A_r}{\partial z} - \frac{\partial A_z}{\partial r} \right]_\theta + \frac{1}{r} \left[\frac{\partial}{\partial r} (r A_\theta) - \frac{\partial A_r}{\partial \theta} \right]_z \quad (2.48)$$

The subscript represents the direction of the vector in Equation (2.48). Considering axial symmetry and Equation (2.48), Equation (2.26) is rearranged to Equation (2.49).

$$\frac{\partial^2 A_\theta}{\partial r^2} + \frac{\partial^2 A_\theta}{\partial z^2} + \frac{1}{r} \frac{\partial A_\theta}{\partial r} - \frac{A_\theta}{r^2} = -\mu_0 j_0 \quad (2.49)$$

A square mesh, as shown in Figure 2.5, was used to calculate Equation (2.49) using the finite difference method.

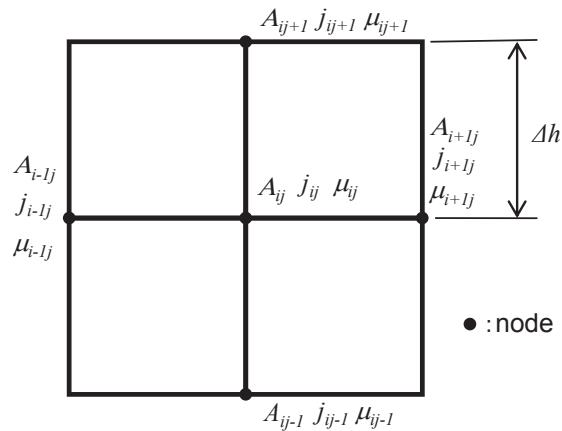


Figure 2.5 Computational mesh for calculating the magnetic field using the finite difference method.

The boundary conditions are fixed as the vector potential A_θ of the θ -direction, the electric current density j_θ of the θ -direction, and the relative magnetic permeability μ_r at the node. Δh is the mesh length of one side of the grid. The subscripts i and j express the number of the grid in the r and z coordinates, respectively. Equation (2.49) is modified to the difference form, as represented by Equation (2.50).

$$\frac{A_{\theta i+1j} - 2A_{\theta ij} + A_{\theta i-1j}}{\Delta h^2} + \frac{A_{\theta ij+1} - 2A_{\theta ij} + A_{\theta ij-1}}{\Delta h^2} + \frac{\Delta h(A_{\theta i+1j} - A_{\theta i-1j})}{2r} - \frac{A_{\theta ij}}{r^2} = -\mu_{0ij} j_{0ij} \quad (2.50)$$

Rearranging Equation (2.50) with respect to $A_{\theta ij}$ results to Equation (2.51).

$$A_{\theta ij} = \frac{r^2}{4r^2 + \Delta h^2} \left\{ A_{\theta i+1j} + A_{\theta i-1j} + A_{\theta ij+1} + A_{\theta ij-1} + \frac{\Delta h(A_{\theta i+1j} - A_{\theta i-1j})}{2r} + -\mu_{0ij} j_{0ij} \Delta h^2 \right\} \quad (2.51)$$

Equation (2.51) is calculated with respect to the potential $A_{\theta ij}$ at all nodes repeatedly until the calculation residual is stabilized. Finally, Equation (2.21) is formulated in the cylindrical coordinates system, and the magnetic flux density \mathbf{B} is calculated using the $A_{\theta ij}$ distribution. If the specific boundary conditions are reproduced in the same way as the actual experimental setup, such as the electric current density \mathbf{j} at an electrode, and the relative magnetic permeability μ_r at the sheath of electrode, the complex magnetic field can be calculated in two-dimensional coordinate.

2.5 Measurement of Parameters

2.5.1 Measurement of Adhesion Force

As described in section 2.3.3, the adhesion forces acting on FJS-1 particles were experimentally measured from the centrifugal force by using the ultra-centrifuge (CS ISOFNX, Hitachi Koki), as shown in Figure 2.6. The coefficient of the adhesion force was estimated from the results. In the measurement, the particles adhered to the rotating capsule, and then the rotating speed was increased stepwise and the centrifugal forces acting on the particles were calculated from the speed and the separated particle weight, as shown in Equation (2.52).

$$\mathbf{F} = m\omega_c^2 \mathbf{b} \quad (2.52)$$

where ω_c and \mathbf{b} are the angular velocity of the capsule and vector from the rotating shaft to particles, respectively. The diameters of the particles thrown out of the capsule were measured optically at each speed, and the adhesion force that balanced the centrifugal force was determined. The measured value consists of the non-electrostatic adhesion force and the electrostatic adhesion force. From the measured value, the coefficient of the adhesion force α in Equation (2.30) was deduced.

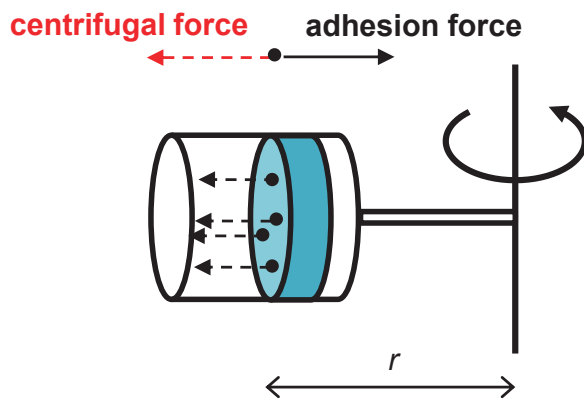


Figure 2.6 Diagram of experimental setup used for measuring the adhesion force using centrifugal force.

Figure 2.7 shows the measured adhesion force acting on each particle. The adhesion force applied to particles larger than 50 μm could not be measured because the gravitational force disturbed the adhesion to the capsule. As shown in Figure 2.7, the measured adhesion force shows a large dispersion because it was easily affected by the contact and surface conditions of the particles. Therefore, it was assumed that the adhesion force would increase linearly with particle size, and two approximate equations for the maximum and minimum adhesion force were derived. In the subsequent theoretical and numerical calculations, these coefficients were used for the adhesion force.

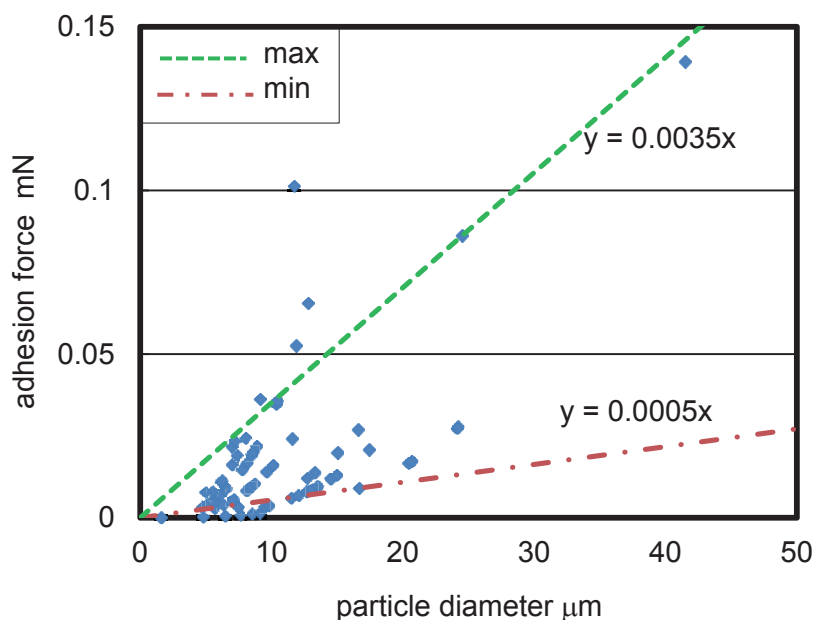


Figure 2.7 Measured distribution of adhesion force acting on particles, deduced from the balance of centrifugal force (x and y coordinates are the particle diameter and adhesion force, respectively).

2.5.2 Measurement of Particle Charge

The charge distribution of bulk FJS-1 particles was measured using the Faraday cage and free-fall system to calculate the Coulomb force. Figure 2.8 shows the setup of the Faraday cage. The particles were indrawn to the inner conductive cage, which was insulated from the outer cage. Then, the voltage V between both ends of the capacitor connecting the inner and outer cage was measured using the electrometer (R8252, Advantest). When the capacitance C of the electrometer and capacitor are known, the total charges Q of the indrawn bulk particles can be calculated using Equation (2.53).

$$Q = \frac{C_{\text{electrometer}} + C_{\text{capacitor}}}{V} \quad (2.53)$$

Because the balance between the gravitational force and the Coulomb force is critical to evaluate the particle dynamics in the electrostatic force, the charge density was deduced. The measured charge density ranges from -0.002 to $-0.01 \mu\text{C/g}$.

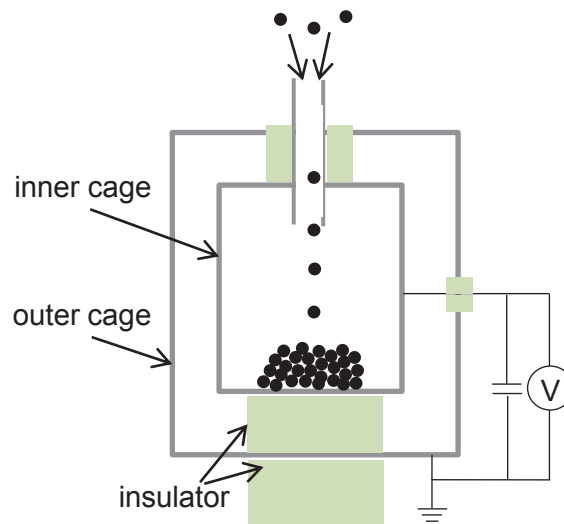


Figure 2.8 Configuration of the Faraday cage used to measure the charge density of bulk particles.

Figure 2.9 shows the measurement setup of the free-fall system. The parallel plate electrodes, to which the 5 kV of DC voltage was applied, were set at a distance of 170 mm and a height of 270 mm. When the particles were supplied to the system by passing through a 1 mm gap, the particles fell down, moving right or left from the centerline of the supplied point owing to the electrostatic force. A wind shelter was placed around the system to prevent airflow in the space between the plate electrodes. A picture of all fallen particles that settled on an adhesive sheet on the grounded lower plate was taken using a high-precision scanner (CanoScan 9000F, Canon), and is shown in Figure 2.10. The distances between the touchdown positions of each fallen particle and the centerline were measured using an image analyzer. In this measurement,

the electrification states of the particles were not controlled, and particles existing in a natural state were directly supplied to the measurement system. The motion equation of i -th particle is given by Equation (2.54), represents the motion of the falling particles in the experiment.

$$m_i \ddot{\mathbf{x}}_i = -6\pi\eta R \dot{\mathbf{x}} + \mathbf{F}_{Coulomb} + \mathbf{F}_{dielectrophoresis} + \mathbf{F}_g \quad (2.54)$$

The Coulomb force, dielectrophoresis force, and gravitational force, which are represented by Equations (2.3), (2.16), and (2.31), respectively, affect particle dynamics. The external electrostatic field \mathbf{E} was calculated using a two-dimensional finite difference method, as described in section 2.4.1. The geometry of the experimental setup was taken into consideration and the electric parameters were used as boundary conditions. The relative permittivity ϵ_r of the acrylic plate in Figure 2.9 is 3.1. All parameters except the particle charge in Equation (2.54) are known; therefore, the charge of the particle can be calculated using the distance from the centerline.

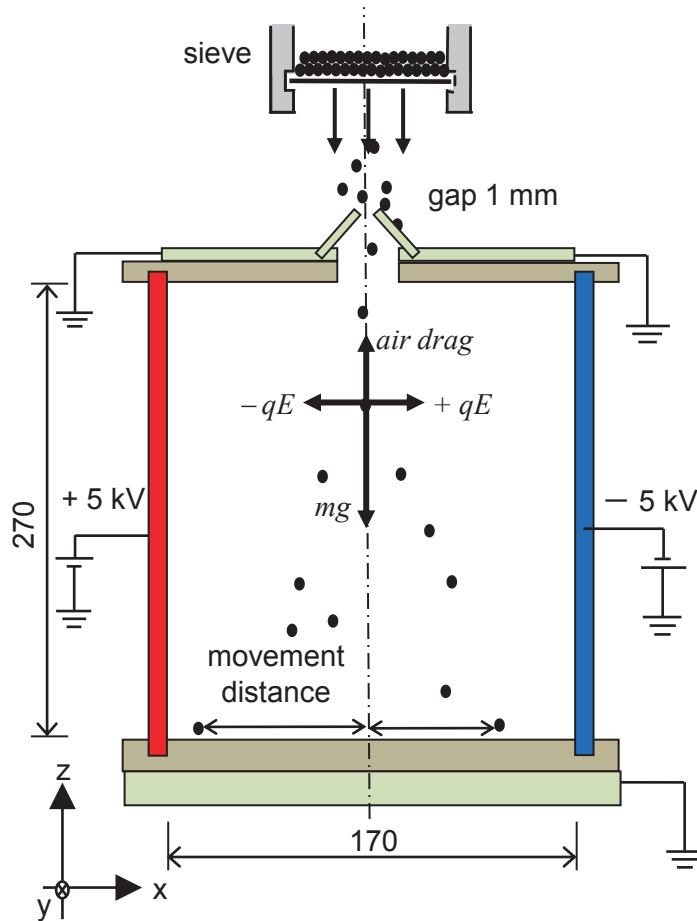


Figure 2.9 Configuration of the experimental setup for the free-fall method used to measure the charge density of individual particles.

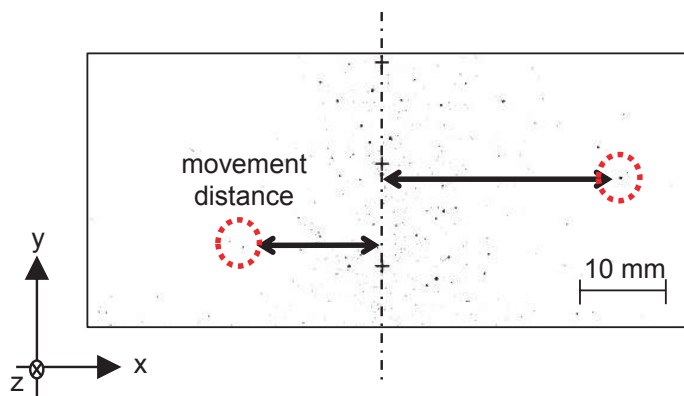


Figure 2.10 Illustration of fallen particles on the lower adhesive sheet using the free-fall method.

Figure 2.11 shows the measured charge distribution of the lunar regolith simulant FJS-1 that ranged from 100 μm to 1.13 mm in diameter. The charges of particles with the same diameter were not equal, and they were randomly charged in negative and positive polarities. Because FJS-1 has a wide variety of compositions, the charge quantities and polarities are non-uniform. Moreover, the particles interacted with each other mechanically, and an exchange of charges occurred between the particles during collisions. The charge density was assumed to decrease with the particle size, and two approximate equations for the maximum allowable values of the positive and negative charge densities were derived. The reason why the charge densities measured using the Faraday cage and free-fall system were different was because the Faraday cage measured the density of the bulk particles, and the summation of the negative and positive charges was close to zero. If the charge of each particle is required, the free-fall system results are more appropriate for use.

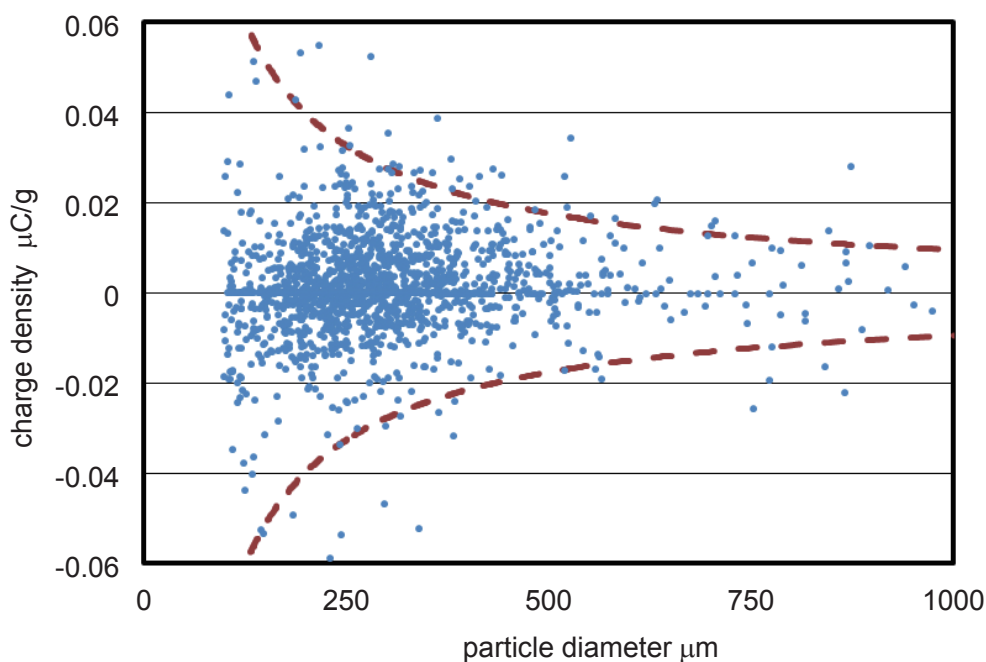


Figure 2.11 Measured charge density distribution of FJS-1 particles using the free-fall method.

2.5.3 Measurement of Dielectrophoresis Force

As described in section 2.3.2, the dielectrophoresis force can be calculated using Equation (2.16), and the external electrostatic field E can also be calculated by the finite difference method, as described in section 2.4.1. Although Equation (2.16) is conventionally used to calculate the dielectrophoresis force, it is reported in the literature [7] that Equation (2.16) should be utilized for small particles less than 1 mm in diameter. Therefore, it is necessary to estimate the dielectrophoresis force acting on particles larger than 1 mm in diameter and to confirm whether Equation (2.16) can be utilized for large particles. The actual dielectrophoresis force was measured by conducting a model experiment; the result and the theoretical value were compared to confirm the accuracy of Equation (2.16). Figure 2.12 shows the experimental setup used to measure the force. Because the size of simulant FJS-1 is less than 1 mm, a glass bead 2 mm in diameter was used as an alternative material. The particle was suspended using a nylon wire (length: 60 mm, diameter: 100 μm) from an acrylic cantilever (length: 70 mm, width: 5 mm, thickness: 0.5 mm, Young's modulus: 7.2 GPa), and a DC voltage was applied to a parallel screen electrode (wire diameter: 1.3 mm, pitch: 10 mm, gap: 5 mm) to generate the dielectrophoresis force produced by the non-uniform electrostatic field. The electrostatic field was calculated using the finite difference method, as described in section 2.4.1, and by considering the geometry of the experimental setup and using the electric parameters as boundary conditions. The voltage applied to the electrodes was a parameter of the experiment and calculation.

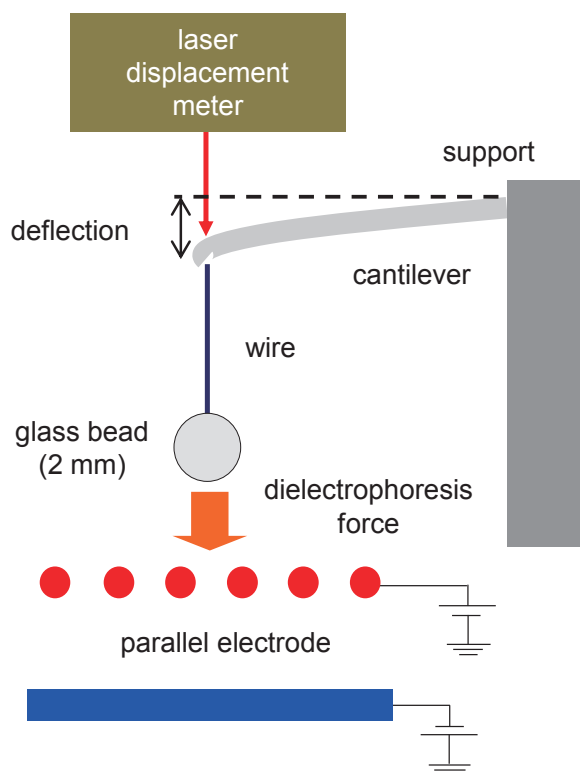


Figure 2.12 Configuration of the experimental setup used to measure the dielectrophoresis force applied to a particle in a non-uniform electrostatic field.

The particle was attracted to the electrodes, and the resultant deflection of the cantilever was measured using a laser displacement meter (LT-8010, Keyence). The force acting on the particle was calculated by multiplying the measured deflection to the cantilever stiffness. The particle charge was neutralized by using alcohol before the experiment; therefore, only the dielectrophoresis force and gravitational force acted on the particle. By eliminating the influence of gravitational force, it was possible to determine the dielectrophoresis force alone. Figure 2.13 shows the measured dielectrophoresis force and the theoretical value calculated using Equation (2.16). Although there is a small difference between the experimental and calculated results, the values agreed fairly well. Therefore, Equation (2.16) was deemed to be adequate for estimating the dielectrophoresis force.

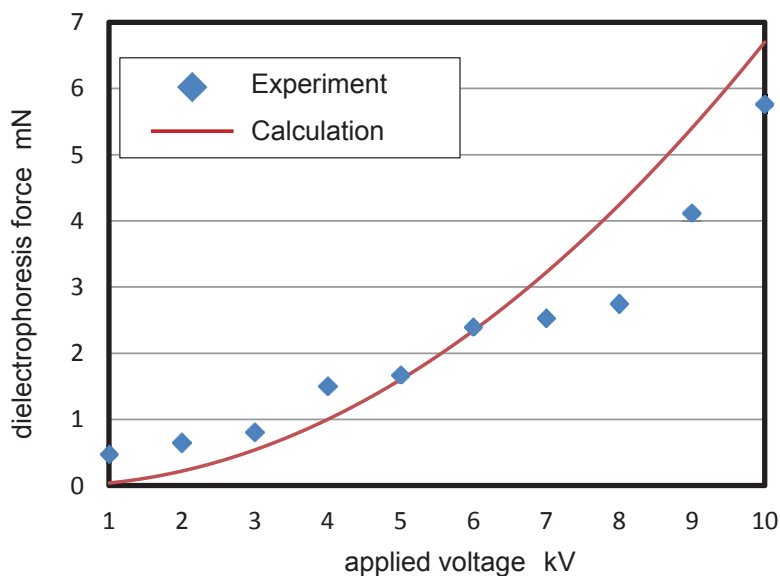


Figure 2.13 Measured and calculated dielectrophoresis forces acting on a glass particle 2 mm in diameter.

2.6 Comparison of External Forces

2.6.1 Effect of Electrostatic Force

From the results of the model experiments and the calculations of the electrostatic and magnetic fields described above, the balance of external forces acting on the particles can be estimated. The calculation model is shown in Figure 2.14. Electrostatic forces such as the Coulomb force and the dielectrophoresis force were calculated in this model. The external electrostatic field E was calculated using the finite difference method, considering the boundary conditions of the actual experimental setup in Figure 2.14. Because the bulk of the particle layer was assumed to be composed of FJS-1, the permittivity of the particle layer was fixed to that of FJS-1. For the calculation parameters, the particle diameter was altered within the range of 10 μm to 10 mm. The charge densities of particles were determined using the approximate equation for the maximum allowable value of the positive charge densities, corresponding to the particle diameter, as shown in Figure 2.11.

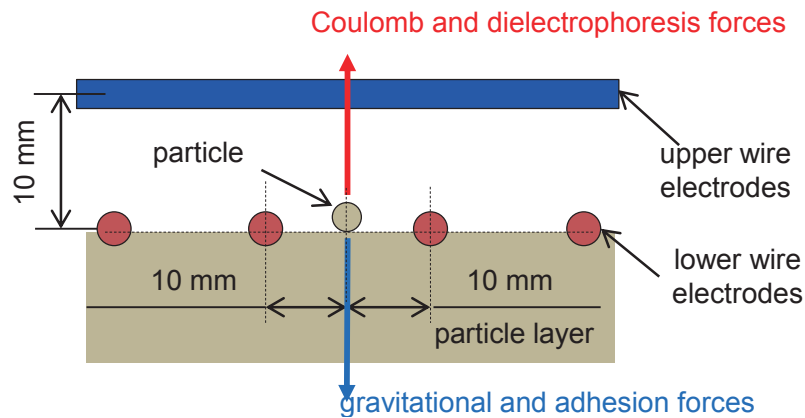


Figure 2.14 Calculation model for comparing the balance of external forces acting on a particle when an electrostatic field is applied (applied voltage: 10 kV_{p-p} , coefficient of adhesion force α : 0.00027, specific gravity of particle: 2.7 g/cm^3 , relative permittivity of particle ϵ_0 : 3.0).

Figure 2.15 shows the calculation results of for the forces acting on the particle. The adhesion force is the highest in particles smaller than $20 \mu\text{m}$ in diameter (Figure 2.15, adhesion force area) because it is proportional to the particle diameter and becomes dominant as the particle diameter decreases. When the diameter increases to larger than $20 \mu\text{m}$, the Coulomb force becomes dominant against particles ranging from $20 \mu\text{m}$ to $500 \mu\text{m}$ (Figure 2.15, Coulomb force area). Therefore, it is expected that the handling of charged particles will be successful by controlling the electrostatic field. For particles larger than $500 \mu\text{m}$ in diameter, the gravitational force is highest at 1-G (Figure 2.15, gravitational force area) because the gravitational force is proportional to the cube of the particle diameter. Particles larger than 1 mm would not float in a 1-G environment, and the electrostatic handling of particles is difficult. However, in low-gravity environments, similar to that on the Moon (gravitational acceleration: 1.6 m/s^2), the Coulomb force maintains its dominant effect on particles larger than 1 mm and less than 4 mm in diameter, as shown in Figure 2.15. The results confirm that the electrostatic force can be used effectively in low-gravity environments, and the performance of the electrostatic handling technology is improved in low-gravity. For example, on a small asteroid similar to Itokawa (gravitational acceleration: $8.6 \times 10^{-5} \text{ m/s}^2$), the gravitational acceleration can be neglected and particles larger than $20 \mu\text{m}$ can be manipulated freely if the electrostatic field is optimally created. In addition, the dielectrophoresis force is proportional to the cube of the particle diameter, and it becomes larger than the adhesion force as the particle diameter increases as shown in Figure 2.15. Therefore, even in a case where the particle is not charged electrostatically, the particles can be moved by the dielectrophoresis force.

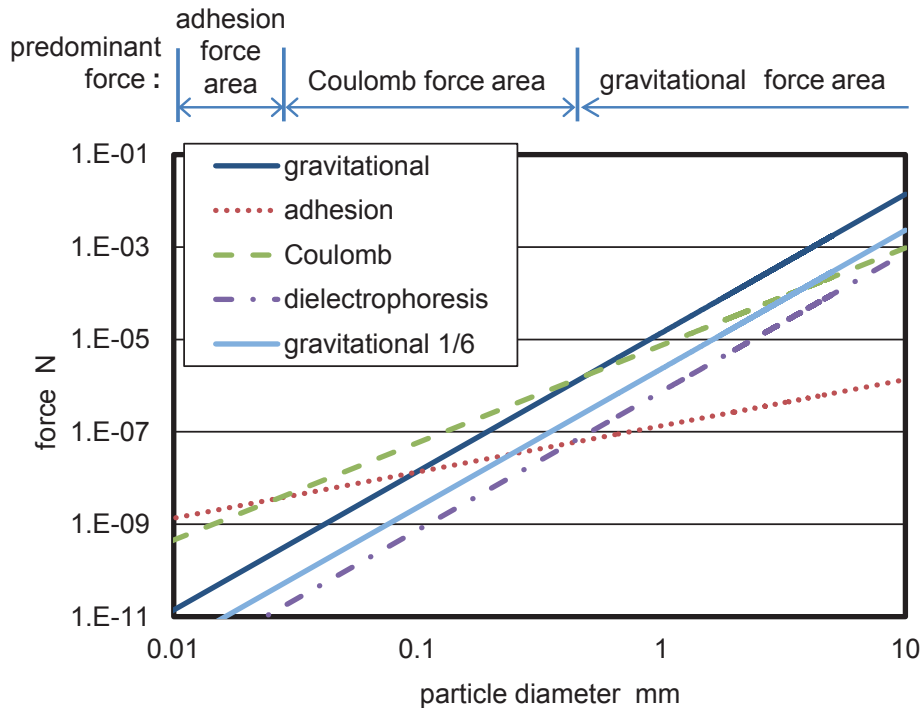


Figure 2.15 Forces acting on a particle ranging from 10 μm to 10 mm in diameter in an electrostatic field (applied voltage: 10 kV_{p-p}, coefficient of adhesion force α : 0.00027, specific gravity of particle: 2.7 g/cm³, relative permittivity of particle ϵ_0 : 3.0).

2.6.2 Effect of Magnetic Force

In addition to the effect of the electrostatic force, the magnetic force was estimated as well. The calculation model is assumed as shown in Figure 2.16. The external magnetic field \mathbf{B} was calculated using the finite difference method, considering the boundary conditions of the actual experimental setup shown in Figure 2.16. The relative magnetic permeability μ_r of the lunar regolith was assumed to be 1.01. Moreover, the magnetic force applied to the particle (the relative permeability of iron $\mu_r = 5,000$) was also calculated assuming a case where the particle contains a rich nanophase iron. The particle diameter was changed in the range of 10 μm to 10 mm as calculation parameters.

Figure 2.17 shows the calculation results of forces acting on the particle. If the relative magnetic permeability of the particle is assumed to be 1.01, the magnetic force is smaller than the adhesion force in the case when the particle diameter is less than 500 μm , because the magnetic force decreases with the cube of the diameter. The magnetic force will exceed the adhesion force when the particle is larger than 500 μm in diameter as shown in Figure 2.17. The magnetic force is similar to the gravitational force in 1/6-G as in the case where 5,000 AT of electric current is applied. AT is the product of an ampere applied to a coil and wire turns, and it is a unit for magneto-motive force. It can be assumed that the magneto-motive force should be larger than 5,000 AT to move the lunar regolith simulant. When the relative magnetic permeability of the particle is assumed to be 5,000 similar to that of an iron particle, the adhesion force is still highest for particles smaller than approximately 20 μm in diameter (Figure 2.17, adhesion force area). For particles larger than

about 20 μm in diameter, the magnetic force is dominant (Figure 2.17, magnetic force area). If a particle has a large relative magnetic permeability, a particle larger than 20 μm can be handled using the magnetic force when the magneto-motive force is higher than approximately 5,000 AT.

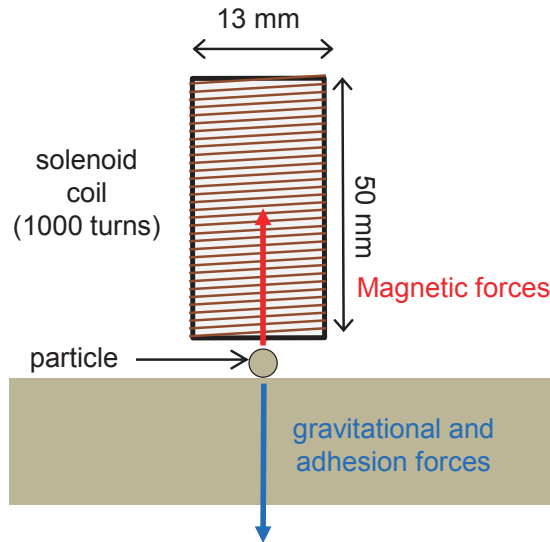


Figure 2.16 Calculation model for comparing the balance of external forces acting on a particle when a magnetic field is applied (applied magneto-motive force: 5,000 AT, coefficient of adhesion force α : 0.00027, specific gravity of particle: 2.7 g/cm^3).

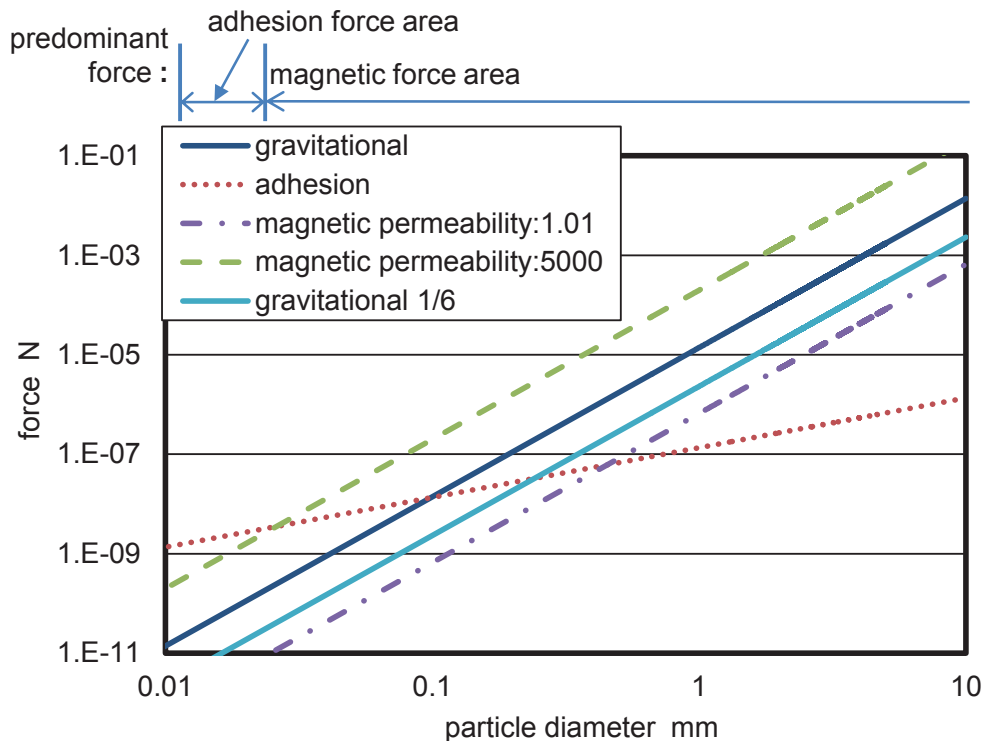


Figure 2.17 Forces acting on a particle ranging from 10 μm to 10 mm in diameter in a magnetic field (applied magneto-motive force: 5,000 AT, coefficient of adhesion force α : 0.00027, specific gravity of particle: 2.7 g/cm^3).

2.6.3 Disturbance of Air Drag

The balance of forces including the air drag was also estimated using the calculation models shown in Figures 2.14 and 2.16. For simplicity, Equation (2.32) was used for calculating air drag. The velocity of the particle was assumed to be 0.5 m/s in air.

Figure 2.18 shows the calculation results of forces acting on a particle ranging from 10 μm to 10 mm in diameter. For particles smaller than approximately 20 μm , air drag is dominant because its effect is proportional to the particle diameter, similar to the adhesion force. Actually, air drag must not exceed the other forces; however, the results confirm that particles smaller than 20 μm are significantly affected by air drag. It is necessary to consider the difference in the dynamics of small particles in air and vacuum environments.

Following the estimations described in sections 2.6.1, 2.6.2 and 2.6.3, the balance of forces acting on the particles in the electrostatic and magnetic fields could be roughly evaluated, and the systems using the electrostatic and magnetic forces are expected to be useful in specific conditions. However, these simple estimations could not take into account the dynamic motions of particles and the interactions between particles; the actual dynamics is more complex than these estimations. Therefore, it is necessary to conduct experiments and perform numerical calculations by assuming more practical conditions.

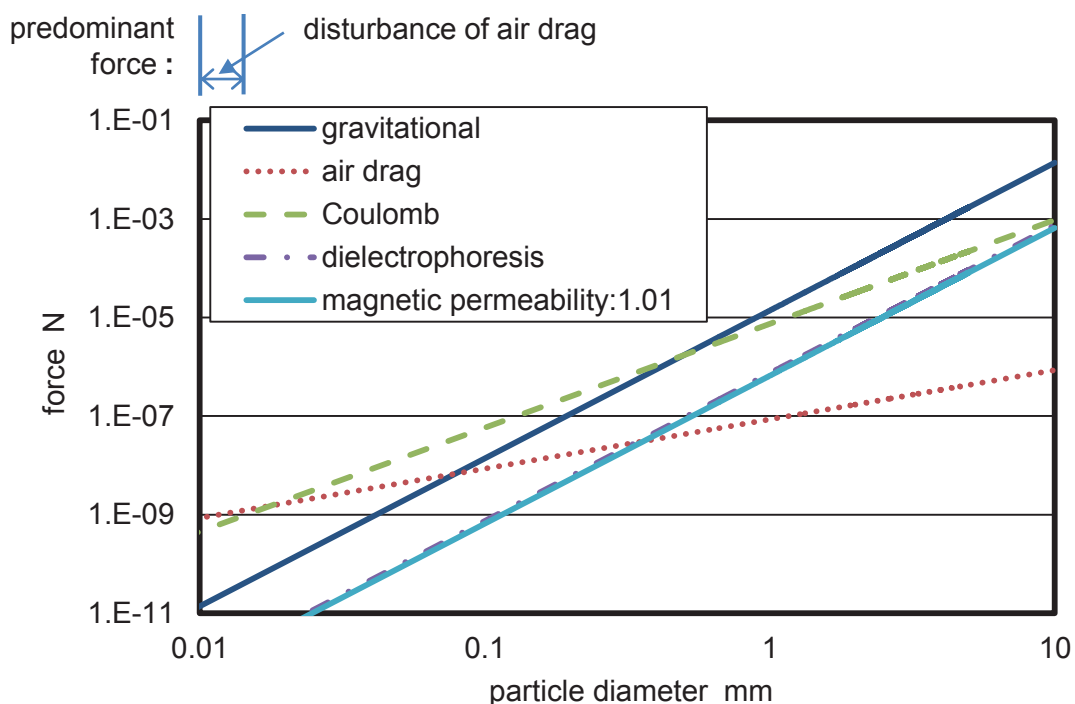


Figure 2.18 Forces acting on a particle less than 10 mm in diameter (applied voltage: 10 kV_{p-p}, applied magneto-motive force: 5,000 AT, coefficient of adhesion force α : 0.00027, specific gravity of particle: 2.7 g/cm³, relative permittivity of particle ϵ_0 : 3.0, particle velocity: 0.5 m/s, viscosity coefficient: 1.82×10^{-5} Pa·s).

2.7 Numerical Calculation of Particle Motion

2.7.1 Distinct Element Method

As described in the preceding section, although the system using electrostatic and magnetic forces is expected to be useful in space, the performance and particle dynamics in space must be investigated by experiments and numerical calculations that consider actual conditions. Because experiments involving the reproduction of vacuum and low-gravity conditions are not easy, and because experimentally-based parametric studies are difficult to conduct in terms of cost and duration, the numerical calculations based on the DEM are indispensable [14]. In this section, the methodology of the DEM is described.

The basic principle of the DEM is Newton's equation of motion, as represented by Equation (2.1) and (2.2). When Equation (2.1) and (2.2) are solved repeatedly using the Runge–Kutta method at each short time step, the velocity, position, angular velocity, angle, and the trajectory of a moving particle can be calculated [6]. Any external force and torque can be easily considered by adding forces and torques to the right hand side of Equation (2.1) or (2.2). In this research, the torque acting on a particle is assumed to be zero, because particles similar to lunar regolith have irregular shapes and the rotation of the particles is disturbed by high-rolling friction. Only Equation (2.1) is considered. The Coulomb force, dielectrophoresis force, magnetic force, gravitational force, adhesion force, and air drag are considered by adapting each calculation model. The theoretical equations are already described in the previous sections. The DEM has some advantages, one of which is that the specific parameters of each particle can be evaluated. For example, if the size distribution or charge distribution of particles is known, the distribution can be reproduced in calculations and the effect can be investigated. The advantage is effective for investigating the dynamics of particles that have a wide variety of compositions and geometric configurations similar to the lunar regolith described in section 1.1.2. In addition, the DEM can take into account the interactions within particles; therefore, both single and plural particles can be calculated. Moreover, it is easy to include the effect of complex electrostatic and magnetic fields to particle dynamics. For example, if the external electrostatic field \mathbf{E} and magnetic field \mathbf{B} are calculated before the DEM calculation using the methods described in sections 2.4.1 and 2.4.2, those values at various particle position can be looked up at each time step in the DEM calculation. The theoretical equations of the external forces were already described in the previous sections. Other specific procedures for conducting the DEM calculation such as how to treat the interaction of particles are explained in this section. On the other hand, the DEM has a disadvantage for the calculation load because the time of calculating the mechanical, electrostatic, and magnetic interactions for all particles increases proportionally with the square of the particle number. The method for reducing the calculation load is also proposed in this section.

2.7.2 Soft Sphere Model

When a particle collides with another particle, the mechanical interaction is conventionally calculated by using a soft sphere model [14-16]. In this model, the mechanical interaction forces in the normal and tangential directions are estimated based on the Voigt model, shown in Figure 2.19, from the Hertzian contact theory and Mindlin contact theory, respectively. An overlap of particles is assumed to be an elastic deformation, and the repulsive and frictional forces are produced owing to the elastic deformation of colliding particles.

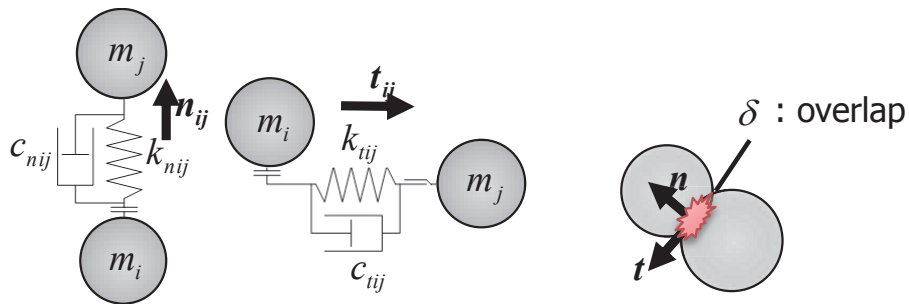


Figure 2.19 Voigt model for calculating the contact force between particles.

The normal force $\mathbf{F}_{mech.nij}$ from the i -th particle to the j -th particle is represented by Equation (2.55).

$$\mathbf{F}_{mech.nij} = -k_{nij} |\delta_{nij}|^{\frac{3}{2}} \mathbf{n}_{ij} - (c_{nij} \mathbf{v}_{ij} \cdot \mathbf{n}_{ij}) \mathbf{n}_{ij} \quad (2.55)$$

where k_{nij} , $|\delta_{nij}|$, \mathbf{n}_{ij} , c_{nij} , and \mathbf{v}_{ij} are the spring constant based on the Hertzian contact theory, the particle overlap, the normal unit vector from the center of particle i to that of particle j , the damping constant, and the relative velocity of particle i to j , respectively. The first term of Equation (2.55) is the static reaction force and the second term is the damping force. The spring constant k_{nij} and the damping constant c_{nij} are calculated using Equation (2.56) and (2.57), respectively.

$$k_{nij} = \frac{4}{3} \sqrt{\frac{R_i R_j}{R_i + R_j}} \left(\frac{1 - \nu_i^2}{\beta_i} + \frac{1 - \nu_j^2}{\beta_j} \right)^{-1} \quad (2.56)$$

$$c_{nij} = \gamma \sqrt{\frac{m_i m_j}{m_i + m_j}} k_{nij} |\delta_{nij}|^{\frac{1}{4}} \quad (2.57)$$

Here, ν , β , and γ are the Poisson's ratio, Young's modulus, and coefficient of restitution, respectively. In a no slip case, the tangential force $\mathbf{F}_{mech.tij}$ exerted by the i -th particle on the j -th particle consists of the static reac-

tion force and the damping force, as represented by Equation (2.58).

$$\mathbf{F}_{mech.tij} = -k_{ij}\boldsymbol{\delta}_{ij} - c_{ij}\mathbf{v}_{ij} \quad (2.58)$$

The spring constant k_{ij} and the damping constant c_{ij} in the tangential direction are calculated using Equations (2.59) and (2.60), respectively.

$$k_{ij} = 8 \sqrt{\frac{R_i R_j}{R_i + R_j} \left(\frac{2 - v_i^2}{L_i} + \frac{2 - v_j^2}{L_j} \right)^{-1}} |\boldsymbol{\delta}_{nij}|^{\frac{1}{2}} \quad (2.59)$$

$$c_{ij} = \gamma \sqrt{\frac{m_i m_j}{m_i + m_j}} k_{ij} \quad (2.60)$$

Here, L is the modulus of rigidity. Conversely, if slip occurs, the tangential force is limited by the friction force by using the friction coefficient μ_d , as represented by Equation (2.61).

$$\mathbf{F}_{mech.tij} = -\mu_d \left| k_{ij} \boldsymbol{\delta}_{ij} \right| \frac{\mathbf{v}_{ij}}{|\mathbf{v}_{ij}|} \quad (2.61)$$

The moment $\mathbf{M}_{mech.ij}$ from the i -th particle to the j -th particle consists of the contact torque, which is the first term on the right-hand side of Equation (2.62), and rotational friction, which is the second term on the right-hand side of Equation (2.62).

$$\mathbf{M}_{mech.ij} = R_j \mathbf{n}_{ij} \times \mathbf{F}_{mech.tij} - R_i \mu_f \left| \mathbf{F}_{mech.nij} \right| \frac{\dot{\boldsymbol{\theta}}_j}{|\dot{\boldsymbol{\theta}}_j|} \quad (2.62)$$

Here, μ_f is the rotational friction coefficient. The calculated mechanical force and torque are added to the right hand side of Equations (2.1) and (2.2) of Newton's law, respectively. By setting a small time step for the DEM process, multi-body collisions can be calculated in the soft sphere model. However, if the particle overlap is large compared with the particle diameter, the solution of the mechanical force will diverge. Therefore, the time step must be set sufficiently small; however, this will result in an increase in calculation load. The calculation load is one of the issues on the soft sphere model.

2.7.3 Hard Sphere Model

The hard sphere model is another tool that can be used to calculate particle collisions [16, 17]. This model is used to calculate particle velocities after collision based on the conservation law of momentum. In this model, the calculation of a particle collision and that of the external force are separated, and the time step of the

DEM is not limited by the effect of the collision, similar to that of the soft sphere model. If the particle collisions occur rarely in a calculation model, a large time step can be set as long as it does not affect the particle motions. However, because the hard sphere model is based on the conservation law of momentum, the model cannot calculate multi-body collision. For this reason, the hard sphere model is rarely utilized in calculations that involve many particles crowded in a small area. In the hard sphere model, only one pair of two-particle collision at a particular moment must be processed owing to the conservation law of momentum. Multiple pairs of two-particle collisions cannot be calculated at the same moment; thus, it is important to consider the order of the collision pairs in the hard sphere model.

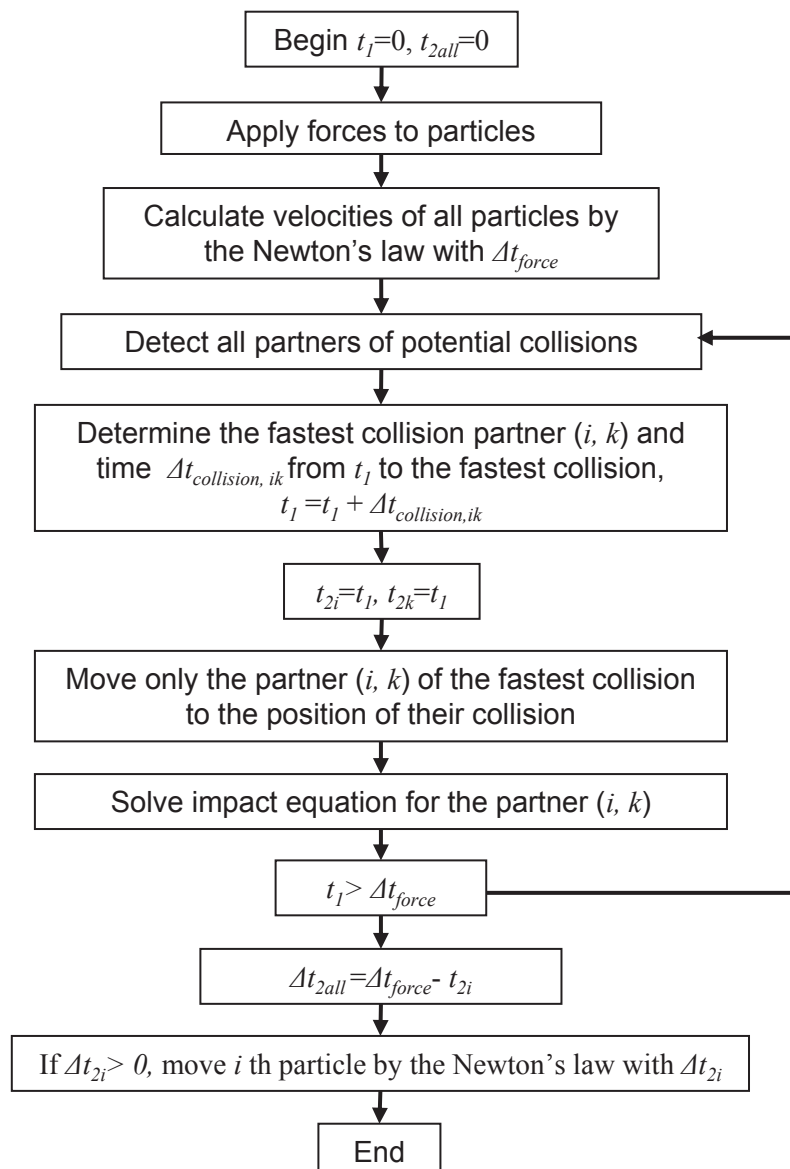


Figure 2.20 Calculation algorithm for the hard sphere model for one step.

Figure 2.20 shows the algorithm of the hard sphere model for one step. When the calculation process reaches the “End,” the process returns to “Begin”, and then the calculation continues until it is stopped. In the first step of the algorithm, the external forces acting on particles are calculated, considering the initial conditions of the particles. t_1 and t_2 are the elapsed time of the entire calculation process and of each particle, respectively. Then, the updated particle velocities are calculated with the time step Δt_{force} for calculating the effects of external forces. From the updated velocities and former positions, all partners of potential collisions are predicted, and the fastest partner of the i -th and k -th particles and the time $\Delta t_{collision,ik}$ from t_1 to their collision are determined. At that time, t_1 is updated with $\Delta t_{collision,ik}$. The i -th and k -th particles are moved based on Newton’s law with $\Delta t_{collision,ik}$ and t_{2i} and t_{2k} are updated by $\Delta t_{collision,ik}$. The fastest collision between the i -th and k -th particles is calculated by the impact equation based on the conservation law of momentum, and their velocities are updated. The method of calculating the impact equation will be described later. If the elapsed time of the entire calculation process t_1 is larger than the time step Δt_{force} for calculating the effect of external forces, the calculation of the collisions are stopped, and all particles are moved to their individual position at the next time step based on Newton’s law. Otherwise, the calculation process, which involves detecting the fastest collision partner and calculating the impact equation, is continued.

The velocities and angular velocities of the i -th and k -th particles can be calculated by the impact equations based on the conservation law of momentum, are represented by Equations (2.63), (2.64), (2.65), and (2.66) [16-18].

$$\dot{\mathbf{x}}_i^* = \dot{\mathbf{x}}_i + \frac{\mathbf{J}_{ki}}{m_i} \quad (2.63)$$

$$\dot{\mathbf{x}}_k^* = \dot{\mathbf{x}}_k - \frac{\mathbf{J}_{ki}}{m_k} \quad (2.64)$$

$$\dot{\boldsymbol{\theta}}_i^* = \dot{\boldsymbol{\theta}}_i - \frac{R_i}{I_i} \left(\mathbf{n}_{ki} \times \mathbf{J}_{ki} + \mu_f |\dot{\boldsymbol{\theta}}_i| \mathbf{J}_{ki} \cdot \mathbf{n}_{ki} \right) \quad (2.65)$$

$$\dot{\boldsymbol{\theta}}_k^* = \dot{\boldsymbol{\theta}}_k - \frac{R_k}{I_k} \left(\mathbf{n}_{ki} \times \mathbf{J}_{ki} + \mu_f |\dot{\boldsymbol{\theta}}_k| \mathbf{J}_{ki} \cdot \mathbf{n}_{ki} \right) \quad (2.66)$$

where \mathbf{J} and \mathbf{n}_{ki} are the impulsive force from the k -th particle to the i -th particle and the normal vector from the k -th to the i -th particle, respectively. The asterisk $*$ denotes the velocity or angular velocity after collision. In Equations (2.65) and (2.66), if the particles are rotating during the collision, the rolling friction is assumed to be proportional to the angular velocity and the vertical impulsive force. The relative velocities \mathbf{v} and \mathbf{v}^* of particles at the point of collision before and after collision are represented by Equation (2.67) and (2.68), respectively.

$$\mathbf{v} = (\dot{\mathbf{x}}_i - \dot{\mathbf{x}}_k) - (R_i \dot{\boldsymbol{\theta}}_i + R_k \dot{\boldsymbol{\theta}}_k) \times \mathbf{n}_{ki} \quad (2.67)$$

$$\mathbf{v}^* = (\dot{\mathbf{x}}_i^* - \dot{\mathbf{x}}_k^*) - (R_i \dot{\boldsymbol{\theta}}_i^* + R_k \dot{\boldsymbol{\theta}}_k^*) \times \mathbf{n}_{ki} \quad (2.68)$$

The relative velocities \mathbf{v} after collision can be represented by the velocities before collision using the coefficient of restitution γ and normal vector as Equation (2.69).

$$\mathbf{n}_{ki} \cdot \mathbf{v}^* = -\gamma (\mathbf{n}_{ki} \cdot \mathbf{v}) \quad (2.69)$$

By combining and arranging Equations (2.63), (2.64), (2.65), (2.66), (2.67), (2.68), and (2.69), the impulsive force in the normal direction \mathbf{J}_n can be calculated by Equation (2.70).

$$\mathbf{J}_{nki} = \frac{-(1+\gamma)\mathbf{n}_{ki} \cdot \mathbf{v}}{\frac{1}{m_i} + \frac{1}{m_k}} \quad (2.70)$$

In the case of slip, the impulsive force in the tangential direction \mathbf{J}_t can be calculated using Coulomb's law, which is represented by Equation (2.71).

$$\mathbf{J}_{tki} = \mu_d |\mathbf{J}_{nki}| \quad (2.71)$$

In the no slip condition, the subtraction between \mathbf{v}^* and \mathbf{v} is represented by Equation (2.72).

$$\mathbf{v}^* - \mathbf{v} = \left(\frac{7}{2m_i} + \frac{7}{2m_k} \right) \mathbf{J}_{ki} - \left(\frac{5}{2m_i} + \frac{5}{2m_k} \right) \mathbf{n}_{ki} (\mathbf{J}_{ki} \cdot \mathbf{n}_{ki}) \quad (2.72)$$

Using Equation (2.73), Equation (2.72) can be modified into Equation (2.74).

$$\mathbf{n}_{ki} \times \mathbf{v}^* = -y (\mathbf{n}_{ki} \times \mathbf{v}) \quad (2.73)$$

$$\mathbf{J}_{tki} = \frac{-(1+y)\mathbf{t}_{ki} \cdot \mathbf{v}}{\frac{7}{2m_i} + \frac{7}{2m_k}} \quad (2.74)$$

where y and \mathbf{t} are the coefficient of restitution in the tangential direction and the tangential vector from the k -th to the i -th particle, respectively. If \mathbf{J}_{tki} in no slip case is larger than that in the slip case, as shown in Equation (2.75), \mathbf{J}_{tki} is saturated, as it is in the slip case.

$$\mu_d |\mathbf{J}_{nki}| < \frac{-(1+y)\mathbf{t}_{ki} \cdot \mathbf{v}}{\frac{7}{2m_i} + \frac{7}{2m_k}} \quad (2.75)$$

The impulsive force \mathbf{J}_{ki} consists of \mathbf{J}_{nki} and \mathbf{J}_{tki} as shown by Equation (2.76).

$$\mathbf{J}_{ki} = \mathbf{J}_{nki} \mathbf{n}_{ki} + \mathbf{J}_{tki} \mathbf{t}_{ki} \quad (2.76)$$

The velocities and angular velocities of particles after collision can be calculated by substituting the impulsive force \mathbf{J}_{ki} into Equations (2.63), (2.64), (2.65), and (2.66). When the i -th particle collides with another object such as a plate or wall that is significantly large compared to the particle, it is assumed that such an object is a k -th particle with an infinitely large diameter and mass.

2.7.4 Modified Hard Sphere Model

The mechanical interaction force between particles should not affect the dynamics of particles agitated by the electrostatic and magnetic fields largely because the particles are not densely distributed. Therefore, the hard sphere model, which has the possibility of reducing the calculation load of the DEM, was chosen in this research. Because the conventional hard sphere model has to process each pair of two-particle collision in the order of their occurrence and it cannot calculate plural pairs at the same moment, the model is not appropriate to apply to dynamics of particles agglutinated to each other owing to the adhesion force and the electrostatic and magnetic interactions of particles. In this case, particle collisions will occur frequently, and the time step must be set as small, which makes the calculation load large. Therefore, the conventional hard sphere model was modified in this research.

A flowchart of calculation algorithm used in the modified hard sphere model is shown in Figure 2.21 [18, 19] for one time step. At the first calculation process, the summation of the external forces \mathbf{F} acting on each particle is calculated. Then, particle velocities and positions at the next step Δt_{force} are calculated by Newton's law. After updating the velocities and positions, all the collisions between the next step and the last step are predicted from the velocities and positions at the next and the last steps. Then, the time $\Delta t_{collision,ik}$ between the last time step and the moment when a collision occurs for all pairs of two-particle collisions are calculated using Equation (2.77) [20].

$$\Delta t_{collision,ik} = \frac{-(\mathbf{x}_i - \mathbf{x}_k) \cdot (\dot{\mathbf{x}}_i - \dot{\mathbf{x}}_k) - \sqrt{\left((\mathbf{x}_i - \mathbf{x}_k) \cdot (\dot{\mathbf{x}}_i - \dot{\mathbf{x}}_k) \right)^2 - (\dot{\mathbf{x}}_i - \dot{\mathbf{x}}_k)^2 \left((\mathbf{x}_i - \mathbf{x}_k)^2 - (R_i - R_k)^2 \right)}}{(\dot{\mathbf{x}}_i - \dot{\mathbf{x}}_k)^2} \quad (2.77)$$

Equation (2.77) is derived from the relative positions and velocities of particles, as shown in Figure 2.22. The relationship between the i -th and k -th particles is represented by Equation (2.78).

$$\left| (\mathbf{x}_i - \mathbf{x}_k) + (\dot{\mathbf{x}}_i - \dot{\mathbf{x}}_k \Delta t_{collision,ik}) \right| = R_i + R_k \quad (2.78)$$

By multiplying Equation (2.78) by itself, Equation (2.77) is derived. In case the inequality in Equation (2.79) is not satisfied, the collision between the i -th and k -th particles is assumed not to occur and that the distance between the particles is increasing.

$$(\mathbf{x}_i - \mathbf{x}_k) \cdot (\dot{\mathbf{x}}_i - \dot{\mathbf{x}}_k) < 0 \quad (2.79)$$

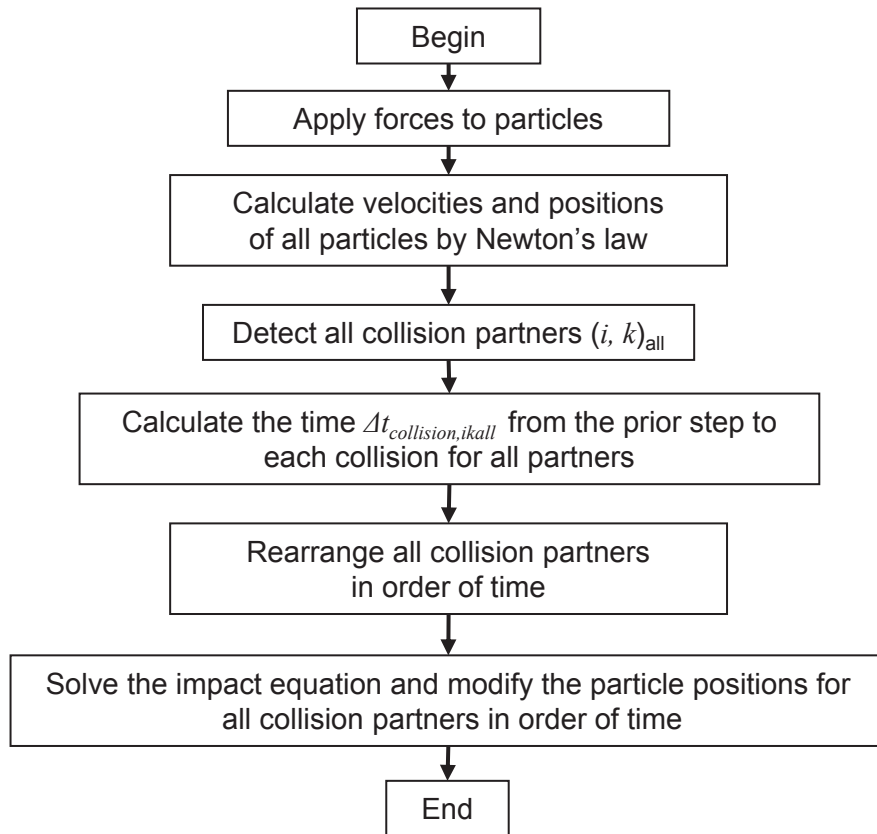


Figure 2.21 Calculation algorithm of the modified hard sphere model for one time step.

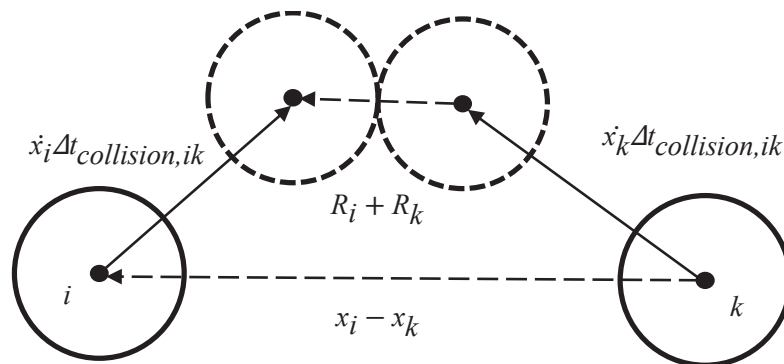


Figure 2.22 Relationship between particle positions and velocities before and during collision.

After calculating $\Delta t_{collision,ik}$ for all collision pairs, the pairs are arranged in ascending order. Then, the collision pairs are calculated by the impact equation. This algorithm can take into account the order of particle collisions, which is important in the hard sphere model, even though all particles can be moved at the same moment. If an overlap of colliding particles occurs, the positions of the particles overlapping with each other are modified by Equation (2.80).

$$\mathbf{x}_i = \mathbf{x}_i + \left(\frac{\frac{4}{3}\pi R_i^3}{\frac{4}{3}\pi R_i^3 + \frac{4}{3}\pi R_k^3} \right) \mathbf{n}_{ki} \quad (2.80)$$

where *overlap* and *h* are the amount of overlapping in the normal direction and the gap between particle surfaces, respectively. The gap *h* is assumed to be 0.4×10^{-9} m because the Van der Waals's attractive force balances Born's impulsive force at the distance. As the gap *h* is set, the small distance between particles occurs continuously, and the times $\Delta t_{collision,ik}$ for all collision pairs are calculated repeatedly.

Figure 2.23 shows the concepts of the calculation models. Because the soft sphere model includes the mechanical forces, $F_{mech.nij}$ and $F_{mech.tij}$, the forces must be added to the right hand side of motion Equation (2.1), and the time step has to be made extremely small to avoid divergence in the calculation of mechanical forces. In contrast, the hard sphere model is a type of event-driven calculation. The calculation of external forces is separated from that of particle collision, which is conducted during the long interval of applying external forces. Because plural collisions cannot be processed, the calculation load increases if many collisions occur, and parallel computing is not compatible with the hard sphere model. In the modified hard sphere model, the time step can be set relatively large, and all collisions can be processed at the same moment. In addition, because the collision calculations are processed in order of occurrence, parallel computing is also not compatible with the modified hard sphere model.

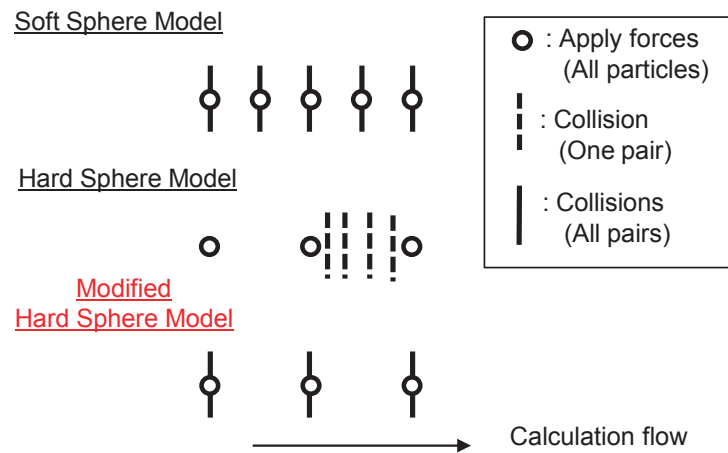


Figure 2.23 Timing of calculating external forces and particle collisions in the soft sphere model, the conventional, and modified hard sphere models.

2.7.5 Accuracy of Modified Hard Sphere Model

A simple particle collision model was used to confirm the accuracy of the modified hard sphere model. As shown in Figure 2.24, three particles are assumed to collide with each other. In this calculation, it is assumed

that external forces are not applied to particles but initial velocities are provided. Considering the relative positions and velocities of the particles, a collision between the i -th and j -th particles will occur and then a collision between the j -th and k -th particles will occur in order. This particle motion is calculated using the soft sphere model and the modified hard sphere model. Rolling friction was neglected in the soft sphere model calculation. In addition, two types of calculations using the modified hard sphere model were conducted to confirm the effect of the arrangement of the collision order. One type contains the process of the arrangement of particle collisions, while the other does not consider it. In each calculation, the time step was selected as a parameter, and an adequate time step was evaluated.

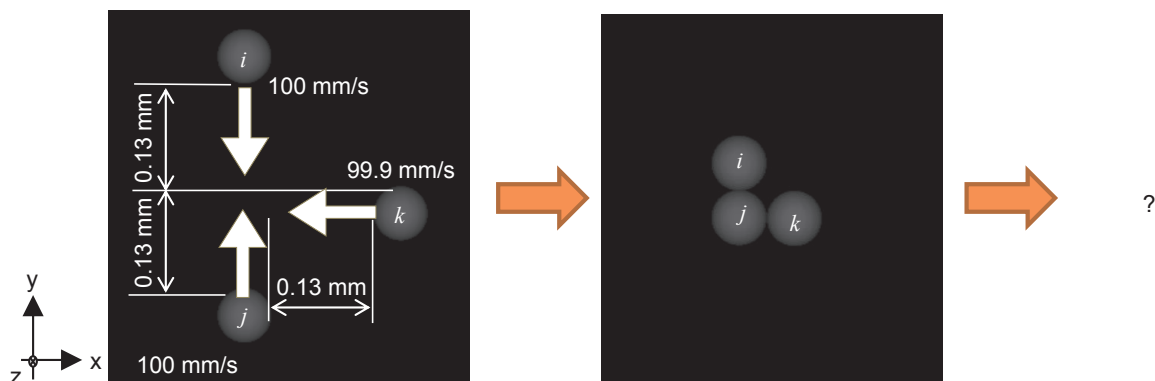


Figure 2.24 Calculation model to confirm the accuracy of the modified hard sphere model.

Figure 2.25 shows the motion of the particles after the calculation, and Figure 2.26 shows the positions of particles in the y -direction. When the time step is 1.0×10^{-8} s, the particles reach almost the same position in all calculation models, as shown in Figure 2.26. In the calculation of the soft sphere model, the particle motions become unstable as the calculation progresses when the time step is large, and the particles move beyond the borders of the image of Figure 2.25 when the time step is 1.0×10^{-6} s. Moreover, the calculation diverges when the time step is 1.0×10^{-5} s. In the calculation of modified hard sphere model, the divergence does not occur; however, the particle motions in the case where the collision order is considered are clearly different from the motions in the case that does not consider it, when the time step is 1.0×10^{-5} s. This is because a collision between the j -th and k -th particles, followed by a collision between the i -th and j -th particles, were calculated in order in the case that did not consider the collision order. Therefore, it is important to take the collision order into account as demonstrated by the modified hard sphere model.

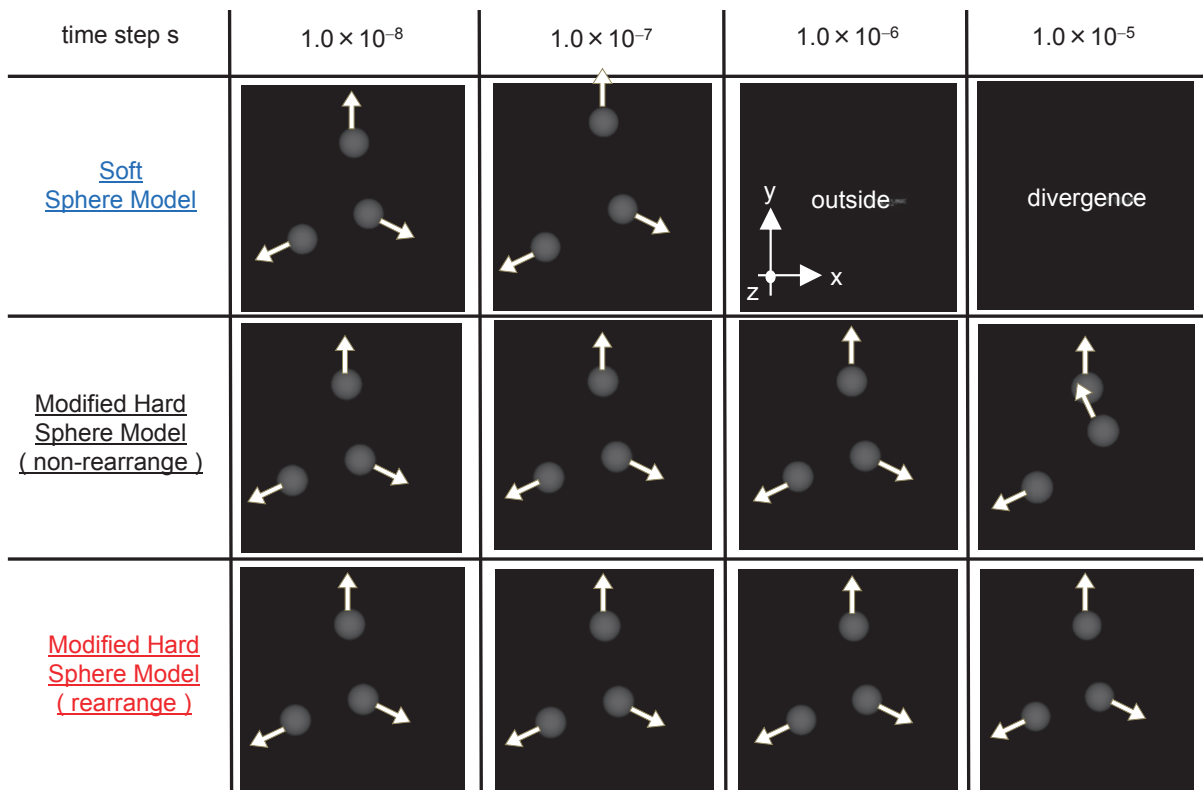


Figure 2.25 Calculated particle motions using the soft sphere model and the modified hard sphere model when collision order is considered and not considered.

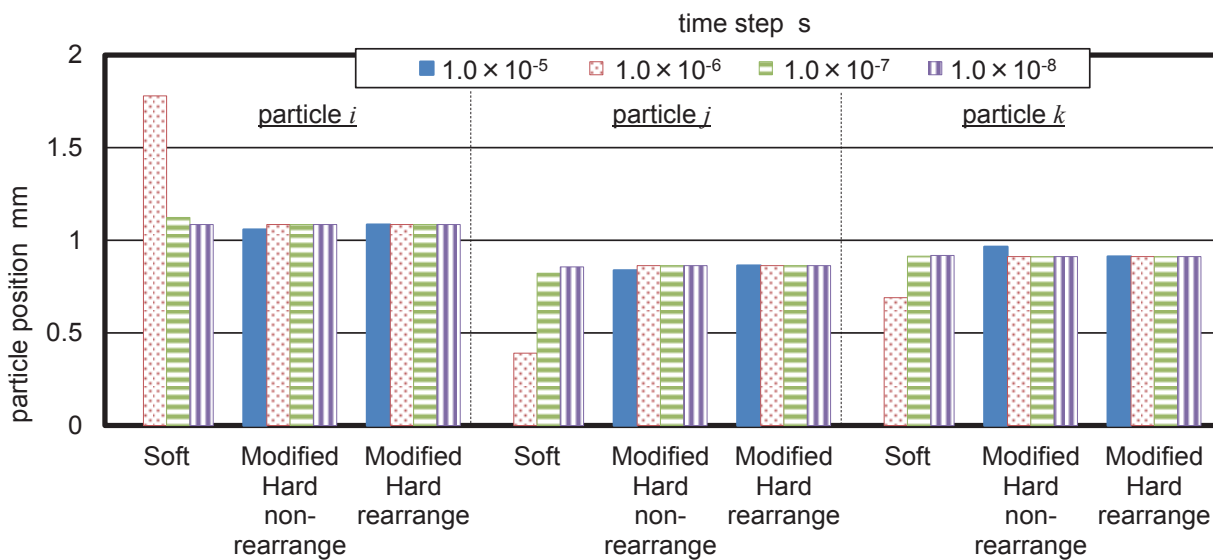


Figure 2.26 Calculated particle positions in the y-direction using the soft sphere model and the modified hard sphere model when collision order is considered and not considered (Initial positions of particles, i : 1.13 mm, j : 0.8 mm, k : 0.93 mm).

Figure 2.27 shows the computation time expended in each calculation repeated for 1,000,000 times. Because the calculation of the soft sphere model diverges when the time step is 1.0×10^{-5} s, the computation time in this condition is eliminated from Figure 2.27. The computation time increases when the time step is decreased in all calculation models. The computation time in the soft sphere model is larger than that in the modified hard sphere model in same time step, because the calculation process of the hard sphere model is simpler than that of the soft sphere model, as described in sections 2.7.2 and 2.7.3. The proposed modified model can calculate particle motions and reduce the calculation load to approximately 1/3,000 of that required in the soft sphere model, while preserving particle collision calculation accuracy, as shown in Figures 2.26 and 2.27.

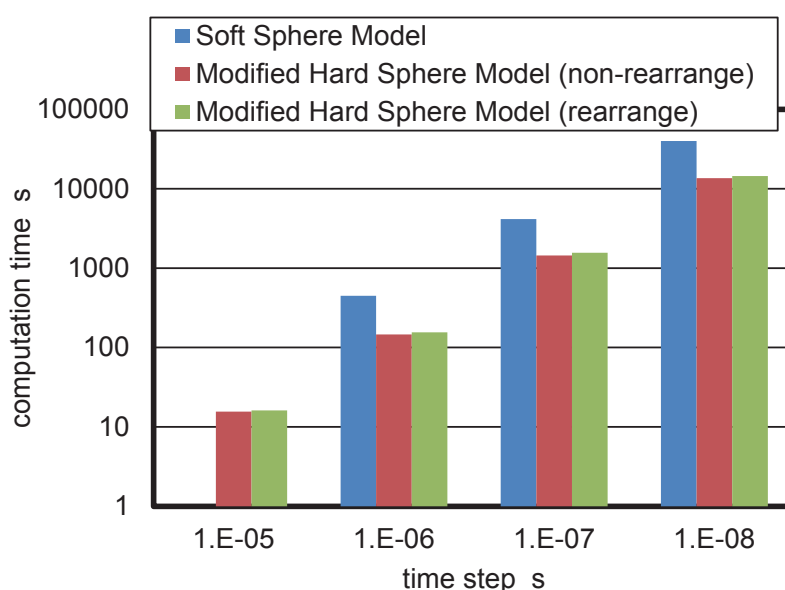


Figure 2.27 Computation times expended in calculations repeated 1,000,000 times using the soft sphere model and modified hard sphere model when collision order is considered and not considered.

2.7.6 Electrostatic and Magnetic Interactions between Particles

In the DEM calculations, the electrostatic and magnetic interactions within particles affect their dynamics, and the effect cannot be neglected. The Coulomb force, dielectrophoresis force, and magnetic force are mainly affected by these interactions, and their calculation methods have to be modified. In this section, the calculation methods that consider these interactions are described.

Equation (2.3) of Coulomb's law considers only the external electric field generated by the experimental setup. When the electrostatic field \mathbf{E} is generated by the charges of other particles, the field can be calculated using Equation (2.5) of Poisson's equation. In that case, the electrostatic field \mathbf{E} has to be calculated using the finite difference method repeatedly, which results in large calculation loads. Considering the superposition principle, which can be applied to the electrostatic field, Coulomb's law can be modified as

Equation (2.81).

$$\mathbf{F} = q_i \mathbf{E} - \frac{q_i}{4\pi\epsilon_0} \sum_{i < k}^N \frac{q_k \mathbf{r}_{ki}}{|\mathbf{r}_{ki}|^3} \quad (2.81)$$

Here, N and \mathbf{r} are the number of all particles and the position vector from k -th to i -th particle. The first term of Equation (2.81) is the Coulomb force from the external electrostatic field \mathbf{E} , and the second term is that from the charge of other particles. Before the DEM calculation, the external electrostatic field \mathbf{E} is calculated by the finite difference method in advance. During the DEM, the first term is calculated by looking up the electrostatic field \mathbf{E} at the position of the particle, and the second term is calculated for all other particles.

Equations (2.9) and (2.17) for the dielectrophoresis force and magnetic force, respectively, can be modified because the electrostatic and magnetic dipole moments are affected not only by the external electrostatic field \mathbf{E} and magnetic field \mathbf{B} but also by the electrostatically and magnetically polarized particles, respectively. The electrostatic field \mathbf{E}^* and the magnetic field \mathbf{B}^* which are affected by other dipole moments can be represented as Equation (2.82) and (2.83), respectively.

$$\mathbf{E}_i^* = \mathbf{E}_i + \sum_{i < k}^N \mathbf{E}_{ki} \quad (2.82)$$

$$\mathbf{B}_i^* = \mathbf{B}_i + \sum_{i < k}^N \mathbf{B}_{ki} \quad (2.83)$$

The first terms on the right hand side of Equation (2.82) and (2.83) are the external electrostatic field \mathbf{E} and the magnetic field \mathbf{B} , respectively, and the second terms are the electrostatic field \mathbf{E} and magnetic field \mathbf{B} generated by the dipole moment in other particles. In addition, the fields generated by the dipole moments are represented by Equation (2.84) and (2.85) [15].

$$\mathbf{E}_{ki} = \frac{1}{4\pi\epsilon_0} \left(\frac{3\mathbf{P}_{ele,k} \cdot \mathbf{r}_{ki}}{|\mathbf{r}_{ki}|^5} \mathbf{r}_{ki} - \frac{\mathbf{P}_{ele,k}}{|\mathbf{r}_{ki}|^3} \right) \quad (2.84)$$

$$\mathbf{B}_{ki} = \frac{4\pi}{\mu_0} \left(\frac{3\mathbf{P}_{mag,k} \cdot \mathbf{r}_{ki}}{|\mathbf{r}_{ki}|^5} \mathbf{r}_{ki} - \frac{\mathbf{P}_{mag,k}}{|\mathbf{r}_{ki}|^3} \right) \quad (2.85)$$

The simultaneous equations of (2.12), (2.82) and (2.84) for the electrostatic dipole moments of plural particles can be calculated by substituting the electrostatic field \mathbf{E}^* into \mathbf{E} of Equation (2.12). Similarly, the simultaneous equations of (2.19), (2.83) and (2.85) can be calculated for the magnetic dipole moments of plural particles. The direct method of calculating the simultaneous equations results to a large calculation load. Thus, the equations are calculated by the iteration method, where the calculations are continued until the

electrostatic and magnetic dipole energies become stable. The electrostatic energy U_{ele} and the magnetic energy U_{mag} are represented by Equations (2.86) and (2.87), respectively.

$$U_{ele} = -\frac{1}{2} \sum_{i=1}^N \mathbf{p}_{ele,i} \cdot \mathbf{E}_i^* \quad (2.86)$$

$$U_{mag} = -\frac{1}{2} \sum_{i=1}^N \mathbf{p}_{mag,i} \cdot \mathbf{B}_i^* \quad (2.87)$$

Finally, the dielectrophoresis force and magnetic force considering the particle interaction can be calculated, respectively, by substituting the calculated electrostatic field \mathbf{E}^* and the electrostatic dipole moment \mathbf{p}_{ele} into Equation (2.9), and the magnetic field \mathbf{B}^* and magnetic dipole moment \mathbf{p}_{mag} into Equation (2.17).

2.7.7 Cyclic Boundary Condition and Detection Method for Particle Collisions

Although the modified hard sphere model can reduce the calculation load, the load is still large. A large part of the calculation load involves the detection of collisions because the detection time is proportional to the square of the particle quantity. The cyclic boundary condition and cells for the detections are applied to reduce the number of the detections.

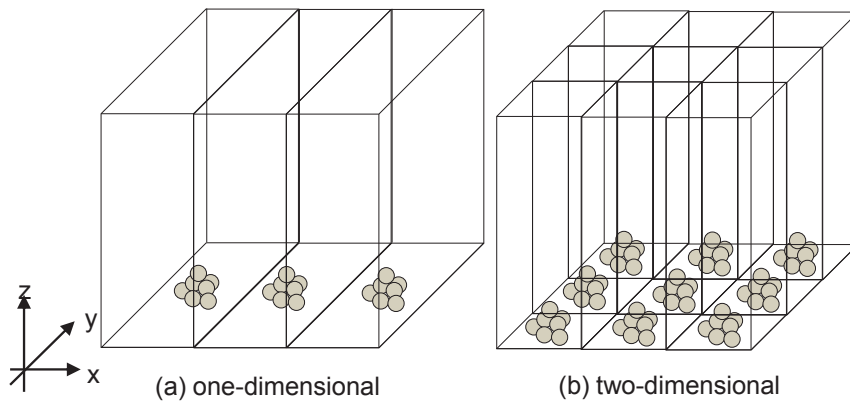


Figure 2.28 Cyclic boundary conditions of DEM in one-dimensional and two-dimensional systems.

As shown in Figure 2.28, two types of boundary conditions are applied in this research; such as one- and two-dimensional systems. If the same pattern of particle geometry appears repeatedly in the x -direction (Figure 2.28 (a)), the calculation area is segmented between the patterns. The particles in one area are calculated, and if the particle reaches the end of the area, the particle is moved to the other end. Similarly, the cyclic boundary conditions can be applied to the x - y two-dimensional system (Figure 2.28 (b)). The number of particles can be reduced in case of the boundary conditions of one- and two-dimensional systems,

and the calculation load can also be decreased.

The introduction of detection cells for particle collisions is useful for the reduction of calculation loads in the DEM. As shown in Figure 2.29, the cells are mapped in the calculation area in one-, two-, and three-dimensional systems. In the case where three cells are applied in the x -direction (Figure 2.29, one-dimensional cells), the detections of collisions about the i -th particle needs to be applied to particles in the same cells, and the number of the detections is reduced to $1/3$ that in the case in which the cells are not applied. In the case where nine cells are applied in the x - and y - directions (Figure 2.29, two-dimensional cells), the number of detections is reduced to $1/9$ of that in the case without applying the cells. In the case of three-dimensional cells, the calculation loads can be similarly reduced. If the two- or three-dimensional cells are used and their cell size is set to be small, the number of detections is further reduced. Actually, the number of calculating detections is proportional to the number of particles when sufficiently small cells are applied. In addition, the numbers of cells in the case of two- and three-dimensional cells are proportional to the square and cube of that in the case using one-dimensional cells, respectively, and it requires a significant computer memory. Moreover, managing the cells also increases the calculation load; therefore, the optimum number of cells has to be applied, depending on how the particles are distributed in the calculation area.

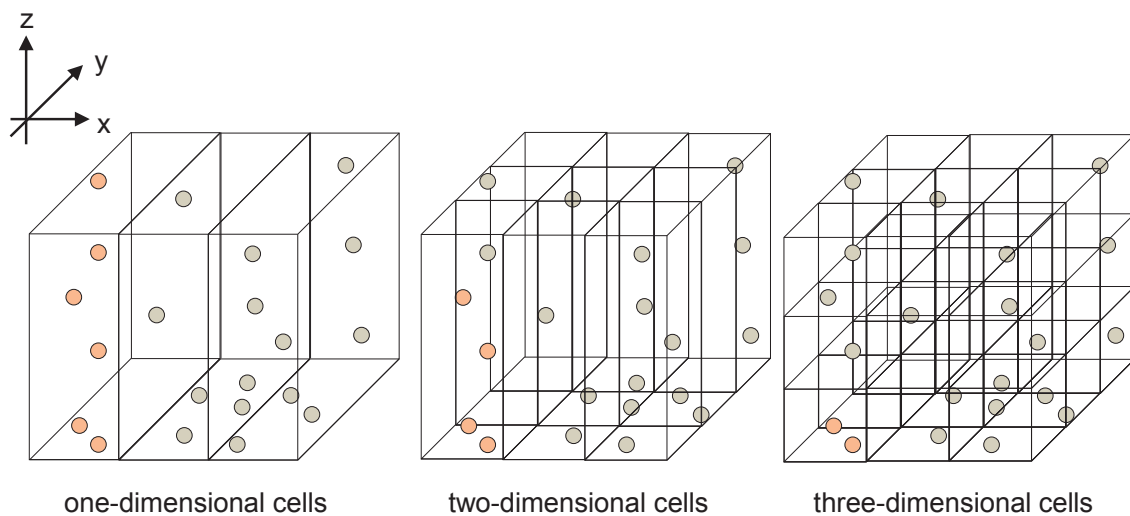


Figure 2.29 Detection cells for particle collisions to reduce calculation load in DEM.

2.8 Summary

The motion equation for a particle and the constitutive equations for external forces were described in this chapter to understand the particle dynamics in electrostatic, magnetic, and space environments. In addition, model experiments were conducted to evaluate the specific values used in the equations by considering an actual particle, such as lunar regolith. In addition, the balance of external forces was evaluated to achieve insights that can be used to develop a system capable of handling particles by using the electrostatic and mag-

netic forces. The insights achieved in this section are: (1) lunar regolith particles, ranging from 20 μm to 500 μm in diameter, can be moved by the Coulomb force in 1-G environment, and particles larger than 500 μm in diameter can be moved in a low-gravity environment similar to that on the Moon and on asteroids; (2) lunar regolith particles with small relative magnetic permeability can be moved by the magnetic force in low-gravity environments, and particles with large relative permeability can be moved in a 1-G environment; and (3) particles smaller than 20 μm are significantly affected by the adhesion force and air drag; however, the effect of air drag can be neglected in a vacuum. From the calculation results, systems that can handle particles using the electrostatic and magnetic forces are expected to be useful in the space environment. However, these estimations were conducted with a simple assumption; therefore, demonstrations of the system in experiments and numerical calculations are necessary to confirm the results of the simple calculation. Moreover, the methodology of the DEM, which is the key numerical calculation used in this research, was also described. The hard sphere model of the DEM was modified to adapt the method to this research. The modified DEM can reduce the calculation load, which is one of the most important issues of the DEM, to 1/3,000 compared with the conventional DEM. In addition, the introductions of cyclic boundary conditions and detection cells for particle collisions are useful for further reducing the calculation load.

Chapter 3 Electrostatic Dust Shield System Used for Lunar and Mars Exploration Equipment

3.1 Introduction

As described in section 1.1.3, a serious problem with lunar dust during the Apollo missions was its intrusion into the gaps of mechanical drives installed on the equipment used for extravehicular activity. Lunar dust was responsible for several fatal mechanical problems [1]. To address this problem, mechanical dust shield systems [2-5] and the Dust-Tolerant Connector [6] were developed in previous studies. Although these systems demonstrated high mitigation performance when tested against lunar regolith simulants, the life cycles of the systems had to be improved because they had to withstand contact with a rotating shaft, casing, and particles, and system wear was determined to be unavoidable. To support the mechanical systems and extend their lifetimes, it is necessary to develop new dust mitigation technology that can prevent dust intrusion into mechanical gaps and can be easily adapted to mechanical systems.

In this study, the electrostatic shield system was developed. The electrostatic system utilized the Coulomb force and dielectrophoresis force to remove particles that are about to intrude into mechanical gaps. As described in section 2.6.1, it is expected that the electrostatic force can move lunar regolith particles smaller than 500 μm in diameter by using the electrostatic force in the Earth environment. Because the sizes of the particles subjected to the issue range from approximately one micrometer to several hundred micrometers, which are smaller than the mechanical gaps, the electrostatic force could be used. The electrostatic system has several advantages, such as no mechanical drives, ease of control, low-power consumption, and adaptability to mechanical systems. It is expected that the electrostatic system can increase the lifetime of the mechanical shields and connectors for long-term exploration missions on the Moon and Mars. In this chapter, two types of electrostatic shield systems were developed (plate and plate + wire configurations), and their performances were experimentally evaluated in the Earth environment. In addition, because the Coulomb force is significantly affected by particle charge, the effect of the charge on the system performance was investigated as well. Moreover, a numerical calculation based on the DEM of the modified hard sphere model, as described in section 2.7, was conducted, and the calculated results were compared to the experimental results to confirm the accuracy of the numerical calculations. By using the numerical calculation, the performance of the system in the lunar and Martian environments was predicted. Part of this work has been published in literature [7].

3.2 Experiment

3.2.1 System Configuration

Figure 3.1 shows the mechanism of the electrostatic dust shield system. It consists only of insulated elec-

trodes and a power supply, as shown in Figure 3.1 [7]. The electrodes are set at both sides of a mechanical gap, and one electrode is grounded. When a high voltage of alternative standing wave is applied to the other electrode, an electrostatic field is created near the gap, and the resultant Coulomb force and dielectrophoresis force can attract particles that are about to intrude into the gap. When the polarity of the voltage is changed, the direction of the electrostatic field reverses, and particles are shifted outward.

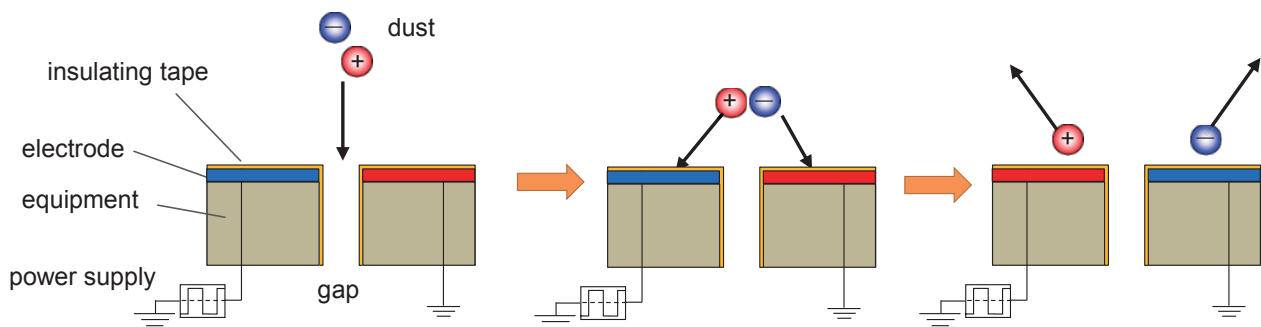


Figure 3.1 Mechanism of removing particles by using electrostatic dust shield system.

Two types of electrodes were utilized in this research: the plate type and plate + wire type. Both types are shown in Figure 3.2. The plate type consists of two acrylic plates (thickness = 2 mm, gap between plates = 1 mm, area of the gap = 30 mm², relative permittivity $\epsilon = 3.1$), copper plate electrodes (width = 5 mm, thickness = 0.08 mm, gap between electrodes = 1 mm), and insulative polyamide tape (thickness = 0.06 mm, relative permittivity $\epsilon = 3.1$), as shown in Figure 3.2 (a). The gap between the acrylic plates is set to be 1 mm, as a matter of convenience for the evaluation of the experiments. However, the actual mechanical gap of the exploration equipment is assumed to be much smaller than 1 mm. Therefore, the actual performance of this electrostatic system will be better compared to the performance achieved for this research. The plate + wire type consists of the copper plate electrodes and wire electrodes (diameter = 0.4 mm, distance of each wire = 1.25 mm, gap = 3.0 mm, insulated), as shown in Figure 3.2 (b). In the plate + wire type, the electrostatic flux line can be created laterally between the wire electrodes. It can be expected that the particles falling between electrodes are ejected laterally along the electrostatic flux lines passing through the space between wires; thus, the shield performance will be better compared with that of the plate type.

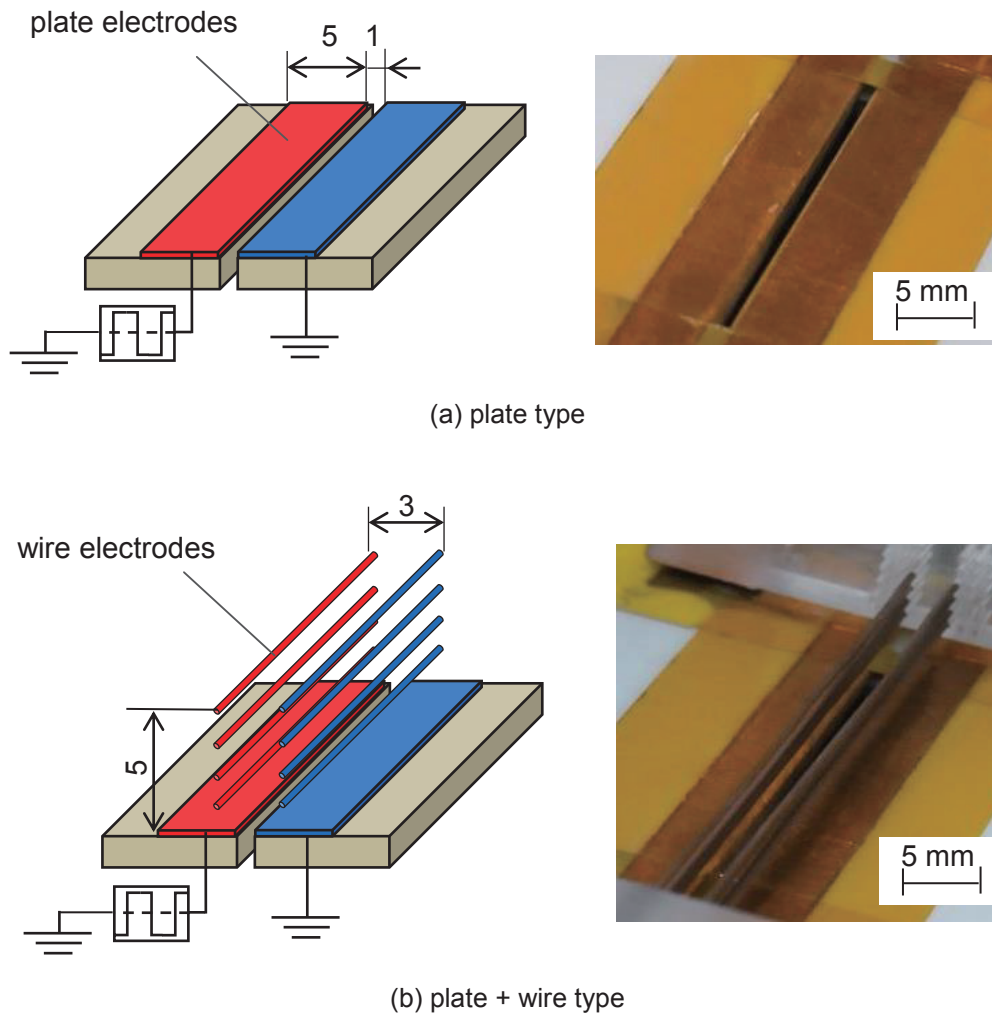


Figure 3.2 Configurations of (a) plate and (b) plate + wire electrodes with photographs.

The power supply consists of two DC power supplies (HJPM-5P0.6, Matsusada Precision), a microcomputer (Arduino Uno, Arduino), and a switching circuit, as shown in Figure 3.3. The DC power supplies generate positive and negative DC high voltage, and the microcomputer generates the digital signal as the frequency is altered. The positive and negative voltages are switched alternately as their phases are shifted by 180° using the switching circuit consisting of Photo MOS semiconductors, corresponding to the frequency of the digital signal. Then, the rectangular high voltage is supplied from one output.

The electrostatic dust shield system can be installed in any equipment as the shape of the electrodes is adaptable to different types of mechanical gaps, such as line and circular gaps. The application of the mechanical shield system is shown in Figure 3.4. JAXA has developed a brush seal made of fluorine resin, a labyrinth seal made of aluminum and SUS304, and mechanical seals made of Varilip[®] and Variseal[®] [2-4]. NASA has considered the application of a spring-loaded Teflon seal, such as Bal Seal[®] [5], as described in section 1.3.2. The electrostatic system can support the mechanical shield as well as the mechanical connectors to expand the life cycle of the mechanical systems.

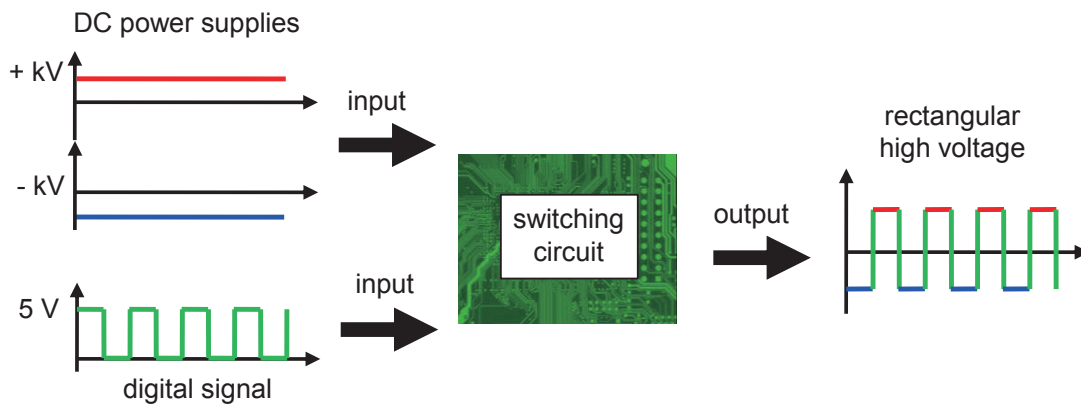


Figure 3.3 Configuration of power supply used to generate rectangular high voltage.

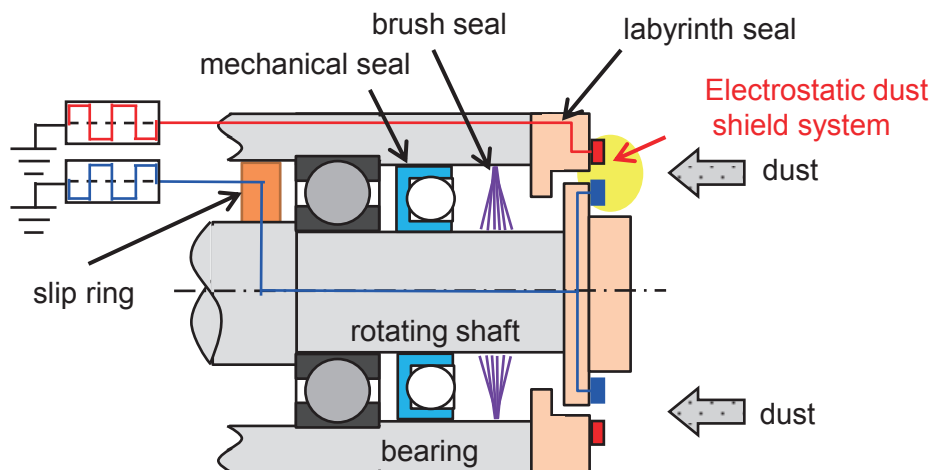


Figure 3.4 Application of electrostatic shield system to support mechanical shield systems.

3.2.2 Experimental Setup

Figure 3.5 shows the experimental setup [7]. The particles were fed into the gap between the acrylic plates by using the particle supplier. The particle supplier consisted of an electromagnetic shaker (G-2005D, Shinken), a mechanical sand sieve (aperture = 106 μm), and an acrylic base. The supply rate of the particles was kept constant by arranging the vibrational acceleration and the frequency of the electromagnetic shaker. The distance between the sieve and the gap was 40 mm. The lunar regolith simulant FJS-1 was used for the experiments. The properties of the simulant were summarized in section 1.1.2. Before the simulant was set on the sieve, the size was sorted with the maximum size of less than 106 μm by using another sieve because the particles should be smaller than the mechanical gap. The particles were supplied to the mechanical gap at a rate of 5.0 $\text{g/s}\cdot\text{m}^2$ for 120 s. The particles that were not removed by the electrostatic dust shield system passed through the mechanical gap and were collected in a tray and measured. The experiment was conducted in

two cases when the electrostatic dust shield system was operated and not operated. The difference between the amounts of collected particles for two cases was evaluated as the shield rate. The size distributions of the collected particles were analyzed using a particle analyzer (Morphologi G3, Malvern). The particle motions were observed using a high-speed microscope camera (FASTCAM SA5, Photoron).

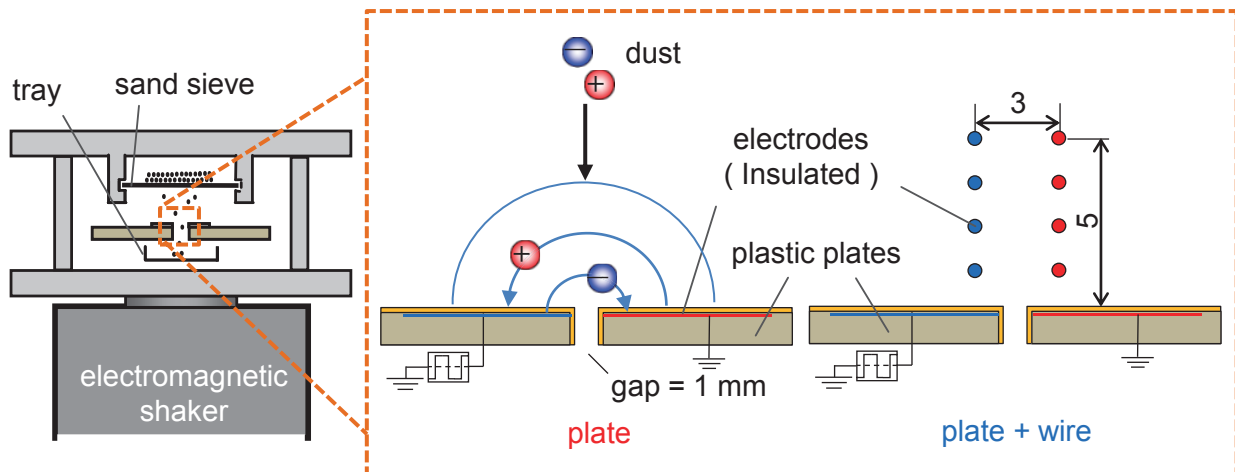


Figure 3.5 Configurations of electrostatic dust shield system.

3.2.3 Control of Particle Charge

Because the Coulomb force is affected by the particle charge, it is assumed that the system performance is highly dependent on the charge. To confirm the effect, the particles were discharged and charged electrostatically by UV neutralization and corona charging, respectively, before the experiments. A UV lamp (handy UV lamp 1408, AS ONE) was used to neutralize the charge. The ultra violet light ejected from the lamp exposed the atoms and molecules in air, and the electrons were separated from the atoms and molecules. The atoms and molecules change as positive ions and negative ions are generated when the separated electrons bond with other atoms and molecules. When the generated negative and positive ions and electrons freely collide with the material near the UV lamps, the material is electrostatically neutralized. In addition, the corona charging equipment, as shown in Figure 3.6, was used to charge the particles. When a DC high voltage of -6.0 kV was applied to the tungsten wire electrode (0.1 mm in diameter), the corona discharge occurred near the electrodes, and the resultant positive and negative ions were generated. The positive ions were attracted to the wire electrodes by the Coulomb force along with the electric flux line. On the other hand, most of the negative ions flowed toward the grounded casing electrode, and some of the ions collided with particles resting below the wire electrode.

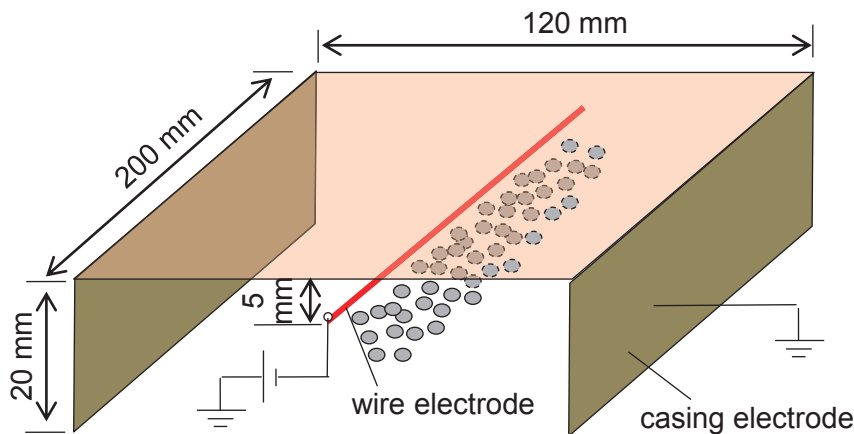


Figure 3.6 Corona charging equipment to charge particle negatively.

Figures 3.7, 3.8, and 3.9 show the charge distributions of the particles in the cases where untreated particles, particles neutralized by UV lamp, and particles charged by corona discharge were used, respectively. The particle charges were measured by the free-fall method, as described in section 2.5.2. Although the maximum size of the particles is approximately 200 μm in Figure 3.7, 3.8, and 3.9, that size is the aggregation of particles smaller than 106 μm . The particle charges, which are neutralized by the UV lamp and charged by corona charging, are not equal; however, they are randomly charged positively and negatively, as shown in Figure 3.8 and 3.9. Figure 3.10 shows the number ratios of charge distributions and the average charges. As shown in the figure, the ratio of the number of particles neutralized by the UV lamp is relatively uniform, which means that the most of the particles are lightly charged. On the other hand, the ratio of the number of particles charged by the corona discharge shows a broad distribution, which means that the particles are heavily charged compared with those neutralized by the UV lamp. Although the negative corona discharge is applied, the particles are randomly charged not only negatively but also positively. This is because the particles interact mechanically and electrostatically with each other, and the electrons provided by corona discharges moves between particles. However, the peak of the charge distribution in Figure 3.10 was shifted negatively, so the effect of the negative corona charging apparently appeared. The untreated, neutralized, and charged particles were set on the sand sieve and used for the experiments. The effect of the charge on the system performance was investigated.

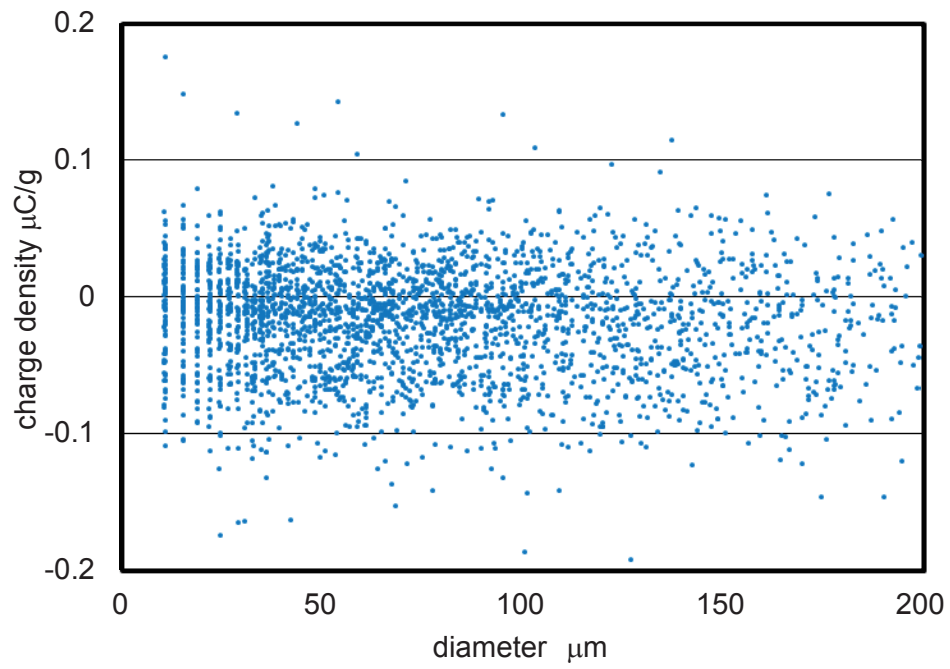


Figure 3.7 Charge density distribution of untreated lunar regolith simulant particles.

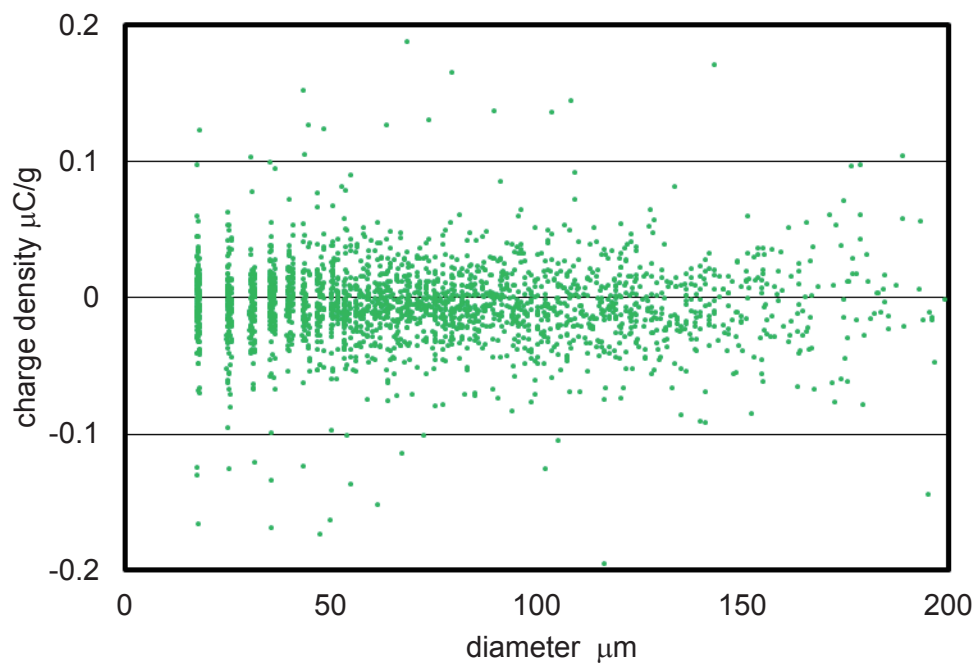


Figure 3.8 Charge density distribution of lunar regolith simulant particles neutralized by UV lamp.

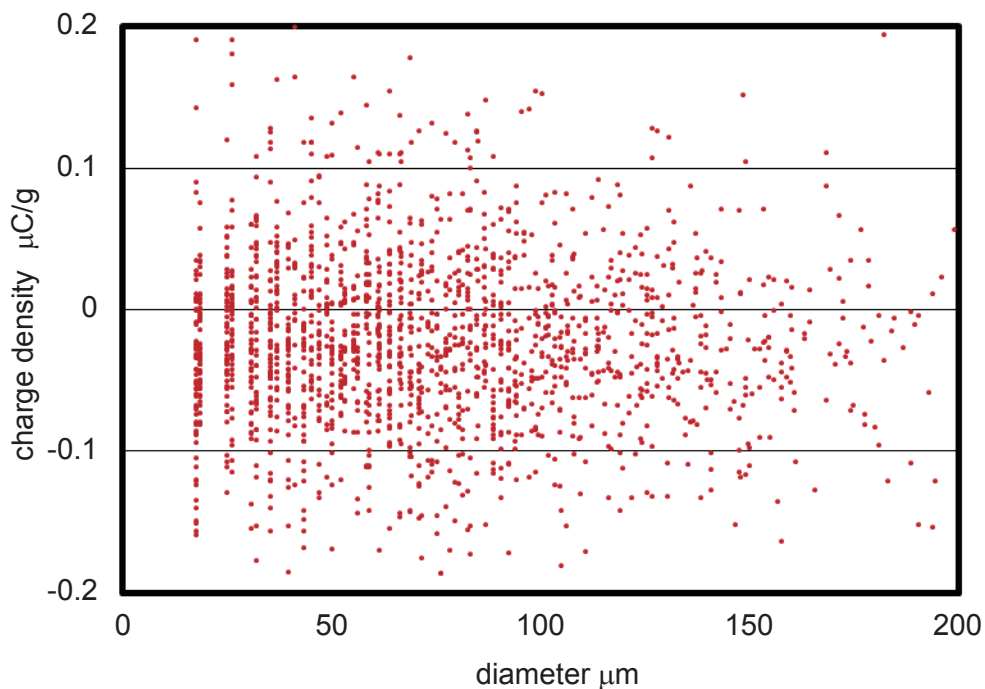


Figure 3.9 Charge density distribution of lunar regolith simulant particles charged by negative corona discharge.

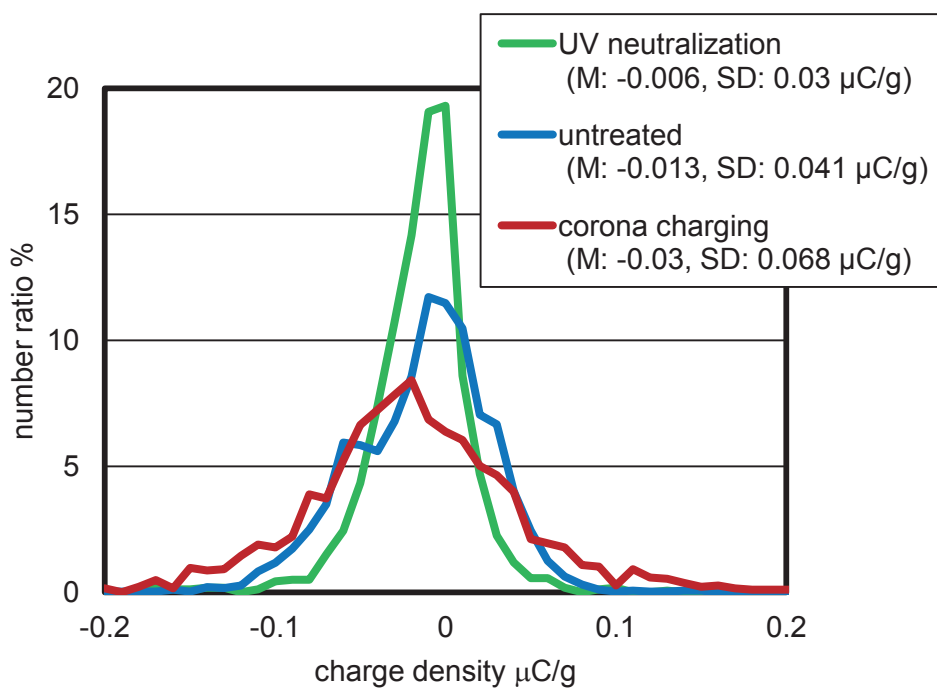


Figure 3.10 Charge density distribution of untreated, neutralized, and corona charged lunar regolith simulant particles (M: Mean, SD: Standard Deviation).

3.3 Numerical Calculation

Numerical calculations based on the modified hard sphere model of the DEM were conducted to analyze the particle motions in the electrostatic field and to predict system performance in the space environment. The basic procedure of the calculation was described in section 2.7, and some specific conditions of the calculations are described in this section. The external forces on the right hand of Equation (2.1), such as the Coulomb force, dielectrophoresis force, adhesion force, gravitational force, and air drag, represented by Equations (2.81), (2.16), (2.30), (2.31), and (2.37), respectively, were considered. The electrostatic field E was calculated using the finite difference method as described in Chapter 2, reproducing the geometry and electrostatic properties of the electrostatic dust shield systems. In the DEM calculation, the calculation area was set as $0.017 \times 0.03 \times 0.04 \text{ m}^3$, and the geometries of the actual experimental setup, such as the electrode shapes and positions, were reproduced. The particles of 10,000 were used for the calculation, and the diameters and charges were randomly assigned corresponding to the actual size and charge distributions of regolith particles less than $106 \text{ }\mu\text{m}$ in diameter. The particles larger than $20 \text{ }\mu\text{m}$ fell freely from a height of 40 mm to the mechanical gap. In the Earth condition, the velocity of small particles did not exceed terminal velocity because of air drag; therefore, the particles fell slowly. This required long calculation time. Considering that the velocity of small particle easily reaches terminal velocity, small particles were supplied from 20 mm above the mechanical gap to reduce the calculation load. The particle charge distribution q was created by using normal random number, and the average was $-0.01 \text{ }\mu\text{C/g}$ that is the charge density of the bulk particles measured using the Faraday gauge as shown in section 2.5.2, while the standard deviation was $0.06 \text{ }\mu\text{C/g}$. The time step for the Runge–Kutta calculation was set to be $1.0 \times 10^{-5} \text{ s}$, and the DEM calculation was performed until all particles reached near the height of plate electrodes.

Table 3.1 Conditions for the numerical calculations for the electrostatic dust shield system on the Earth, Moon, and Mars.

Conditions	Earth	Moon	Mars
Gravitational acceleration m/s^2	9.8	1.6	3.7
True density of particle kg/m^3	2,700 (FJS-1)	2,700	2,170
Atmospheric pressure hPa	1,013	High vacuum	7.5
Viscosity coefficient $\text{Pa}\cdot\text{s}$	1.8×10^{-5}	-	1.0×10^{-5}

In cases where the space environments are assumed, some parameters were replaced with actual conditions, such as gravitational acceleration, atmospheric pressure, and specific gravity of the particle, as shown in Table 3.1. The true density of particles in the Martian environment was determined to be the bulk density obtained from the literature [8] divided by a porosity of 0.7. Because the Martian atmosphere consists of CO_2 , and the atmosphere's viscosity coefficient and mean free path were calculated using

Equations (2.33) (2.40). The air drag in the Martian atmosphere was calculated using the Cunningham correction represented by Equation (2.37). In the lunar environment, the air drag was neglected. The weights of particles collected in the tray that settled below the mechanical gap were measured.

3.4 Results and Discussion

3.4.1 Basic Characteristic of Electrostatic Dust Shield System on Earth

Figure 3.11 (a) and (b) show the experimental and calculated results of the effects of applied voltage and frequency, respectively. In addition, Figures 3.12 and 3.13 show the observed and calculated particle motions. As shown in Figure 3.11 (a), the shield rate was improved with an increase in the applied voltage, simply because the strength of the electrostatic field increased owing to the high voltage applied. Comparing the results of the plate and plate + wire types, the performance of the plate + wire type was better than that of the plate type. This is because the supplied particles were ejected toward the outside, passing through the space between wire electrodes, as shown in Figure 3.12. When the applied voltage is higher than $3 \text{ kV}_{\text{p-p}}$, gas discharge occurred near the plate electrodes; therefore, the voltage of $3 \text{ kV}_{\text{p-p}}$ is the maximum in the Earth environment. In vacuum environments similar to that on the surface of the Moon, a voltage higher than $3 \text{ kV}_{\text{p-p}}$ can be applied because gas discharge cannot occur in a vacuum. From the results shown in Figure 3.11 (b), the performance at frequencies less than 10 Hz was better than that over 10 Hz in cases of using plate and plate + wire types. This is because the polarity of the applied voltage changes before the particles are removed sufficiently far from the mechanical gap, as shown in Figure 3.13. Although the optimum frequency is less than 10 Hz on the Earth, the frequency in a vacuum is higher than 10 Hz because there is no air drag and particles can move faster. It can be observed from Figures 3.11, 3.12, and 3.13, that the calculation results agreed fairly well with the experimental results, quantitatively and qualitatively. Therefore, the calculation method is sufficiently accurate for simulating particle dynamics in the electrostatic field. The system performance in the lunar and Martian environments was predicted using the numerical calculation.

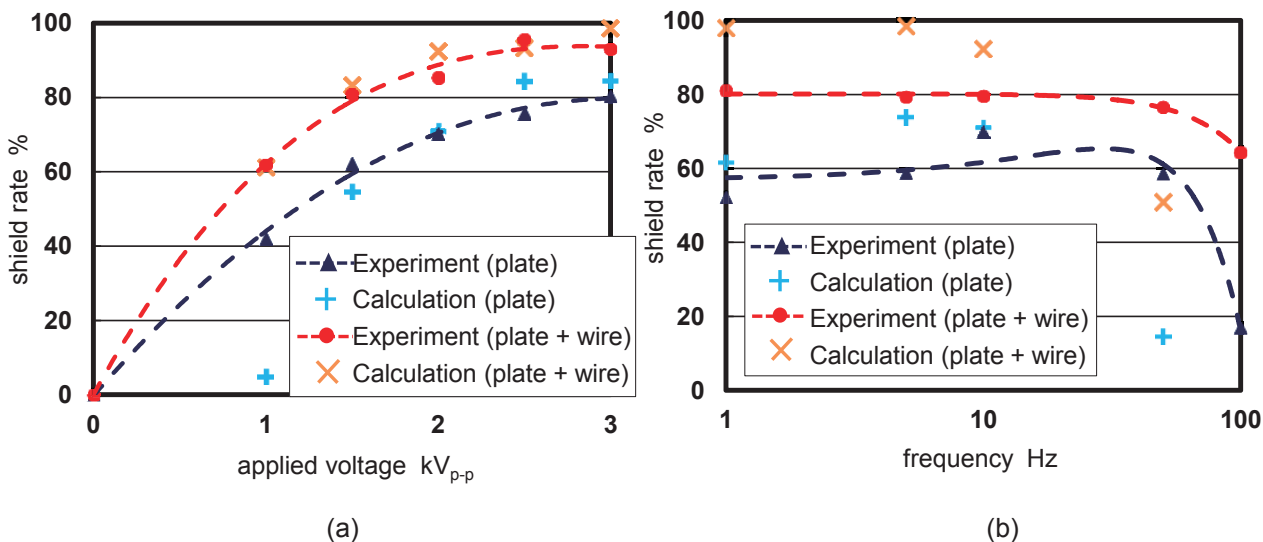


Figure 3.11 Shield rates versus (a) applied voltage (frequency: 10 Hz, untreated particles) and (b) frequency (applied voltage: 2.0 kV_{p-p}, untreated particles), in air and 1-G gravity environment. 1-G is equal to 9.8 m/s².

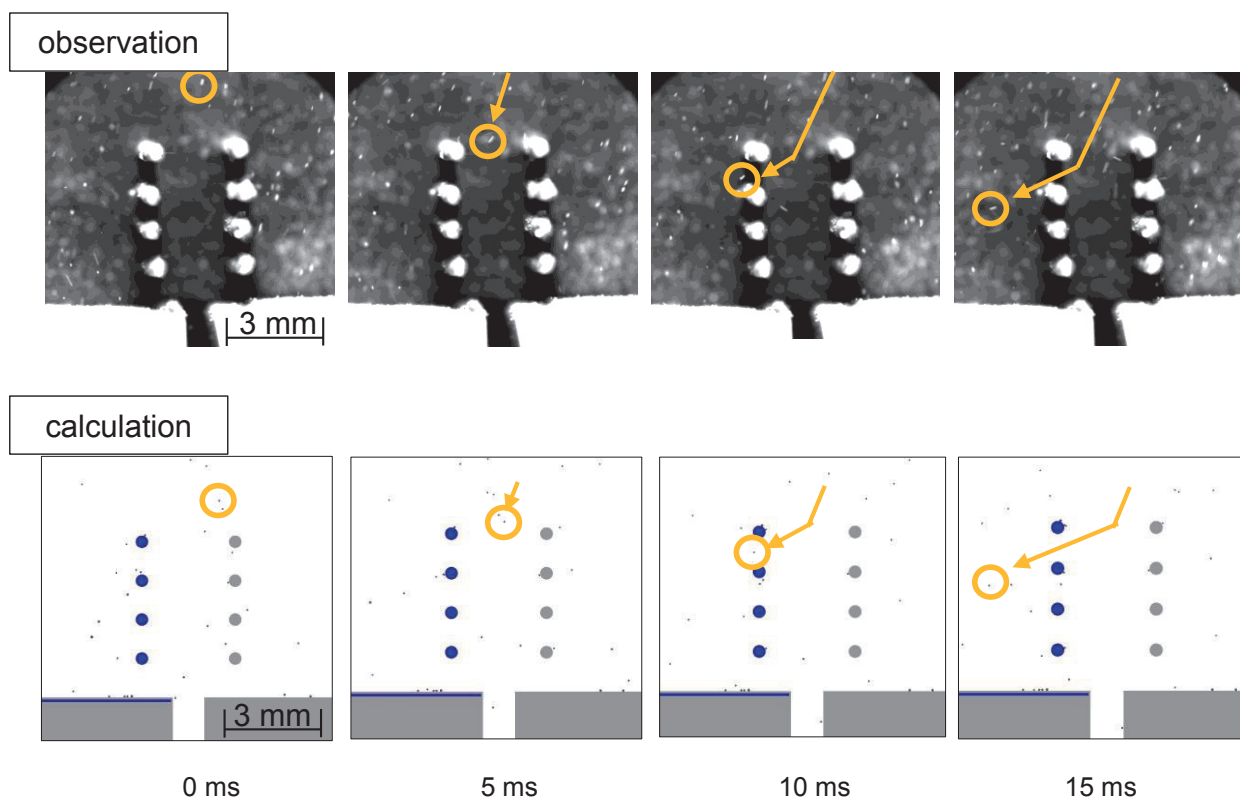


Figure 3.12 Observed and calculated particle motion (voltage: 3.0 kV_{p-p}, frequency: 10 Hz, untreated particles, in air and 1-G gravity environment).

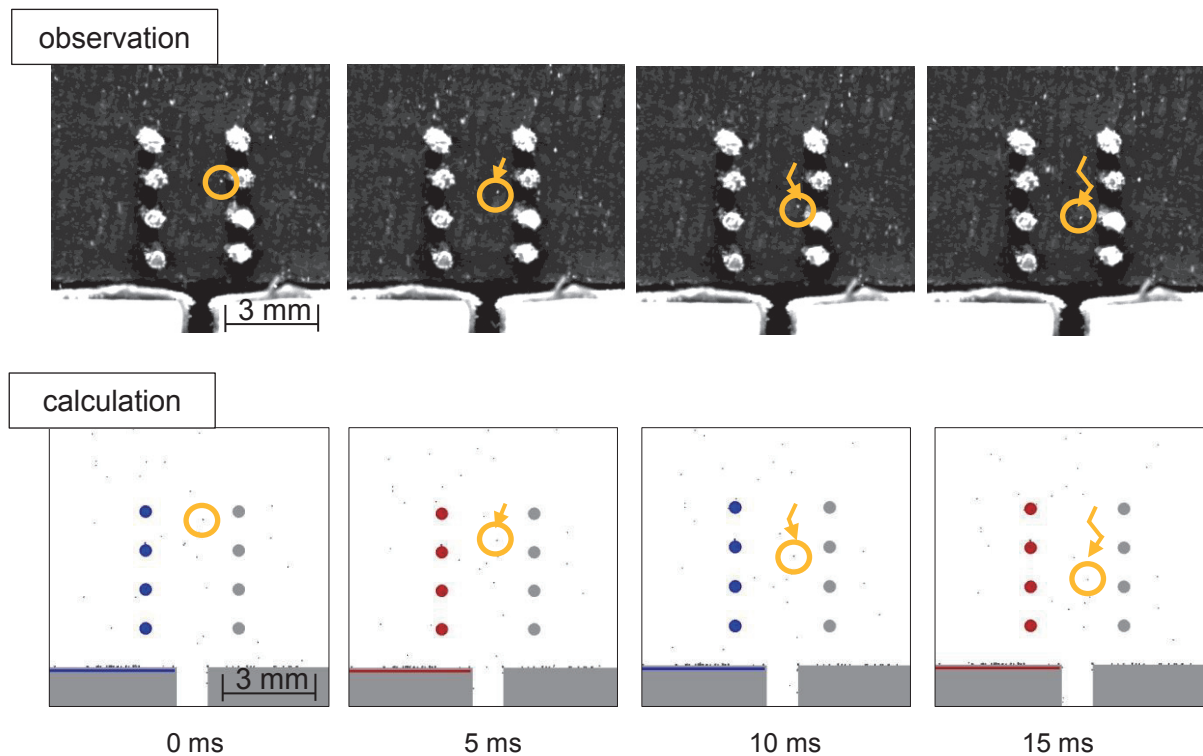


Figure 3.13 Observed and calculated particle motion (voltage: 2.0 kV_{p-p}, frequency: 100 Hz, untreated particles, in air and 1-G gravity environment).

The size distributions of the experimentally collected particles in the tray are shown in Figure 3.14 (a). In addition, the charge density distribution of the untreated particles used in numerical calculations and that of particles collected in the tray are shown in Figure 3.14 (b). Although it can be observed that most of the particles that are not heavily charged are removed by the system in Figure 3.14 (b), the particles do not intrude into the gap even in the case without using the electrostatic shield system. Figure 3.14 (a) and (b) indicate that large particles and particles that have small charge density intrude easily into the mechanical gaps. For large particles, the charge density, which represents the rate between the particle mass and charge, decreases with an increase in particle diameter, as shown in Figure 3.14 (b). The effect of the electrostatic force decreases with charge density, and this makes the removal of particles difficult. This tendency agreed closely with the prediction described in section 2.6.1. In addition, because the performance was improved in the case of the plate + wire system, and because the number of collected small particles that can be easily removed were comparably decreased, the size distribution of particles collected in this case shifted toward the large size, as compared with that of the plate type.

Figure 3.15 shows the system performance when untreated, neutralized, and charged particles are used. The performances in all cases were improved by an increase in applied voltage in the following order: charged particles, untreated particle, and neutralized particles. From the results, the particles that have small charge density are barely removed using the electrostatic system; therefore, an additional method that is not dependent on the particle charge is required to improve the performance.

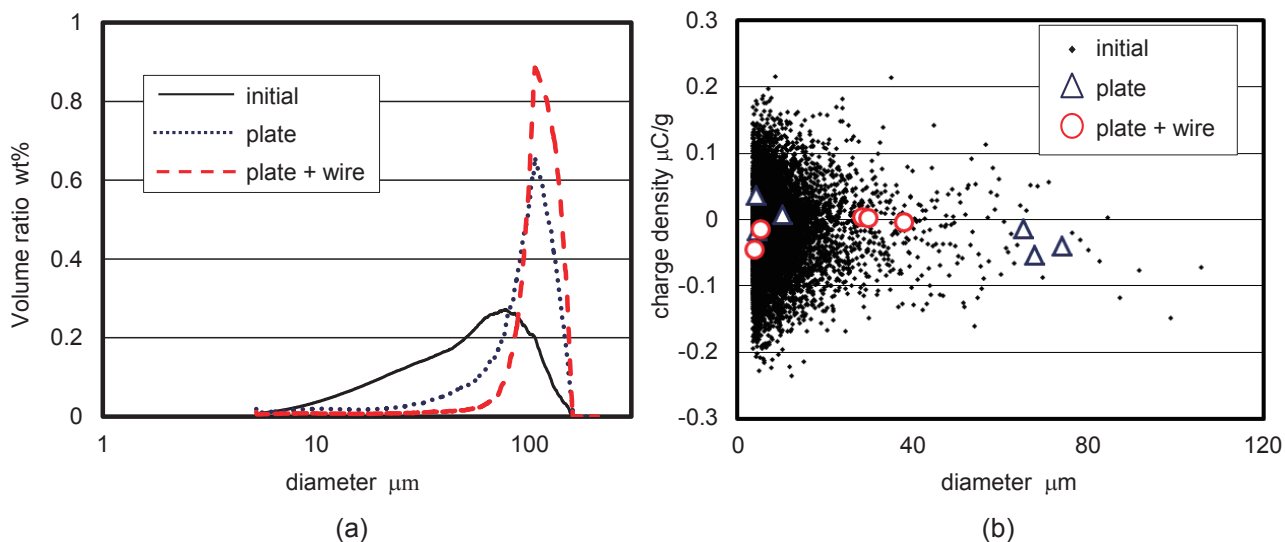


Figure 3.14 (a) Measured particle size distributions and (b) charge density distributions of initially fed particles and particles falling into gap of plate and plate + wire types (voltage: $3.0 \text{ kV}_{\text{p-p}}$, frequency: 10 Hz, untreated particles, in air and 1-G gravity environment).

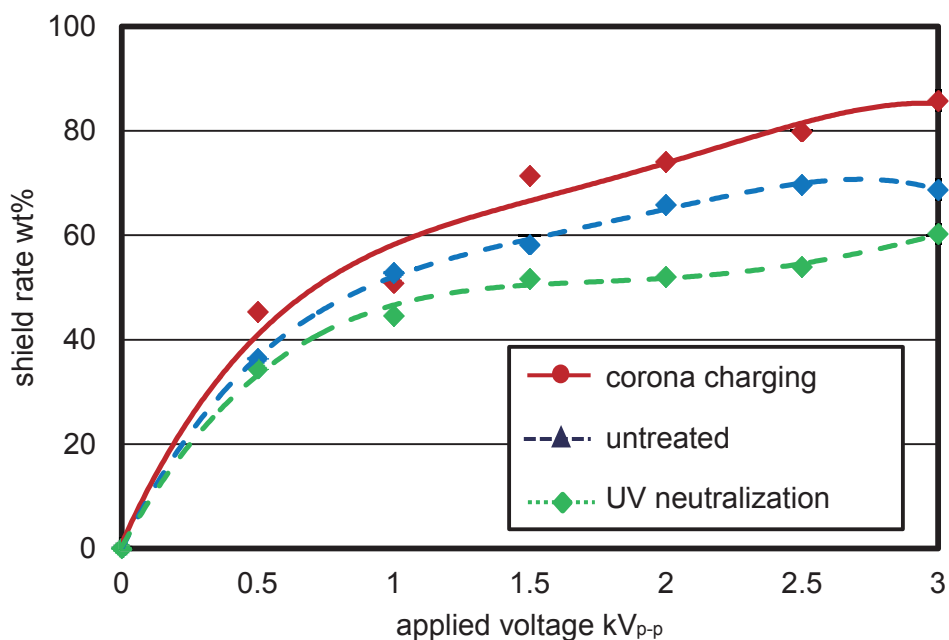


Figure 3.15 Shield rate versus applied voltage for untreated, neutralized, and charged particles (frequency: 10 Hz, plate type, in air and 1-G gravity environment).

3.4.2 Shield Performance in Space Environments

The system performances were predicted not only on the Earth but also on the Moon and Mars. Figures 3.16 and 3.17 show the calculated performance on the Moon and Mars, respectively. Assuming that the particles on the Moon and Mars are heavily charged because of the effect of cosmic rays and solar wind, the calcula-

tion where the particles are heavily charged were also conducted as well. In these calculations, the frequency of the applied voltage was fixed at 10 Hz, which is the optimum condition obtained from the experiments on the Earth. Figure 3.16 shows that the performance on the Moon is improved compared with that on the Earth owing to the small gravitational force and absence of air drag. Moreover, as gas discharge does not occur in the lunar environment, a voltage higher than 3 kV_{p-p} , which is the maximum voltage on the Earth, can be applied. When the high voltage is applied, the performance is improved as shown in Figure 3.16. In particular, for heavily charged particles, the performance reaches almost 95% using the plate + wire type electrodes.

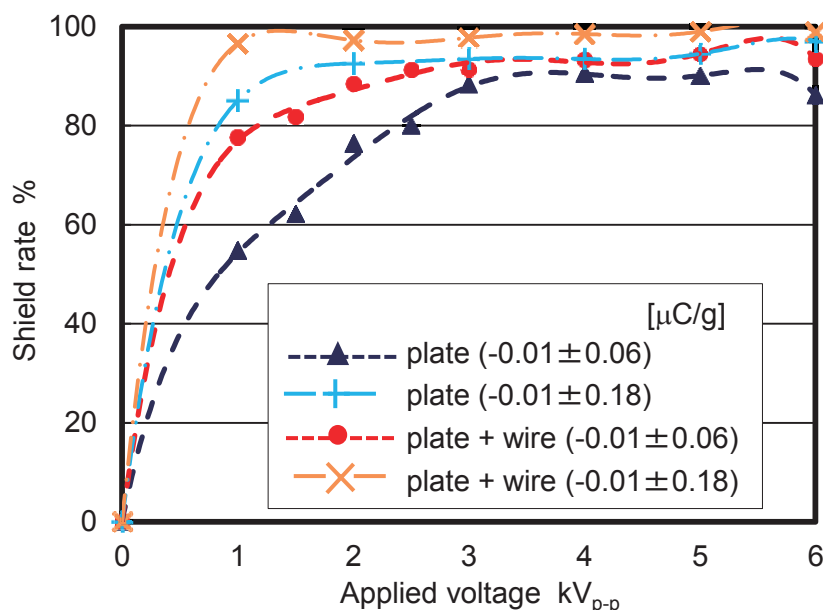


Figure 3.16 Calculated shield rate versus applied voltage of the electrostatic dust shield system on Moon (frequency: 10 Hz).

The gas discharge limit is much smaller on the Mars than on the Earth. It is assumed that 0.15 kV_{p-p} is the maximum voltage on the Mars. Figure 3.17 shows that the performance drops in the Martian environment, compared with the results on the Earth when the same charge distribution is assumed. When the particle charge on the Mars is same as that on the Earth, the performance becomes negative because a small Coulomb force cannot repel the particles outside owing to the small applied voltage and because the dielectrophoresis force attracts a small amount of particles toward the mechanical gap. However, the performance is improved as the particle charge increases. The performance reaches approximately 75% of the shield rate when it is assumed that the particles on the Mars are charged five times higher than those on the Earth. Therefore, if the particles are heavily charged, the electrostatic shield system is expected to be a useful method for removing the particles on the Mars.

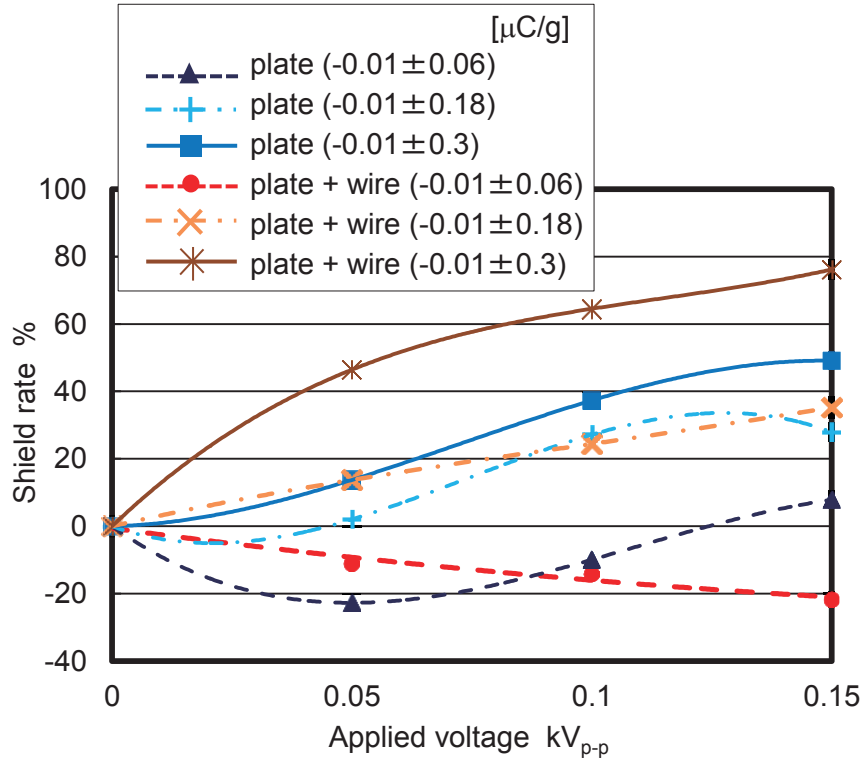


Figure 3.17 Calculated shield rate versus applied voltage of the electrostatic dust shield system on Mars (frequency: 10 Hz).

3.4.3 Power Consumption

Because power consumption is one of the key factors that determine application in space environments, the power consumption of the electrostatic dust shield system was measured using the circuit shown in Figure 3.18 (a). The electrostatic dust shield system is assumed as the capacitance in Figure 3.18 (a). When the rectangular high voltage is applied to the shield system, the voltages V_1 and V_2 at both ends of the shunt resistance (resistance $R_S = 98.4 \text{ k}\Omega$) are measured, as shown in Figure 3.18 (b). The electric current I_S can be calculated from the voltage drop at the resistance as represented by Equation (3.1). Because the voltage applied to the capacitance is known, the power consumption for a moment w at the capacitance can be calculated. The electric current flows each time when the polarity of the applied voltage is altered. The power consumption W for one period can be represented as Equation (3.2).

$$I_S = \frac{V_1 - V_2}{R_S} \quad (3.1)$$

$$W = 2f \int_0^{\frac{1}{2f}} V_2 I_S dt \quad (3.2)$$

Here, f is the frequency of the applied voltage. Because the power consumption is assumed to be proportional to the length of the mechanical gap, the power consumption per unit length of the electrostatic dust shield system is deduced. Figure 3.19 shows that the power consumption increases with the square of the applied voltage. The power consumptions of the plate and plate + wire types are not very different, because most of the electric current is consumed near the mechanical gap and plate electrodes. Because the electric current flows each time when the polarity of the applied voltage is changed, the power consumption increases linearly with the frequency, and operation under low frequency is preferable for the system. Although the power consumption increases with the size of the shield system, it is extremely small when the system is 1 m in size. The shield system has many advantages in terms of power consumption.

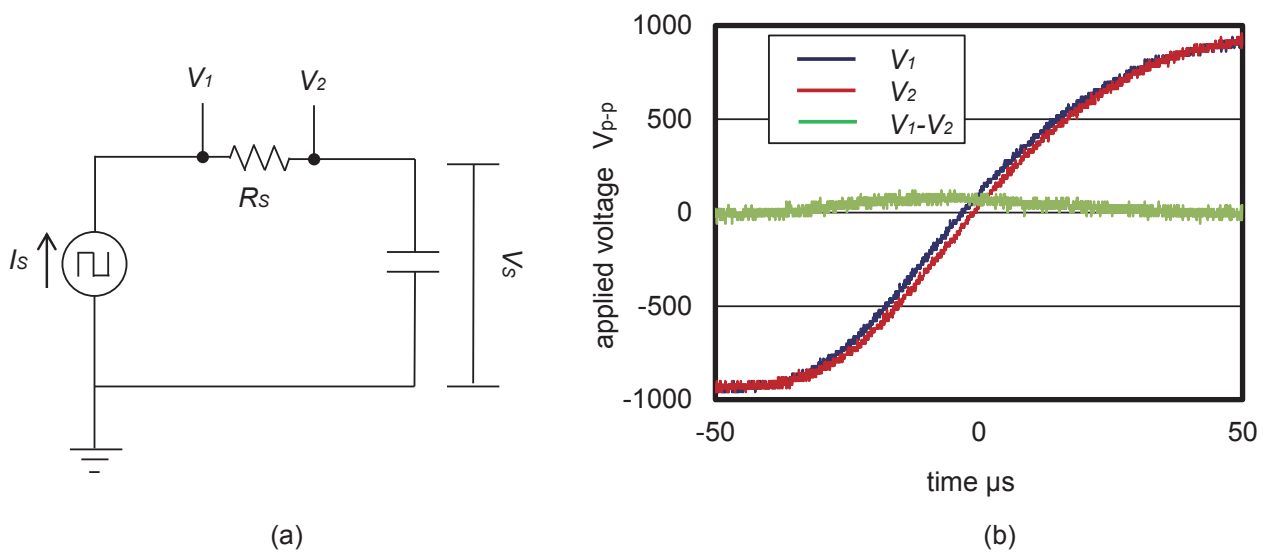


Figure 3.18 (a) Diagram of circuit used for measuring power consumption of the electrostatic dust shield system, and (b) measured voltage waveform at both ends of resistance and the voltage drop (voltage: 1 kV_{p-p}, frequency: 10 Hz, plate + wire type).

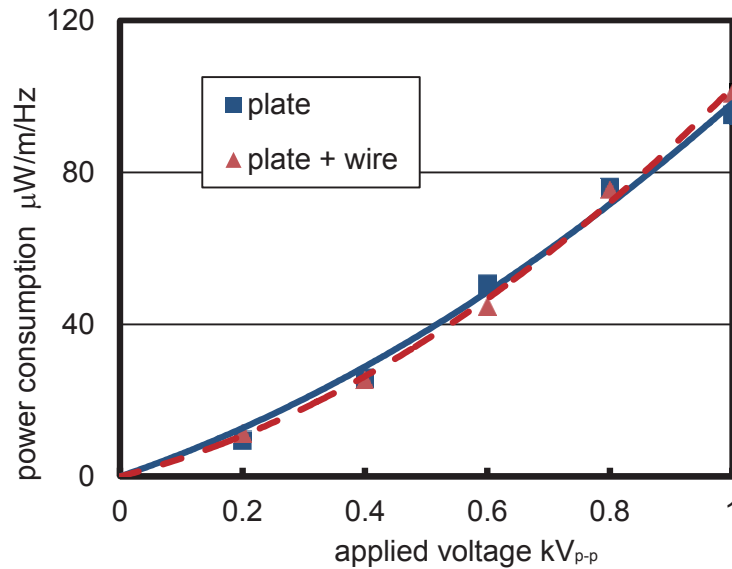


Figure 3.19 Power consumption of electrostatic dust shield system versus applied voltage.

3.5 Summary

To achieve long-term exploration on the Moon and Mars, the electrostatic dust shield system was developed. Its performance on the Earth, Moon, and Mars was evaluated by conducting experiments and numerical calculations. The accuracy of the calculation method was confirmed by comparing the experimental results with the results of numerical calculations. The insights achieved from the experimental and calculation results are shown below.

1. The electrostatic dust shield system can remove most of the particles that are about to enter into the mechanical gaps. The performance of the plate + wire configuration was better than that of the plate type, and the shield rate reached approximately 95% for the plate + wire type.
2. The electrostatic dust shield system worked well against heavily charged particles. Although the limit of gas discharge is much lower on the Mars than it is on the Earth, and high voltage cannot be applied to the shield system, the system can work effectively even in the Martian environment if the particles are heavily charged.
3. The performance of the shield system is expected to improve in the Moon environment owing to the small gravitational force and absence of air drag.
4. The power consumption of the shield system is extremely low, which is a big advantage.

Based on these results, the electrostatic dust shield system is expected to be usable in future lunar and Mars exploration missions.

Chapter 4 Particle Size-Sorting System for Lunar Regolith Using Electrostatic Traveling Wave

4.1 Introduction

As described in section 1.1.4 and 1.3.3, ISRU is necessary for conducting long-term exploration missions on the Moon. Size sorting is one of the key processes in ISRU [1] because the components and properties of lunar regolith vary with diameter [2]. In particular, the extraction of particles smaller than 10 μm in diameter from lunar regolith is important in ISRU, because those particles are rich in np-Fe^0 [2], and can therefore be used as lunar construction materials for landing pads, paved roads, and habitats [3]. In addition, to improve chemical processing in ISRU, it is crucial to use small particles with relatively large specific surface area to increase the reaction rate of particle chemical processing [1].

Size sorting is conducted conventionally by utilizing the balance of forces acting on particles. Pneumatic and mechanical methods have been used in terrestrial applications, such as cyclone sorting, sedimentary sorting, and sieve systems. However, it is difficult to utilize pneumatic methods in space because gas and liquid resources are limited. Mechanical methods, including the rotating cone separator and the vibratory sifter, have been developed for lunar regolith [4, 5]. Because the rotating cone separator utilizes centrifugal force for size sorting, the system must be equipped with mechanical drives [4], and thus mechanical malfunctions and wear caused by small particles have to be addressed. On the other hand, the vibratory sifter uses a sieve for size sorting [5]; therefore, the system must require periodic cleaning of accumulated particles to prevent clogging [6]. However, an additional mechanical cleaning system will make the system more complex and increase the risk of failure. When considering long-term ISRU, a new type of size-sorting system that can work reliably in the lunar environment is necessary.

To achieve this, a unique size-sorting system that utilizes the electrostatic traveling wave [7, 8] is developed to extract small particles. The particles transported by the traveling wave are sorted using the balance between the electrostatic and gravitational forces acting on the particles, which depend on the particle diameter, as described in section 2.6.1. In this chapter, the variation in particle charges during transport was experimentally investigated because particle charge significantly affects particle motion and it is critical to the success of size sorting. The measured particle charges were used to calculate particle motion during transport in air and vacuum environments using the DEM of the modified hard sphere model, as explained in section 2.7. In addition, demonstrations of particle size sorting were experimentally conducted in a vacuum environment. From the predictions shown in section 2.6.1, it can be assumed that particles smaller than 20 μm are significantly affected by air drag; therefore, the effects of air and vacuum were also investigated in the experiments and numerical calculations. Finally, the performance of size sorting on the Moon was predicted by numerical calculations. Part of this work was published in literature [9].

4.2 System Configuration

The electrostatic size-sorting system mainly consists of three parts, as shown in Figure 4.1 [9]. One is the power supply that generates the four-phase rectangular voltage. The waveforms of generated voltages are shown in Figure 4.2. The power supply explained in section 3.2.1 was duplicated in four pairs, and the phases of the output voltages were shifted to 90° by using a microcomputer. The second part is the particle conveyor in which parallel copper electrodes (thickness: $18\ \mu\text{m}$, width: $0.3\ \text{mm}$, pitch: $1.3\ \text{mm}$) are printed on a flexible polyimide substrate (thickness: $0.1\ \text{mm}$, width: $128\ \text{mm}$, length: $490\ \text{mm}$), as shown in Figure 4.3. The surface of the conveyor is covered with an insulating film made of a polyimide film (thickness: $12.5\ \mu\text{m}$) to prevent electrical breakdown between the electrodes. The last part is the collection box located at the end of the conveyor. When voltage is applied to the parallel electrodes, an electrostatic traveling wave is created on the surface of the conveyor, and particles on the conveyor follow the wave propagating to the right. Because the gravitational force significantly affects the motion of large particles, large particles cannot float at a higher altitude than the small particles in a vacuum; thus, the large particles pass underneath the collection box. On the other hand, the small particles that float and reach the collection box are collected. Four collection boxes were installed at heights of 100, 150, 200, and 250 mm above the conveyor. The electrostatic size-sorting system utilizes only the electrostatic force, and it does not require a gas or liquid. The power consumption of the system is very low, similar to the electrostatic dust shield system described in section 3.4.3. The electrostatic size-sorting system does not require periodic cleaning of the conveyor surface; therefore, it could be operated reliably on the Moon. The lunar regolith simulant FJS-1 was used for the experiment. The simulant was sorted before the experiments by using a mechanical sieve, as its maximum diameter was less than approximately $106\ \mu\text{m}$.

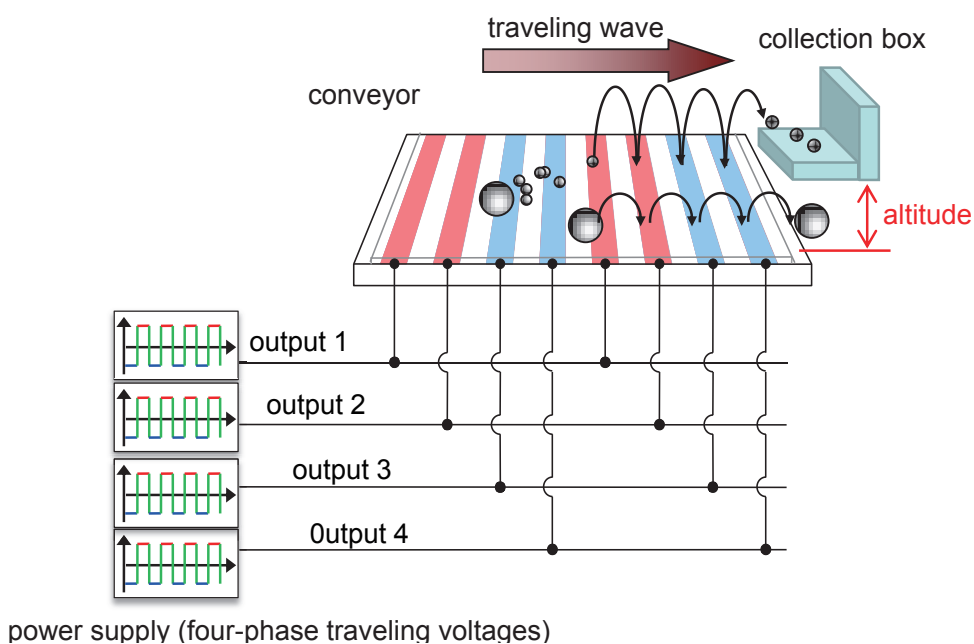


Figure 4.1 Configuration of electrostatic size-sorting system using electrostatic traveling wave.

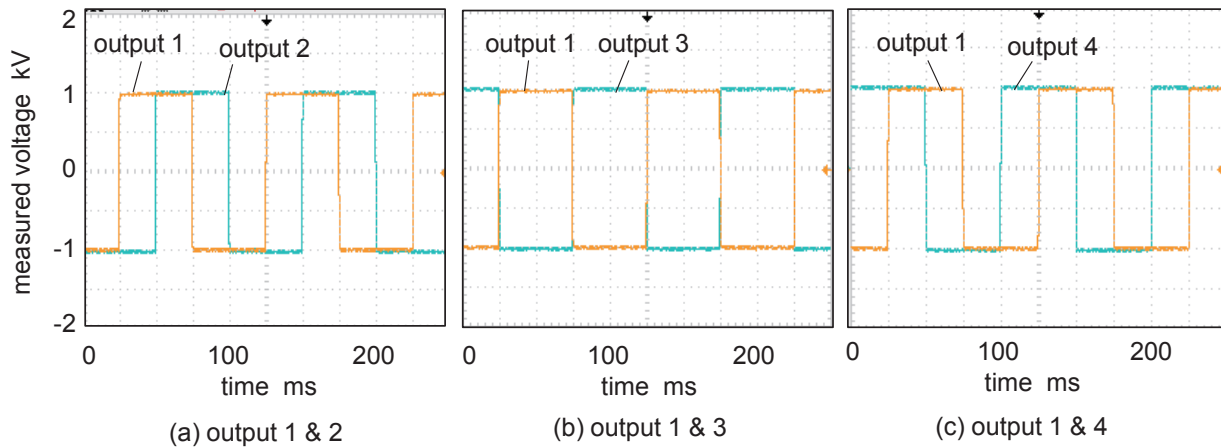


Figure 4.2 Waveforms of four-phase traveling wave.

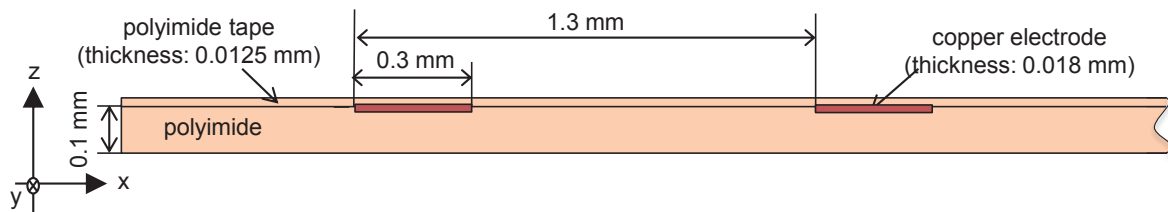


Figure 4.3 Cross-sectional diagram of electrostatic conveyor.

4.3 Measurement of Particle Charge

4.3.1 Free-Fall Method

Particle dynamics in an electrostatic field are affected by the particle charge, and the particle charge variation during transport on the conveyor was investigated. The charge quantities of each particle were measured by utilizing the free-fall system. The measurement setup is almost the same as the setup shown in section 2.5.2. Although the setup shown in section 2.5.2 can detect particles larger than $20\ \mu\text{m}$, the size-sorting system in this chapter focuses on particles smaller than $20\ \mu\text{m}$; therefore, the setup of the free-fall method was modified as shown in Figure 4.4. The conveyor with parallel plate electrodes was placed above the free-fall system. The particles that initially settled at 30 mm, 100 mm, and 150 mm from an edge of the conveyor were transported toward the edge and supplied to the free-fall system. To reduce the scattering of particles, two layers of slits were used at the inlet of the free-fall system. After the DC voltage was applied to the parallel plates, the supplied particles fell, moving right or left from the centerline owing to the electrostatic force. To prevent the effect of airflow in the space between the plate electrodes, a wind shelter was installed around the system. After supplying the particles, the distances between the centerline and fallen particles on the glass plate were measured using a particle image analyzer (Morphologi G3/G3S, Malvern) which can detect particles in one micrometer scale. The procedure used to calculate the charge of a particle by using the measured distance was described in section 2.5.2.

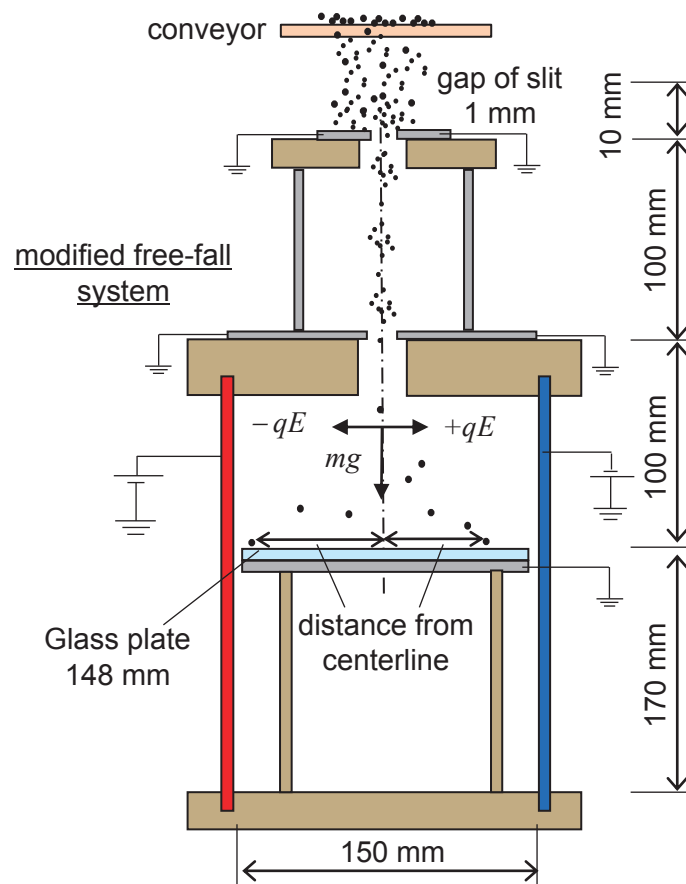


Figure 4.4 Diagram of modified free-fall system used to measure particle charge.

4.3.2 Effect of Tribocharging on Conveyor

Figure 4.5 shows the measured charge distribution of particles transported at 30 mm and 150 mm, respectively. The modified free-fall system could detect particles smaller than 100 μm . The measured charges are shown as the charge density. As shown in Figure 4.5, the charges of particles with the same diameter were not equal, and they were randomly charged in negative and positive polarities; this tendency is similar to the previous results shown in section 2.5.2. In addition, the particles transported at 150 mm have slightly larger charges than those particles transported at 30 mm. The standard deviations of the charge distributions are shown in Figure 4.6. As shown in Figure 4.6, although the particle charges are uneven, the charge of transported particles increased with a decrease in particle diameter; therefore, it is expected that small particles move higher than large particles, and size sorting of small particles using the balance between the electrostatic and gravitational forces is possible. For reference, Figure 4.6 also shows the standard deviation of the previous results obtained using the free-fall system in section 2.5.2. It shows the charge distributions of particles that were not transported on the conveyor and not electrostatically treated before being supplied to the free-fall system; the minimum size is approximately 106 μm . The transported particles have larger charges

than the untreated particles because the transported particles are charged by tribocharging, which in turn is caused by friction with the polyimide surface of the conveyor. In addition, the charges of transported particles increases as the transport distance increases.

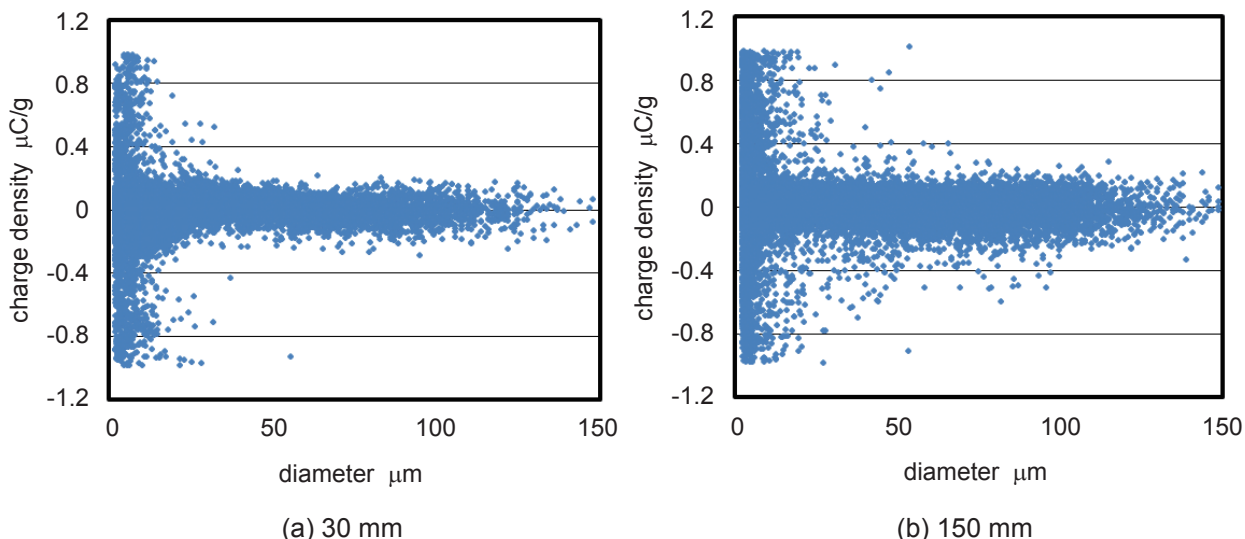


Figure 4.5 Charge distributions of transported particles at (a) 30 mm and (b) 150 mm, measured using modified free-fall system.

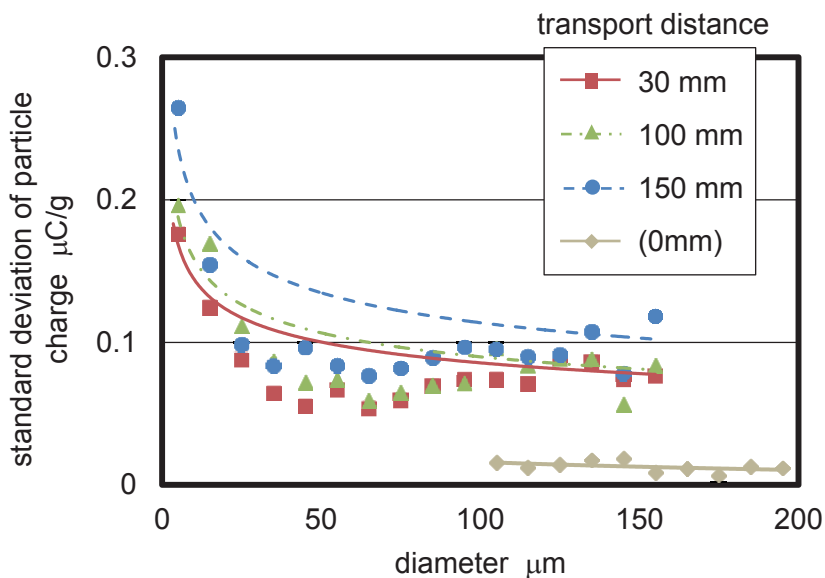


Figure 4.6 Standard deviation of the charge densities of particles transported for 30 mm, 100 mm, and 150 mm, measured by modified free-fall method in air and 1-G gravity environment and charge densities of untreated particles, measured by previous free-fall method. 1-G is equal to 9.8 m/s^2 .

4.4 Numerical Calculation

To analyze the particle motions and predict the system performance in space, numerical calculations were conducted using the modified hard sphere model of the DEM. The basic procedure of the calculation was described in section 2.7, and some specific conditions of the calculations are explained in this section. As the external forces acting on particles, the Coulomb force, gravitational force, and air drag represented by Equations (2.3), (2.29), and (2.31), respectively, were considered. The torque acting on particles was assumed to be zero. The electrostatic field \mathbf{E} was calculated by using the finite difference method as described in section 2.4.1, reproducing the geometry and electrostatic properties of the conveyor and electrodes. Assuming that the electrostatic field in the y -direction was zero, the two-dimensional electrostatic field was calculated as shown in Figure 4.7. Because the pattern of the electric field appears repeatedly in the x -direction, the cyclic boundary condition was applied to both the right and left ends of the calculation domain as shown in Figure 4.7 (a). In addition, the Neumann condition was applied to both the upper and lower ends of the calculation domain. The calculated equipotential line is shown in Figure 4.7 (b). In the DEM calculation, the calculated electrostatic field \mathbf{E} at the center of the particle was used to calculate the Coulomb force and dielectrophoresis force.

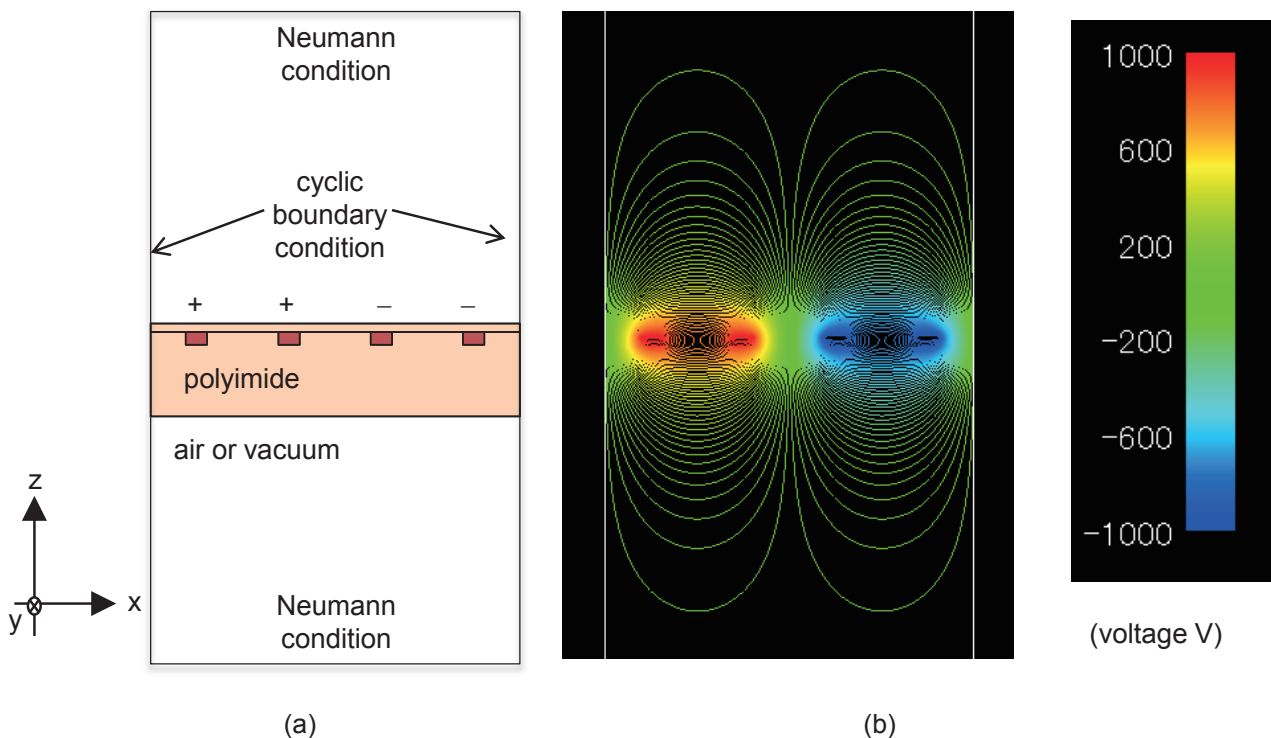


Figure 4.7 (a) Calculation model of the electrostatic field, and (b) calculated equipotential line (applied voltage: 2 kV_{p-p}).

The calculation area of the DEM was set to be $0.0052 \times 0.06 \text{ m}^2$, and the length of the z -direction was assumed as infinity. The height of the conveyor surface was set to be zero in the z -direction. When particles collide with the conveyor, the mechanical interactions were calculated using the modified hard sphere model, as described in section 2.7.4. To reduce the calculation loads, periodic boundary conditions were applied at the ends of the calculation area in the x - and y - directions, similar to the calculation of the electrostatic field. The actual size distribution of regolith particles was reproduced, and 300,000 particles were set randomly on the conveyor. The particle properties were assumed equal to that of the lunar regolith simulant FJS-1. The particle charges were reproduced using the standard deviation measured in section 4.3. The particles were transported in one direction by the Coulomb force produced by the traveling wave. The time step for the Runge–Kutta calculation was set to be $1.0 \times 10^{-5} \text{ s}$, and the DEM calculation was conducted for 1.0 s. In the lunar environment, air drag was neglected and the gravitational acceleration was set to be 1.6 m/s^2 . During the calculation, maximum heights of each floating particle were calculated.

4.5 Experiment in Vacuum

To confirm the performance of the electrostatic size-sorting system in a vacuum, experiments were conducted in an air and vacuum chamber of the JAXA Chofu Aerospace Center. The vacuum chamber and the experimental setup are shown in Figure 4.8, while the diagram is shown in Figure 4.9. In vacuum conditions, the particles were fed from the right side of the conveyor by using a vibration supplier. The supplier consists of a mechanical sieve (mesh size: 0.5 mm) and a DC vibration motor (FA-130RA, Mabuchi Motor). The experimental procedure is as follows. (1) Lunar regolith simulant FJS-1 of 5 g was set on the sieve before evacuating the air. (2) The evacuation of air took approximately 1 h. After the vacuum environment reached below $1.5 \times 10^{-2} \text{ Pa}$ in the chamber, a DC voltage of 2.0 V was applied to the motor for 10 s. The sieve was vibrated for 10 s to feed the particles to the conveyor passing through the openings of the sieve. (3) The applied DC voltage was turned off for 50 s, and the fed particles were transported by the electrostatic traveling wave. (4) Processes (1) and (2) were repeated for 15 min. (5) Air was injected into the chamber. After the air injection restored the atmospheric pressure, the collected particles in collection boxes were sampled and analyzed using a particle image analyzer (Morphologi G3/G3S, Malvern). The same experimental procedure was conducted in air without evacuating and restoring air.

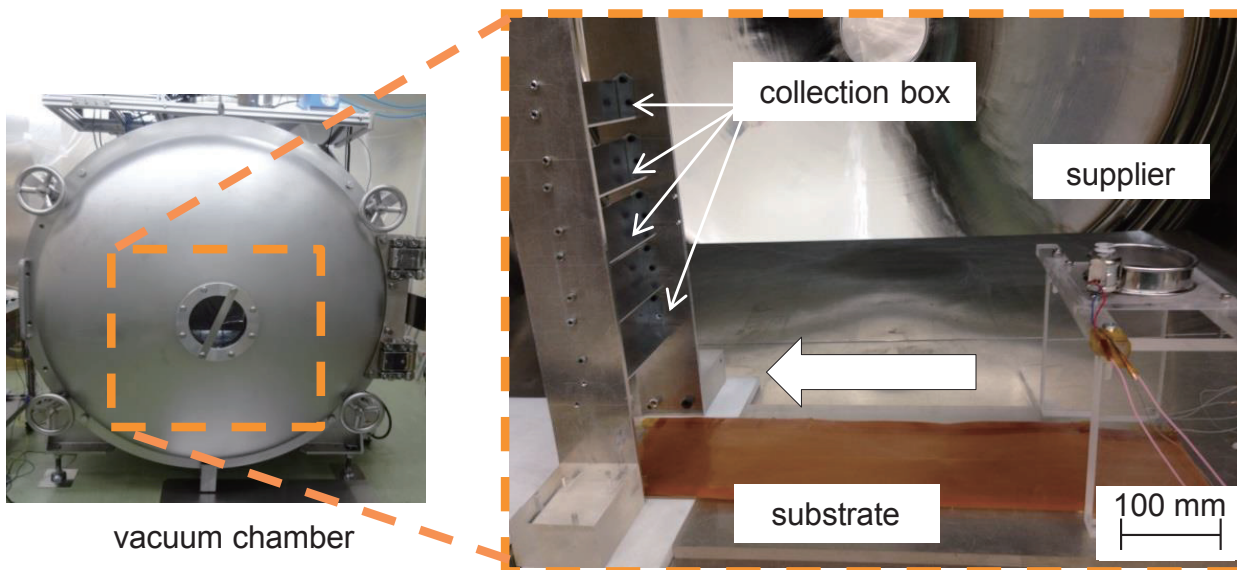


Figure 4.8 Photographs of the vacuum chamber and the experimental setup in the chamber.

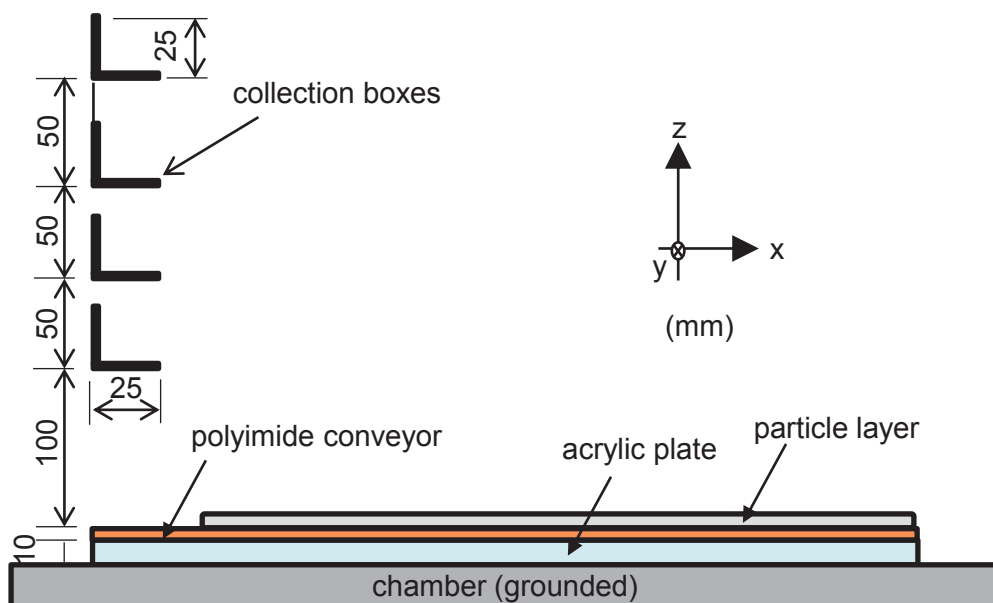


Figure 4.9 Diagram of the size-sorting system in the vacuum chamber.

4.6 Results and Discussions

4.6.1 Size Sorting in Vacuum

Figure 4.10 (a) and (b) show the calculated particle motions in air and vacuum environments, while Figure 4.11 (a) and (b) show the maximum heights of the particles in air and in a vacuum, respectively. Only the particles of 30,000 are shown in Figure 4.10 (a) and (b) for viewing clarity. Figure 4.10 shows that the parti-

cles in air and in a vacuum can be transported in one direction by the electrostatic traveling wave. The particles float higher in the vacuum than those in the air owing to the absence of air drag. In addition, Figure 4.11 (a) shows that the small particles do not float higher than the large particles in air because a relatively large air drag acts on the small particles. On the other hand, because there is no air drag in vacuum, the small particles reach higher altitudes than the large particles, as shown in 4.11 (b). This corresponds to the tendency of the measured charge distribution, as shown in Figure 4.6. From the calculation results, the size sorting of the particles is expected to succeed only in the vacuum environment by using the collection box. In addition, when the collection box is set at higher positions, it can collect smaller particles.

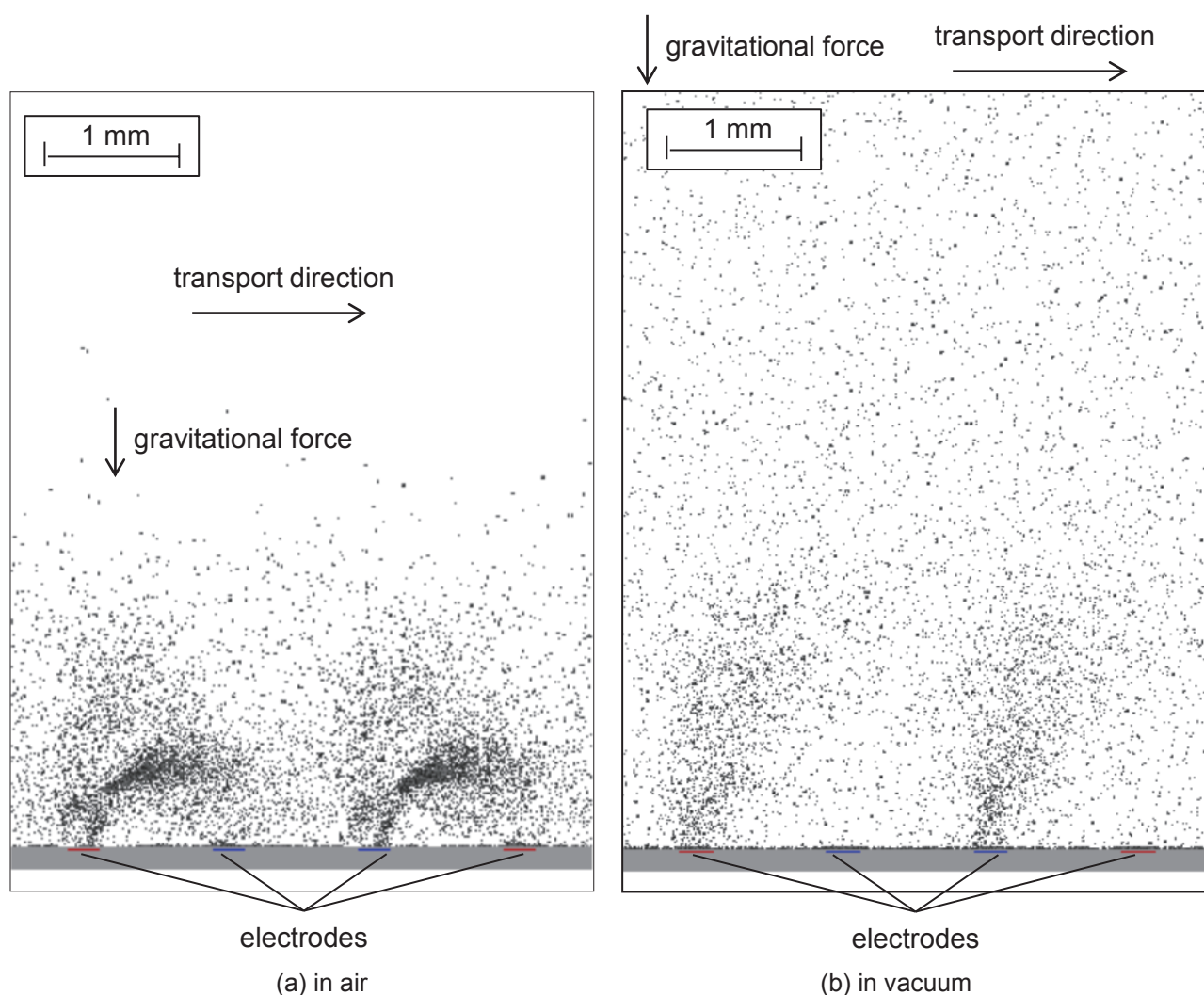


Figure 4.10 Calculated particle motions at 1-G gravity in (a) air and (b) vacuum environments (applied voltage: 2.0 kV_{p-p}, frequency: 10 Hz). 1-G is equal to 9.8 m/s².

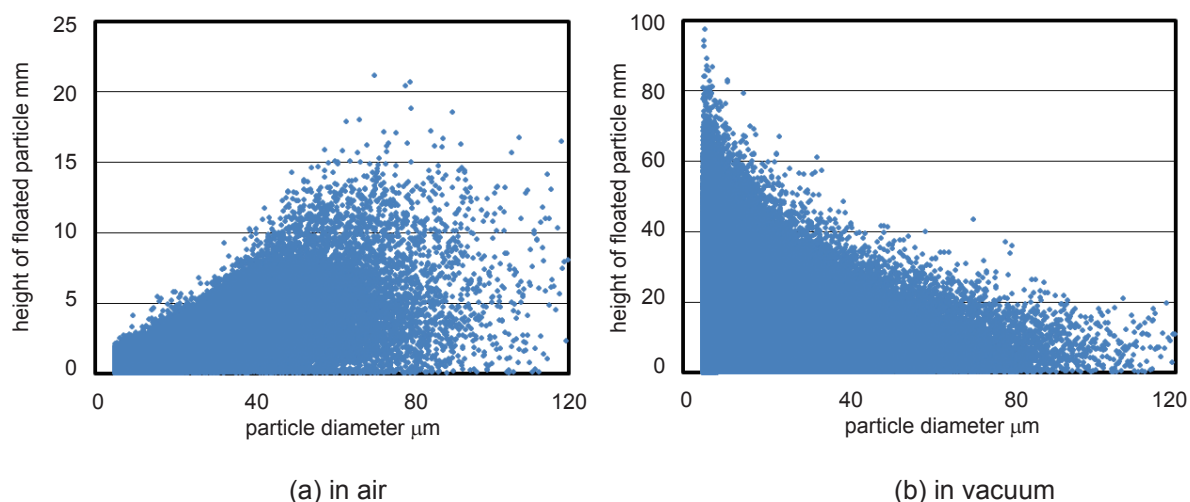


Figure 4.11 Maximum heights of floating particles transported by electrostatic traveling wave at 1-G gravity in (a) air and (b) vacuum environment (applied voltage: $2.0 \text{ kV}_{\text{p-p}}$, frequency: 10 Hz).

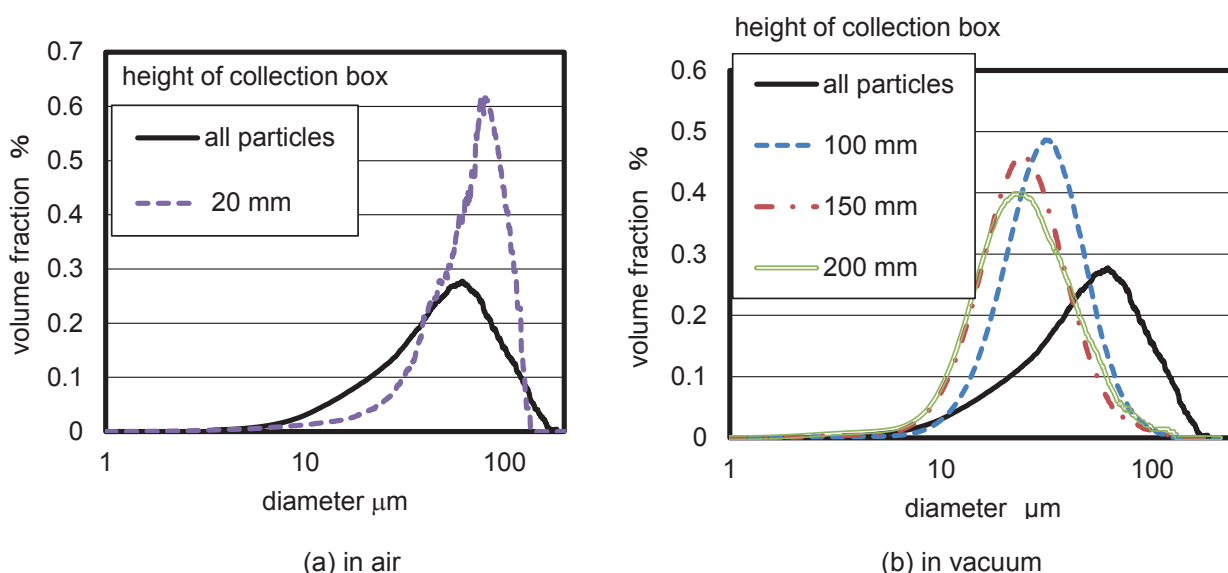


Figure 4.12 Measured volume fractions of particles transported and sorted by electrostatic traveling wave at 1-G gravity (a) in air and (b) in vacuum environments (applied voltage: $2.0 \text{ kV}_{\text{p-p}}$, frequency: 1 Hz).

Particle size sorting was performed by using the electrostatic traveling wave in air and in a vacuum ($\sim 1.5 \times 10^{-2} \text{ Pa}$), and the measured size distributions of the sorted particles in each collection box are shown in Figure 4.12 (a) and (b), respectively. As predicted by the numerical calculations shown in Figure 4.11 (a), the size sorting of small particles in air was not successful because of air drag, and the particles collected in the box at 20 mm have larger diameters than all particles. In addition, the peak of the size distribution was approximately 80 μm . The calculation results shown in Figure 4.11 (a) show that the particles ranging from 70 μm to 90 μm can be collected by the collection box when set at a distance of 20 mm, and it agrees fairly well with the experimental results as shown in Figure 4.12 (a). Figure 4.12 (b) shows that the size sorting of small

particles was experimentally successful in a vacuum. This system could effectively collect particles smaller than $20\ \mu\text{m}$, and the collection box could collect smaller particles when set at a higher position. In the experiments, although the collection box positioned at $250\ \text{mm}$ could collect small particles less than approximately $20\ \mu\text{m}$ in diameter, the total amount of collected particles in the box was extremely small, and the image analyzer could not detect the particles. If we use a large amount of regolith particles ($> 5\ \text{g}$) for the experiments, the number of collected particles in the box at $250\ \text{mm}$ increases, and the image analyzer can detect the small particles. Although the calculation results reproduce a trend similar to the experimental results in the case of air, the calculated particles do not reach altitudes as high as the measured particles in the vacuum. This is because the particles in the vacuum were more heavily charged than the particles in air. Gas discharge does not occur in a vacuum owing to the absence of air, and the particles can keep large amount of charge on their surfaces. Therefore, the particle charges in the vacuum were assumed to be 5 times greater than that in air, as shown in Figure 4.13 (a). To reproduce the experimental results in the numerical calculations, the size-sorting performance was calculated using the assumed charge distribution, as shown in Figure 4.13 (b). The calculated particles can reach the heights of collection boxes set at $100\ \text{mm}$, $150\ \text{mm}$, and $200\ \text{mm}$ as high as the measured particles in vacuum, and the calculated performances of the size sorting in Figure 4.13 (b) reproduce the experimental results in Figure 4.12 (b) fairly well.

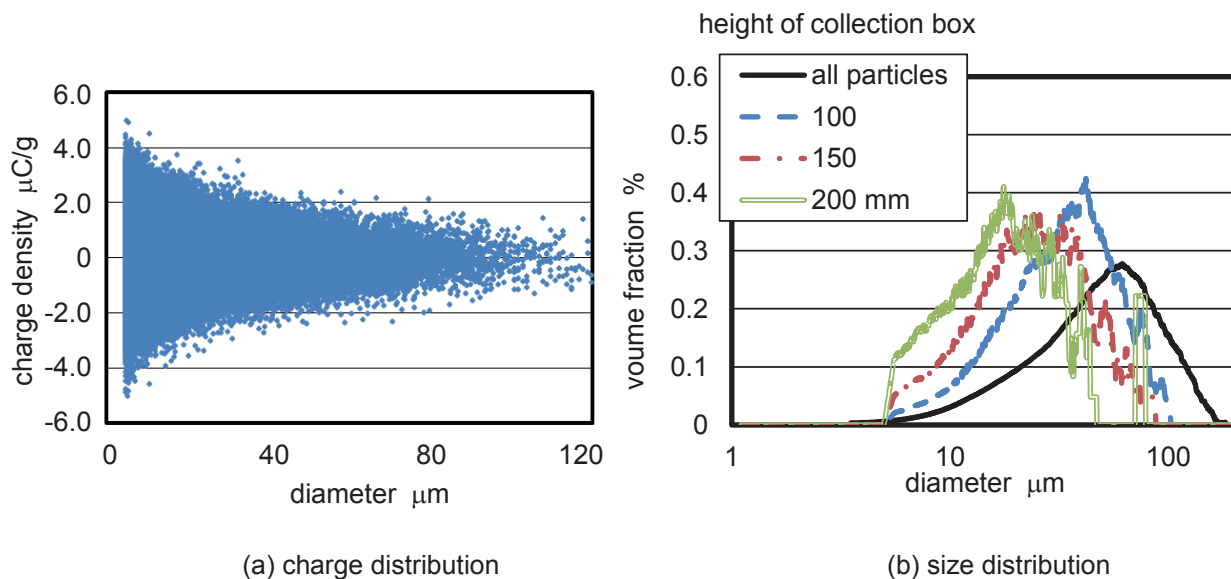


Figure 4.13 (a) Charge distribution of particles used in numerical calculations, assumed to reproduce experimental results, and (b) calculated volume fractions of particles transported by electrostatic traveling wave at 1-G gravity and in vacuum environment (applied voltage: $2.0\ \text{kV}_{\text{p-p}}$, frequency: $1\ \text{Hz}$).

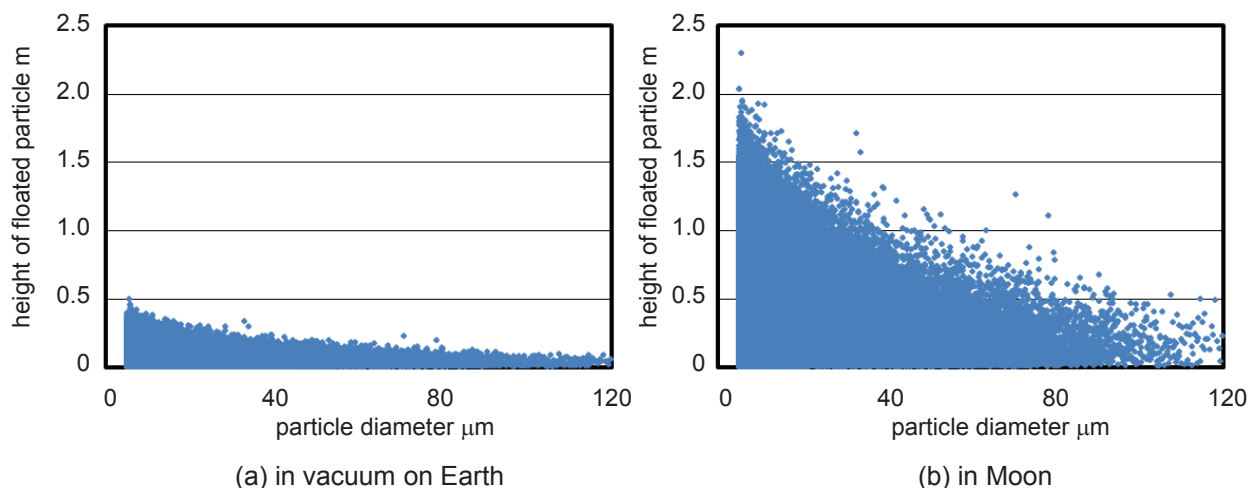


Figure 4.14 Maximum heights of floating particles transported by electrostatic traveling wave in (a) vacuum at 1-G gravity and (b) in Moon environment (applied voltage: 2.0 kV_{p-p} , frequency: 10 Hz).

4.6.2 Size Sorting in Moon Environment

Figure 4.14 (a) and (b) show the maximum heights of each particle in a vacuum on the Earth and the Moon, respectively. As shown in Figure 4.14, the particles in the lunar environment float higher than those in the vacuum, owing to the small gravitational force. Figure 4.15 shows the calculation results of size sorting in the lunar environment. Because Figure 4.14 indicates that the collection box should be set at a higher position on the Moon than that in the vacuum and 1.0-G environments, the box was set as 100 mm, 500 mm, 1,000 mm, and 1,500 mm in the calculations. Figure 4.15 shows that size sorting on the Moon is successful, as the collection box was set higher than that on the Earth. Moreover, if the collection box is set much higher, the size-sorting performance will be improved. In particular, particles with a diameter of approximately $10 \mu\text{m}$ can be collected effectively when the box is set at 1.5 m.

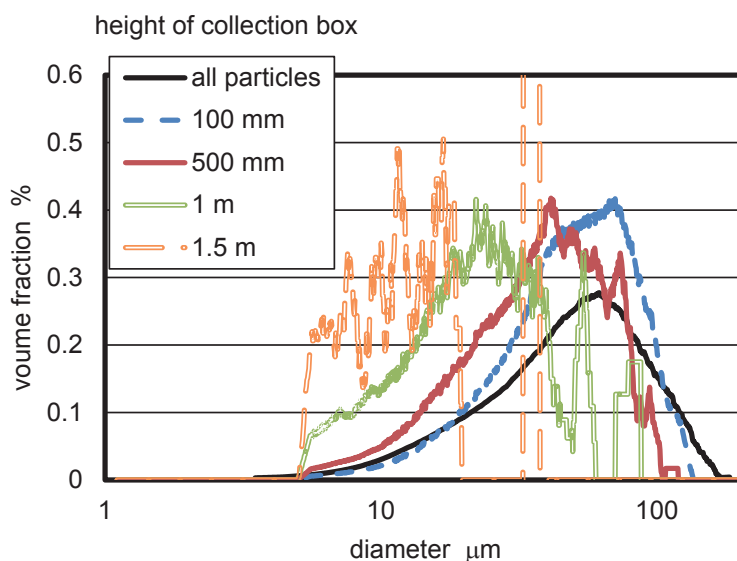


Figure 4.15 Calculated volume fractions of particles transported by electrostatic traveling wave in the lunar environment (applied voltage: 2.0 kV_{p-p} , frequency: 1 Hz).

4.7 Summary

The electrostatic size-sorting system for lunar regolith was developed for future ISRU missions. The system utilizes the electrostatic traveling wave, and a new function of size sorting was added to the system. The size-sorting performances in air, vacuum (1.0-G), and lunar environments were evaluated by conducting experiments in a vacuum (1.0-G) and by numerical calculations. The insights achieved from the results are shown below.

1. Particles transported on the polyimide surface by the traveling wave were charged mainly by tribocharging, and small particles had relatively large charge densities compared to large particles.
2. Although the small particles transported did not reach high altitudes in air owing to air drag, the small particles can float higher than the large particles in a vacuum.
3. It was experimentally demonstrated that particles smaller than 20 μm in diameter were sorted effectively using the electrostatic size-sorting system in vacuum. In addition, the numerical calculation results using the DEM qualitatively reproduced the experimental results in air.
4. The numerical calculation predicted that the size-sorting performance will be successful on the Moon, and the system is expected to extract particles smaller than 10 μm .

Based on these insights, the electrostatic size-sorting system could play an important role in future ISRU missions on the Moon.

Chapter 5 Sampling of Regolith on Asteroids Using Electrostatic Force

5.1 Introduction

As discussed in section 1.3.4, it is important to develop a sampling system that can work effectively in space environments in order to conduct successful sample return missions. In previous studies, mechanical and pneumatic sampling systems have been developed, such as the bullet firing system installed on Hayabusa and Hayabusa-2 [1, 2], adhesive-based sampling [3], tethered sampling [4, 5], the brush wheel sampler [6], the bucket drum regolith excavator [7], scooping [8], drilling [9], and the touch-and-go sample acquisition mechanism (TAGSAM) that was installed on the OSIRIS-REx [10]. Although each sampling system has advantages and disadvantages, one of the most important factors of such a system is its operating reliability in unpredictable environments that may disrupt normal operation.

The electrostatic sampler is developed to serve as an easy-to-control sampling system with a simple configuration that is suitable for space operations. The electrostatic sampler employs the Coulomb force and dielectrophoresis force to capture regolith particles and transport them to a collection capsule. This electrostatic sampler is very simple, is not mechanically driven, does not require complicated controls, and does not contaminate particles, making it highly reliable in space environments. In this chapter, the electrostatic sampler has been developed for sample return missions and its performance has been evaluated in vacuum and low-gravity environment similar to that of an asteroid surface by conducting experiments and numerical calculations. As predicted in section 2.6.1, sampling in the 1-G environment on the Earth is impossible owing to the effect of gravitational force; therefore, numerical calculations were conducted. These calculations predicted the sampling performance in a vacuum and in low gravity environments by using the DEM, as described in section 2.7. Moreover, demonstrations of lunar regolith particle sampling, ranging from several micrometers to one millimeter in diameter, were conducted in a low-G environment created by the parabolic flight of an aircraft. There may also be large particles on the surface of an asteroid, with diameters of 1.0 mm or larger, such as those on asteroid Itokawa investigated by the Hayabusa mission [11] and on asteroid Eros investigated by the NEAR-Shoemaker spacecraft [12]. Therefore, large particle sampling (using 4 mm diameter rocks and 2 mm diameter glass particles) were also conducted in low gravity, by utilizing the parabolic flight of an aircraft. The sampling of large particles is expected to be more difficult than that of small particles because the balance of forces acting on the particles varies depending on the particle diameter. In particular, the gravitational force becomes dominant as the particle diameter increases because the force is proportional to the cube of the diameter, as described in section 2.6.1, and it hinders the sampling of large particles. In this chapter, the effect of gravity on the sampling of large particles in the electrostatic field was investigated by numerical calculations and experiments. Part of this work was published in literatures [13, 14].

5.2 System Configuration

Figures 5.1 and 5.2 show the sampling procedure of the electrostatic sampler and a photograph of the device, respectively [13, 14]. When rectangular two-phase high voltage is applied between the parallel screen electrodes attached to the lower end of the sampling tube (inner diameter: 50 mm, acrylic composition) (Figure 5.1 (a)), the resultant Coulomb force and dielectrophoresis force act on the particles near the electrodes, and some agitated particles pass through the openings of the screen electrodes. The power supply described in section 3.2.1 was modified and used for this sampling system. Because the sampler requires a two-phase standing wave, the power supply was duplicated for two pairs, and the output voltages were shifted to 180° by using the microcomputer. Two types of parallel electrodes were used: Type 1 (1.3 mm, pitch: 5 mm, gap: 5 mm) and Type 2 (wire diameter: 1.3 mm, pitch: 10 mm, gap: 10 mm), and are shown in Figure 5.3. Type 1 was used for sampling of small particles, and Type 2 was used for the sampling of large particles. Large particles cannot pass through the narrow windows of Type 1, and easily clog at its windows. In a microgravity environment, the captured particles would be transported to a collection capsule, which is located at the upper 150 mm of the screen electrodes owing to their own inertial force. After several seconds of operation, the collection capsule was closed with a stopper plate to keep the particles in the capsule (Figure 5.1 (b)). During the operation, the behavior of the particles was observed during the sampler operation using a high-speed camera (GZ-V590, JVC Kenwood). After the experiments, the weights of the collected particles were measured, and the particles were analyzed using a particle image analyzer (Morphologi G3/G3S, Malvern). Because this system uses a very small electrostatic force, it would not disturb the motion of the spacecraft. In addition, the system can be designed to be compactly. Moreover, the electrostatic sampler is also compatible with other sampling systems, such as the impact sampling systems used in the Hayabusa and Hayabusa-2 because the electrostatic sampler can automatically capture floating particles without precise control.

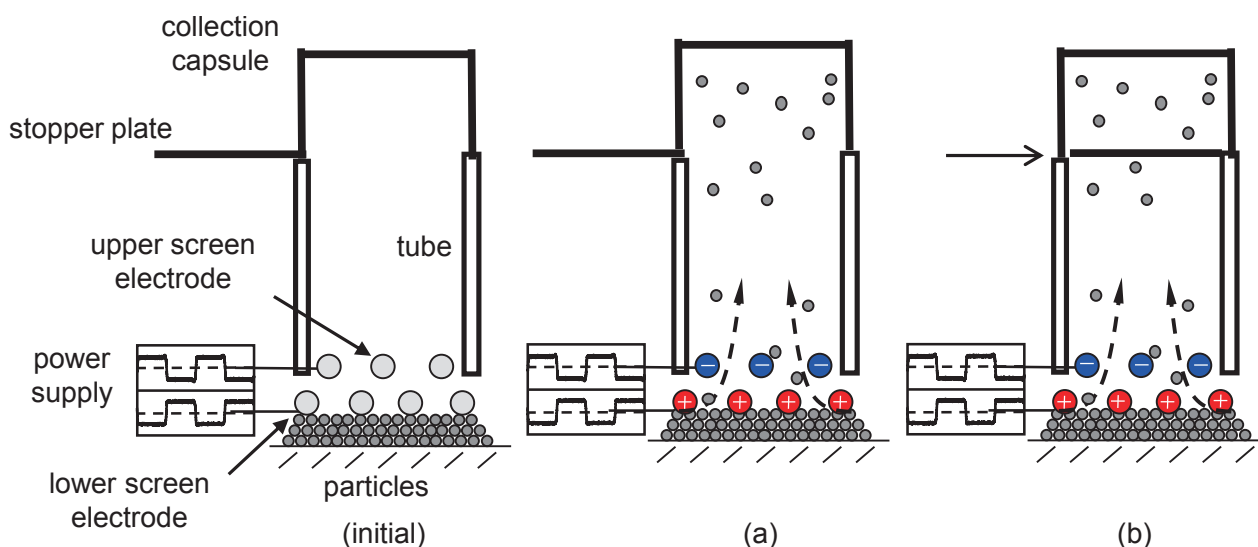


Figure 5.1 Sampling procedure using electrostatic sampler: initial condition, (a) capturing regolith, and (b) closing collection capsule.

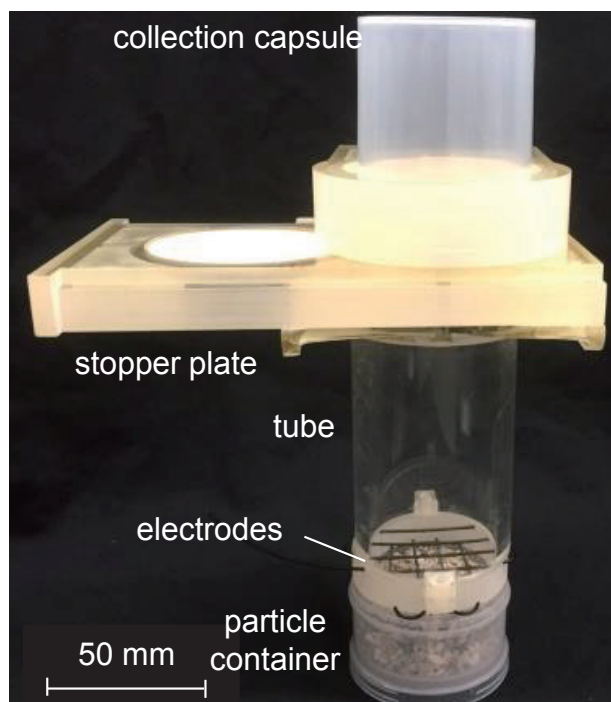
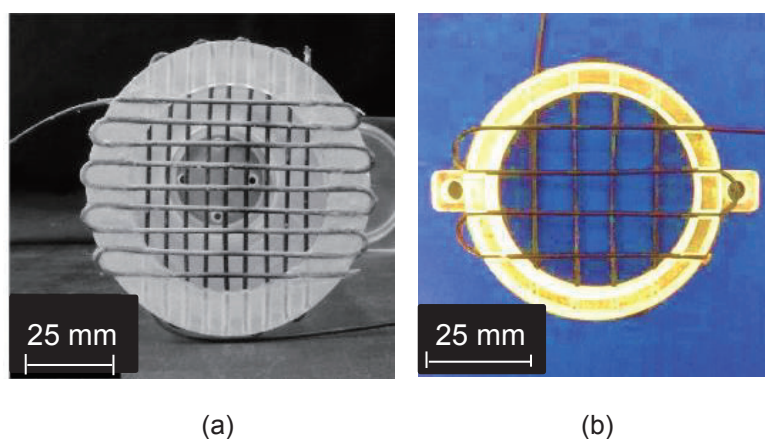


Figure 5.2 Photograph of electrostatic sampler.



(a)

(b)

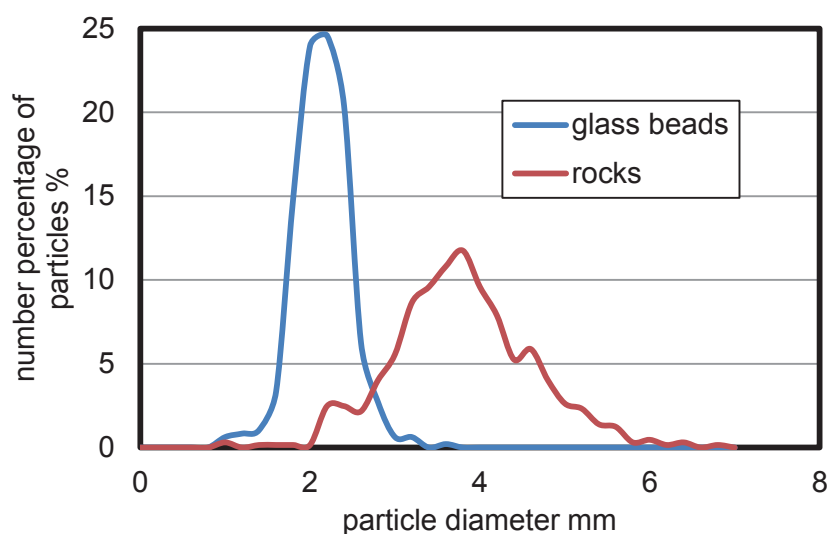
Figure 5.3 Photographs of screen electrodes for (a) small particles (Type 1) and (b) large particles (Type 2).

The lunar regolith simulant FJS-1 was used as the experimental material for small particle sampling. The properties of the simulant were described in section 1.1.2. As alternative to large particles, glass beads and rocks were used for the experiment. Photographs and size distributions of the glass beads and rocks are shown in Figure 5.4. Most of the glass beads were approximately 2 mm in diameter. The glass beads were primarily made of silicon dioxide, which is the main component of lunar regolith, as described in section 1.1.2. On the other hand, most of the rocks were approximately 4 mm in diameter, and their compositions were similar to those of lunar regolith. The particles were initially set in the container (height: 30 mm, inner diameter: 50 mm) below the parallel screen electrodes.



(a) glass beads

(b) rocks



(c) size distribution

Figure 5.4 Photographs of (a) glass beads and (b) rocks; (c) size distribution of particles.

5.3 Particle Dynamics under Operation of Electrostatic Sampling System

Positively and negatively charged particles would be captured by the Coulomb force because the electrostatic sampler uses an alternating electrostatic field. In addition, uncharged particles are also expected to be captured successfully because the dielectrophoresis force acts on them in a non-uniform electrostatic field. Because the electrostatic field strength increases closer to the electrodes, the dielectrophoresis force acts on particles basically as an attractive force to the electrodes. Figure 5.5 shows the motions of particles that are agitated and captured by the sampler. If the Coulomb force and dielectrophoresis force exceed the adhesion force between the particle and asteroid, the particles float (rest state). If the gravitational force is extremely low in a microgravity environment, such as on the asteroid Itokawa (gravitational acceleration: $8.6 \times 10^{-5} \text{ m/s}^2$ [15]), the floating particles are driven by the Coulomb force, dielectrophoresis force, and their own inertial force between the parallel screen electrodes (agitated state). In the agitated state, if the polarity of the

applied voltage changes before the particles pass through the openings of the upper electrode, the particles vibrate between the electrodes. When the particles approach the upper electrodes (between the agitated and suspended states), their successful capture depends on their inertial force. If the particles are efficiently accelerated between the parallel electrodes, some of them can pass through the upper electrodes (suspended state), and the inertial and Coulomb forces, which act as repulsive forces against the asteroid surface, would push them upward. In a vacuum, the motions of particles are not affected by air drag; therefore, the particles are easily transported to the collection capsule.

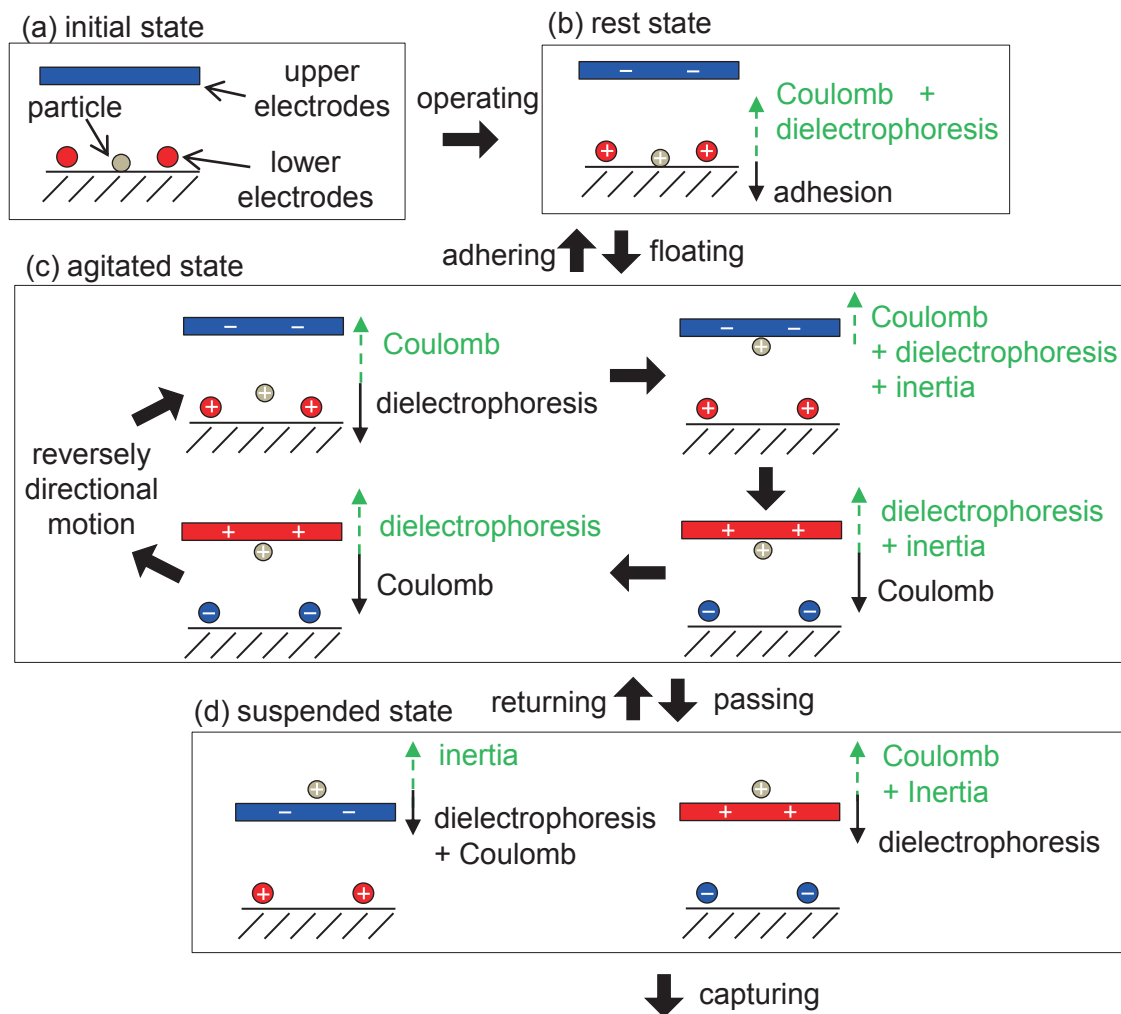


Figure 5.5 Changes in particle motions under electrostatic sampler operation: (a) initial state, (b) rest state (adhering with asteroid), (c) agitated state (vibrating between parallel electrodes), and (d) suspended state (passing through upper electrode).

5.4 Effect of Dielectrophoresis Force on Large Particles

As described in section 2.6.1, the dielectrophoresis force is dominant on large particles. Although the static dielectrophoresis force can be evaluated using the model experiments and theoretical calculation, as de-

scribed in section 2.6.1, the dynamic force in the alternating electrostatic field was not clarified. An experimental investigation is difficult because the electron motion, which induces the electrostatic dipole moment in the particle, cannot be observed. The electron motion is affected by the conductivity and permittivity of the particles. Therefore, considering the electrostatic properties of particles, the effect of the dielectrophoresis force on the particle motion was investigated by conducting numerical calculations.

The differential form of the dielectrophoresis force is represented by Equation (5.1). The force is calculated by integrating $\rho_c \mathbf{E}$ over the particle volume V_p . The charge density ρ_c and electrostatic field \mathbf{E} are calculated by solving the following coupled Poisson's equation of differential form (5.2) and conservation of charge (5.3).

$$\mathbf{F} = \int_{V_p} \rho_c \mathbf{E} dV_p \quad (5.1)$$

$$\nabla \cdot (\varepsilon_0 \varepsilon_r \nabla \phi) = \rho_c \quad (5.2)$$

$$-\frac{\partial \rho_c}{\partial t} = \nabla \cdot (\sigma_p \mathbf{E}) \quad (5.3)$$

where ϕ , ε_r , ε_0 and σ_r are the electrical voltage potential, relative permittivity (1.0 for air, 3.0 for particle), permittivity of free space (8.8×10^{-12} [F/m]), and conductivity, respectively. Equations (5.2) and (5.3) were calculated by the finite difference method, as described in section 2.4.1. The calculation method described in section 2.4.1 was expanded in three-dimensions. The conductivity was set at the same element as the permittivity. Because the conductivity of the asteroid regolith is unknown, it was selected as a parameter in the calculation. The particle charge density ρ_c was assumed to be zero as an initial condition. These equations were calculated iteratively with a time step Δt , which was determined to be negligibly small relative to a time constant of particle charge polarization as determined by $\varepsilon_r \varepsilon_0 / \sigma_r$. Figure 5.6 shows the calculation model. One particle (diameter: 1 mm) was set at a height on the lower surface of the lower electrode, and then, an AC voltage (10 kV_{p-p}, 9 Hz) was applied to the parallel screen electrodes.

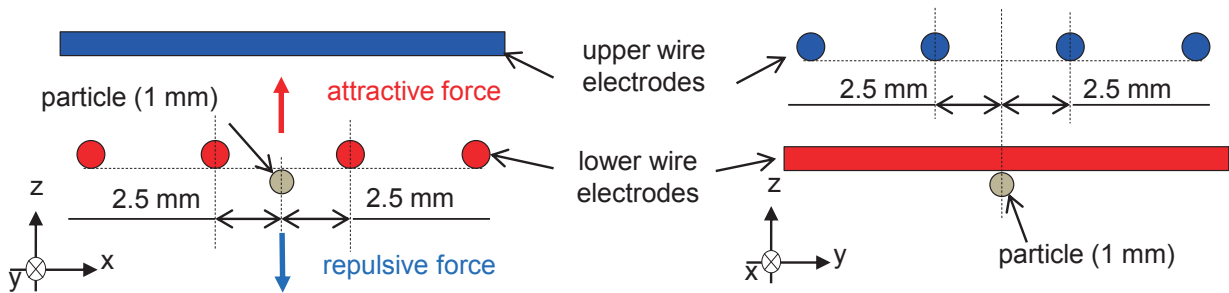


Figure 5.6 Schematic model for calculating dielectrophoresis force.

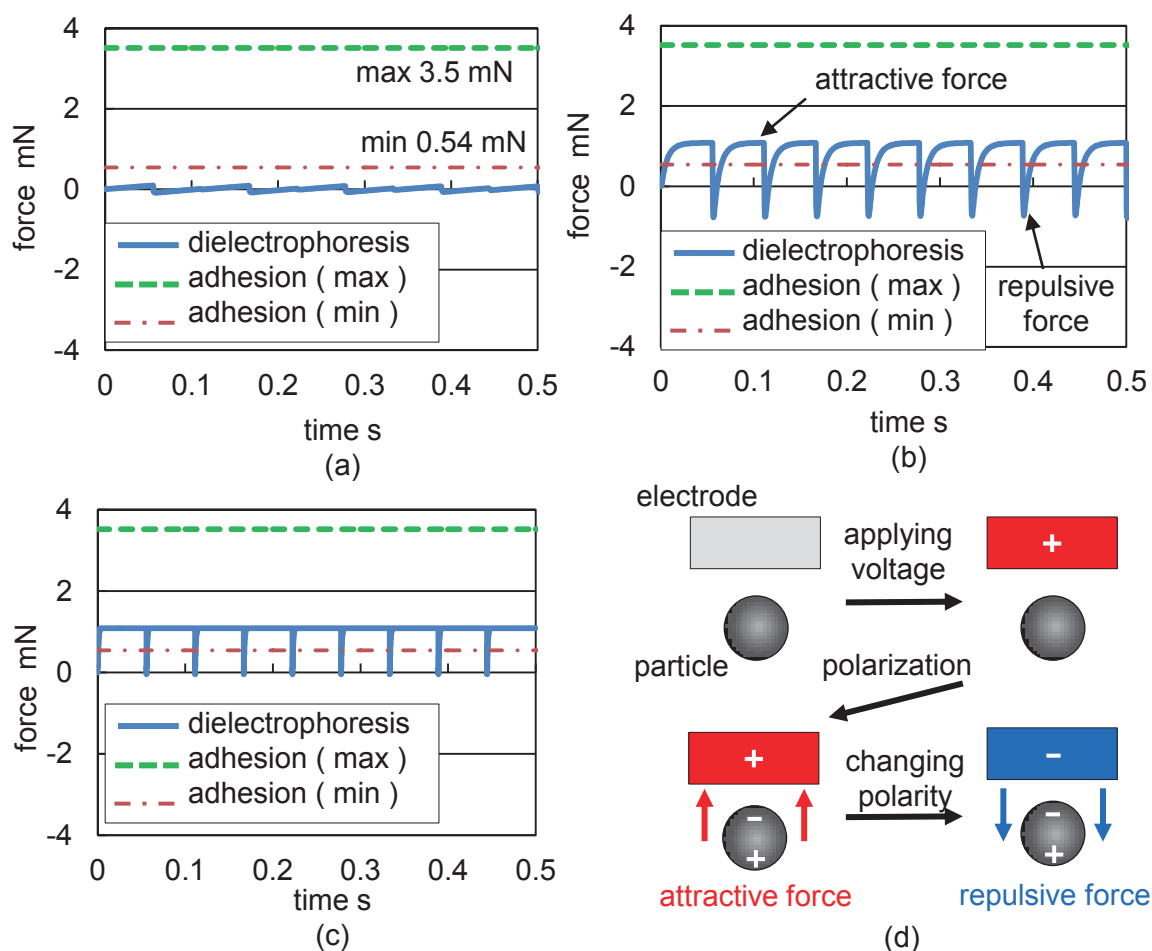


Figure 5.7 Calculated dielectrophoresis force acting on (a) insulative ($\sigma = 1.0 \times 10^{-10} \Omega^{-1}\text{m}^{-1}$), (b) resistive ($\sigma = 1.0 \times 10^{-8} \Omega^{-1}\text{m}^{-1}$), and (c) conductive ($\sigma = 1.0 \times 10^{-6} \Omega^{-1}\text{m}^{-1}$) particles. (d) Mechanism of dielectrophoresis force as attractive force and repulsive force.

Figure 5.7 shows the calculated dielectrophoresis force acting along the z -axis, where the attractive force in the upper direction is positive. To compare the adhesion force acting on particle, the calculated adhesion force is also shown in Figure 5.7. Because the adhesion force varies widely, the measured maximum and minimum adhesion coefficients α are used to calculate the adhesion force. For an insulative particle ($\sigma = 1.0 \times 10^{-10} \Omega^{-1}\text{m}^{-1}$) (Figure 5.7 (a)), the particle is polarized slowly, and an extremely weak attractive force acts on the particle. In this case, the dielectrophoresis force can be neglected. On the other hand, for a conductive particle ($\sigma = 1.0 \times 10^{-6} \Omega^{-1}\text{m}^{-1}$) (Figure 5.7 (c)), the particle polarizes quickly, and a large dielectrophoresis force that exceeds the minimum adhesion force acts on the particle. For a resistive particle ($\sigma = 1.0 \times 10^{-8} \Omega^{-1}\text{m}^{-1}$) (Figure 5.7 (b)), attractive and repulsive forces act on the particle, as shown in Figure 5.7 (d). When a positive voltage is applied to the electrode, a negative and positive charge is induced in the upper and lower surface of the particle, respectively. The attractive force is generated between the negative charge and positive electrodes. Subsequently, even when the polarity of the applied voltage changes, the charge polarization remains in the particle and the repulsive force is generated between the negative charge and the negative electrode. This force is larger than the minimum adhesion force. However, because the time

duration is extremely short, it would actually not affect the motion of floating particles in the agitated and suspended states. For the calculated results, the particles with conductivity exceeding $1.0 \times 10^{-8} \Omega^{-1} \text{m}^{-1}$ are expected to be captured successfully using the dielectrophoresis force. On the other hand, for conductivity lower than $1.0 \times 10^{-10} \Omega^{-1} \text{m}^{-1}$, the dielectrophoresis force would be negligibly small compared to the adhesion force.

5.5 Numerical Calculation

Numerical calculations using the modified hard sphere model of the DEM were conducted to analyze the particle motions and predict the sampler performance. The basic procedure of the calculation was described in section 2.7, and several specific conditions of the calculations are described in this section. As for the external force acting on particles, the Coulomb force, dielectrophoresis force, gravitational force, adhesion force, and air drag were considered. The forces are calculated by Equations (2.3), (2.16), (2.30), (2.31), and (2.32), respectively. The torque acting on the particles was assumed to be zero. The air drag was neglected in the vacuum environment. The electrostatic field \mathbf{E} was calculated using the finite difference method, as described in section 2.4.1, reproducing the geometry and electrostatic properties of the conveyor and electrodes. In the DEM calculation, the electrostatic field \mathbf{E} at the position of the particle was used to calculate the Coulomb force and dielectrophoresis force. The calculation area of the DEM was set to be $0.18 \times 0.18 \text{ m}^2$, and the length of the z -direction was assumed as infinity. The geometry of the experimental setup was reproduced in the calculation of the collision between the setup and particles. 20,000 lunar regolith simulant (FJS-1) particles, 5,000 glass bead particles, and 4,000 rock particles were used for the calculations, and the particles were randomly set below the parallel electrodes. The coefficient of the adhesion force α was assumed to be 0.00027. The charge distribution of lunar regolith q measured by the free-fall method, as described in section 2.5.2 was used in the DEM calculation. The dielectrophoresis force should be calculated dynamically by using the method explained in section 5.4; however, the method is not realistic in the DEM calculation because of the large calculation load. From the results obtained in section 2.5.3, Equation (2.16) is used if the particles are conductive. Otherwise, the dielectrophoresis force can be neglected. The time step for the Runge–Kutta calculation was set to be $1.0 \times 10^{-5} \text{ s}$. Because the calculated number of small particles is greater than that of large particles, a short calculation time was set in the case of small particles. The small particles that reached 50 mm in height within 1.0 s were assumed to be collected. Similarly, the large particles that reached a height of 120 mm within 5.0 s of operation were assumed to be collected.

5.6 Experiment in Low-Gravity Environment

In light of the prediction described in section 2.6.1, the sampling of particles at 1-G was considered to be impossible. To confirm particle sampling performance, sampling demonstrations were performed in a low-gravity environment, which was reproduced for approximately 20 s by the parabolic flight of an aircraft

operated by Diamond Air Service, as shown in Figure 5.8. Each experiment was conducted while the gravitational acceleration was stabilized below 0.01-G. The collected particles in the collection box were weighted and analyzed using a particle image analyzer (Morphologi G3/G3S, Malvern). The particle motions were observed using a high-speed video camera (GZ-V590, JVC KENWOOD).

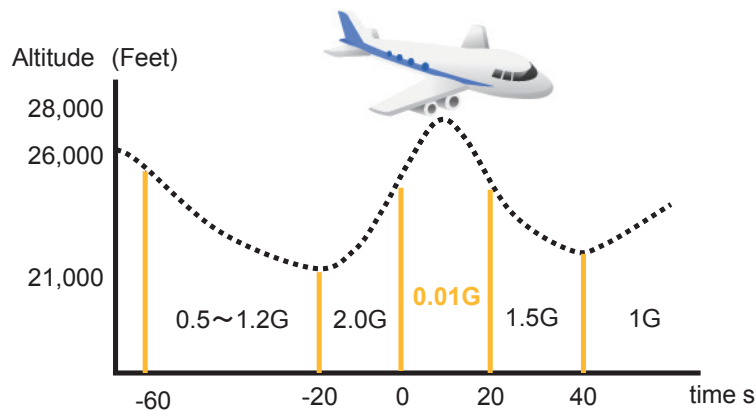


Figure 5.8 Diagram of aircraft parabolic flight.

5.7 Results and Discussions

5.7.1 Sampling of Small Particles

Figure 5.9 shows the calculated particle motions in air and in the zero-G environment under the application of rectangular high voltage ($10 \text{ kV}_{\text{p-p}}$ 20 Hz). The particle colors indicate the dominant force. Conductive and insulative particles can be agitated, and some agitated particles passed through the openings of the upper electrodes. In addition, the particles adhering to other particles can also be captured as agglomerate. Figure 5.10 shows the calculated amount of collected particles versus the frequency of the applied voltage. The calculated result shows that an optimum frequency exists. At low frequency, infrequent polarity changes during the 1.0 s operation resulted in low performance. On the other hand, a large amount of stirred-up particles vibrate between the parallel screen electrodes at high frequency. This tendency is similar to the electrostatic dust shield system described in section 3.4.1. Furthermore, more conductive particles are collected compared with insulative particles because of the effect of the dielectrophoresis force. Figure 5.9 (b) shows that floating insulative particles are agitated by the Coulomb force, and high-frequency operations cause a vertical flip-flop motion of the particles, leading to low performance. On the other hand, some conductive particles are agitated by the dielectrophoresis force, as shown in Figure 5.9 (a). The dielectrophoresis force is not affected by the frequent polarity change in the applied voltage; thus, it transports a large amount of particles passing through the windows of the upper electrodes. In the agitated and suspended states, the motions of floating particles can be controlled by the optimum frequency of approximately 5 Hz for operation in air and vacuum conditions.

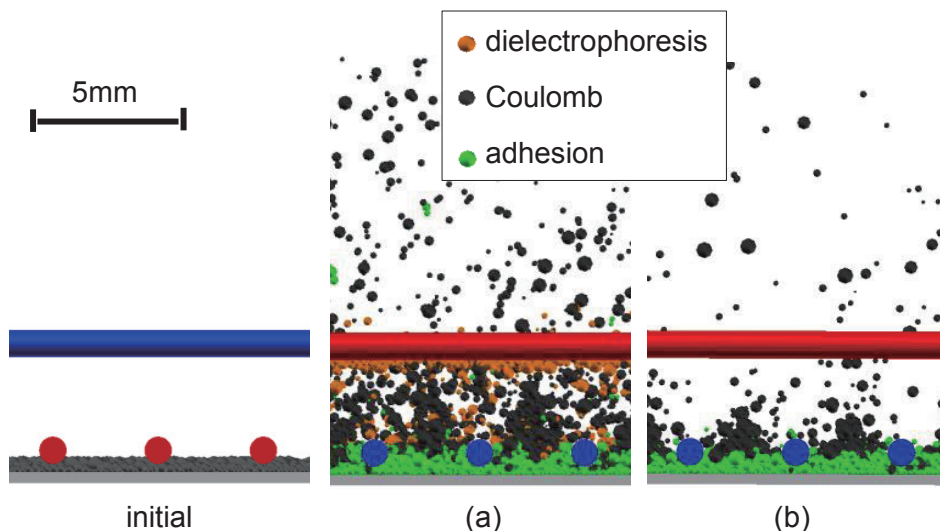


Figure 5.9 Calculated motions of particles: (a) conductive and (b) insulative particles in air and 0-G environment under the application of 20 Hz and 10 kV_{p-p} voltage. Particle colors indicate dominant external force acting on particles. 1-G is equal to 9.8 m/s².

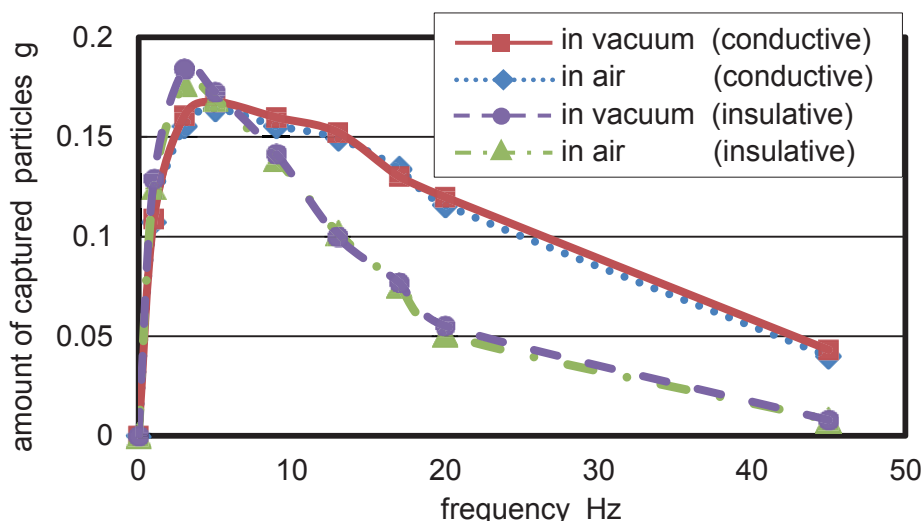


Figure 5.10 Calculated amounts of captured particles versus frequency in air and 0-G gravity environment (10 kV_{p-p}).

Figure 5.11 shows the calculated amount of collected particles versus the applied voltage. Because applied voltage is limited below 10 kV_{p-p} in air owing to gas discharge, the results in cases where the applied voltages is larger than 10 kV_{p-p} in air are reference values. The amount of collected particles increases with the applied voltage, simply because the high Coulomb and dielectrophoresis driving forces are applied to the particles in a high electrostatic field. However, the amount of collected conductive particles saturates under an applied voltage of 10 kV_{p-p} or higher because a large dielectrophoresis force acts on the particles as an attractive force toward the electrodes.

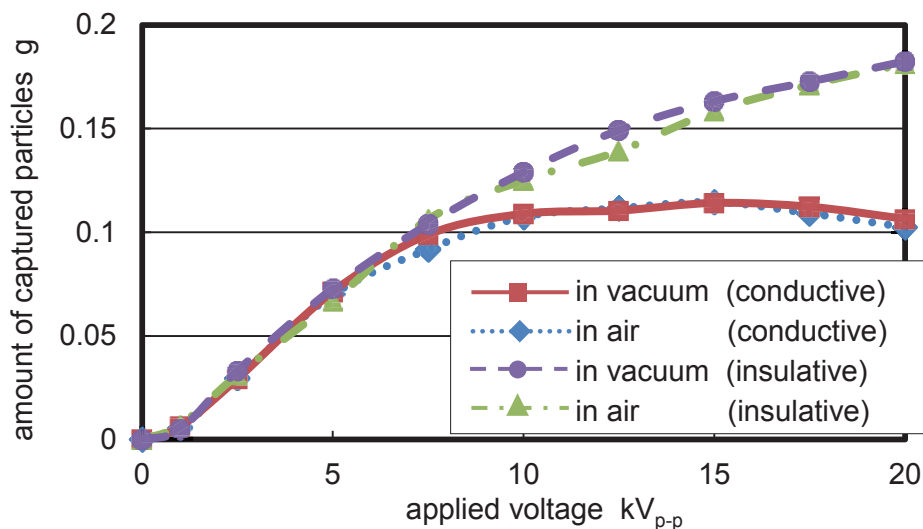


Figure 5.11 Calculated amounts of captured particles versus applied voltage in air and 0-G gravity environment (1.0 Hz).

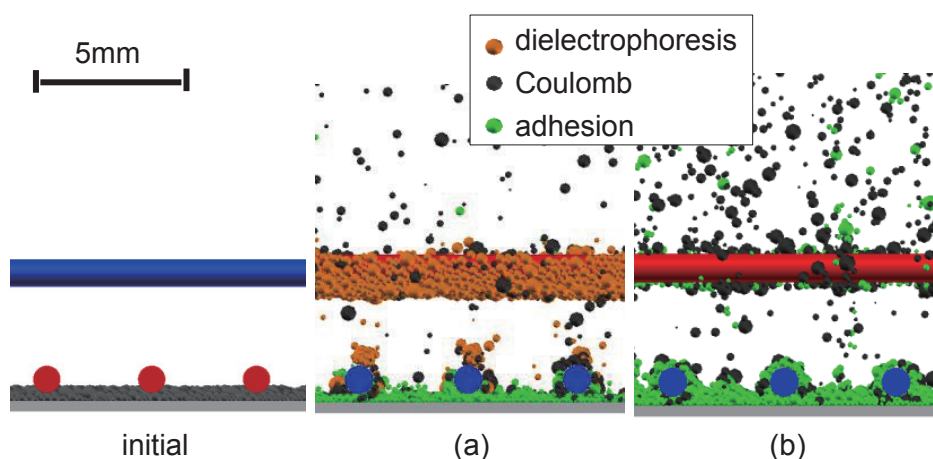


Figure 5.12 Calculated motions of particles: (a) conductive and (b) insulative particles in air and 0-G gravity environment under the application of 1.0 Hz and 20 kV_{p-p} voltage (particle colors indicate dominant external force acting on particles).

Figure 5.12 shows the calculated particle motions when the high voltage of 20 kV_{p-p} is applied. The results show the difference between the conductive and insulative particle motions clearly. Large amounts of conductive particles adhere to the electrodes by the dielectrophoresis force, and they cannot move. On the other hand, the sampling of low-conductivity particles would be easier under high-voltage operation. In vacuum conditions, the applied voltage is not limited by the occurrence of gas discharge; therefore, the performance would be improved further in a vacuum with the applied high voltage.

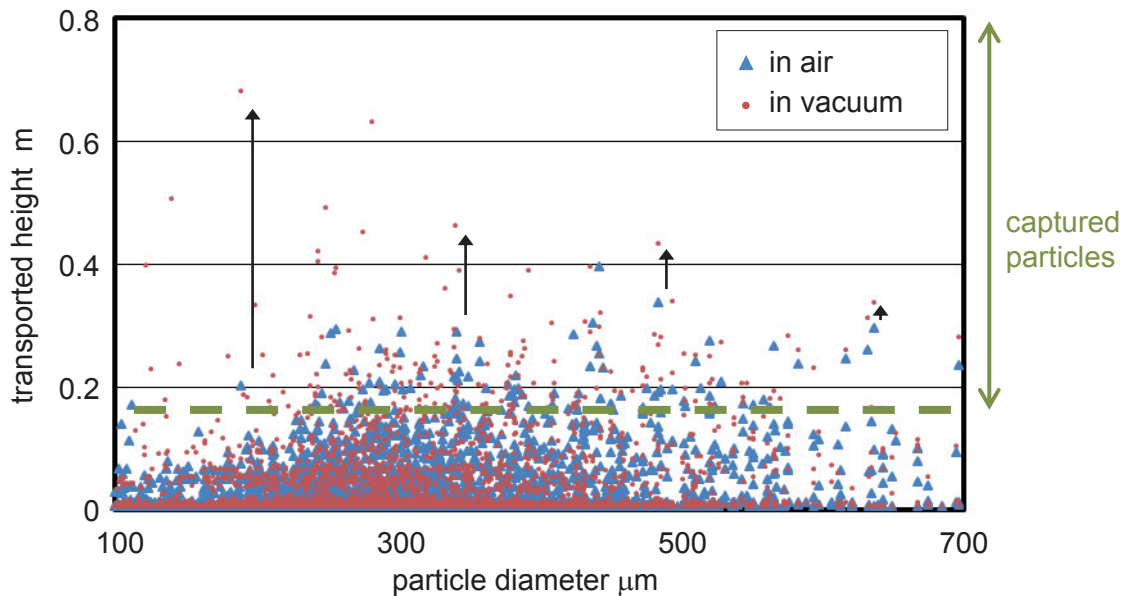


Figure 5.13 Calculated maximum heights of particles transported by electrostatic sampler at 0-G gravity in air and in vacuum within a 1.0 s operation ($10 \text{ kV}_{\text{p-p}}$, 1.0 Hz).

In the numerically calculated results for frequency and voltage characteristics, similar trends are observed in air and vacuum conditions; however, the performance is slightly better in a vacuum than in air because small particles are highly affected by air drag. Figure 5.13 shows the calculated maximum heights reached by the floating particles in air and in a vacuum within 1.0 s of application of a $10 \text{ kV}_{\text{p-p}}$ rectangular voltage. Some small particles reach high altitudes in a vacuum because of the small air drag, and the tendency is similar to that shown in Chapter 4.

To confirm the performance of the sampler in a low-gravity environment, experiments were conducted in air and a low-G environment reproduced by the parabolic flight of an aircraft. Although the experiments were conducted in conditions of 1-5 Hz, which are approximately the optimum frequencies of the applied voltage predicted by the numerical calculations, experiments at frequencies greater than 1 Hz were not successful because maintaining a low-G was difficult and some problems occurred during the experiments in low-G operation. Figures 5.14 and 5.15 show the calculated and observed particle motions in air and zero-G environment when the rectangular voltage of $10 \text{ kV}_{\text{p-p}}$ is applied, respectively. Regolith particles near the lower screen electrode were agitated by the alternating electrostatic field, and some agitated particles passed through the openings of the electrodes (Figure 5.15) as predicted by the numerical calculations shown in Figure 5.14. For operation in a 1-G environment, the particles that floated reaching only a few millimeters above the upper electrode and then fell down to the ground because of the gravitational force and air drag. On the other hand, in the low-G environment, some floating particles reached the collecting capsule located 150 mm above the screen electrodes. A substantial amount of regolith ($\sim 900 \text{ mg}$) containing not only small particles but also particles larger than 0.5 mm in diameter was successfully captured, as shown in Figure 5.16 (a) and (b). Figure 5.16 (c) shows the size distribution of the initially settled and captured particles.

Relatively large particles compared with the initially settled particles were captured because small particles in air experienced relatively large air drag and did not reach the capsule. This phenomenon agreed with the predictions in sections 2.6.1 and 2.6.3.

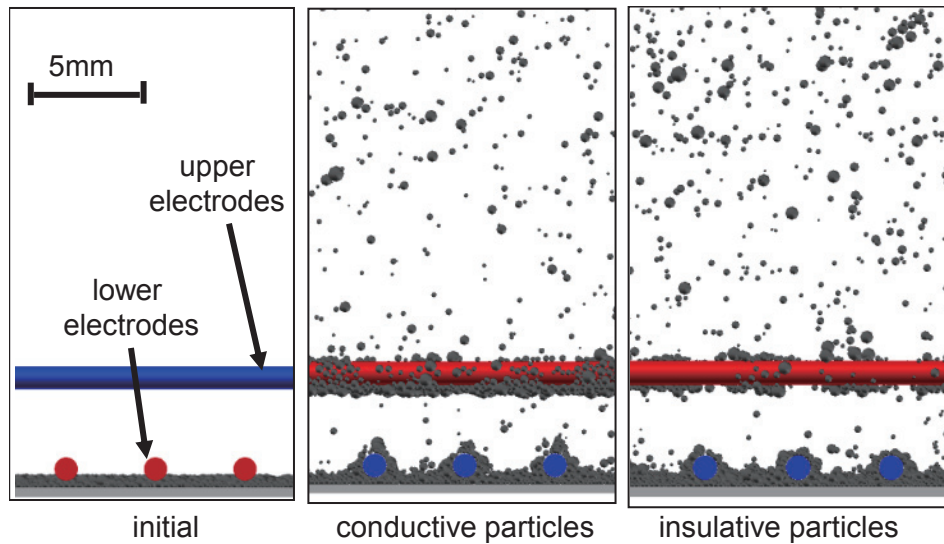


Figure 5.14 Calculated particle motions in air and 0.01-G gravity environment under application of 1.0 Hz and 10 kV_{p-p} voltage. 1-G is equal to 9.8 m/s².

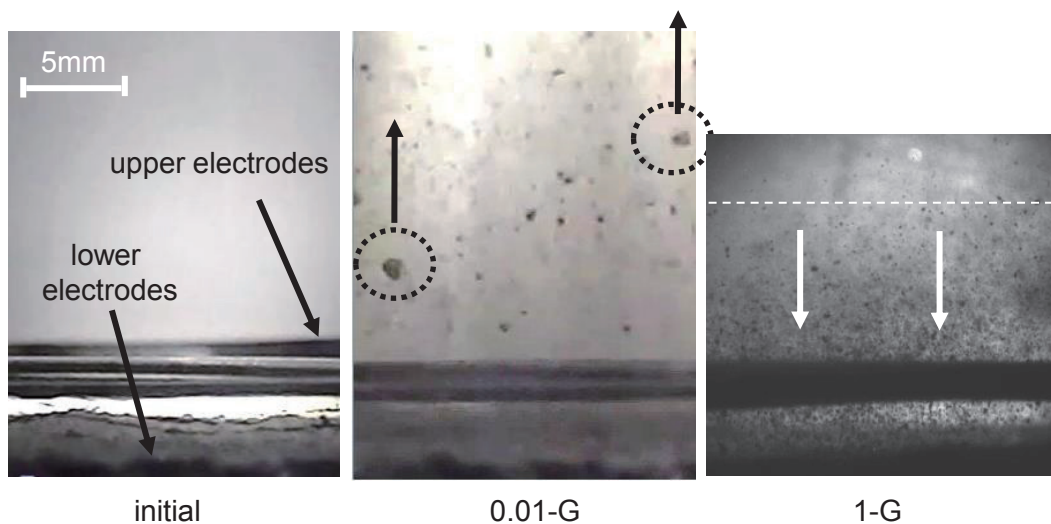


Figure 5.15 Observed particle motion in air at 1-G and 0.01-G gravity environments under application of 1.0 Hz and 10 kV_{p-p} voltage. 1-G is equal to 9.8 m/s².

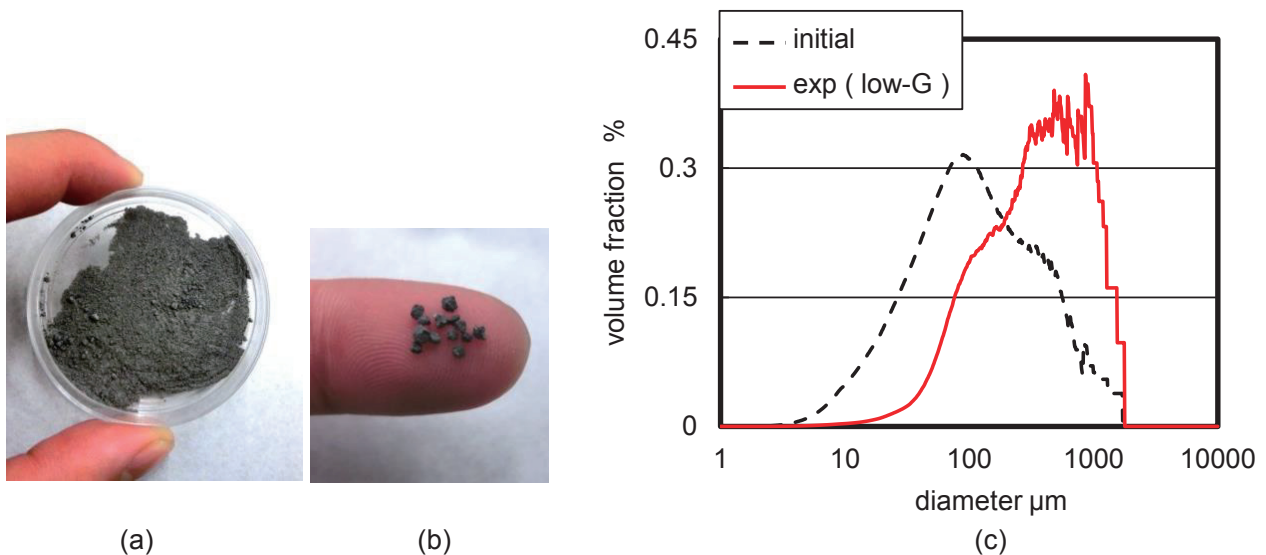


Figure 5.16 Captured FJS-1 lunar regolith simulant after the operation in air and 0.01-G gravity environment under application of 1.0 Hz and 10 kV_{p-p} voltage: (a) captured particles (approximately 900 mg), (b) captured particles (larger than 0.5 mm in diameter), and (c) volume distributions of initial and captured particles.

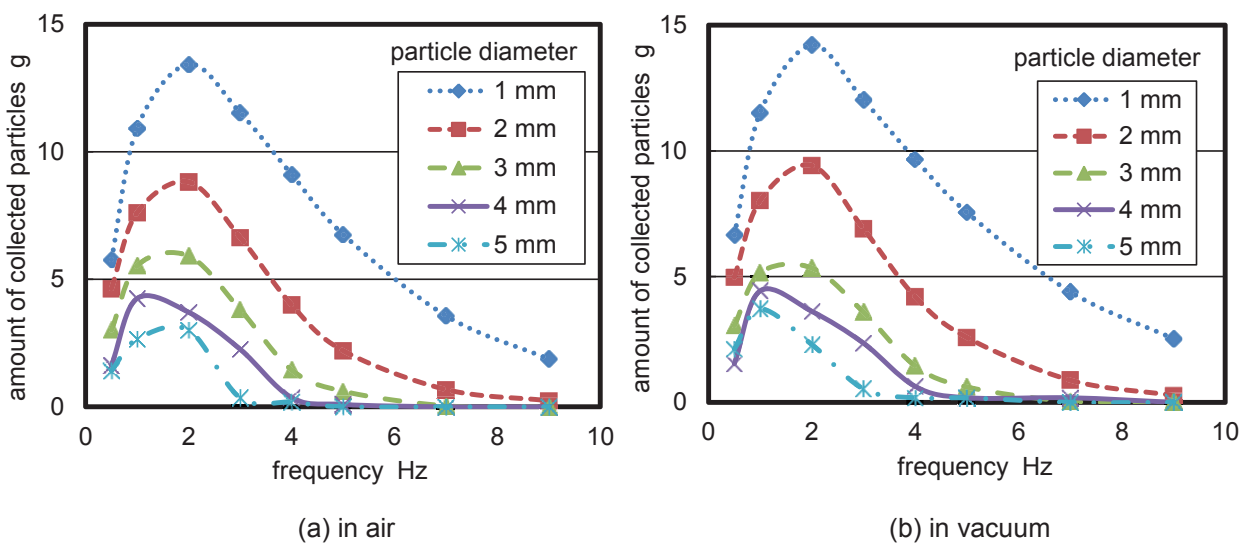


Figure 5.17 Calculated amounts of collected particles when alternating voltage of 10 kV_{p-p} is applied (a) in air and (b) in vacuum at 0.00001-G gravity.

5.7.2 Sampling of Large Particles

Figure 5.17 (a) and (b) show the calculated amounts of collected large particles for each diameter with respect to the frequency of the applied voltage in air and in a vacuum, respectively. The calculations were performed under the application of 10 kV_{p-p} voltage at 0.00001-G. Figure 5.17 (a) shows that the optimal frequency, which is approximately 1–3 Hz for the applied voltage, exists for all particles. Under low-frequency conditions, the polarity of the voltage changes a few times within 5.0 s, and the number of sampling oppor-

tunities decreases. As a result, the sampler performance worsens. On the other hand, the highly frequent change in polarity prevents the particles that are in vertical vibrational motion between the parallel screen electrodes from passing through the opening of the upper electrode. These tendencies are common in the results of small particle sampling. The amount of collected particles decreases as the particle diameter increases. This is because a relatively large dielectrophoresis force, which is a body force, acts on large particles that are affected by the relatively small Coulomb force. Air drag is not the reason why the sampling of large particles is difficult, because the amount of collected particles in air is almost same as that in a vacuum, as shown in Figure 5.17 (a) and (b). In addition, the gravitational force is negligible.

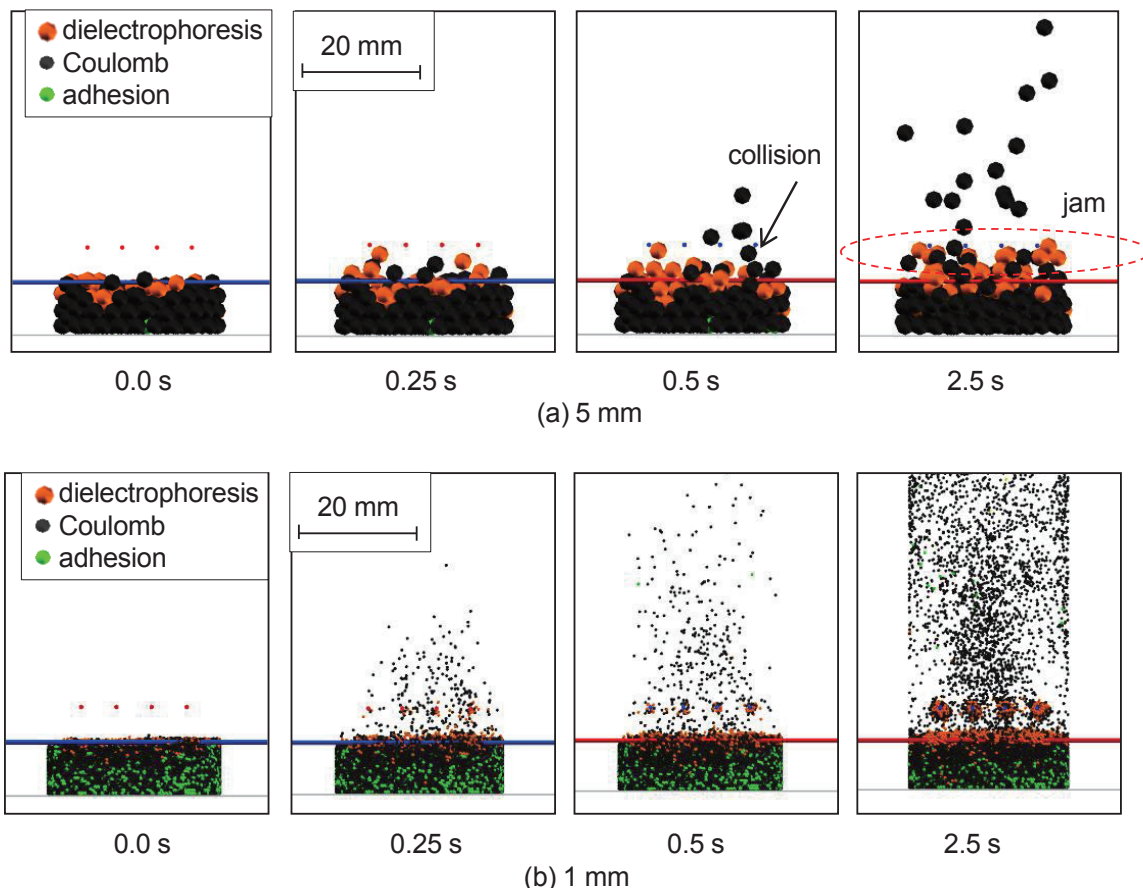


Figure 5.18 Calculated behaviors of particles, (a) 5 mm and (b) 1 mm in diameter, when alternating voltage of 10 kV_{p-p} is applied in vacuum and at 0.00001-G gravity.

Figure 5.18 shows the calculated particle behavior. The colors indicate the dominant external force. As shown in Figure 5.18, the particles between the parallel electrodes are significantly affected by the dielectrophoresis force. The dielectrophoresis force acts as an attractive force to the electrodes, as the electrostatic field strength increases with closer to the electrodes. The dielectrophoresis force tears particles off the asteroid (Figure 5.18 (a), 0.0 s) and attracts them to the space between the parallel electrodes (Figure 5.18 (a), 0.25 s). Subsequently, although some particles are transported above the upper screen electrode by the Cou-

lomb force, the dielectrophoresis force keeps most of the particles between the parallel screen electrodes (Figure 5.18 (a), 2.5 s). The second reason why the sampling of large particles is difficult is simply because large particles easily jam the screen electrodes. Figure 5.18 (b) shows that small particles 1 mm in diameter smoothly pass through the screen electrodes and numerous particles are transported upward. On the other hand, particles 5 mm in diameter collide with the upper electrodes (Figure 5.18 (a), 0.5 s). Furthermore, the particles between the parallel electrodes obstruct other particles from passing through the upper electrodes (Figure 5.18 (a), 2.5 s). The pitch of the screen electrodes should be larger than the size of the target particle when sampling large particles.

Figure 5.19 (a) shows the calculated amounts of collected large particles with respect to the gravitational acceleration, while Figure 5.19 (b) shows the results with respect to the frequency in a 0.01-G environment. As Figure 5.19 (a) shows, the success of sampling depends on the gravitational acceleration. Although the amounts of collected particles are saturated at a gravitational acceleration less than 0.0001-G for particles 1–4 mm in diameter, the amounts decrease as the gravitational acceleration increases higher than 0.0001-G. Because the gravitational force prevents particles from moving, few particles are collected at 0.01-G as shown in Figure 5.19 (b). Particles 5 mm in diameter could not be collected at 0.01-G, and particles 1–5 mm in diameter could not be collected at 0.1-G or higher. The amount of collected particles 5 mm in diameter increases as the gravitational acceleration decreases below 0.0001-G, and the amount becomes saturated at less than 0.000001-G. The calculated results indicate that the sampling of particles is easier at low levels of gravitational acceleration. It is expected that the sampling of particles ranging from 1 mm to less than 5 mm in diameter will be successful in a low-gravity environment that is less than 0.001-G.

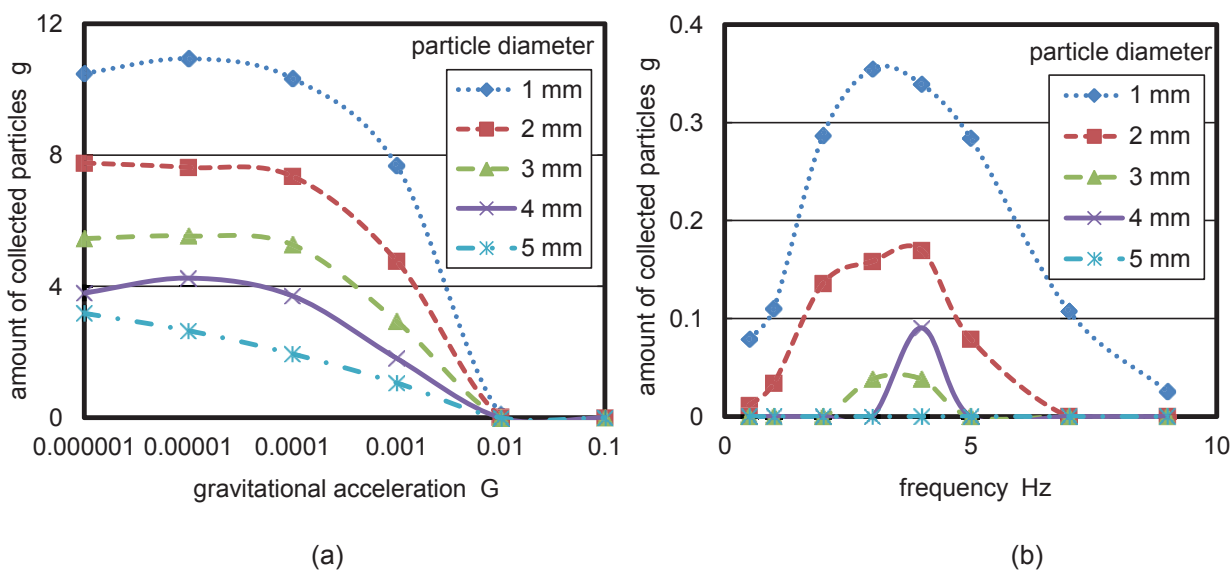


Figure 5.19 Calculated amounts of collected particles (a) against gravitational acceleration under the application of 10 kV_{p-p} at 1 Hz in air, and (b) against frequency of applied voltage under the application of 10 kV_{p-p} in air at 0.01-G gravity.

The sampling experiments were performed in a low-gravity environment, which was reproduced by the parabolic flight of an aircraft for approximately 20 s. Figure 5.20 shows the fluctuation in gravitational acceleration during the parabolic flight, and the average gravitational acceleration for each experimental condition of large particle sampling. The parabolic flight was conducted in such a manner so as to maintain a gravitational acceleration higher than 0-G, and in fact it was maintained at approximately 0.01-G. The average gravitational acceleration was greater at a frequency of 3 Hz than at other frequencies.

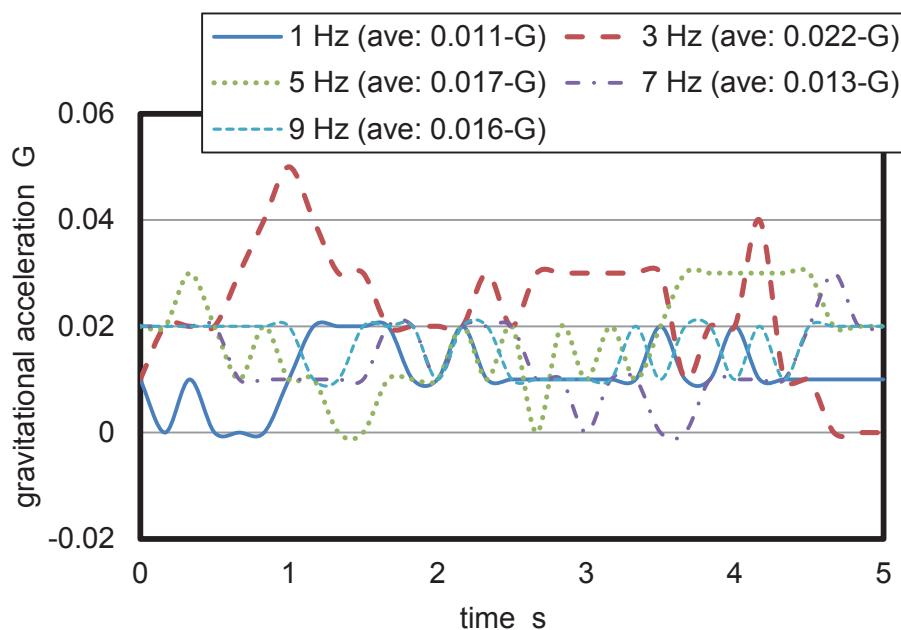


Figure 5.20 Fluctuation of gravitational acceleration during parabolic flight of aircraft in each experiment when frequency of applied voltage is varied.

Figure 5.21 shows the observed behaviors of glass beads, and Figure 5.22 shows the calculated results for the 2 mm particles. These observations were made when the alternating voltage of 10 kV_{p-p} and 1.0 Hz is applied in air at 0.01-G. The particle motions were observed from an angle that differed from the value used in the calculation. Glass beads near the lower electrodes were agitated, and some passed through the openings of the electrodes (Figure 5.21, 0.25 s). The particles reached the collection capsule, as predicted by the numerical calculation, as shown in Figure 5.22.

The results of the experiment and the calculation indicated that some particles adhered to the surface of the electrode (Figures 5.21 and 5.25, 1.0 s). The reason for this is that a large dielectrophoresis force attracts particles to the electrode. Figure 5.23 (a) shows the calculated and measured amounts of collected particles. At a frequency of 5 Hz, glass beads of 0.18 g were successfully sampled, as shown in Figure 5.23 (b). The measured value agreed quantitatively with the calculated results. As shown in Figure 5.20, at a frequency of 3 Hz, the amount of collected particles was smaller because the average gravitational acceleration was higher than that under other conditions, and this worsened the performance.

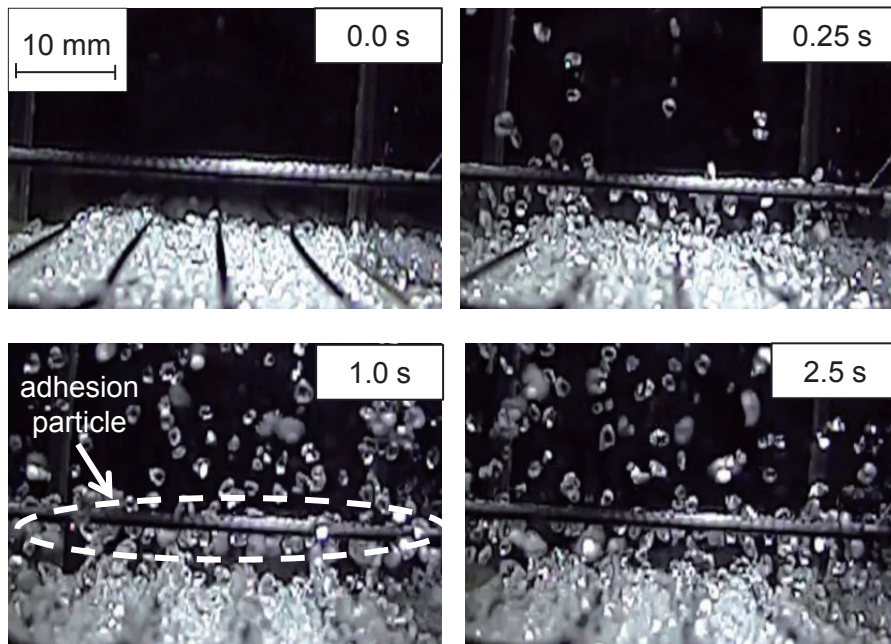


Figure 5.21 Observed motions of glass beads 2 mm in diameter when alternating voltage of 10 kV_{p-p} and 1 Hz is applied in air at 0.01-G gravity.

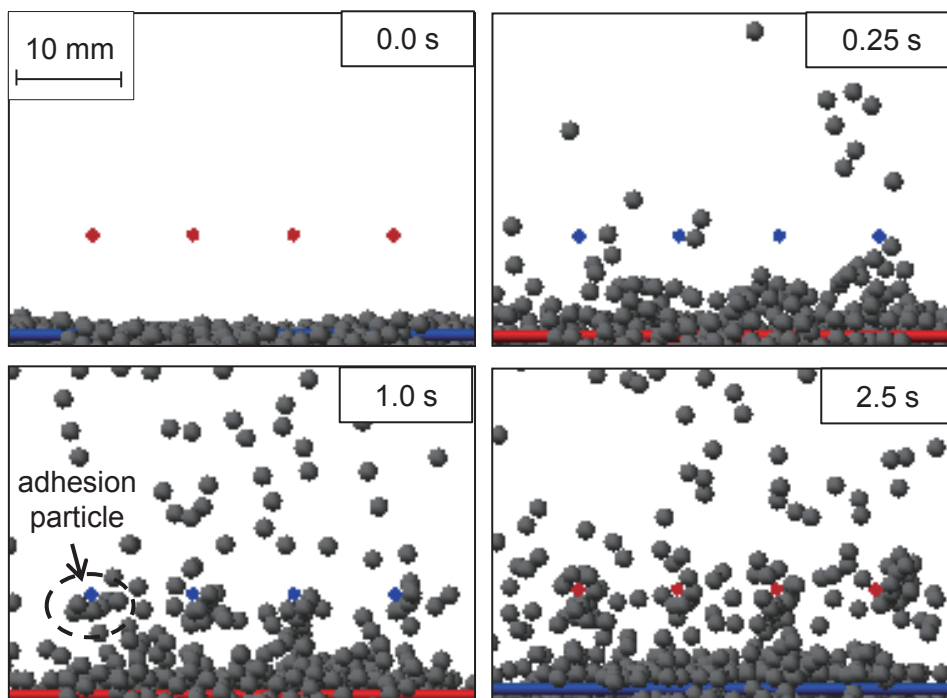


Figure 5.22 Calculated motions of particles 2 mm in diameter when alternating voltage of 10 kV_{p-p} and 1 Hz is applied in air at 0.01-G gravity.

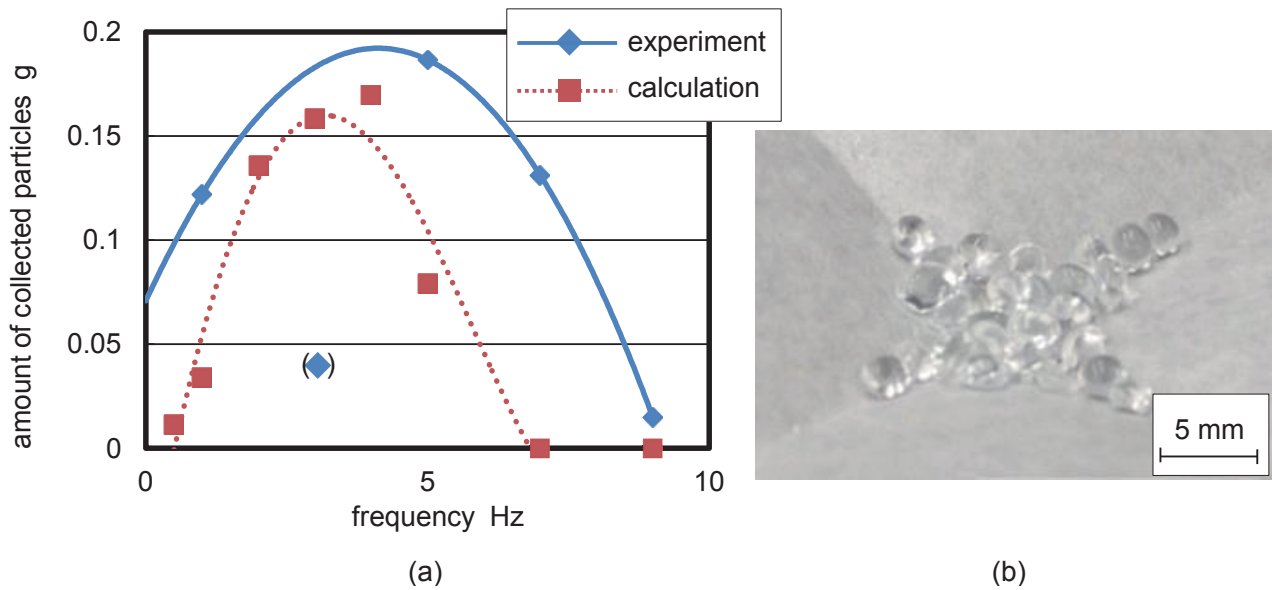


Figure 5.23 (a) Calculated and measured amounts of collected glass bead when alternating voltage of 10 kV_{p-p} and 1 Hz is applied in air at 0.01-G gravity, and (b) collected glass beads with mass of 0.18 g.

Figures 5.24 and 5.25 show the observed motions of rocks and the calculated motions of particles 4 mm in diameter under the application of 10 kV_{p-p} at 1.0 Hz in air at 0.01-G, respectively. Although the rocks were agitated and some passed through the openings of the electrodes (Figure 5.24, 0.25 s), the particles could not reach the collection capsule and fell down immediately because of the relatively large gravitational force acting on the large particles (Figure 5.24, 1.0 s). These results were consistent with the numerical calculation, as shown in Figure 5.25. As predicted, particles larger than 3 mm in diameter could be sampled in a low-gravity environment of less than 0.001-G, as shown in Figure 5.19 (a). The results of the experiment and the calculation show that some particles would adhere to the electrode because of the dielectrophoresis force. In the experiment, particles gathered between the parallel electrodes, forming a bridge from the lower electrode to the upper electrode. After the bridge was created, the particles could not move and disintegrated.

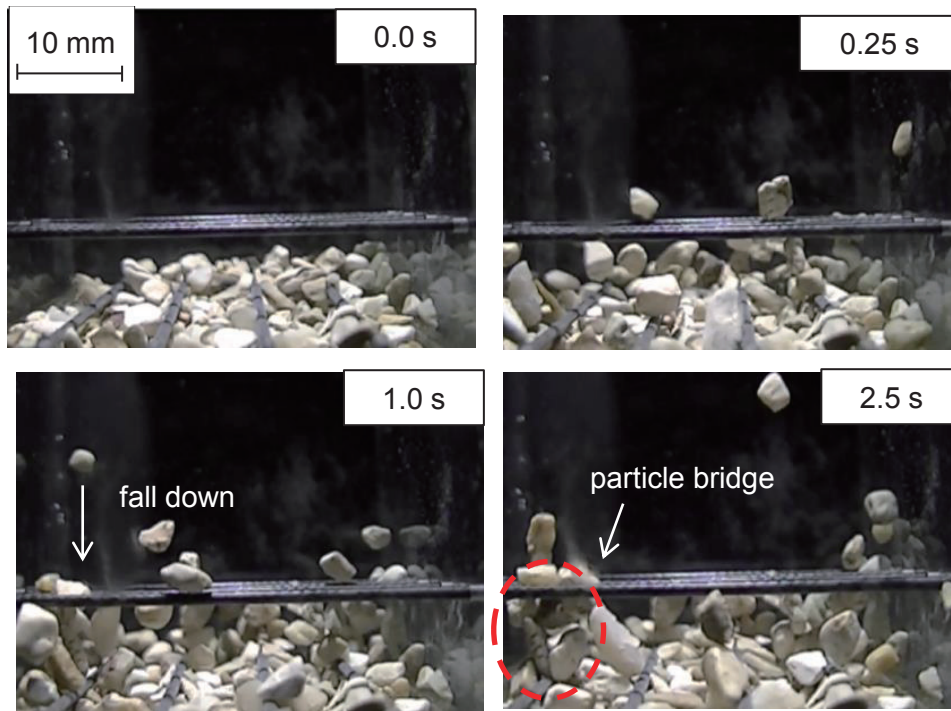


Figure 5.24 Observed motions of rocks 4 mm in diameter under application of $10 \text{ kV}_{\text{p-p}}$ at 1 Hz in air at 0.01-G.

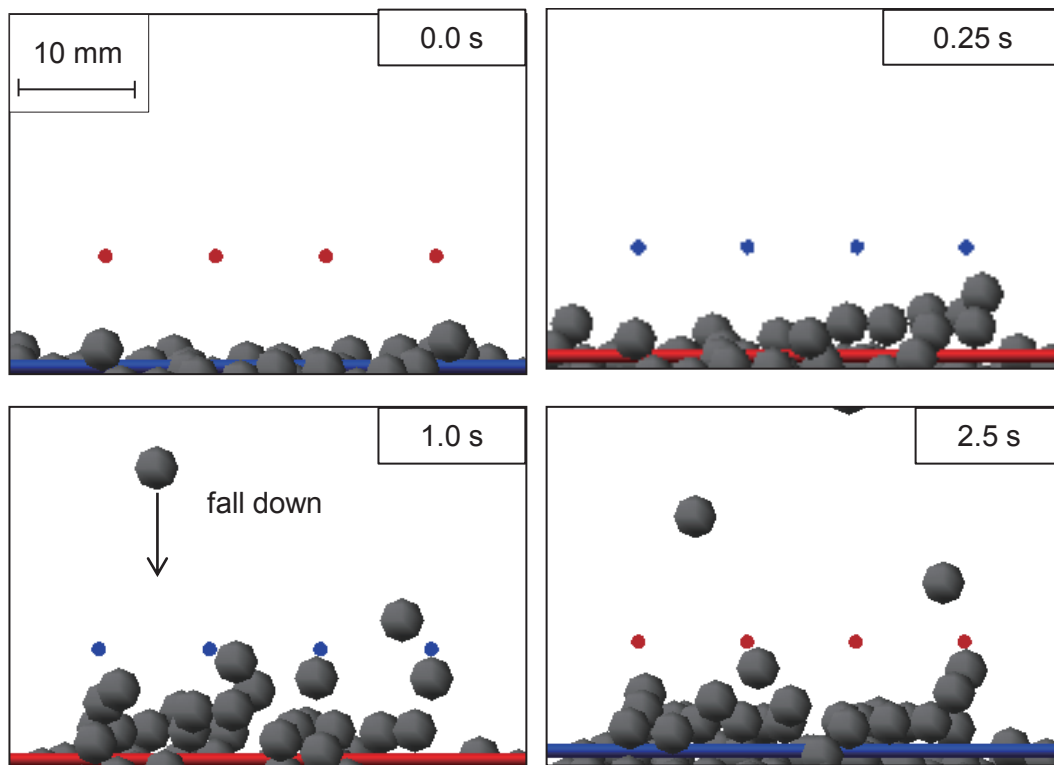


Figure 5.25 Calculated motions of particles 4 mm in diameter under application of $10 \text{ kV}_{\text{p-p}}$ at 1 Hz in air at 0.01-G gravity.

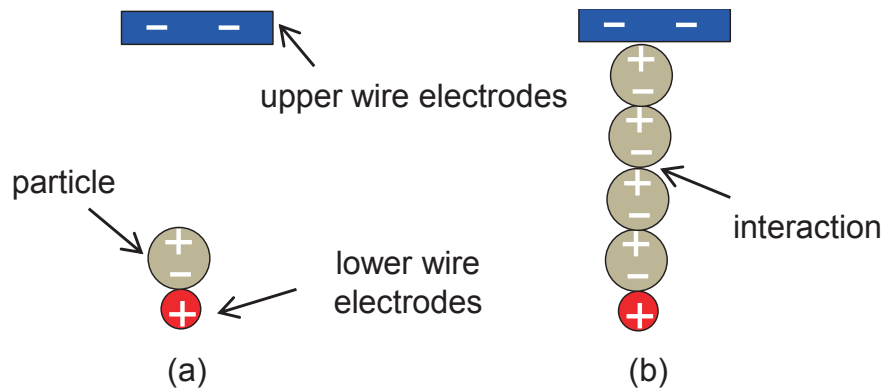


Figure 5.26 Mechanism of (a) particle adhering to electrode and (b) interaction of particles caused by the dielectrophoresis force.

The particles formed the bridge because the interactions among them were affected by a polarization force. Figure 5.26 shows the assumed mechanism for the creation of the particle bridge. If a single particle exists between parallel electrodes and is close to the lower electrode which has a positive voltage applied, the particle is polarized, and an attractive polarization force is generated between the negatively charged particles and the positively charged electrode (Figure 5.26 (a)). When one particle is near the lower electrode and another is near the upper one, both particles are polarized, and the charges of the reversed polarity create an attractive force between the particles (Figure 5.26 (b)). The simple model calculation was performed to confirm the effect of the electrical interaction. When five particles are between the parallel plate electrodes and high voltage is applied to the electrodes, as shown in Figure 5.27, a uniform electrostatic field was created and it induces an electric dipole moment in the particles. In this model, the energy of the electric dipole moment U_{ele} can be calculated using Equation (2.86). The energy U_{ele} can be calculated by solving Equations (2.12), (2.82) and (2.84), and by substituting the calculated electrostatic field \mathbf{E}^* and the electrostatic dipole moment \mathbf{p}_{ele} into Equation (2.86). The energies are calculated in three types of particle positions, such as vertical, skew, and horizontal arrangements.

Figure 5.28 (a) shows the electric energy of each particle. The energies of particles lined in vertical line are the smallest. Figure 5.28 (b) shows the schematic dipole moments created in particles. The particles tend to be stabilized in the case of vertical, skew, and horizontal arrangements, in that order, and the particle chain was created in the low-G environment. The creation of a particle bridge was experimentally observed for rocks as well as for glass beads. Although the particle bridges obstructed the sampling, some particles that were not part of the bridges were collected.

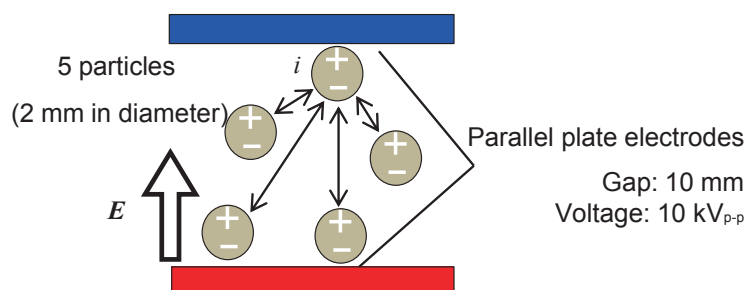


Figure 5.27 Model for calculating the electrostatic interaction between particles.

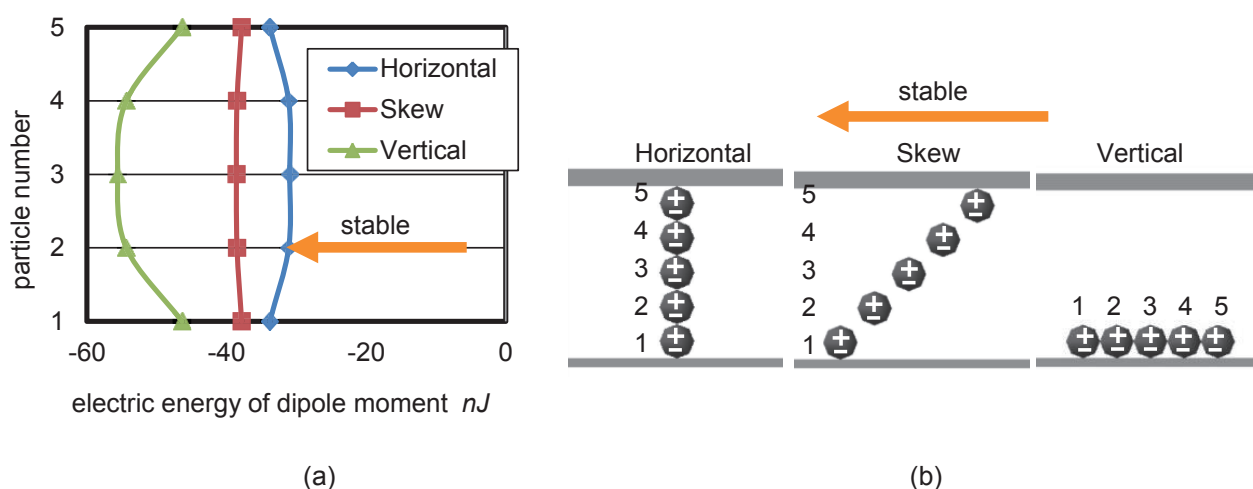


Figure 5.28 (a) Calculated energies of electrostatic dipole moments created in particles, and (b) schematic dipole moment created in particles for each particle line.

5.8 Summary

An electrostatic sampler was developed for reliable sampling of the regolith on an asteroid. The sampler employs Coulomb and dielectrophoresis forces to capture regolith particles and transport them to a collection capsule. The performance in space environments was evaluated by model experiments and numerical calculations. The achieved insights are shown below.

1. The Coulomb force and dielectrophoresis force generated by the sampler captured the lunar regolith particles, and the sampler can transport the particles to a collection capsule in 0.01-G environment. The sampler succeeded in capturing a substantial amount (~ 900 mg) of lunar regolith simulant containing small particles as well as particles larger than 0.5 mm in diameter.
2. The dynamics of particles with conductivity exceeding $1.0 \times 10^{-8} \Omega^{-1} \text{m}^{-1}$ were significantly affected by the dielectrophoresis force. On the other hand, the effect of the dielectrophoresis force can be neglected for particles with conductivities smaller than $1.0 \times 10^{-10} \Omega^{-1} \text{m}^{-1}$.

3. The sampler could successfully collect glass beads 2 mm in diameter at 0.01-G and rocks 5 mm in diameter at a gravitational acceleration below 0.001-G.
4. The calculation results agreed fairly well with the model experiments in the low-gravity environment. The calculation results show that the sampler performance can be improved by applying a higher voltage under lower gravitational acceleration. It is expected that the sampler will work satisfactorily in asteroid environments where high voltage can be applied and gravitational acceleration is extremely small.
5. In low gravity, although the electrostatic force created a particle bridge between parallel electrodes owing to the electric dipole moment of particles, the sampling of other particles were successful.

Based on these results, it is expected that electrostatic sampling from asteroids can be utilized in future sample return missions.

Chapter 6 Sampling of Regolith on the Moon, Mars, and Asteroids Utilizing Magnetic Force

6.1 Introduction

As described in sections 1.1.2 and 2.6.2, the magnetic force can be used to handle magnetic particles in space environments. The existence of magnetic particles on the Moon, Mars, and asteroids was confirmed in previous studies [1-3]. As for the utilization of the magnetic force, the magnetic sampler is developed to collect magnetic particles on the Moon, Mars, and asteroids. The sampler utilizes a magnetic coil gun mechanism [4-6]. It does not have mechanical parts, has a very simple design, and does not need complicated controls, thus making it reliable for space application. In previous studies, the possibility of sampling particles using the magnetic coil gun in space as well as on the Earth has not been sufficiently investigated. In this research, particle motion under the operation of the magnetic sampler was predicted first by using a simple model calculation to establish a basis for the development of the sampler. Consequently, a demonstration of particle sampling was performed on the Earth, and then the basic characteristic of the sampler was established. In addition, the sampling of particles in a vacuum was also experimentally conducted in order to evaluate performance in space. Using the modified hard sphere model of the DEM, the numerical calculation was performed to analyze particle motion, and the sampler performances in a vacuum and in a low-gravity environment was predicted by numerical calculations. Part of this work was published in literature [7].

6.2 System Configuration

Figure 6.1 shows the operation of the magnetic sampler [7], while Figure 6.2 shows a photograph of the magnetic sampler and the design of the electrical circuit. When an electric current is supplied to a solenoid coil (wire turn: 1,000) that is wound around an acrylic tube (inner diameter: 20 mm, outer diameter: 30 mm, length: 50 mm) as shown in Figure 6.2 (a), the resultant magnetic field acts on particles near the lower end of the coil. The particles are magnetically polarized and attracted to the inside of the coil because the magnetic field strength increases toward the center of the coil. The magnetic force acts as an attractive force, pulling the particles to the center (Figure 6.1 (b)). Although the floating particles passed through the center owing to their own inertial force, the particles are pulled back to the center (Figure 6.1 (c)) and vibrate up and down in the coil (Figure 6.1 (c) and (d)), if the current is not terminated. If the electric current is turned off immediately after the particles are attracted by the magnetic force, the particles are transported upward owing to their own inertia force, and sampling is achieved (Figure 6.1 (e)). As shown in Figure 6.2 (b), when DC voltage is applied to the coil, a MOSFET is turned on for a short time (controlled by a microcomputer) and pulse current is supplied to the coil. If the MOSFET is turned on and off repeatedly, plural pulses of the magnetic field are created. As shown in Figure 6.2, the time duration in which the MOSFET is activated is defined as the applied time, and the deactivation time between each pulse is defined as dead time. As pre-

dicted in section 2.6.2, the demonstration of sampling the lunar regolith simulant in the Earth environment is inconvenient, because the simulant has the small relative magnetic permeability and the large magneto-motive force is required to move the particles in 1-G environment. Therefore, soft magnetic particles (average diameter: $35\ \mu\text{m}$, specific gravity: $3500\ \text{kg/m}^3$, relative magnetic permeability: 4.0) were used to conveniently investigate the performance of the magnetic sampler, as shown in Figure 6.3.

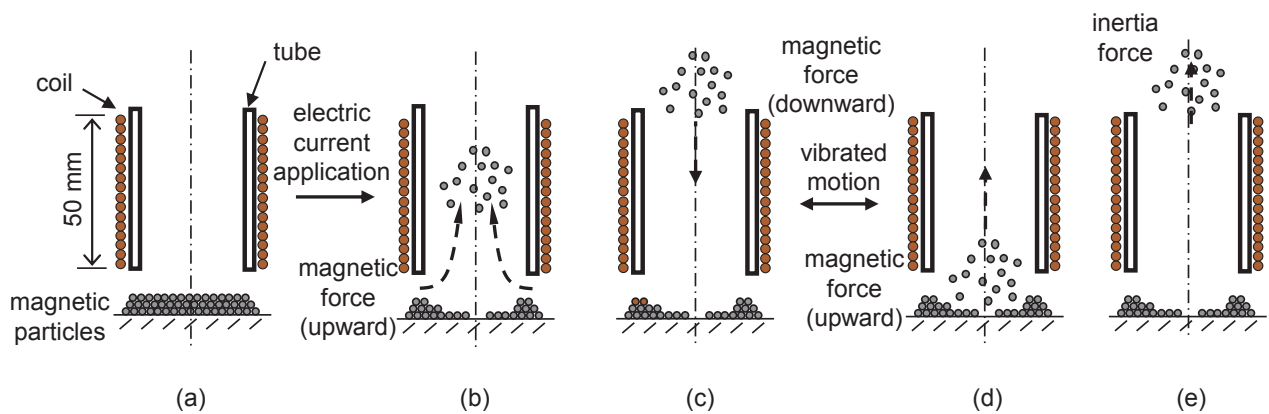


Figure 6.1 Sampling procedure using magnetic sampler: (a) initial condition, (b) capturing, (c) (d) vibrating, and (e) ejecting of particles.

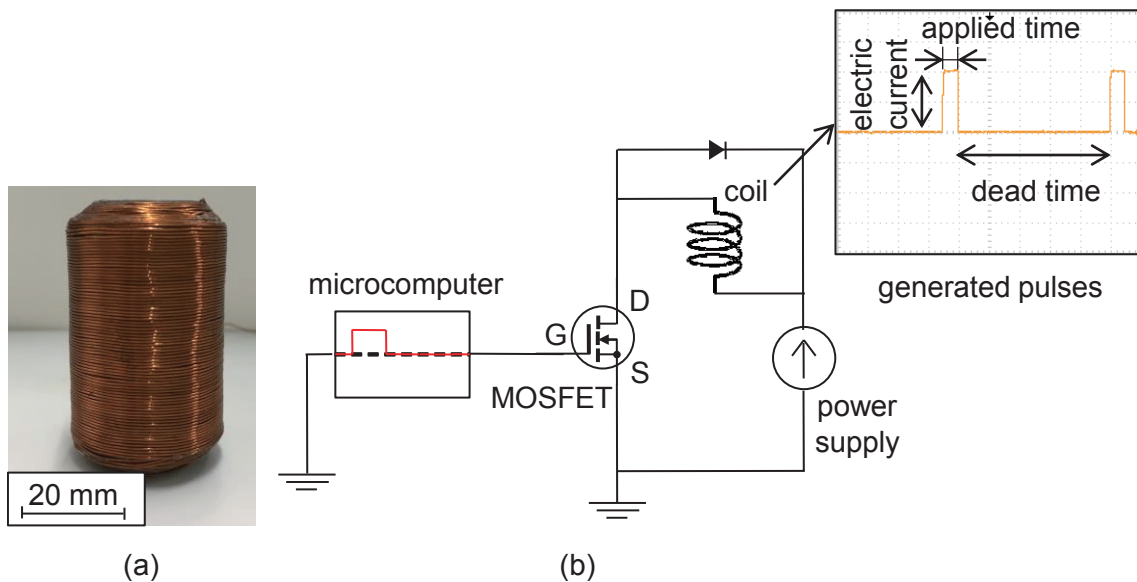


Figure 6.2 (a) Photograph of magnetic sampler and (b) electrical circuit to generate pulse current.

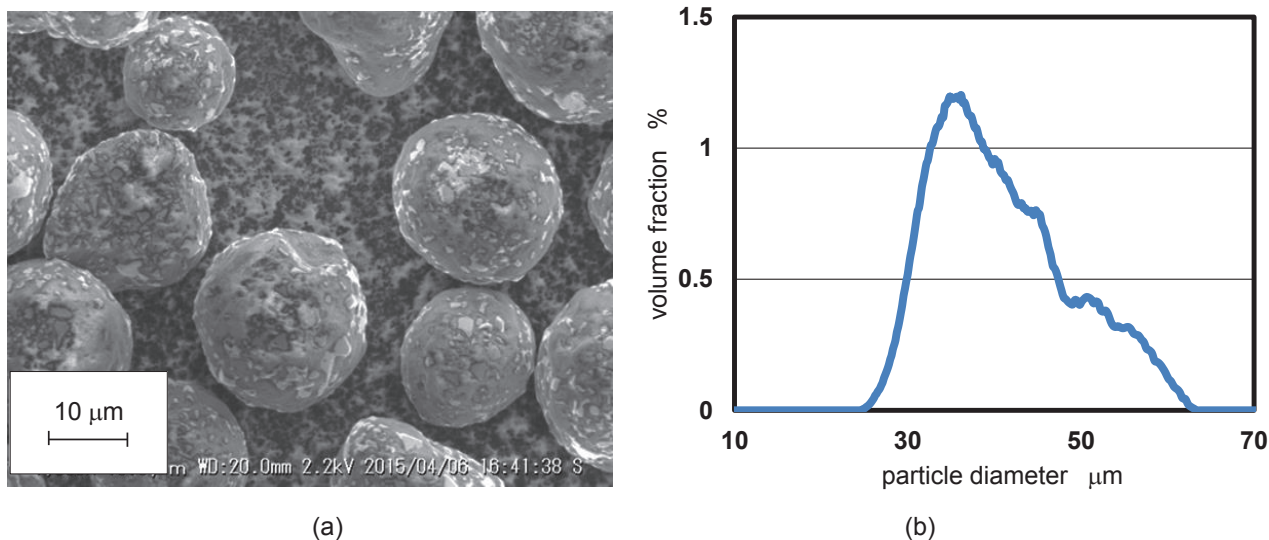


Figure 6.3 (a) SEM photograph of magnetic particles and (b) their size distribution.

6.3 Calculation of Particle Motion in Simple Model

6.3.1 Calculation Methodology

The motion of a single particle (diameter: 35 μm , relative permeability: 4.0), which is affected by one pulse of the magnetic field was analyzed to determine the basic characteristics of particle dynamics in the magnetic field. The calculation procedure is similar to the DEM shown in section 2.7. The motion equation (2.1) of the magnetic particle, which is affected by the magnetic force, gravitational force, adhesion force, and air drag, was calculated using the Runge–Kutta method. As Equation (2.1) is calculated only along a right angle to the horizontal in a short time step, the single-axis trajectory of the particle can be followed. The time step for the Runge–Kutta calculation was to be 1.0×10^{-5} s, and the initial position of particle was assumed to be at the inlet of the coil. The initial velocity and acceleration were assumed to be zero. The air drag equation (2.37) was calculated using the drag coefficient C_D , which is determined by Reynolds number of the moving particle. In the vacuum environment, the air drag was neglected. The calculation method of the magnetic flux density B using the finite difference method was described in section 2.4.2. The electric current density, which is obtained by dividing the electric current by the cross-sectional area, was set at the position of the wire electrode. The calculated magnetic flux density B on the central axis of the coil was used for the calculations.

6.3.2 Calculated Motion of Single Particle

Figure 6.4 (a), (b), (c), and (d) shows the calculated particle trajectories in air at 1-G, in air at 0.00001-G, in a vacuum at 1-G, and in a vacuum at 0.00001-G. The gravitational acceleration of 0.00001-G is similar to that of the Itokawa asteroid. The magneto-motive force of 5,000 AT was fixed in all conditions. The AT is a

product of an ampere applied to a coil and wire turns, and is unit of magneto-motive force. The applied time was varied as the calculation parameter. As shown in Figure 6.4 (a) and (b), the altitude of the floating particle increases with the applied time in 1-G at 0.00001-G, and the floating particle reaches the position near 0.025 mm, which is the center of the coil, and maintains its position in the condition of the long applied time. After the magnetic field is turned off, the particle falls down at constant speed in 1-G; however, the particle does not fall down in 0.00001-G owing to the extremely small gravitational force. The reason why the particle maintains its position at the center of the coil is because of the relatively large air drag that disturbs the movement of the small particle. In both 1-G and 0.00001-G, the particle cannot reach the outlet of the coil, and a successful sampling of the small particle would be difficult in air. The reduction of gravity would not contribute to better performance of the sampler. If the effect of air drag is eliminated in the vacuum, the particle moves more dynamically than that in air, as shown in Figure 6.4 (a) and (c). In the vacuum, the altitude of the floating particle also increases with the applied time, and the particle reaches the outlet of the coil over 20 ms of applied time. When the applied time is much longer than 50 ms, the pull-back magnetic force is applied to the particle and it cannot pass through the coil. In the condition of over 1,000 ms applied time, the particle vibrates in the coil continuously. In the preferable condition with approximately 20–30 ms of applied time, the particle passes through the coil and the sampling would be successful. In the vacuum at 0.00001-G environments as shown in Figure 6.4 (d), the particle that passed through the coil is transported upward for a long time owing to its own inertial force and negligible air drag. Thus, the vacuum environment substantially affects sampling performance, and the application of the optimum applied time is important for a successful sampling.

Figure 6.5 (a) and (b) show the calculated particle trajectories in air and in a vacuum, respectively, when the magneto-motive force is varied. As shown in Figure 6.5 (a), the large magneto-motive force makes the particle altitude higher and the peak time for the highest altitude shorter, simply because the large magnetic force affects the particle movement. In air, the floating particle cannot get to the outlet of the coil in the all conditions under 10,000 AT. On the other hand, in a vacuum, the floating particle passes through the coil in the 4,000-5,000 AT, as shown in Figure 6.5 (b). In conditions of large magneto-motive forces over 5,000 AT, the particle is pulled back to the coil and the sampling is not successful. The interaction of the magneto-motive force and the applied time determines the particle movement, and the operation of the sampler under the optimal condition appropriate for the environment is necessary.

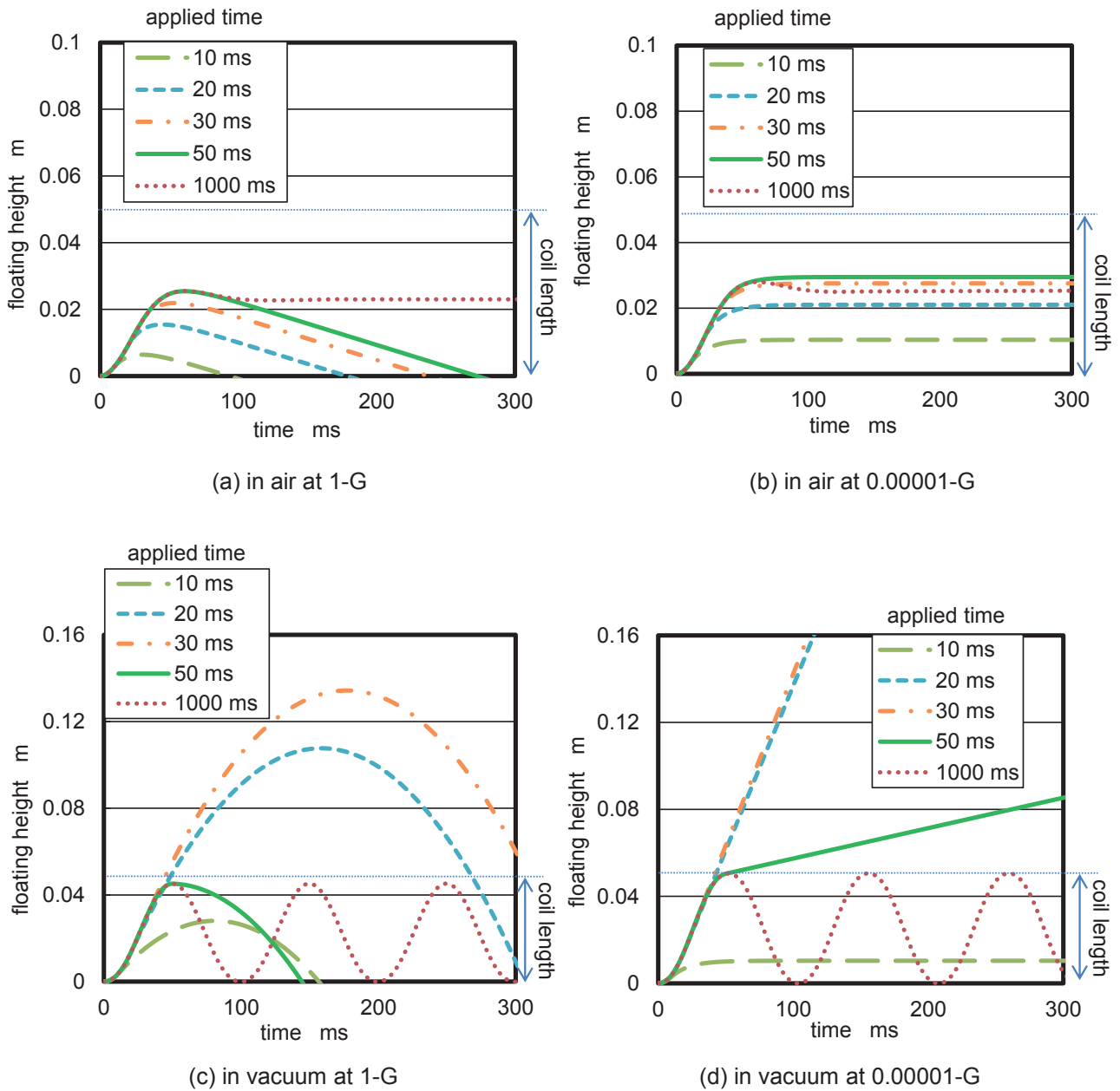


Figure 6.4 Calculated trajectories of a single particle affected by the magnetic sampler (a) in air at 1-G, (b) in air at 0.00001-G, (c) in vacuum at 1-G, and (d) in vacuum at 0.00001-G (magneto-motive force: 5,000 AT, applied time is calculation parameter). 1-G is equal to 9.8 m/s^2 .

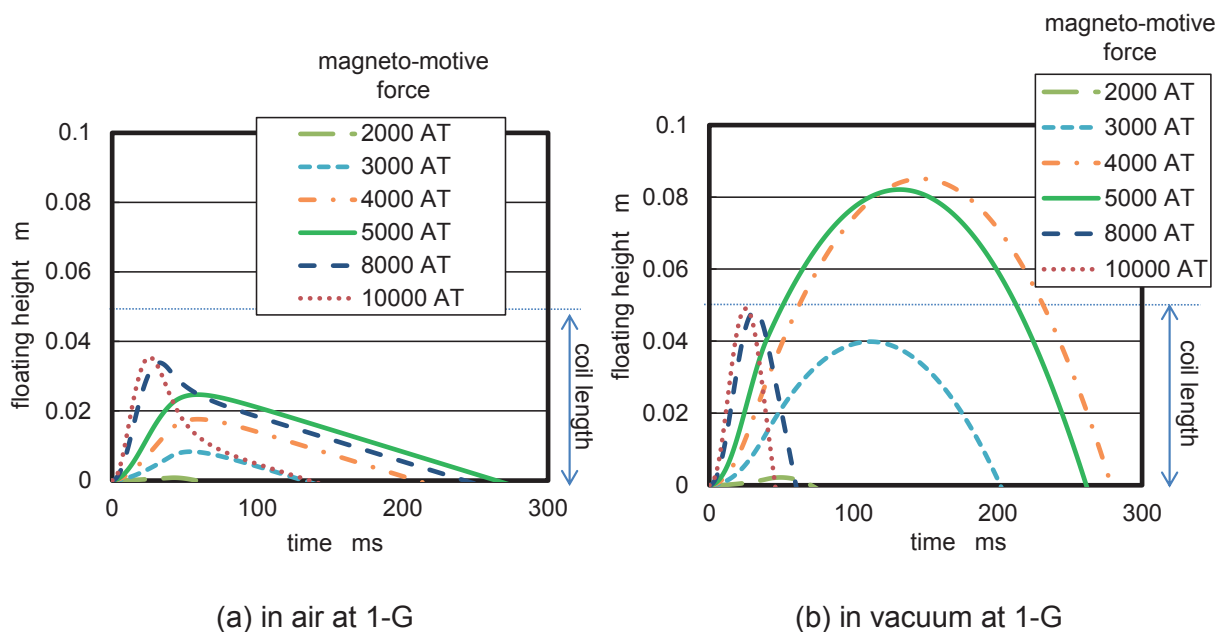


Figure 6.5 Calculated trajectories of a single particle affected by the magnetic sampler (a) in air at 1-G and (b) in vacuum at 1-G (magneto-motive force is calculation parameter, applied time: 40 ms).

6.4 Experimental Procedure

The actual particle dynamics are different from the simple calculation described in the preceding section. This is because the mechanical and magnetic interactions between particles complicate the motions of the particles. Both experiments and numerical calculations were conducted in the Earth environment to determine the actual performance of the sampler. In addition, experiments were also conducted in a vacuum, below 1.5×10^{-2} Pa, created in the vacuum chamber of the JAXA Chofu Aerospace Center, as described in section 4.5. Figure 6.6 shows the experimental setup for the sampling of particles. The sampler was inclined by several tens of degrees with respect to the horizontal because the particles that were agitated by the magnetic sampler at right angles to the horizontal fell down immediately, and performance could not be measured in the 1-G environment. The inlet of the sampler was set near the surface of the soft magnetic particles. When the sampler was turned on, the resultant magnetic force agitated the particles, and some of those that passed through the coil were collected in the sampling boxes ($150 \times 150 \times 50$ mm³), which were arranged in the horizontal direction away from the sampler. The weights of the collected particles in each sampling box were measured to evaluate the sampler performance. The pulse of the magneto-motive force was applied ten times in the experiments. The actual experimental setup in the vacuum chamber is shown in Figure 6.7.

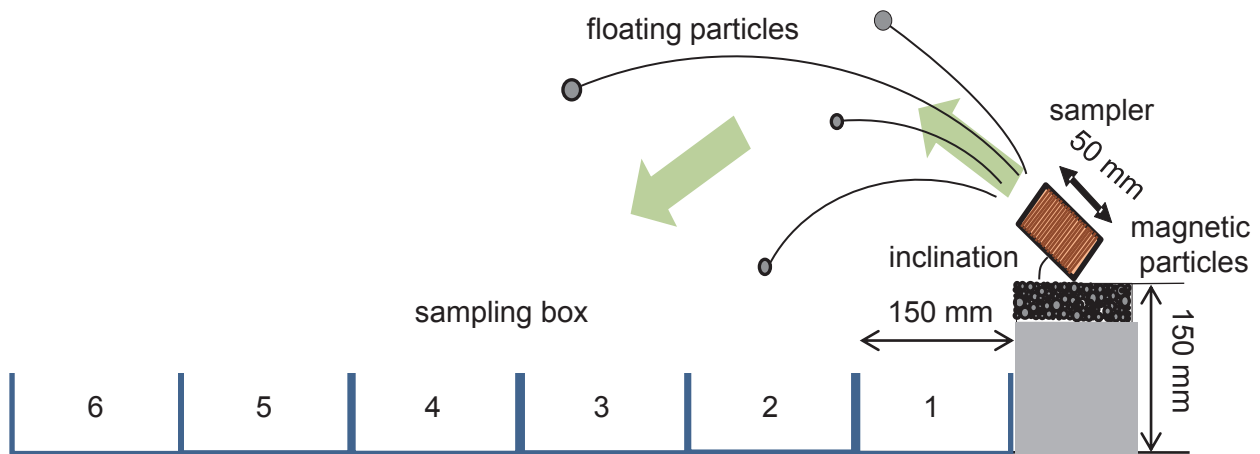


Figure 6.6 Diagram of the experimental setup used for particle sampling.

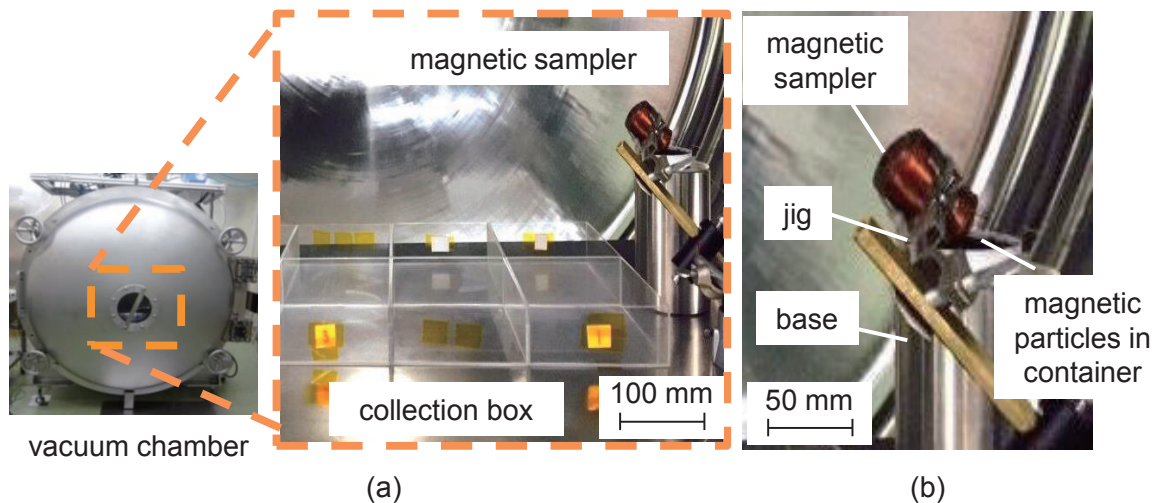


Figure 6.7 Photographs of (a) the experimental setup in the vacuum chamber and (b) magnetic sampler.

6.5 Numerical Calculation

The basic procedure for the numerical calculation was described in section 2.7. It is similar to the method described in section 6.3. Some specific conditions of the calculations are explained in this section. For the external forces acting on particles, the magnetic force, gravitational force, adhesion force, and air drag were considered, and the forces are represented by Equations (2.17), (2.30), (2.31), and (2.37), respectively. The torque acting on the particles was assumed to be zero. In a vacuum environment, air drag was neglected. The magnetic flux density field \mathbf{B} was calculated in a two-dimensional system, as shown in section 6.3. The coefficient of adhesion force α for magnetic particles was assumed to be 0.00027 similar to that of the lunar regolith simulant FJS-1. The effect of magnetic interaction between particles was considered using the method described in section 2.7.6. The calculation area of the DEM was set to be $0.8 \times 0.2 \text{ m}^2$, and the length of the

z -direction was assumed to be infinite. Then, magnetic particles of 5,000 were randomly placed beneath the inlet of the sampler, representing the scale at which in the experiment was reproduced. To reduce the calculation load, it was assumed that the particles move as an agglomerate because they adhere to each other mechanically and magnetically; thus, a particle size of 175 μm , which is five times that of the 35 μm particle, was used for the calculations. Moreover, only one pulse of the magneto-motive force was applied in the calculations. The time step for the Runge–Kutta calculation was set to be 1.0×10^{-5} s, and particle motions were followed for 1 s. At the end of the calculations, the particles that reach each sampling box were assumed to be collected in that box.

6.6 Results and Discussions

6.6.1 Basic Characteristic of Magnetic Sampler

Figure 6.8 (a) and (b) show the experimentally collected particles in air at 1-G as the inclination of the magnetic sampler and the distance between the sampler and particle surface were varied, respectively. As shown in Figure 6.8 (a), the total weight of the collected particles in all of the collection boxes increased with the inclination, because the area of the magnetic field affecting the particle motion was large in the case of large inclination. The magnetic field near the inlet of the magnetic sampler was strong, and the large area acted on the particles in the case of the large inclination. Similarly, the magnetic field became weaker as the distance from the coil and the amount of collected particles decreased as the distance between the sampler and particle surface increased, as shown in Figure 6.8 (b). Although it is preferable that the sampler touches the particle surface and faces the inlet side, the sampler could collect particles that do not touch the sampler and do not face the inlet side. This means that the sampler could work even if the spacecraft is equipped with a sampler that cannot control its own position and the sampler cannot be set precisely at a sampling position. In addition, in terms of the floating distance, the sampler inclined at 45° could collect large amount of particles to faraway collection boxes. In later experiments and calculations, the inclination and the distance were fixed at 45° and 0 mm, respectively, for convenience.

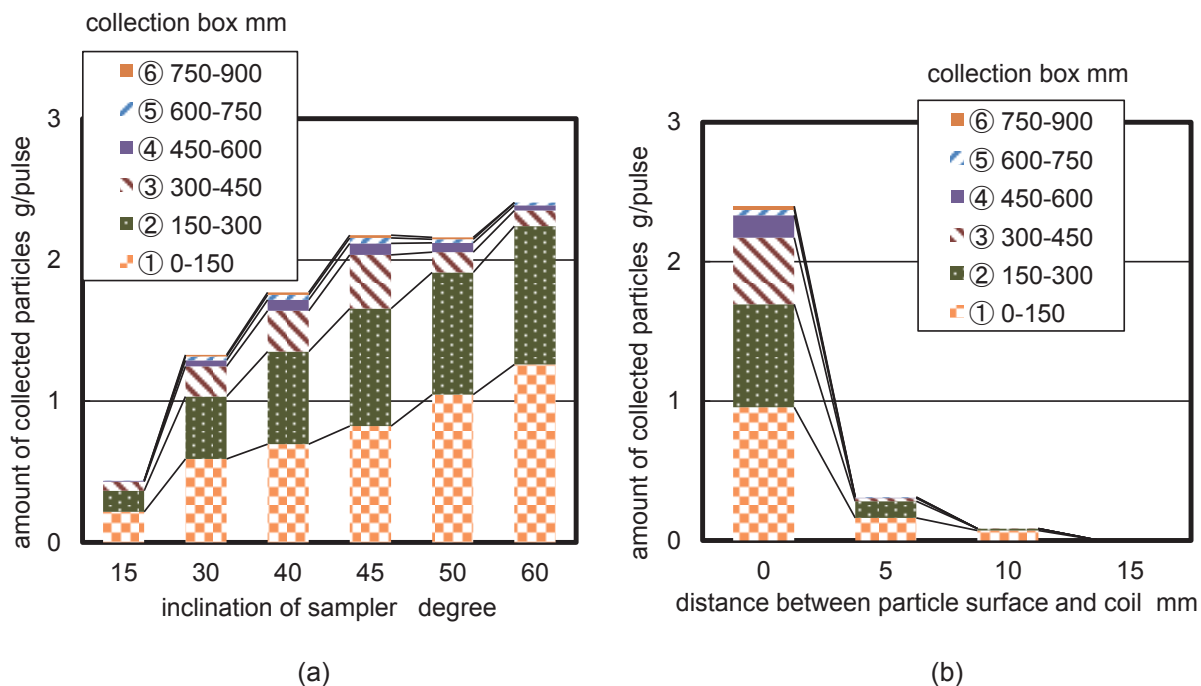


Figure 6.8 Amount of collected particles in each collection box in a 1-G gravity environment in air when (a) inclination of magnetic sampler and (b) distance between particle surface and sampler are varied (applied time: 40 ms, dead time: 500 ms, magneto-motive force: 5,000 AT; (a) distance between sampler and particle surface: 0 mm, (b) inclination of sampler: 45°). 1-G is equal to 9.8 m/s².

Although the analysis of single particle dynamics indicates that the sampling of a single particle is impossible on the Earth owing to air drag, as described in section 6.3. Figure 6.8 (a) and (b) show that the sampling of plural magnetic particles was successful. Figure 6.9 (a) and (b) show the observed motions of small and large amounts of particles (small: 0.01 g, large: 100 g), respectively, at 40 ms after initiating application of constant magneto-motive force. The inclination of the sampler was set to be 90°, and the distance between the sampler and particle surface was set to be 15 mm to make the observation easy. Figure 6.9 (b) shows that a large amount of particles formed their agglutinate and chain, and they floated along the magnetic flux line. As shown in Figure 6.10, the agglutinate and chain formations were caused by the magnetic dipole moment, similar to the effect of the electric dipole moment as explained in section 5.6.2. The inertia of the agglutinated particles is larger than that of a single particle, and the effect of air drag on the particles is comparably smaller. Thus, the agglutinated particles reached higher positions than that of the small amount of particles, as shown in Figure 6.9 (a). The interaction of magnetic particles enhanced the sampling, resulting in improvement of the sampler performance. Figure 6.11 shows the calculated motions of particles in air at 1-G; it also shows that the particles interact with each other. Although the motion analysis of the single 35 μm particle indicates that the sampling is impossible, the calculated result shows that the sampling of plural particles is successful. This is because the calculation considered the interaction of magnetic particles, and treated the aggregated 35 μm particles as a single 175 μm particle.

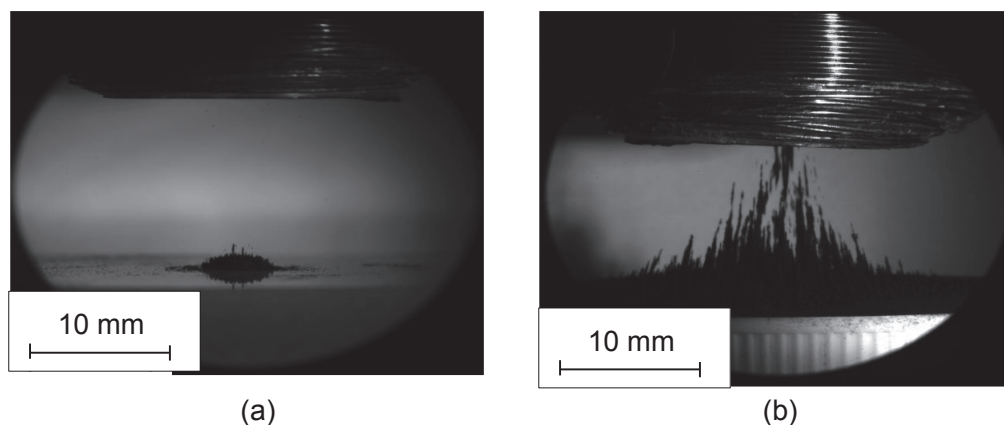


Figure 6.9 Observed magnetic particles after applying 5,000 AT of constant magneto-motive force to the coil in a 1-G gravity environment in air (setting particles (a) 0.01 g, (b) 100 g).

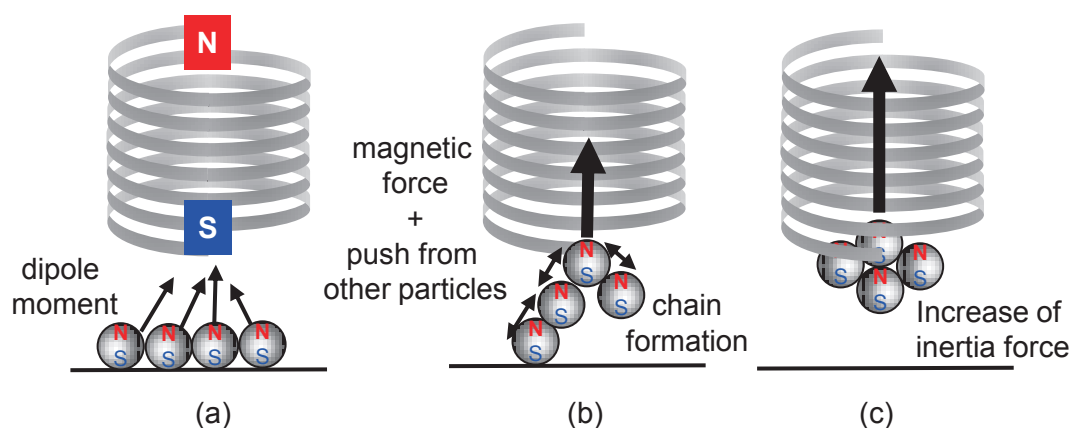


Figure 6.10 Diagram of the interaction of magnetic dipole moments between particles.

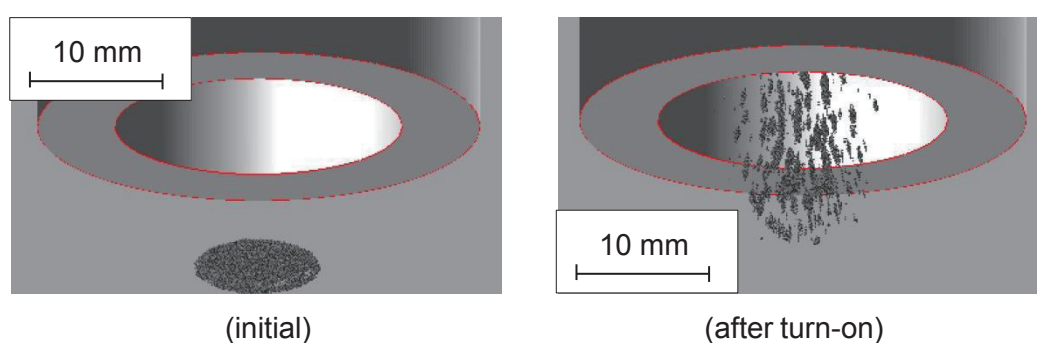


Figure 6.11 Calculated motions of particles in a 1-G gravity environment in air (applied time: 40 ms, magneto-motive force: 5,000 AT, inclination: 45°).

Figure 6.12 shows the experimentally collected particles in air at 1-G when the dead time of applied magneto-motive force was varied. As shown in Figure 6.12, the amount of collected particles increased with the dead time for times below 500 ms because the interaction of particles agitated by different pulses of

magneto-motive force disturbed the particle motion. For instance, when the particles are agitated by the first pulse of magneto-motive force, some particles are ejected from the outlet of the coil while others are pulled back inside the coil. In this case, the particles agitated by the second pulse collide with the particles that are pulled back, thus, the sampling was disturbed. The amounts of collected particles were saturated in cases with a dead time of over 500 ms because the particle interaction was negligible. The dead time should be longer than 500 ms to achieve a large amount of collection. The dead time was fixed as 500 ms in later experiments.

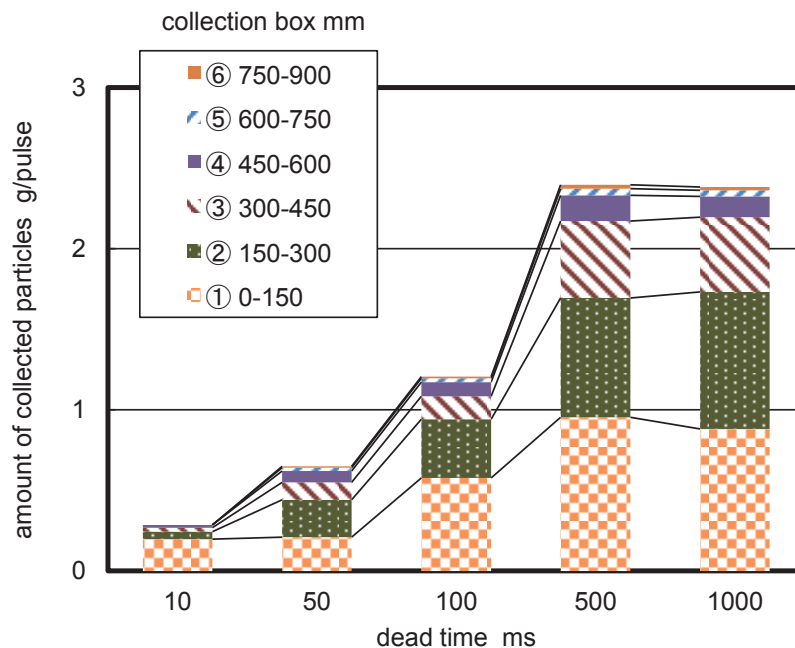


Figure 6.12 Amount of collected particles in each collection box in a 1-G gravity environment in air versus dead time (applied time: 40 ms, magneto-motive force: 5,000 AT).

6.6.2 Sampler Performance in Vacuum Environment

Figure 6.13 (a) and (b) show the experimental results of the amount of collected particles versus the magneto-motive force in air and in a vacuum, respectively. Figure 6.14 (a) and (b) show the calculated results in the same conditions as the experiments. Figures 6.13 and 6.14 show that the samplings of particles were successful in conditions over 2,000–3,000 AT in air and in a vacuum. In addition, the amount of collected particles increases when the magneto-motive force is less than 5,000 AT, simply because a strong magnetic field is created when high magneto-motive force is applied. When the magneto-motive force is over 6,000 AT, the amount of collected particles decreases with the increase in the magneto-motive force, as shown in Figure 6.14 (a) and (b). This is because the peak time for the optimal applied time would be shorter than 40 ms in case of a large magneto-motive force. The trends closely agreed with the single particle analysis described in section 6.3. Regarding the effect of air drag, because the particles move faster in a vacuum than in air, the performance was improved in a vacuum, as shown in Figures 6.13 (b) and 6.14 (b). In addition, the captured particles floated off to the far-off collection box in the vacuum.

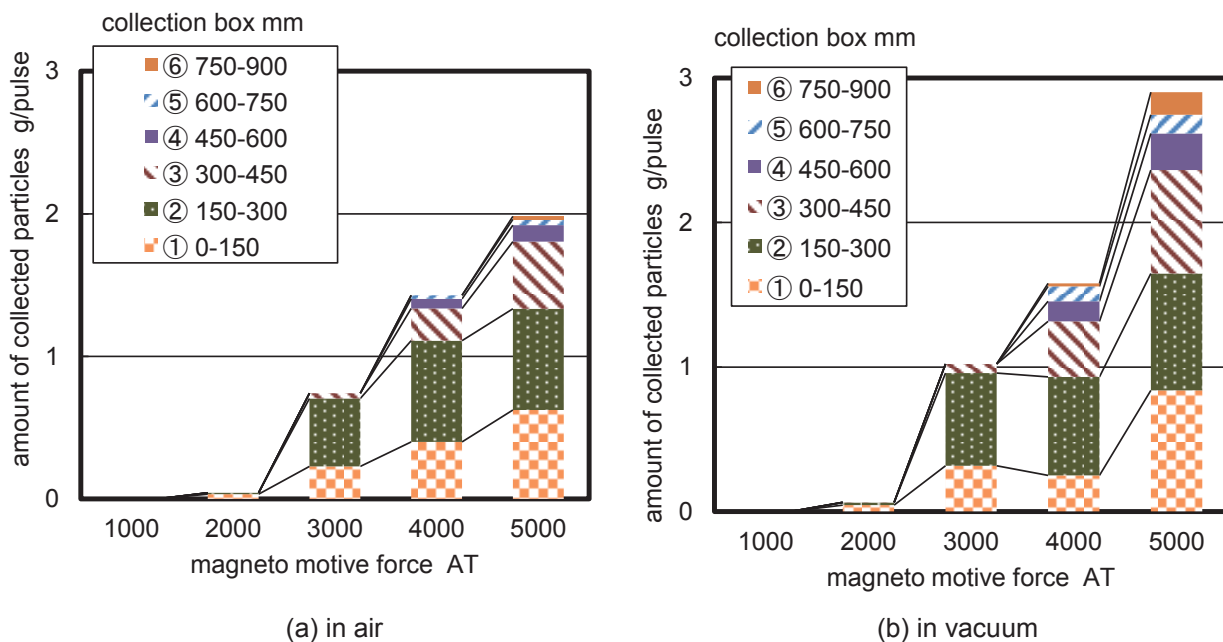


Figure 6.13 Amount of collected particles in each collection box (a) in air at 1-G gravity and (b) in vacuum at 1-G versus magneto-motive force (applied time: 40 ms, dead time: 500 ms).

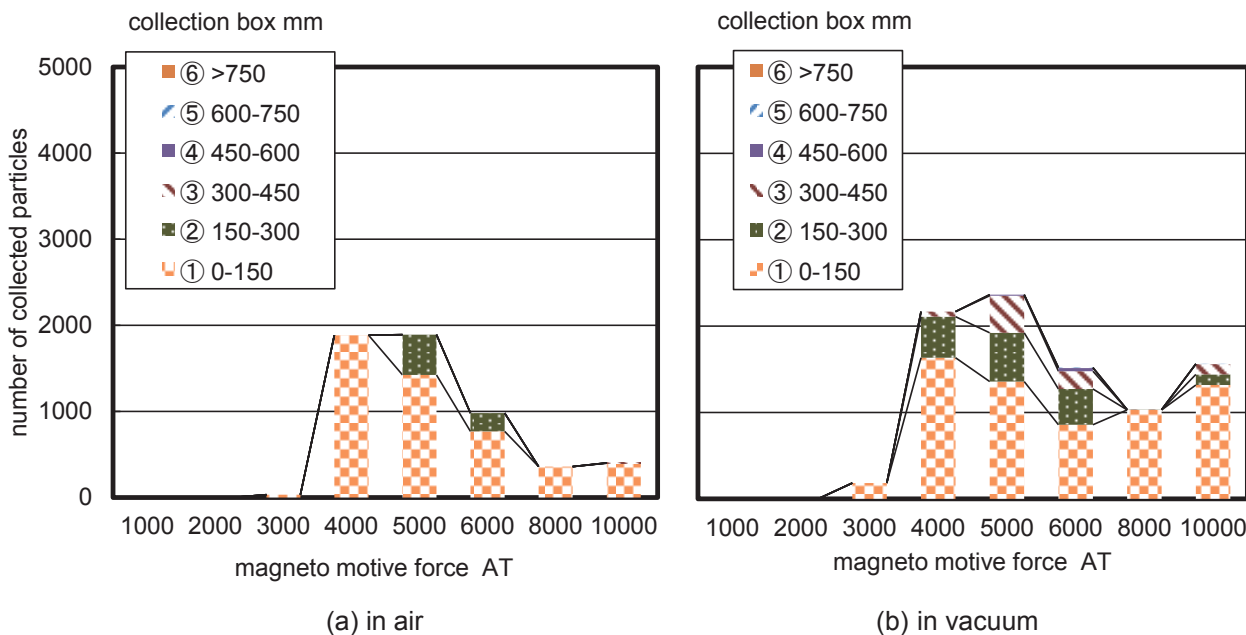


Figure 6.14 Calculated numbers of collected particles in each collection box (a) in air at 1-G gravity and (b) in a vacuum at 1-G versus magneto-motive force (applied time: 40 ms, dead time: 500 ms).

Figure 6.15 (a) and (b) show the experimental results of the amount of collected particles versus the applied time of the magneto-motive force in air and in a vacuum, respectively, while Figure 6.16 (a) and (b) show the calculated results in the same conditions as the experiments. Figures 6.15 and 6.16 show that there was an optimal applied time appropriate for the magneto-motive force of 5,000 AT in air and in a vacuum.

This tendency agreed closely with the results of the single particle analysis. Although the peak time of the applied time in a vacuum was similar to that in air, the sampler performance was improved in a vacuum owing to the absence of air drag as shown in Figure 6.15 (b) and 6.16 (b), and the captured particles floated to the faraway collection box in vacuum. Although the results of the numerical calculation qualitatively agree with the experimental results, the results are quantitatively different because only a small amount of particles were calculated, in order to reduce the calculation load. The numerical calculation method can be used to qualitatively predict the sampler performance in the space environment.

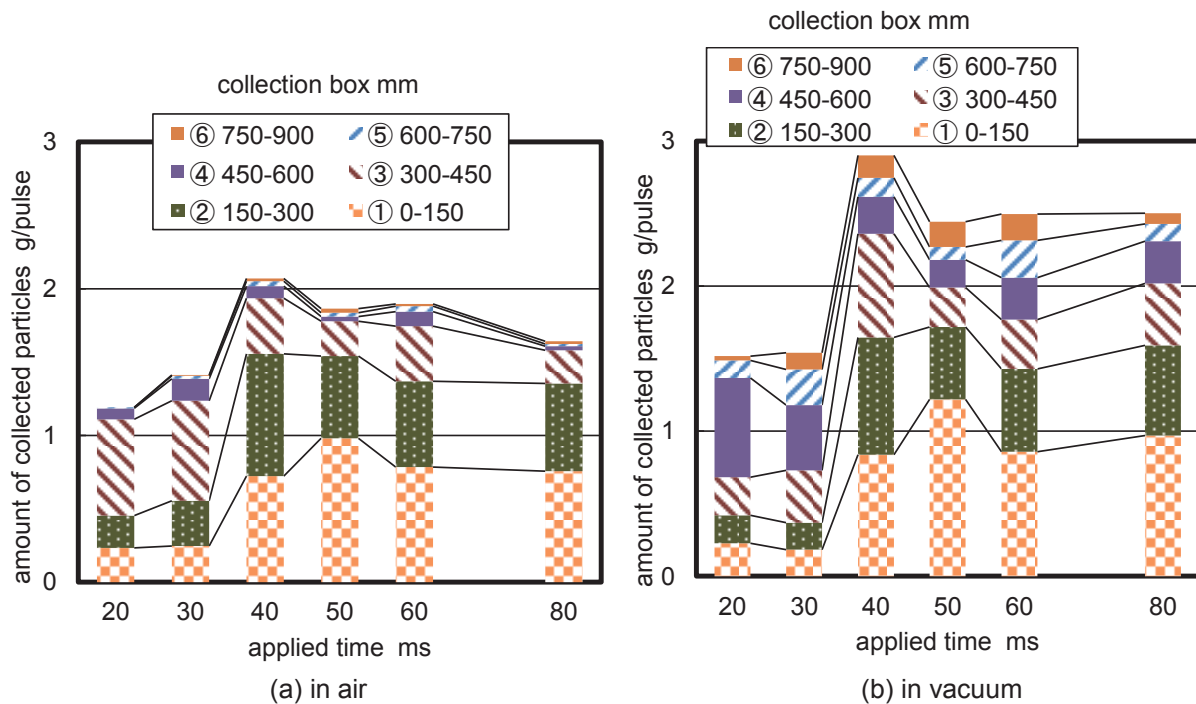


Figure 6.15 Amount of collected particles in each collection box (a) in air at 1-G gravity and (b) in vacuum at 1-G versus applied time (dead time: 500 ms, magneto-motive force: 5,000 AT).

6.6.3 Sampler Performance in Low-Gravity Environment

The performance of the sampler in a micro-G environment was predicted using numerical calculations. Figure 6.17 (a) and (b) show the calculated numbers of collected particles in air at 0.00001-G, and in a vacuum at 0.00001-G, respectively. Although the single particle analysis indicates that micro-gravity would not significantly affect the sampler performance, the calculated numbers of collected particles is much larger in micro-G as shown in Figure 6.17 (a), than that in 1-G, as shown in Figure 6.16 (a). It is assumed that the mechanical and magnetic interaction of particles affects the particle dynamics. In a vacuum at 0.00001-G, the sampler performance is improved further, and large amounts of particles are transported to the collection box farthest from the sampler, as shown in Figure 6.17 (b). Thus, the magnetic sampler is compatible with a vacuum and in low-gravity environments.

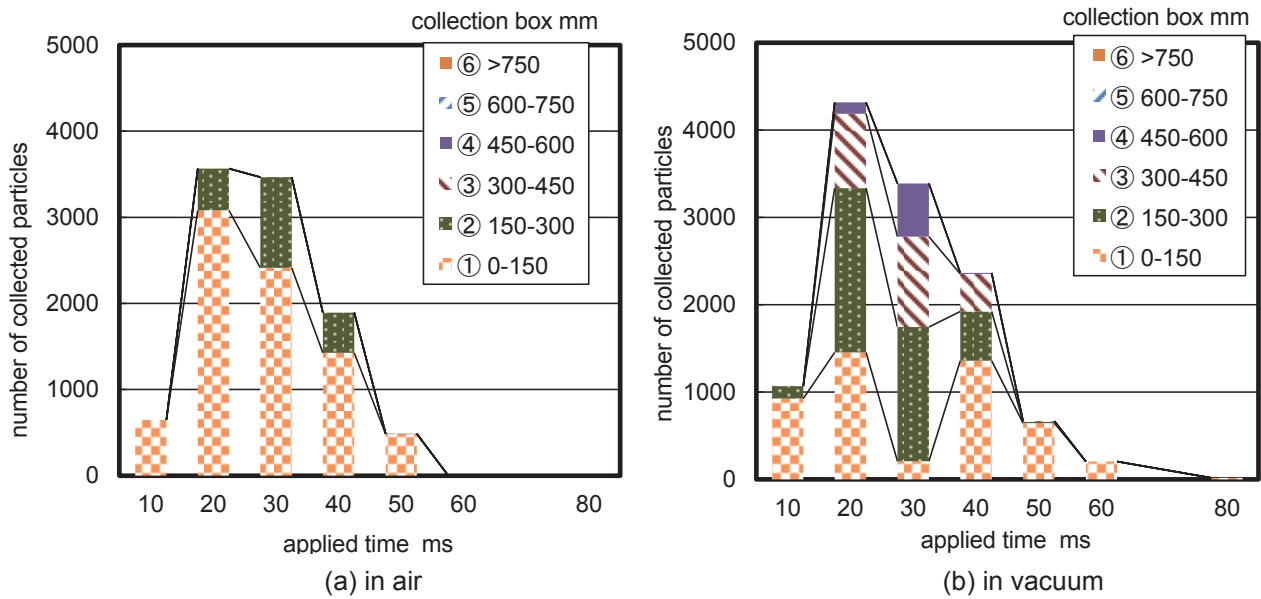


Figure 6.16 Calculated number of collected particles in each collection box (a) in air at 1-G gravity and (b) in vacuum at 1-G versus applied time (dead time: 500 ms, magneto-motive force: 5,000 AT).

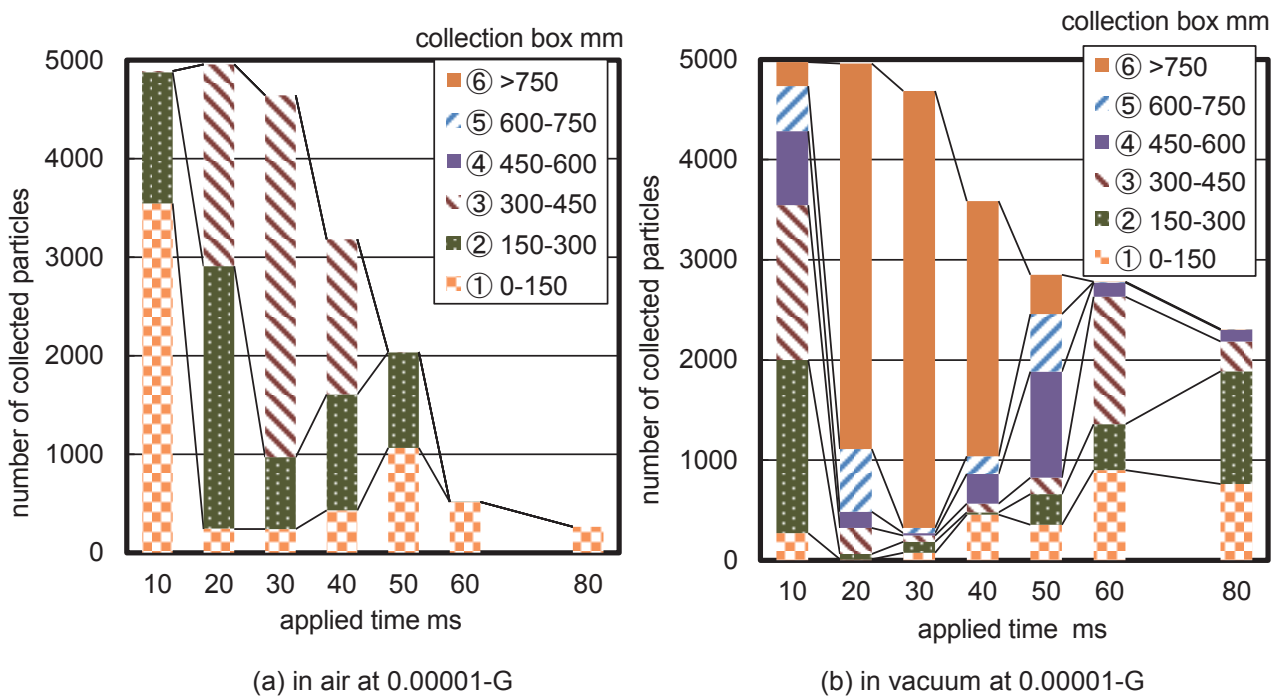


Figure 6.17 Calculated number of collected particles in each collection box (a) in air at 0.00001-G and (b) in vacuum at 0.00001-G when applied time is varied (dead time: 500 ms, magneto-motive force: 5,000 AT).

6.7 Summary

A magnetic sampling system that utilizes a coil gun mechanism was developed to achieve reliable sampling of regolith in space environments. The basic characteristics of the sampler were determined by conducting simple model calculations and parametric experiments. The sampler performance in air, a vacuum, and a

space environment was evaluated by experiments and numerical calculations. The achieved insights from the experimental and calculation results are shown below.

1. The magneto-motive force and the applied time mutually affect the sampler performance, and determining the optimum combination is critical for successful particle sampling.
2. Although the sampling was successful in the case of using plural pulses of the magneto-motive force, the dead time between each pulse should be longer.
3. The inclination of the sampler and the distance between the sampler and particles should be higher and lower for high sampling performance, respectively. However, the sampling is successful when a small gap exists between the sampler and particles, as well as when the sampler is in a horizontal position.
4. The interaction of magnetic particles with each other created a chain and aggregated, and this phenomenon contributed to the improvement of the sampler performance.
5. The effect of vacuum and low gravity environment on sampler performance was confirmed by conducting experiments in vacuum and numerical calculations. The results indicated that the performance was improved in a vacuum and in low gravity.

The sampling mechanism does not require mechanical parts, is a simple design, and does not require a complicated control scheme; thus the sampler has the potential to achieve efficient and reliable particles sampling for future sample return missions on asteroids.

Chapter 7 Vibration Transport of Regolith and its Application in Combination with Electrostatic and Magnetic Samplers

7.1 Introduction

As described in Chapters 3–6, electrostatic and magnetic forces are expected to be used in space environments. The electrostatic system has some advantages, including low-power consumption, easy control, no mechanical drives, and no contamination of impurities. However, the electrostatic force is small and has limited application, such as the cleaning system of regolith particles, sampling system, and size-sorting systems that do not require movement of large amount of particles. Regarding the magnetic system [1], it can be applied only for magnetic particles. A particle-handling system with high tolerance to the dust contamination on the Moon and Mars has been developed for space exploration missions in which a large amount of particles must be transported regardless of the compositions. This system utilizes a mechanism of vibration transport. When particles come into contact with a mechanical plate vibrated by actuators, the vibrated plate repeatedly pushes and transports the particles in one direction. Although this type of mechanism has been utilized in industries, such as food processing and drug development, because it can carry a large amount of particles, the system has not been sufficiently investigated for space application. In a previous study [2], a spiral elevator using this vibration mechanism was developed by NASA. Although the spiral elevator could feasibly transport the JSC-1A lunar regolith simulant, the system was too massive, and it had to be equipped with shaker motors to generate the vibration. In addition, mechanical malfunctions had to be considered.

In this study, two types of vibration transport systems have been developed for space applications. Both systems are equipped with actuators that have no mechanical drives, but have high tolerance for dust contamination. First, the particle motion under the operation of the vibration transport system was investigated using a simple model calculation. Then, a vibration transport system that utilizes the DEA [3–8] was developed as the vibrator for the system. The DEA is made of a lightweight material, such as an elastomer sheet and stretchable electrodes. The vibration transport system has no mechanical drives, and does not need any complicated control; thus making it highly reliable. The transport system has been developed for transporting large amounts of lunar and Martian regolith particles in a horizontal direction. The other vibration system utilizes the electromagnetic vibrator to sample particles from soils on the Moon and Mars. In the development process, the possibility of utilizing the vibration transport for sampling particles and obliquely transporting the particles to a collection box were confirmed. To extend the applicability of the vibration transport, the combinations using the electrostatic sampler and magnetic sampler were also investigated. Part of this work was published in literatures [9, 10].

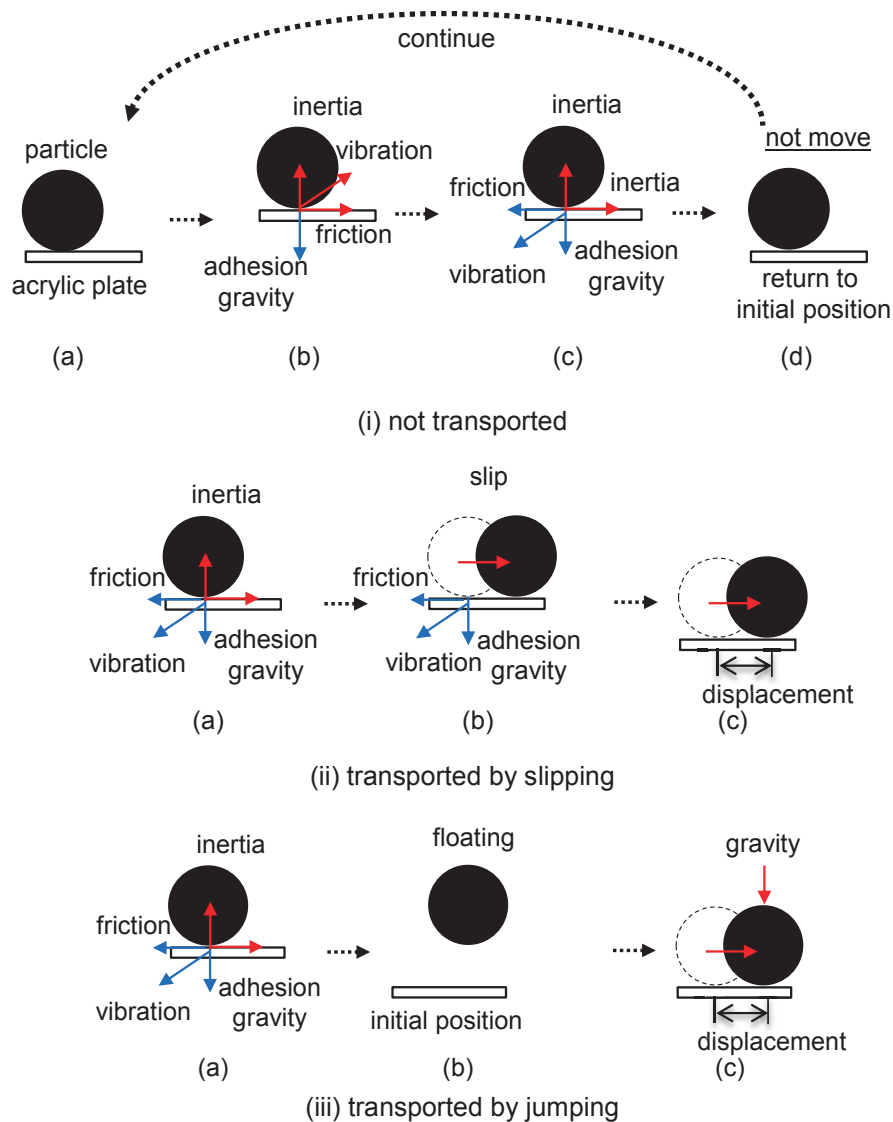


Figure 7.1 Particle motion under vibration transport operation when (i) the particle is not transported, (ii) the particle is transported by slipping on plate and, and (iii) the particle is transported by jumping on plate.

7.2 Calculation of Particle Motion under Operation of Vibration Transport System

7.2.1 Mechanism of Vibration Transport

Figure 7.1 (i) shows a diagram of particle motion on a vibrated plate in the case where a particle was not transported. When the plate moves a small distance in one direction, the particle on the plate simultaneously moves in the same direction, owing to the inertial force and friction force (Figure 7.1 (i) (b)). When the plate starts to return to the normal position (Figure 7.1 (i) (c)), the accelerated particle is pulled back owing to the gravitational force, adhesion force, and friction force. If the inertial force of the particle does not exceed the gravitational force, adhesion force, and friction force, the particle returns to the initial position (Figure 7.1 (i) (d)), which means that the vibration transport failed. In the case when the inertial force in the horizontal direction exceeds the friction force, the particle slips on the plate (Figure 7.1 (ii) (b)) and it moves a small dis-

tance (Figure 7.1 (ii) (c)). If the vibration continues, the small displacement occurs repeatedly. In the case where the inertial force in the vertical direction exceeds the gravitational force and adhesion force, the particle floats in air for a moment (Figure 7.1 (iii) (b)). The particle simply falls below, owing to the gravitational force, and moves at a small distance (Figure 7.1 (iii) (c)). Similar to the slip case, the particle is transported in the horizontal direction as the process is repeated. Although the particle is also transported owing to its own rotation motion on the plate, the lunar and Martian regolith does not rotate easily because of their sharp shape; therefore, slip and floating are the main factors that influence the motions of particles during the process of vibration transport.

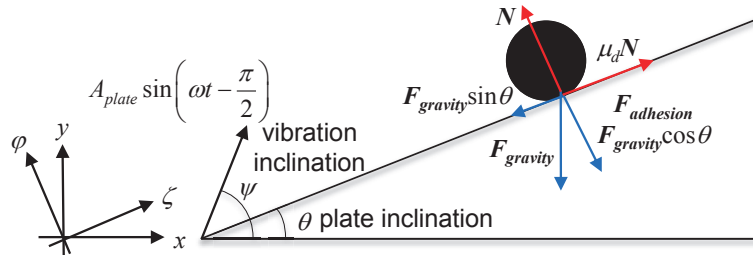


Figure 7.2 Calculation model of particle motion on a vibrating plate.

7.2.2 Calculation Model of Transported Particle

Figure 7.2 shows the calculation model of a particle transported by the vibrating plate that is inclined at an angle of θ and vibrated in the ψ -direction. The motion equation in the ϕ -direction for the particle affected by the gravitational force, adhesion force, and the repulsive force N from the vibrating plate is represented by Equation (7.1).

$$m\ddot{\phi} = -mg \cos \theta - F_{adhesion} + N \quad (7.1)$$

where m , ϕ , g , and θ are the particle mass, particle position, gravitational acceleration, and inclination of the vibrating plate, respectively. The adhesion force is represented by Equation (2.30). The repulsive force N from the vibrating plate in the ϕ -direction is represented by Equation (7.2).

$$N = m\ddot{\phi} + mg \cos \theta + F_{adhesion} \quad (7.2)$$

If the particle does not float above the plate and does not slip on the plate, the particle acceleration is equal to the plate acceleration α_{plate} , which is represented by Equation (7.3).

$$\alpha_{plate} = -A_{plate} \omega^2 \sin\left(\omega t - \frac{\pi}{2}\right) \quad (7.3)$$

where A_{plate} and ω are the amplitude of the vibration and the angular frequency of the plate, respectively. The velocity and position of the particle are calculated from Equation (7.3) when the particle does not float above

the plate and does not slip on the plate. The friction force acting on the particle is represented by Equation (7.4).

$$\mathbf{F}_{friction} = \mu_d m \left(\ddot{\boldsymbol{\varphi}} + \mathbf{g} \cos \theta + \frac{\mathbf{F}_{adhesion}}{m} \right) \quad (7.4)$$

Here, μ_d is the friction coefficient. If the inertial force of the particle is larger than the friction force, as indicated in Equation (7.5), the particle starts to slip on the plate. In this case, the motion equation in the ζ -direction for the particle can be described by Equation (7.6).

$$|\ddot{\zeta}| > \left| \mu_d \left(\ddot{\boldsymbol{\varphi}} + \mathbf{g} \cos \theta + \frac{\mathbf{F}_{adhesion}}{m} \right) \right| \quad (7.5)$$

$$m\ddot{\zeta} = -6\pi\eta R\dot{\zeta} - mg \sin \theta + \mu_d' m \left(\ddot{\boldsymbol{\varphi}} + \mathbf{g} \cos \theta + \frac{\mathbf{F}_{adhesion}}{m} \right) \quad (7.6)$$

Here, ζ , η , R , and μ_d' are the particle position, air viscosity, particle radius, and dynamic coefficient of particle friction, respectively. The particle is affected by air drag, gravitational force, and friction force as represented in the first, second and third term on the right hand side of Equation (7.6), respectively. The direction of the friction force corresponds to the reverse direction of the particle slip. When the plate velocity in the ζ -direction reaches the velocity of the slipped particle, the particle-slip is stopped, and the particle starts to move simultaneously with the plate as represented by Equation (7.3).

If the particle is highly accelerated in the φ -direction, exceeding the gravitational acceleration and adhesion force as shown in Equation (7.7), the particle starts to float.

$$\ddot{\boldsymbol{\varphi}} < -\mathbf{g} \cos \theta - \frac{\mathbf{F}_{adhesion}}{m} \quad (7.7)$$

The motion equations of the floating particle are represented by Equations (7.8) and (7.9).

$$m\ddot{\zeta} = -6\pi\eta R\dot{\zeta} - mg \sin \theta \quad (7.8)$$

$$m\ddot{\boldsymbol{\varphi}} = -6\pi\eta R\dot{\boldsymbol{\varphi}} - mg \cos \theta \quad (7.9)$$

If the particle touches the vibrated plate as indicated in Equation (7.10), the particle begins to move simultaneously with the plate again, as shown in Equations (7.3) and (7.6).

$$\boldsymbol{\varphi} \leq A_{plate} \omega \left(\sin(\psi - \theta) \sin\left(\omega t - \frac{\pi}{2}\right) + 1 \right) \quad (7.10)$$

The initial velocities and positions of the particle in the ζ - and φ - directions were set to be zero. The particle trajectory was followed by solving the motion equation of the particle using the Runge–Kutta method with a small time step, as the parameters of the particle and vibrating plate were altered. In low gravity and vacuum

environments, the gravitational acceleration g was fixed at 1.6 m/s^2 and the air drag was neglected in vacuum. The particle was assumed to be the lunar regolith, and a specific gravity of $2,700 \text{ kg/m}^3$, a diameter of $100 \text{ }\mu\text{m}$, and a coefficient of adhesion force of 0.00027 were used for the calculation as standard parameters. The static friction coefficient of 0.83 for lunar regolith was obtained from the literature [11], and the dynamic friction coefficient was assumed to be $4/5$ of the static value.

7.2.3 Calculated Particle Motions in Earth and Space Environments

Figure 7.3 shows the trajectories of the particle in the φ -direction and ζ -direction when the vibration acceleration of the plate is varied. Figure 7.4 shows those in the ζ -direction over a long duration. The G_v and G are coefficients for the vibration acceleration and gravitational acceleration, respectively, and $1.0\text{-}G_v$ and $1.0\text{-}G$ are equal to 9.8 m/s^2 . Although the particle does not float above the plate when the vibration acceleration is smaller than $2.0\text{-}G_v$, as shown in Figure 7.3 (a), the particle slips on the plate for a small distance in a single round trip of the plate in case of $1.5\text{-}G_v$ and $2.0\text{-}G_v$, and continuous transport is successful as shown in Figure 7.3 (b). At $1.0\text{-}G_v$, the particle vibrates in the same area repeatedly owing to the static friction. When the vibration acceleration is larger than $3.0\text{-}G_v$, the particle floats and touches down repeatedly, and the particle is transported faster in the case of floating than that of slip, as shown in Figure 7.4. In addition, the transport velocity increases with the vibration acceleration in conditions of that less than $9.0\text{-}G_v$. At $9.0\text{-}G_v$, the particle always touches the plate as the height is approximately 0.5 mm where the plate does not accelerate to maximum; therefore, the particle is not accelerated faster in $9.0\text{-}G_v$ than in $7.0\text{-}G_v$. Although the timing of the contact between the particle and plate is important, the vibration acceleration is the key factor for the success of the vibration transport.

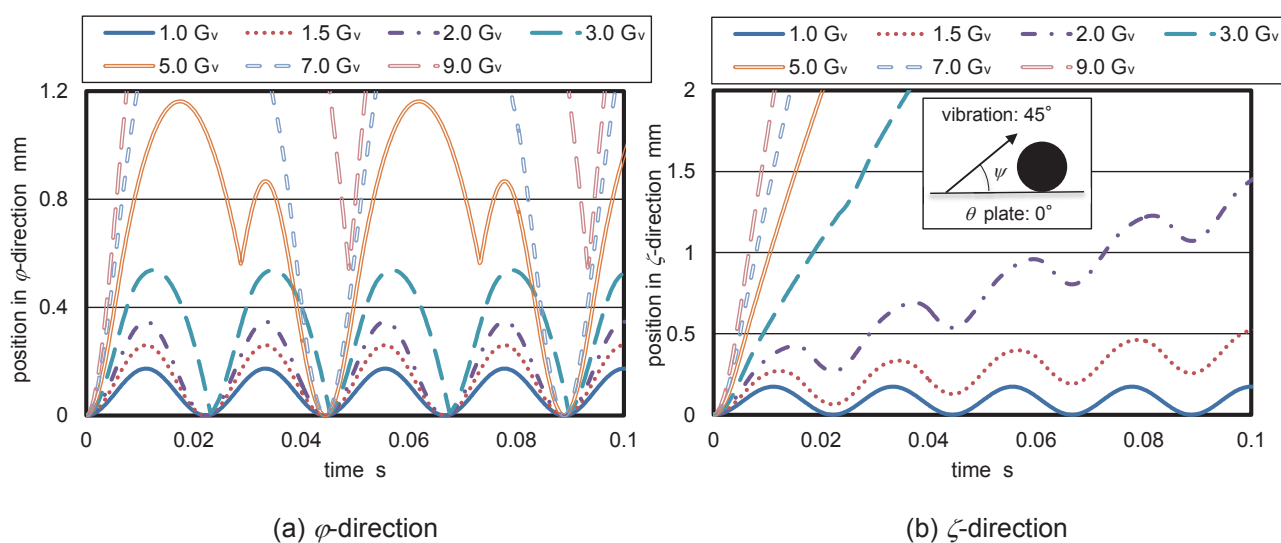


Figure 7.3 Calculated particle motions in (a) φ -direction and (b) ζ -direction during transport when vibration acceleration is varied (vibration frequency: 45 Hz , vibration inclination: 45° , plate inclination: 0° , in air and $1\text{-}G$ gravity environment). $1.0\text{-}G_v$ and $1.0\text{-}G$ are equal to 9.8 m/s^2 .

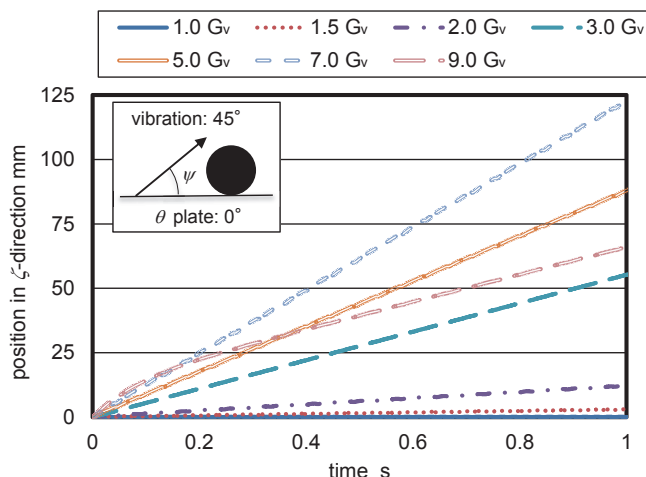


Figure 7.4 Calculated particle motion in ζ -direction during long duration of transport when vibration acceleration is varied (vibration frequency: 45 Hz, vibration inclination: 45°, plate inclination: 0°, in air and 1-G gravity environment). 1.0-G_v and 1.0-G are equal to 9.8 m/s².

Figure 7.5 shows the trajectories of the particle that slipped on the plate in the ζ -direction at 1.5-G_v vibration when the vibration frequency is varied. Because the vibration acceleration is constant, the particle does not float above the plate in all frequencies as shown in Figure 7.5. However, the particle moves faster at low frequencies because the effect of the particle slip is significant at low frequency than that at high frequency. Figure 7.6 shows the trajectories of the particle floating at 5.0-G_v vibration. The jumping particle moves faster at low frequency in the same way as the slipped particle. At low frequency, the particle does not have a long time of contacting with the plate, and the particle is not affected by friction force for a long time. Although a high amplitude of the plate vibration is required at low frequency to achieve the high acceleration, the particle transport is faster at low frequency.

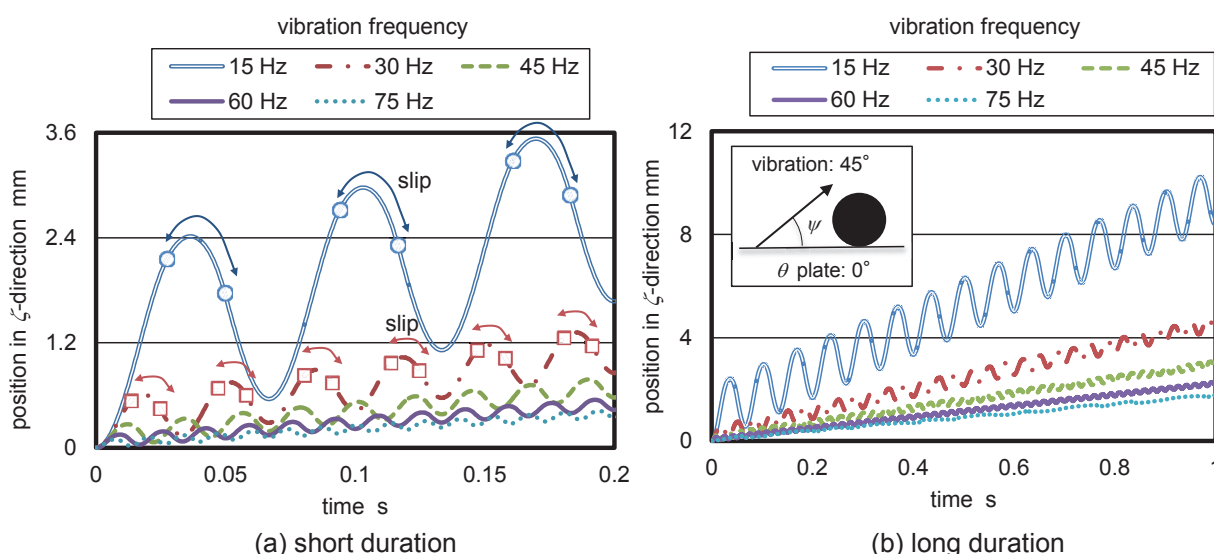


Figure 7.5 Calculated motion of slipping particle in ζ -direction during transport when vibration frequency is varied for (a) short and (b) long durations (vibration acceleration: 1.5-G_v, vibration inclination: 45°, plate inclination: 0°, in air and 1-G gravity environment). 1.0-G_v and 1.0-G are equal to 9.8 m/s².

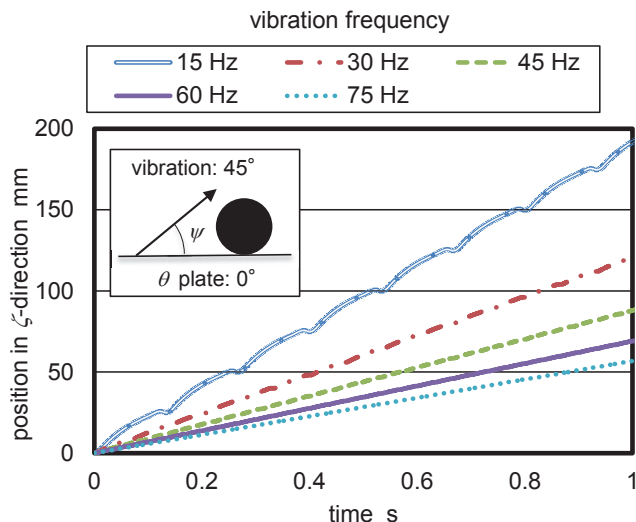


Figure 7.6 Calculated motion of floating particle in ζ -direction during transport as vibration frequency is varied (vibration acceleration: $5.0\text{-}G_v$, vibration inclination: 45° , plate inclination: 0° , in air and $1\text{-}G$ gravity environment).

Figure 7.7 shows the particle trajectories in the ζ -direction at $1.5\text{-}G_v$ and $5.0\text{-}G_v$ vibration, respectively, as the vibration inclination is varied. In $1.5\text{-}G_v$ and $5.0\text{-}G_v$, the slipped and floating particles are not transported when the vibration inclination is set to be 0° and 90° , and the trajectories are eliminated from the figures. As shown in Figures 7.7 (a) and (b), the velocities of the slipped and floating particles are smaller at 15° vibration inclination because the vibration acceleration of the plate in the ϕ -direction is small, which resulted in small friction force. On the other hand, the particle velocity is low at large vibration inclination simply because the force required from the plate to push the particle in the ζ -direction is small. The optimum vibration inclination range for transporting particle is $30^\circ\text{--}45^\circ$.

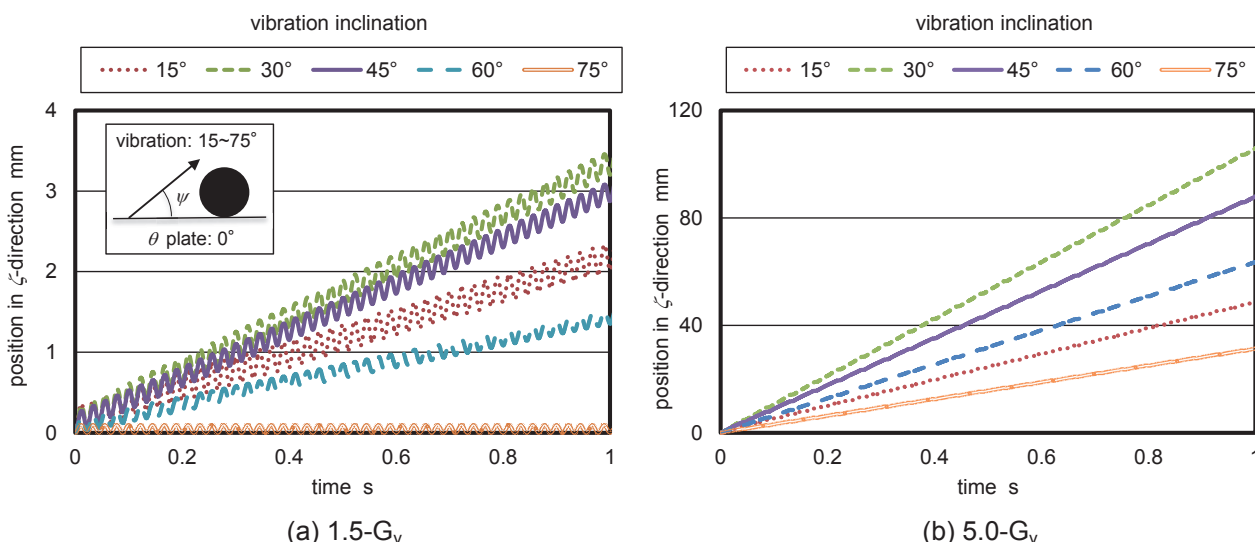


Figure 7.7 Calculated motion of the slipping particle in ζ -direction during transport as vibration inclination is varied (vibration acceleration: (a) $1.5\text{-}G_v$ and (b) $5.0\text{-}G_v$, vibration frequency: 45 Hz , plate inclination: 0° , in air and $1\text{-}G$ gravity environment).

Figure 7.8 shows the trajectories of the large particle, 300 μm in diameter, in the ζ -direction as the vibration acceleration is varied. Compared with Figures 7.3 and 7.4 that show the trajectories of the small particle that is 100 μm in diameter, the large particle is transported faster than the small particle as shown in Figure 7.8. Although Figure 7.3 shows that the small particle cannot be transported in 1.0- G_v , the large particle is transported in that condition, because the effect of the inertial force is larger compared to the adhesion force acting on the large particle. The results indicate that the transport performance is higher when moving large particles.

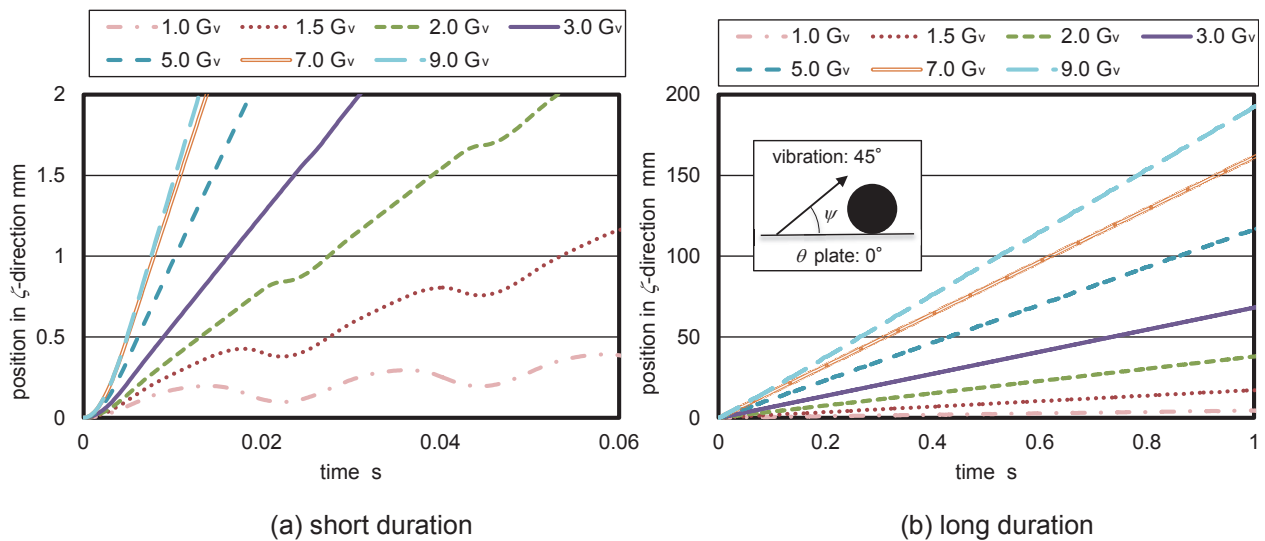


Figure 7.8 Calculated motion of large particle, 300 μm in diameter, in ζ -direction during transport as vibration acceleration is varied for (a) short and (b) long durations (vibration frequency: 45 Hz, vibration inclination: 45°, plate inclination: 0°, in air and 1-G gravity environment). Calculation result in case of particle 100 μm in diameter is shown in Figure 7.3.

Figure 7.9 shows the trajectories of the particle in the ϕ - and ζ - directions, respectively, when the vibration acceleration is varied in the Moon gravity. Although the particle cannot be transported in 1.0- G_v on the Earth gravity as shown in Figure 7.3, the particle can be transported at 1.0- G_v vibration acceleration in one-sixth gravity of the Moon as shown in Figure 7.9 (b) because the gravitational force and the resultant friction force are small, and the slip between the particle and plate occurs easily. As shown in Figure 7.9 (a), the particle easily floats at a higher position in the Moon gravity and the probability of contact with the vibrating plate decreases. The transport velocities of floating particles are smaller in the Moon gravity than in the Earth gravity.

Figure 7.10 shows the particle trajectories in the lunar environment. The particle is transported faster owing to the absence of air drag, which means that transport performance in space is superior to that on the Earth.

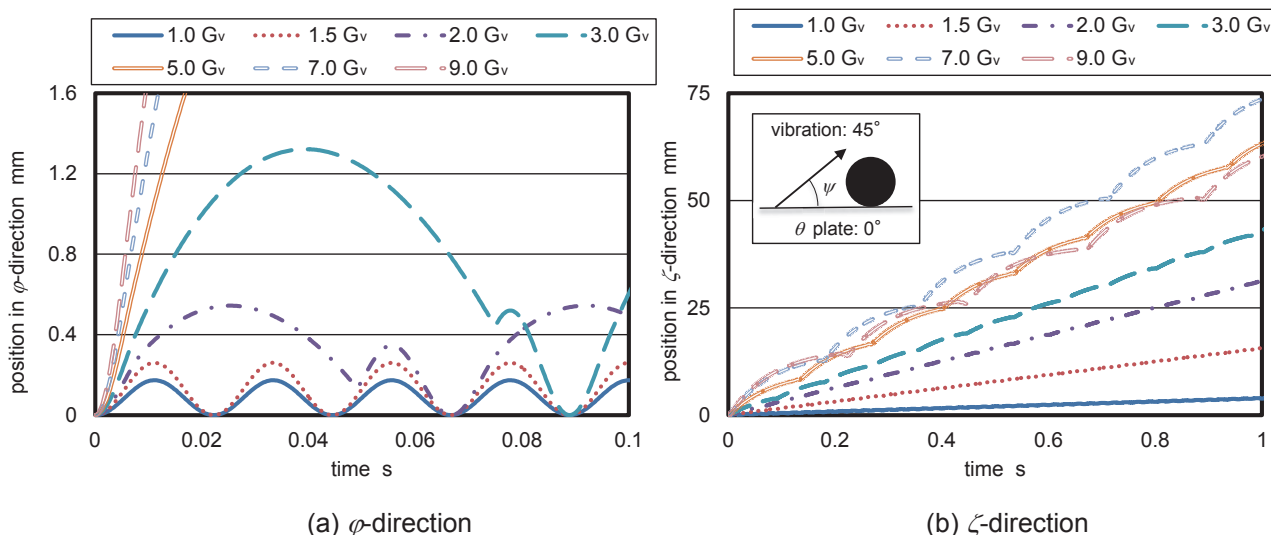


Figure 7.9 Calculated particle motions in (a) ϕ -direction and (b) ζ -direction during transport as vibration acceleration is varied (vibration frequency: 45 Hz, vibration inclination: 45° , plate inclination: 0° , in air and 1/6-G gravity environment). Calculation result in case of assuming air and 1-G environment is shown in Figure 7.3.

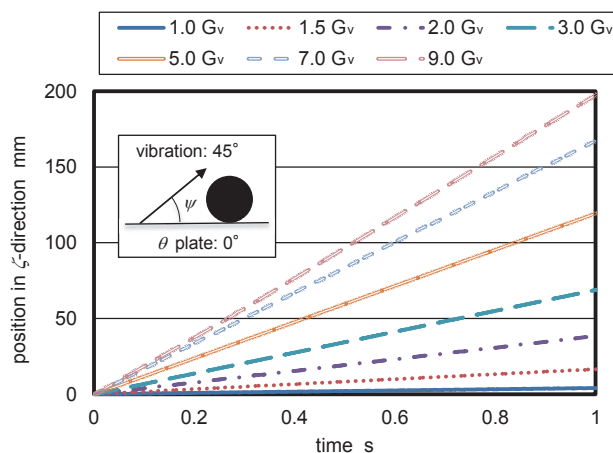


Figure 7.10 Calculated particle motion in ζ -direction during transport as vibration acceleration is varied (vibration frequency: 45 Hz, vibration inclination: 45° , plate inclination: 0° , in vacuum and 1/6-G gravity environment on Moon). Calculation result in case of assuming air and 1-G environment is shown in Figure 7.4.

Figure 7.11 (a) and (b) show the trajectories of the particle in the ζ -direction when the vibrated plate is inclined at 15° , and the vibration inclinations are set to be 45° and 60° , respectively. The figure shows that the particle can be transported in the oblique direction. At 1.5-G_v, the particle is transported in the horizontal direction; however, the transport in the oblique direction is not successful. Large vibration acceleration is required to transport the particle in the oblique direction. In addition, the transport velocity increases at 60° vibration inclination as shown in Figure 7.11 (b), compared to that at 45° as shown in Figure 7.11 (a). When the particle is transported in the oblique direction, the vibration inclination should be set larger than that in the horizontal direction.

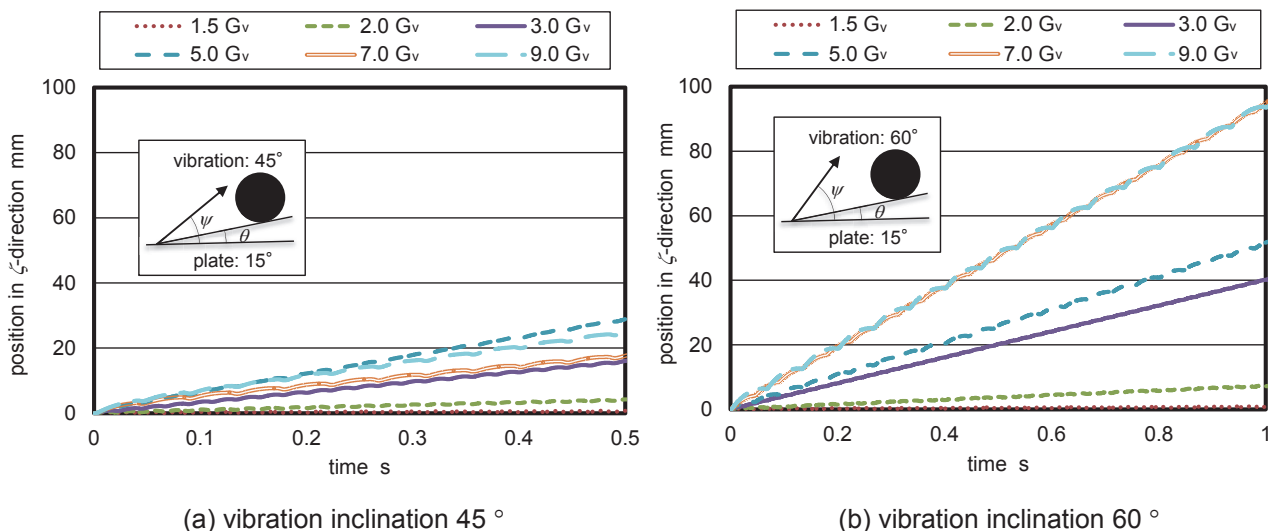


Figure 7.11 Calculated particle motion in ζ -direction during transport as vibration acceleration is varied (vibration frequency: 45 Hz, vibration inclination: (a) 45° and (b) 60° , plate inclination: 15° , in air and 1-G gravity environment). Calculation result in case of vibration inclination at 45° and plate inclination at 0° is shown in Figure 7.4.

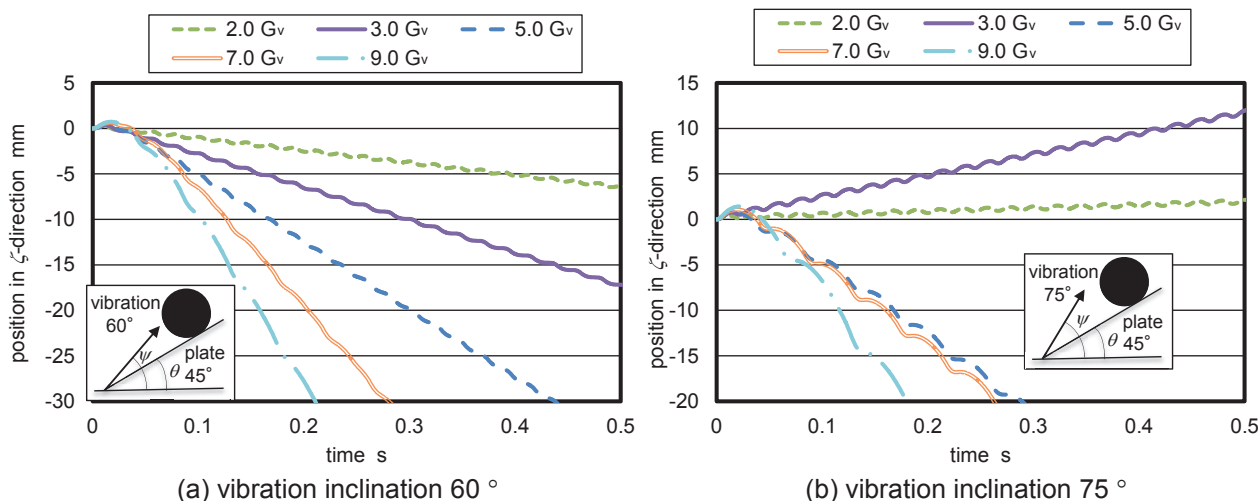


Figure 7.12 Calculated particle motion in ζ -direction during transport as vibration acceleration is varied (vibration frequency: 45 Hz, vibration inclination: (a) 60° and 75° , plate inclination: 45° , in air and 1-G gravity environment).

Figure 7.12 (a) and (b) show the trajectories of the particle in the ζ -direction when the plate is steeply inclined at 45° , and vibration inclinations are set to be 60° and 75° , respectively. Figure 7.12 (a) shows that the particle falls along the surface of the plate owing to the large gravitational force when the vibration inclination is 60° . If the vibration inclination is increased to 75° , the particle can be transported at 45° plate inclination, as shown in Figure 7.12 (b).

Figure 7.13 shows the trajectories of the particle when the plate is inclined at 60° in the Earth and lunar environments. In the Earth environment, the particle cannot be transported obliquely in all conditions of vibration acceleration. The maximum inclination required to transport the particle obliquely is assumed to

be 45° on the Earth. In the lunar environment, the particle can be transported in 60° oblique direction owing to the small gravitational force. The performance of vibration transport is expected to improve in the space environment. Based on these calculated results, the vibration transport system has been developed.

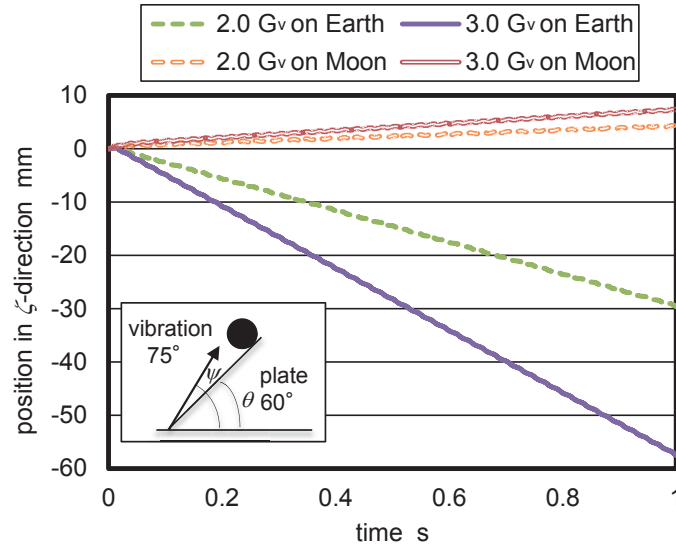


Figure 7.13 Calculated particle motion in ζ -direction during vibration transport on the Earth and Moon (vibration frequency: 45 Hz, vibration inclination: 75° , plate inclination: 60°).

7.3 Vibration Transport System Using Dielectric Elastomer Actuator

7.3.1 Driving Mechanism of Dielectric Elastomer Actuator

For installation in the particle transport system, it is preferable to use an actuator that does not have mechanical drives, has dust tolerance, and has high reliability for the operation in space environments [12]. In this study, the DEA is utilized because it does not require mechanical drives. Figure 7.14 (a) shows the driving mechanism of a sheet-like DEA. An elastomer film with a low Young's modulus is sandwiched between the elastic electrodes. When a high DC voltage is applied to the electrodes, the Maxwell stress, as represented by Equation (7.11) [3], acts on the elastomer film in the compressive direction, and a large displacement of the elastomer occurs along the vertical direction to the compression.

$$F = \varepsilon_r \varepsilon_0 \left(\frac{V}{d} \right)^2 \quad (7.11)$$

where V , ε_r , ε_0 , and d are the applied voltage, relative permittivity, permittivity of free space (8.8×10^{-12} F/m), and thickness of elastomer, respectively. The deformation of the sheet-like DEA is released when the applied voltage is turned off. If an AC voltage is applied to the electrodes, the sheet-like DEA vibrates in the elongation direction. This simple sheet-like DEA can be used for other configurations. For instance, if the sheet-like DEA is rolled and an AC voltage is applied to the electrodes, the cylindrical DEA vibrates in the axial direction, as shown in Figure 7.14 (b).

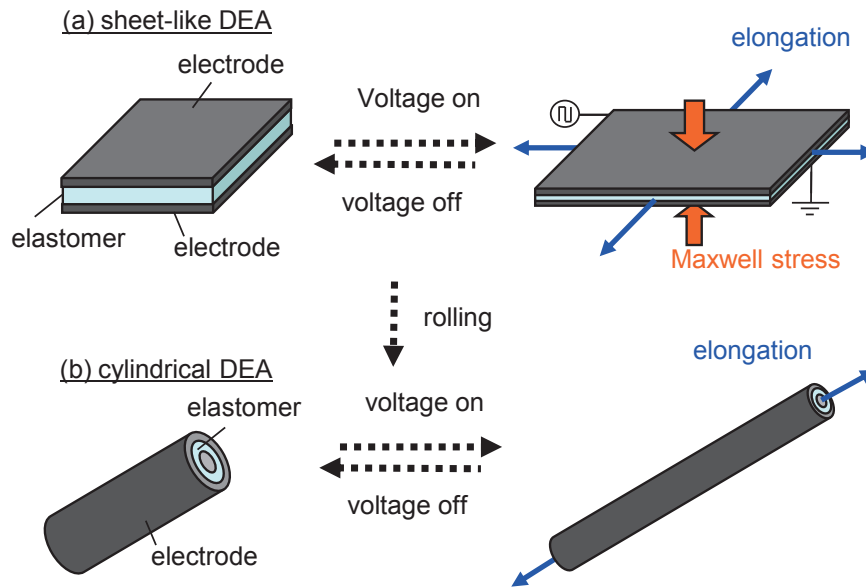


Figure 7.14 Driving mechanisms of (a) sheet-like DEA and (b) cylindrical DEA.

7.3.2 System Configuration of Vibration Transport System Using Dielectric Elastomer Actuator

Two types of vibration transport systems using the DEA were developed. One type utilizes a DEA consisting of the acrylic elastomer sheet VHB4910 (3M, thickness: 1.0 mm, Young's modulus: 0.22 MPa, relative permittivity: 3.21) [9]. The elastomer sheet was stretched to expand its area to $150 \times 150 \text{ mm}^2$ from $50 \times 50 \text{ mm}^2$ to achieve high deformation. The stretched elastomer was sandwiched by carbon grease (Art36-028, STRAIGHT) as stretchable electrodes. One side of the sheet-like DEA was stuck to the top of a spring (diameter: 20 mm, free length: 50 mm, spring constant: 0.22 N/mm) and the opposite side of the sheet was stuck to an acrylic ring (diameter: 50 mm). Because the shape looks like a mountain as shown in Figure 7.15 (a), it is named mountain-shaped DEA. When a high voltage was applied to one surface of the DEA and the other surface was grounded, the DEA was deformed along the axial direction of the spring. When a DC high voltage was applied to the DEA, the displacement of the top was measured using a high-speed camera (FASTCAM SA5, Photron), and the displacement is shown in Figure 7.15 (b). The displacement increased with the square of the applied voltage. When the voltage was larger than 5 kV, the DEA was broken, owing to a breakdown in insulation. When a high voltage of sine wave was applied to the DEA by using a function generator (SG-4115, IATSU) and amplifier (HVA4321, NF Corporation), the DEA vibrated in the axial direction, and the vibration displacement measured using the high-speed camera is shown in Figure 7.16 (a). From the measured displacement, the accelerations were determined as shown in Figure 7.16 (b). The figure shows that the vibration acceleration increased with the applied voltage. The displacement increased with the frequency of applied voltage in the low frequency range; however, the displacement decreases in high frequency range because a certain amount of time is required for the DEA to achieve maximum deformation. The optimum frequency is approximately 30 Hz.

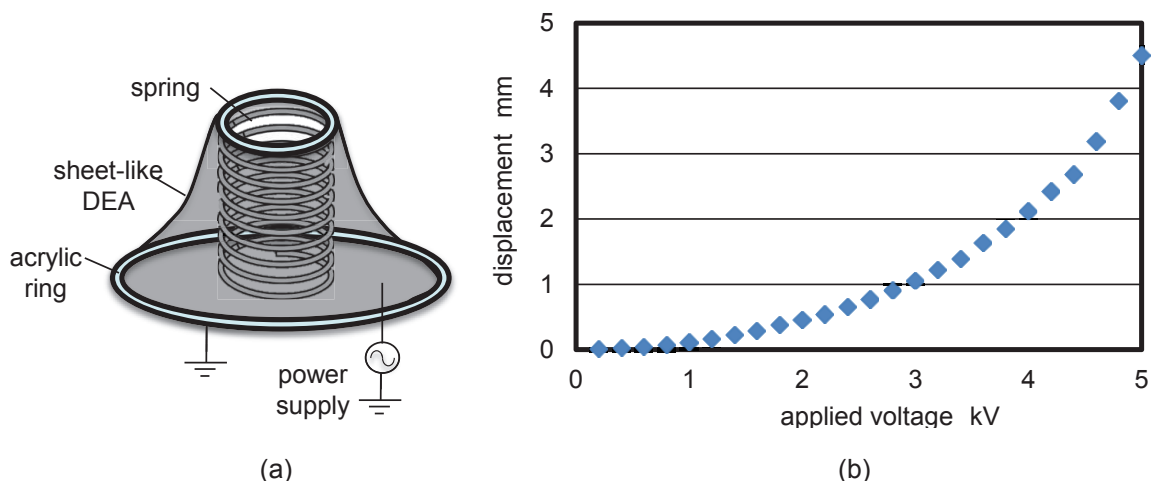


Figure 7.15 (a) Configuration of mountain-shaped DEA using acrylic elastomer sheet, and (b) displacement of mountain-shaped DEA versus DC applied voltage.

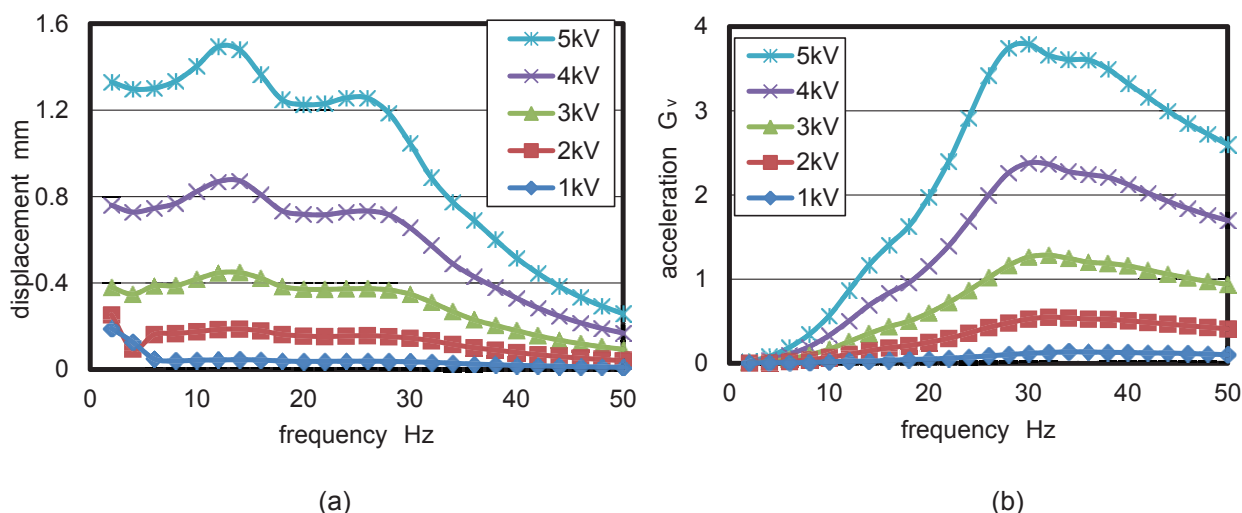


Figure 7.16 (a) Displacement of mountain-shaped DEA and (b) vibration acceleration of mountain-shaped DEA versus applied AC voltage and frequency. 1.0-G_v is equal to 9.8 m/s².

Using two mountain-shaped DEAs, an acrylic plate (area: 250 mm × 250 mm², thickness: 2 mm), four springs (diameter: 11 mm, free length: 22 mm, spring constant: 0.157 N/mm), and attachments for arranging the angle of the DEA to the plate, the vibration transport system was assembled as shown in Figures 7.17 and 7.18 (a). This is called Type-1 for convenience. When an AC high voltage was applied to the mountain-shaped DEA, the displacement of the plate was measured using a high-speed camera (FASTCAM SA5, Photron) and the acceleration determined from the measured displacement is shown in Figure 7.18 (b). When the frequency of applied voltage is approximately 20 Hz, the accelerations of the plate are high at vibration inclination of 45°-75°, as shown in Figure 7.18 (b).

In the experiment using this Type-1 system, 4 g of lunar and Martian regolith simulant, as described in section 1.1.2, was set on the acrylic plate and the transported velocity of the particles as they were moved 100 mm was measured. In addition, because the particle diameter affects the transport performance as de-

scribed in section 7.2.3, the simulant particles sorted smaller and larger than 106 μm using a mechanical sieve were used for the experiments. The applied voltage of 5 kV was fixed, and the frequency of the applied voltage and the DEA inclination were selected as a parameter.

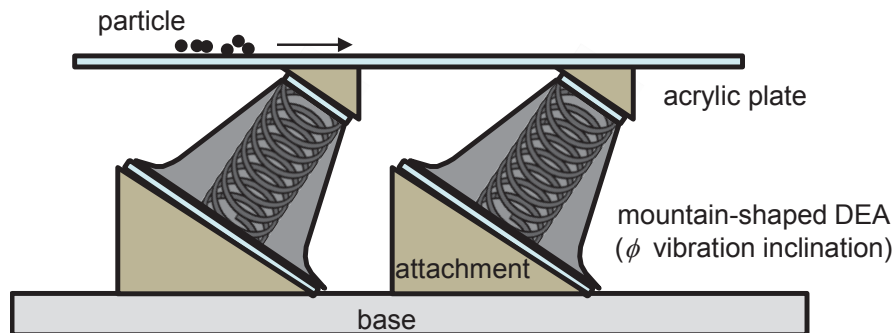


Figure 7.17 Configuration of the Type-1 vibration transport system using the mountain-shaped DEA.

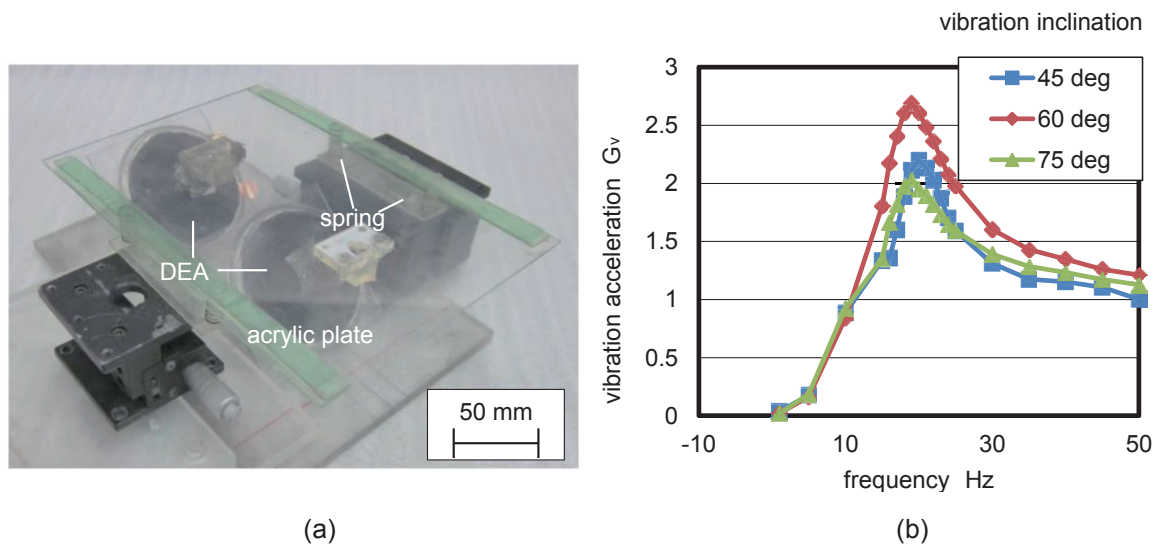


Figure 7.18 (a) Photograph of the Type-1 vibration transport system using the mountain-shaped DEA, and (b) vibration acceleration of the plate in the Type-1 vibration transport system. $1.0\text{-}G_v$ is equal to 9.8 m/s^2 .

Because the mountain-shaped DEA of the Type-1 system was pre-stretched at all times, the performance deteriorated in a short amount of time. Therefore, life cycle is an issue. Consequently, a cylindrical DEA (outer diameter: 12 mm, length: 60 mm) that does not require pre-stretching to achieve large deformation was provided by Toyoda Gosei, as shown in Figure 7.19 (a), and used for the Type-2 vibration transport system. Figure 7.19 (b) shows the displacement of the cylindrical DEA elongation in the axial direction versus the DC applied voltage. The displacement increased with the applied voltage as shown in Figure 7.19 (b), and its effect is different from the mountain-shaped DEA. To avoid insulation breakdown, 1,000 V was set as the maximum voltage. The Type-2 vibration transport system was assembled using the cylindrical DEA as shown in Figures 7.20 and 7.21 (a). The system consists of two cylindrical DEAs, acrylic plates (area: $210\text{ mm} \times 97\text{ mm}^2$, thickness: 2 mm), two springs (free length: 22 mm, spring constant: 0.157

N/mm), and attachments for setting the angle of the DEA to the plate. The alternating high voltage of sine wave generated using a function generator (SG-4115, IATSU) and amplifier (HVA4321, NF Corporation) was applied to the DEA; the resultant vibration was utilized to transport the particles. When an AC high voltage was applied to the cylindrical DEA, the displacement of the plate was measured using a high-speed camera (FASTCAM SA5, Photoron) and the acceleration determined from the measured displacement is shown in Figure 7.21 (b). When the vibration inclination ranges from 60° to 75° , the accelerations of the plate exceeded $1.5\text{-}G_v$ in conditions approximately 40 Hz.

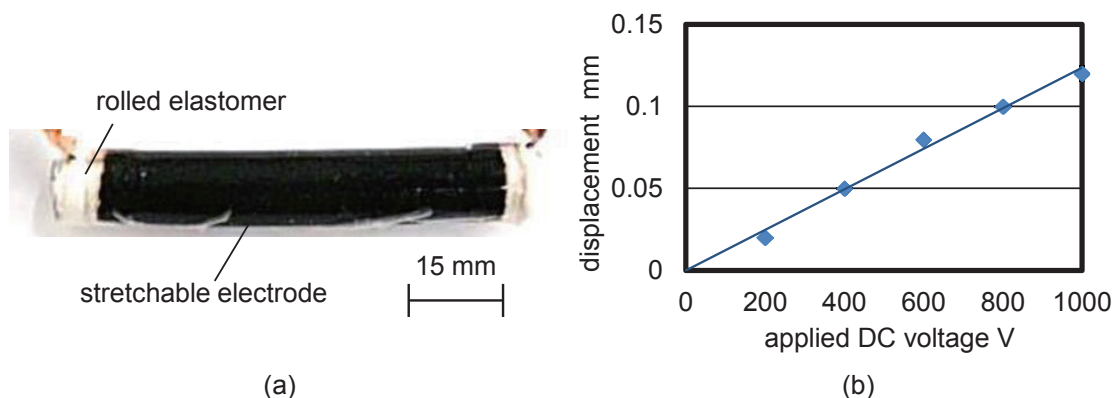


Figure 7.19 (a) Photograph of cylindrical DEA provided by Toyoda Gosei, and (b) displacement of cylindrical DEA versus DC applied voltage.

In the experiment using this Type-2 vibration transport system, the applied voltage of 1,000 V and the frequency of 35 Hz were fixed for transport experiments, and the vibration inclination was varied as a parameter. Both the velocity and amount of the transported particles were evaluated as the performance indices for the Type-2 system. The lunar regolith simulant was fed to the system from one side of the plate using an electromagnetic feeder (CF-01, Sinfonia Technology). Then, the amount of transported particles that reach the collection capsule set on the other side of the plate was measured.

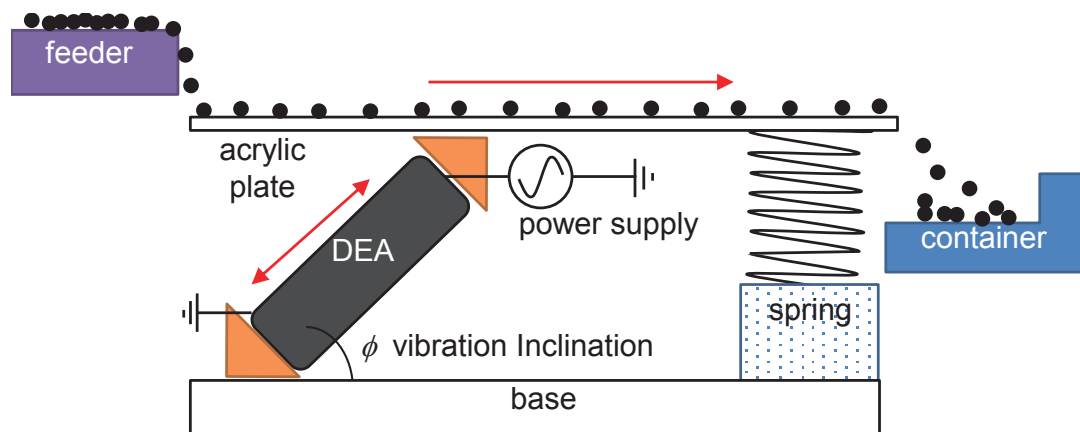


Figure 7.20 Configuration of the Type-2 vibration transport system using the cylindrical DEA.

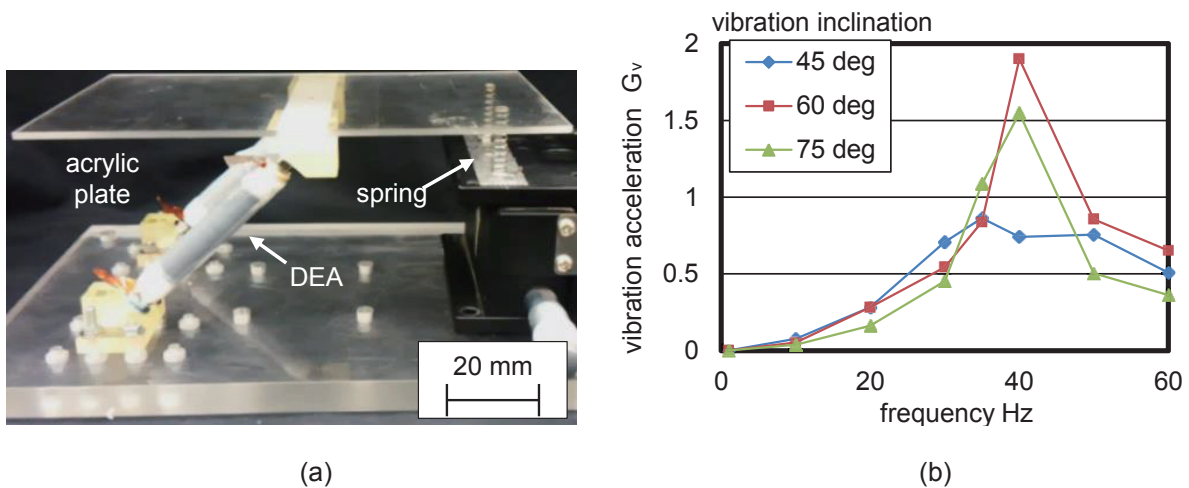


Figure 7.21 (a) Photograph of the Type-2 vibration transport system using the cylindrical DEA, and (b) vibration acceleration of the plate in Type-2 vibration transport system. $1.0\text{-}G_v$ is equal to 9.8 m/s^2 .

7.3.3 Performance of Vibration Transport System Using Dielectric Elastomer Actuator

Figure 7.22 (a) and (b) show the measured velocities of the transported lunar and Martian simulant particles, respectively, by using the Type-1 vibration transport system when the DEA inclination and frequency of applied voltage were varied. When the frequency ranges from 10 Hz to 40 Hz, the transport of particles was successful. Because the vibration acceleration was high in frequencies ranging from approximately 20 to 30 Hz as shown in Figure 7.18 (b), the transported velocities were high in those conditions. Although the acceleration of the plate did not exceed $1.0\text{-}G_v$ when the frequency was approximately 10 Hz, the transport was successful, which means the particles slipped on the plate. For the lunar and Martian particles, the system performance was improved at 60° inclination, and the maximum velocities were approximately 50 mm/s and 70 mm/s, respectively. The measured velocities were similar to the calculated velocities described in section 7.2.3. The reason why the Martian regolith was transported faster than the lunar regolith is because the Martian particles contain relatively large particles. Figure 7.23 (a) and (b) show the measured transport velocities of small, large, and nominal particles for lunar and Martian regolith simulants. As shown in this figure, the transport velocity of large particles was higher than that of small particles for the lunar and Martian regolith. The transport of small particles was more difficult than that of large particles. The tendencies of the experimental results agree closely with the calculation results described in section 7.2.3.

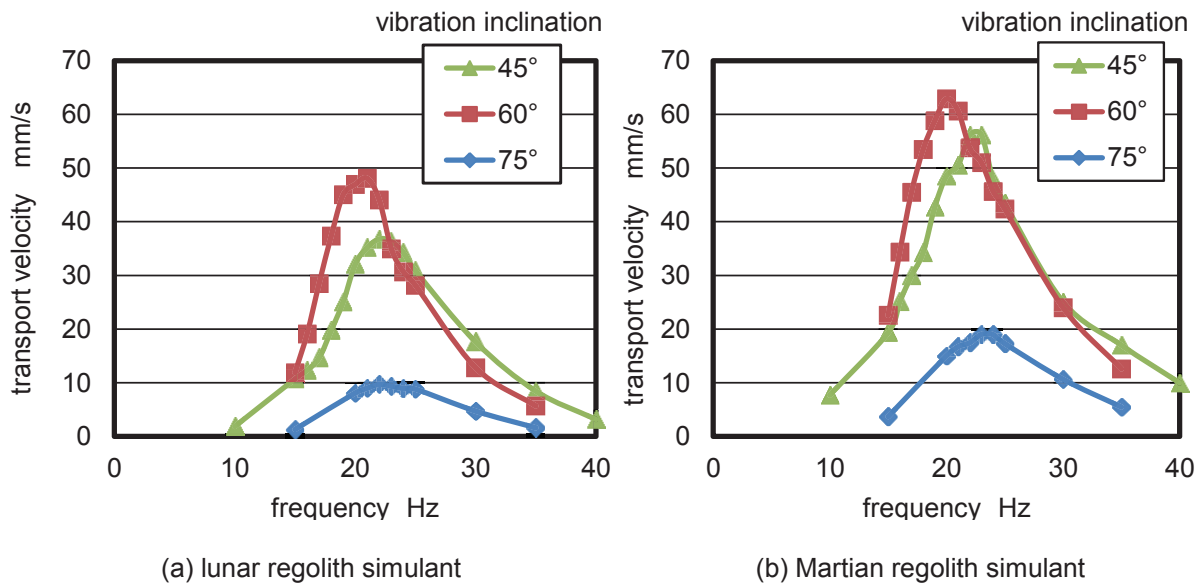


Figure 7.22 Measured transport velocities of (a) lunar regolith simulant and (b) Martian regolith simulant, of nominal particles, as the frequency of applied voltage and vibration inclination were varied in air and 1-G environment (applied voltage: 5 kV).

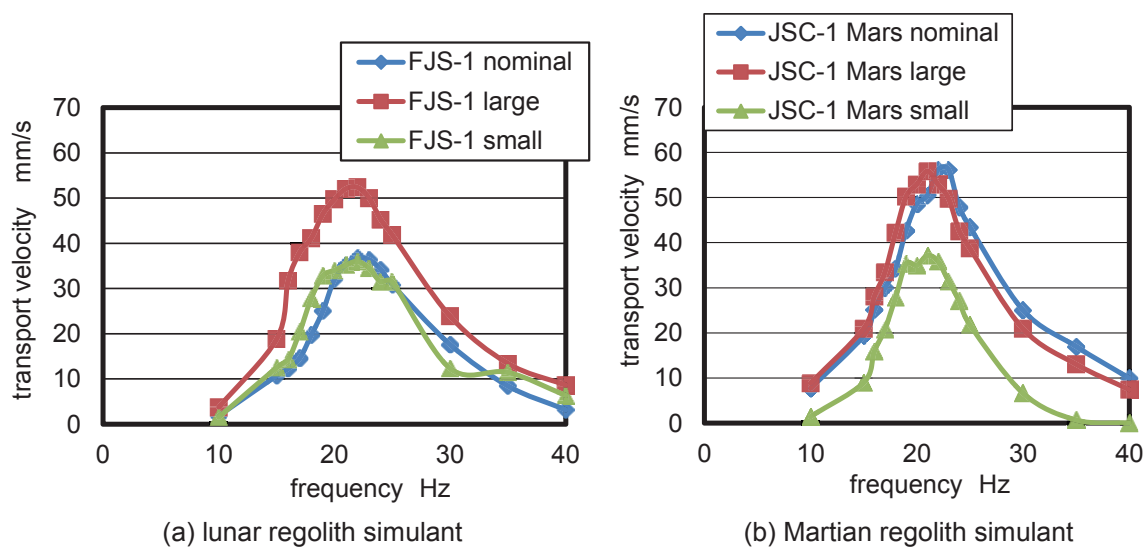


Figure 7.23 Measured transport velocities of small ($< 106 \mu\text{m}$), large ($> 106 \mu\text{m}$), and nominal particles of (a) lunar regolith simulant and (b) Martian regolith simulant as the frequency of applied voltage was varied in air and 1-G environment (applied voltage: 5 kV, vibration inclination: 45°).

Transport performance should be evaluated in terms of the transport velocity and amount of transported particles with respect to the supply rate. The performance of the Type-2 vibration transport system was experimentally confirmed, as shown in Figure 7.24. The measured transport rates of the particles versus the supply rates using Type-2 system are shown in Figure 7.24 as the vibration inclination was varied. Similarly, for the velocity performance of the Type-1 system, the transport rate was higher at the 60° inclination because the vibration acceleration was higher in that condition, as shown in Figure 7.22. At a low-supply rate, the transport rate increased linearly with the supply rate, and particles could be transported at a rate of 1.95

g/s as maximum in the condition of 60° inclination. When the supply rate increased further, the transport rate decreased. Even if a large number of particles were fed to the surface of the plate and the sediment particles also increased, the acceleration of the plate did not decrease. Figure 7.25 shows the effect of the sediment particles on the plate displacement, and the result shows that the displacement of the plate did not decrease with an increase in the amount of sediment particles. The reason why the performance was worsened at a high-supply rate was because the large amount of particles on the surface of the plate disturbed their own transportation. When the supply rate was lower than 1.6 g/s, the particles were smoothly transported, as shown in Figure 7.26 (a) and the velocity was high. On the other hand, under the condition of a high-supply rate of 3.3 g/s, a large amount of transported particles become jammed as shown in Figure 7.26 (b). Thus, the flow of particles was disrupted, which lowered the transportation velocity.

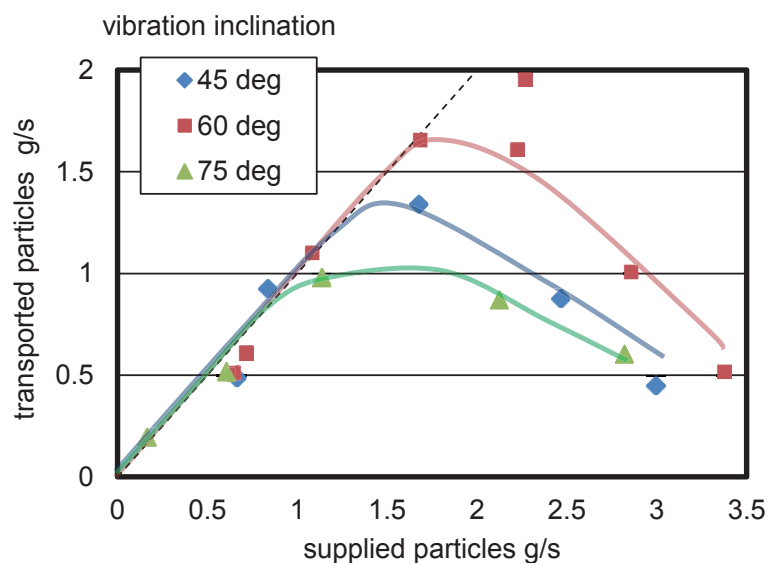


Figure.7.24 Measured transport rate of lunar regolith simulant particles larger than 106 μm in diameter, versus supply rate and vibration inclination in air and 1-G environment (applied voltage: 1,000 V, frequency of applied voltage: 35 Hz).

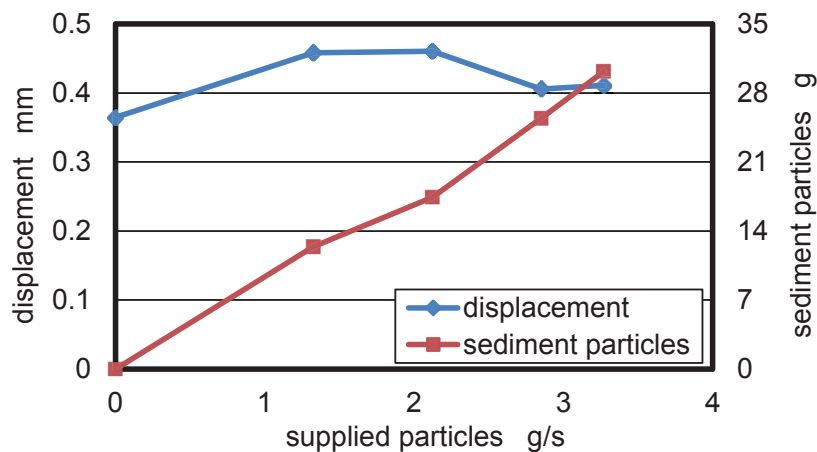


Figure 7.25 Measured displacement and sediment particles on plate versus supply rate in air and 1-G environment (applied voltage: 1,000 V, frequency of applied voltage: 35 Hz, vibration inclination: 60°).

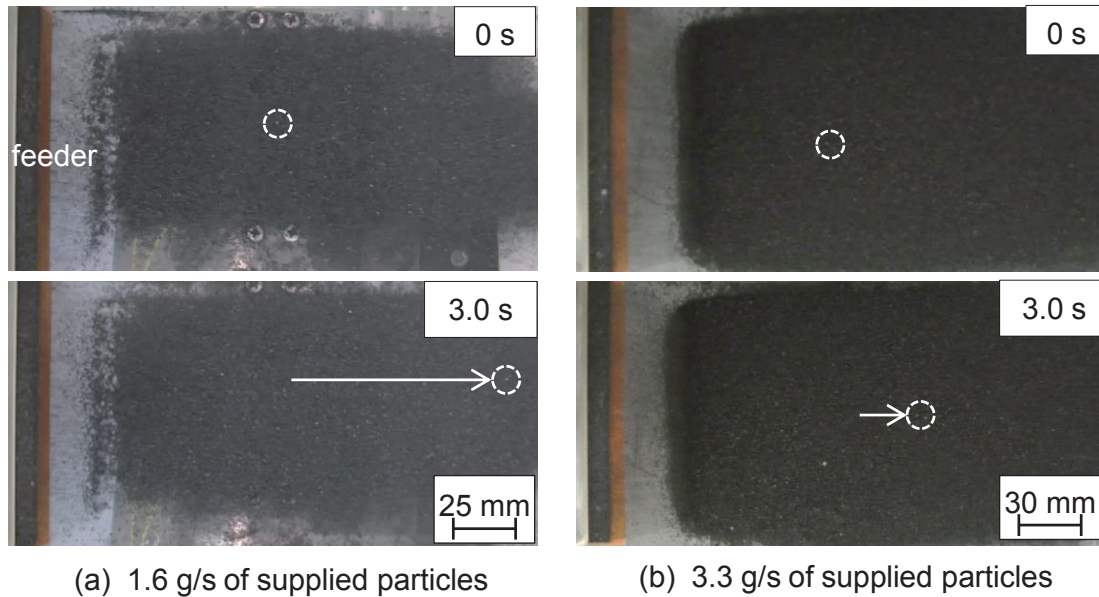


Figure 7.26 Observed transported particles as (a) 1.6 g/s and (b) 3.3 g/s of particles larger than $106\ \mu\text{m}$ were supplied in air and 1-G environment.

The effect of particle diameter on the transport rate was also investigated. Figure 7.27 shows the measured transport rates for lunar regolith simulant particles with diameters larger than $106\ \mu\text{m}$, smaller than $106\ \mu\text{m}$, and nominal sizes. Similar to the transport velocity, the transport rate of large particles was higher than that of small particles, as shown in Figure 7.27. This is because the effect of the inertial force is large compared to the adhesion force acting on the large particle, as predicted in section 7.2.3.

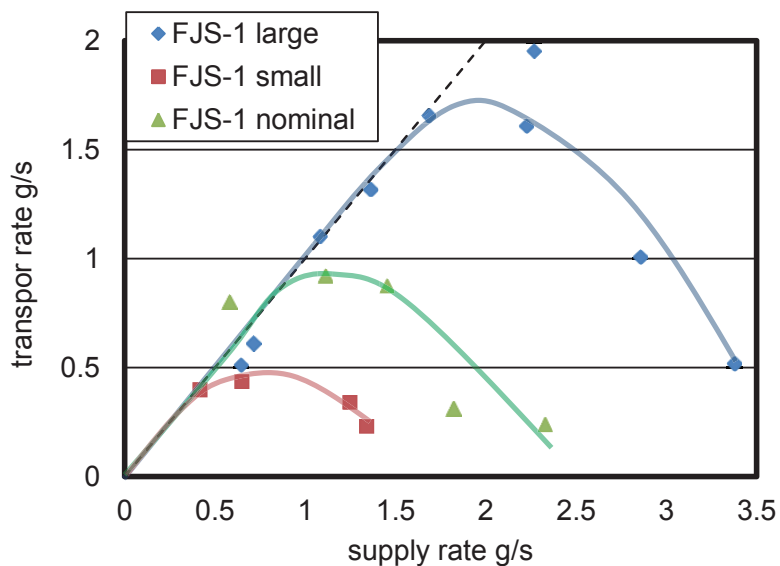


Figure 7.27 Measured transport rate of small ($< 106\ \mu\text{m}$), large ($> 106\ \mu\text{m}$), and nominal lunar regolith simulant versus supply rate in air and 1-G environment (applied voltage: 1,000 V, frequency of applied voltage: 35 Hz, vibration inclination: 60°).

7.4 Vibration Sampling System Using Electromagnetic Actuator

7.4.1 System Configuration

The mechanism of the vibration sampling system that uses an electromagnetic actuator is similar to that of the vibration transport system that uses the DEA. When the acrylic tube was introduced into the bulk of particles in the oblique direction and the tube was vibrated, the particles are transported in the vibrated tube, moving upward and passing through the vibrated tube to the collection box. In order for the actuator to vibrate the tube, an electromagnetic vibrator was utilized. The actuator generates vibration by supplying an electric current to the inner coil and utilizing the resulting magnetic field to attract and release the permanent magnet, repeatedly. In addition, because the actuator does not require mechanical drives similar to the DEA, the system has high tolerance to dust contamination. Although the DEA can be used as the actuator for the sampling system, two types of electromagnetic vibrators were used in the experiments. The transport performance in the horizontal direction was investigated in preceding section, and the vibration transport of particles in the oblique direction is investigated in this section.

Figure 7.28 shows the sampling system using the Type-A electromagnetic vibrator [10]. The dimensions of transparent acrylic tube include a 16 mm outer diameter, 11.6 mm inner diameter, and 330 mm length. The tube, fixed on a conventional electromagnetic vibrator (CF-1, Sinfonia Technology), is vibrated in an oblique direction. The left end of the tube is bent at a right angle and introduced to a capsule that collects the transported regolith. The weight of the collected regolith was measured concurrently with the sampling operation by using an electric balance placed under the sampling capsule. Figure 7.29 shows a photograph of the experimental setup.

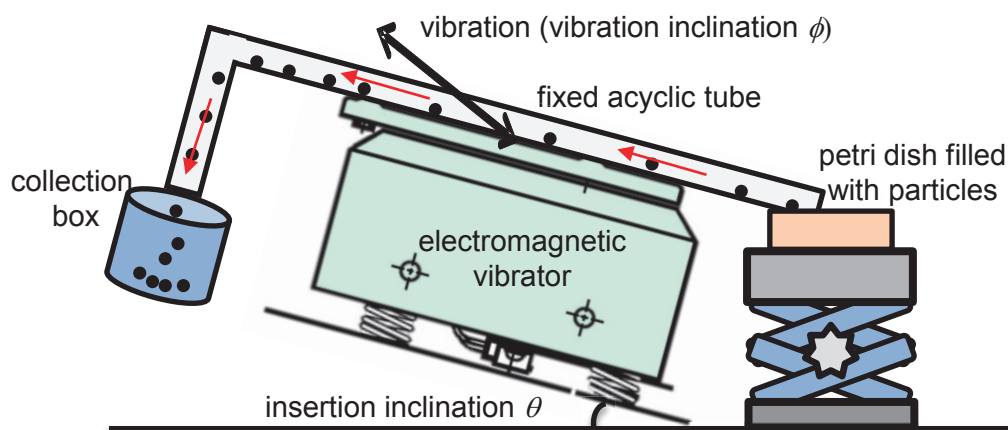


Figure 7.28 Experimental setup of the vibration sampling system using the Type-A electromagnetic vibrator.

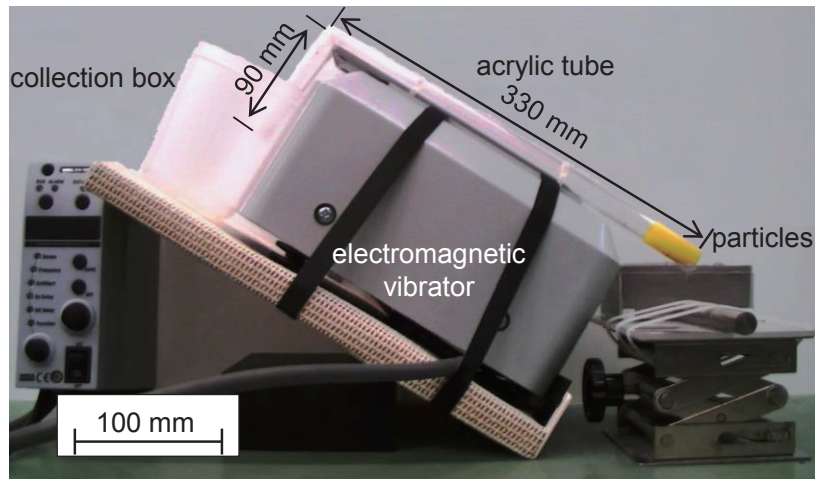


Figure 7.29 Photograph of the vibration sampling system using the Type-A electromagnetic vibrator.

Because the parameters of vibration displacement and frequency cannot be set independently in the case of using the Type-A vibrator, another electromagnetic vibrator (513-B, EMIC) was also used as shown in Figure 7.30 (a), which is the Type-B electromagnetic vibrator. The dimensions of the transparent acrylic tube include a 16 mm outer diameter, 11.6 mm inner diameter, and 200 mm length. The inner and outer diameters are the same as those in Figure 7.30. The tube, fixed on an electromagnetic vibrator, is vibrated in an oblique direction of 45° vibration inclination to generate the transport force. The left end of the tube is bent to 120° and introduced to a capsule that collects the transported regolith. The other side was inserted into the bulk of particles at 15° insertion inclination. The weight of the collected regolith was measured concurrently with the sampling operation using an electric balance placed under the sampling capsule. The frequency and amplitude of the Type-B vibration are independently varied as the experimental parameters. Figure 7.30 (b) shows a photograph of the experimental setup.

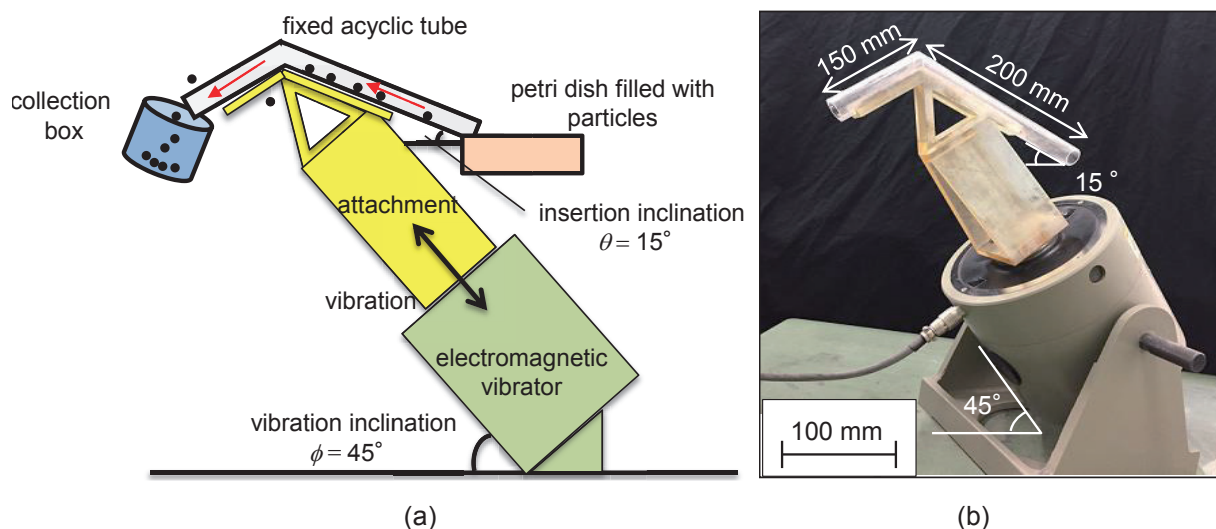


Figure 7.30 (a) Diagram and (b) photograph of experimental setup of vibration sampling system using Type-B electromagnetic vibrator.

7.4.2 Performance of Vibration Sampling and Transport System Using Electromagnetic Vibrator

Figures 7.31 and 7.32 show the weight of the transported lunar and Martian regolith in the capsule plotted against the operating time for the Type-A electromagnetic vibrator. The onset of the excitation is the start of the operating time. The initial penetration rate of the tube into the regolith layer, defined as shown in Figure 7.33 (a), was selected as the experimental parameter. As shown in Figures 7.31 and 7.32, the experiments demonstrated that a substantial amount of regolith was transported upwards against the Earth gravity for a short period, if the end of the tube was immersed in the regolith layer. The transport process is categorized into three phases as illustrated in Figure 7.33 (b). A dead time period (Phase I: 0-2.5 s) exists after the excitation onset because it takes time for the regolith to reach the capsule through the long tube. The transport rate is highest in Phase II, when there is sufficient regolith within the open tube for a plentiful supply of particles, as shown in Figure 7.34 (a). The rate was decreased after a large proportion of the regolith that initially filled the open end of the tube was actually transported to the capsule, i.e., the penetration depth decreased because the surrounding regolith had been removed (Phase III). In this phase, the regolith in the vicinity of the open end of the tube fell down on the sides of the tube opening, and stuck on the outside of the tube because of tube vibration, as shown in Figure 7.34 (b). This condition gradually decreased the transport rate because the tube remained at a fixed location, eventually depleting the amount of regolith in the vicinity of the tube.

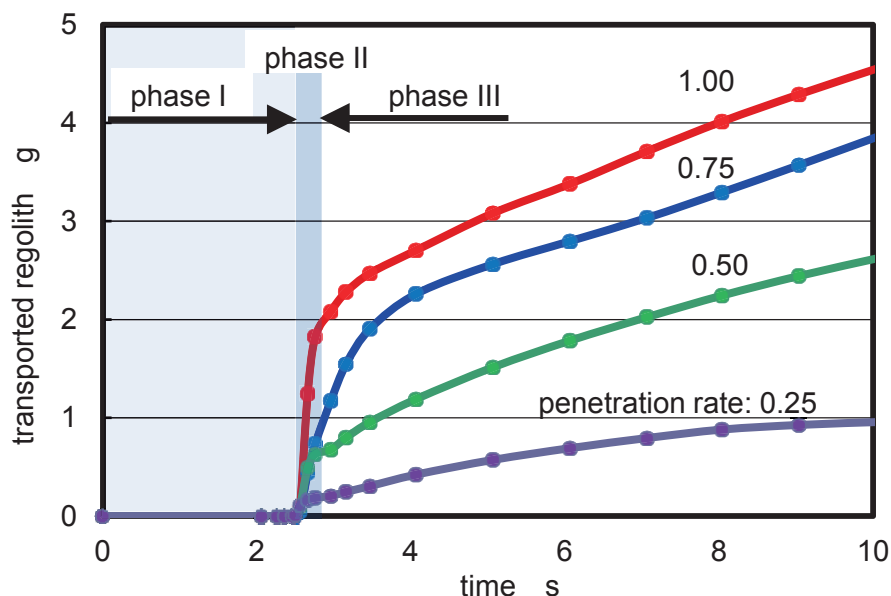


Figure 7.31 Weight of transported lunar regolith simulant in capsule plotted against operating time as penetration rate of tube is varied in air and 1-G environment (vibration acceleration: 7.3-G_v, vibration frequency: 90 Hz, vibration inclination: 35°, insertion inclination: 15°).

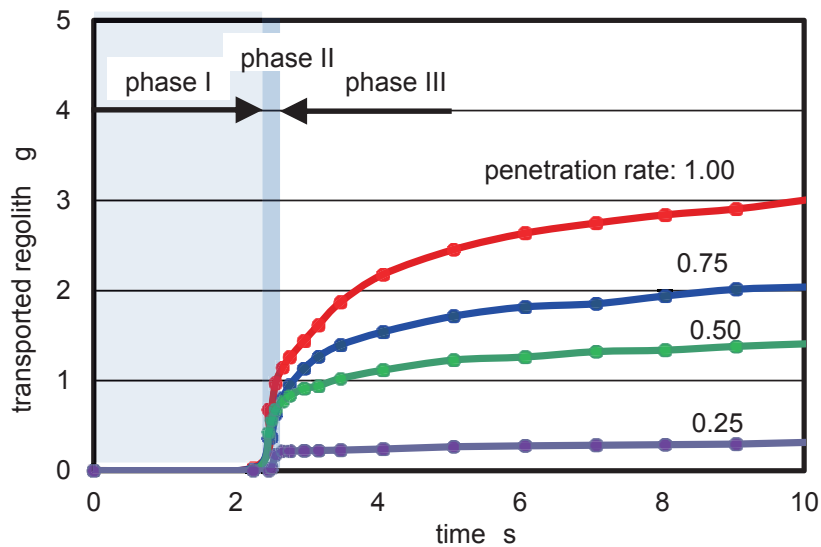


Figure 7.32 Weight of transported Martian regolith simulant in capsule plotted against operating time as penetration rate of tube is varied in air and 1-G environment (vibration acceleration: $7.3\text{-}G_v$, vibration frequency: 90 Hz, vibration inclination: 35° , insertion inclination: 15°).

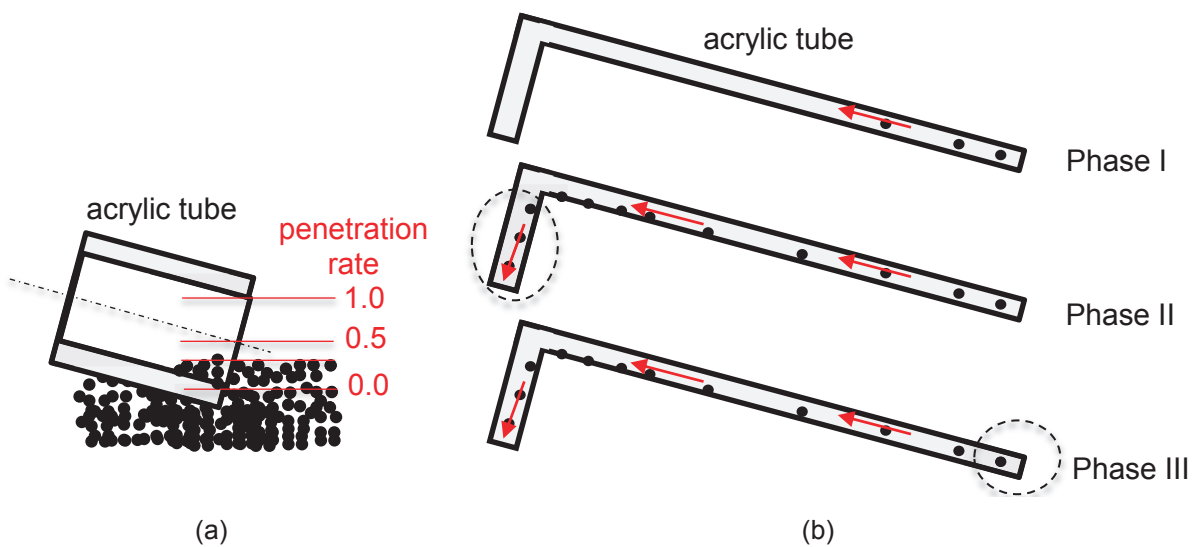


Figure 7.33 (a) Definition of penetration rate of tube in regolith bulk, and (b) schematic of transport process categorized into three phases.

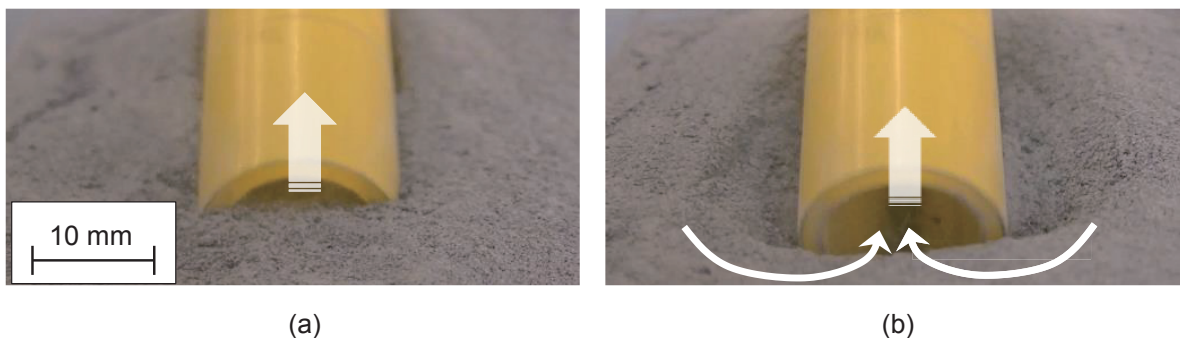


Figure 7.34 Open end of tube immersed in lunar regolith bulk observed during operation in air and 1-G environment; arrows show flow of regolith (vibration acceleration: $7.3\text{-}G_v$, vibration frequency: 90 Hz, vibration inclination: 35° , insertion inclination: 15°): (a) Phase II; (b) Phase III.

Figure 7.35 (a) and (b) show the effect of the insertion inclination of the tube on the transport rate in the case of using lunar and Martian regolith particles. The transport rate is decreased at high-inclination angles. However, a substantial amount of regolith can be raised against gravity and transported even when the inclination is as high as 45° . This behavior agrees well with the calculated results as shown in section 7.2.3. The threshold inclination of the lunar and Martian regolith on the Earth was approximately 45° for the 10 s operation time. If the inclination is higher than the threshold, the particles cannot be elevated against gravity. Because the gravity on the Moon and Mars are one-sixth and three-eighths of that on the Earth, respectively, the threshold of the inclination on the Moon and Mars will be higher than that on the Earth.

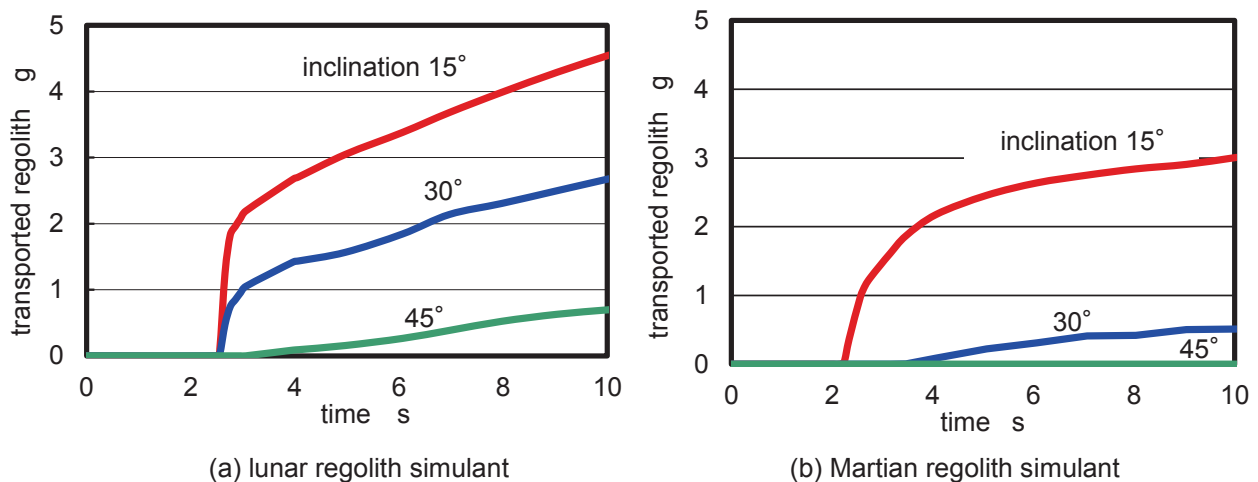


Figure 7.35 Weight of (a) transported lunar regolith simulant and (b) transported Martian regolith simulant in capsule plotted against operating time as insertion inclination of tube is varied in air and 1-G environment (vibration acceleration: $7.3\text{-}G_v$, vibration frequency: 90 Hz, vibration inclination: insertion inclination + 35° , penetration rate: 1.0).

Using the optimum conditions of the penetration rate as 1.0 and the inclination as 15° , the effect of vibration acceleration and vibration frequency was investigated using the Type-B electromagnetic vibrator. Figure 7.36 (a) and (b) show the effect of the vibration acceleration and the frequency on the sampling performance in the case of using the lunar regolith simulant, respectively. As shown in Figure 7.36 (a), the performance was improved with respect to the vibration acceleration, as predicted in section 7.2.3. In addition, Figure 7.36 (b) shows that the performance increased with a decrease in frequency, and the result also agreed closely with the calculated result. However, many particles interacted with each other in the experiments, resulting in a more efficient sampling performance, compared with the calculation results.

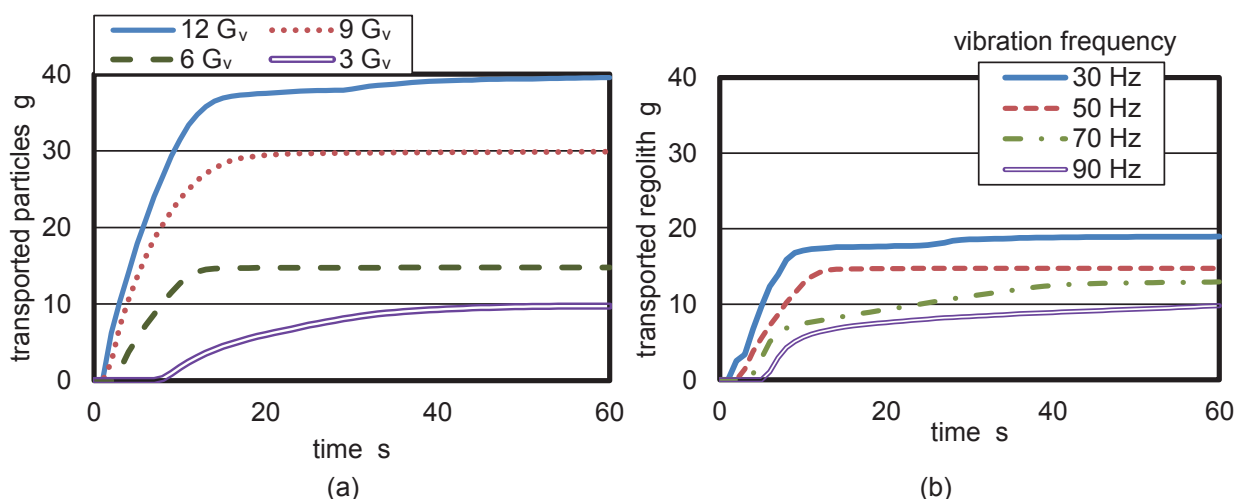


Figure 7.36 Weight of transported lunar regolith simulant in capsule plotted against operating time as (a) vibration acceleration and (b) vibration frequency of tube are varied in air and 1-G environment (vibration frequency: 50 Hz, vibration inclination: 45°, insertion inclination 15°, penetration rate: 1.0).

7.5 Combination of Vibration Sampling with Electrostatic and Magnetic Samplers

7.5.1 Configuration of Experimental Setup

To address the problem that the vibration sampling system cannot capture particles without touching the vibrating tube, the electrostatic sampler and magnetic sampler were attached to the tube of the vibration sampling system. In the case of using the electrostatic sampler, the diagram of the sampling part is shown in Figure 7.37 (a). The parallel screen electrodes made of stainless steel were attached at a slanting angle of 30°, and the initial penetration depth was the experimental parameter as shown in Figure 7.37 (b). The electrodes were initially inserted into the bulk regolith as shown in the Figure 7.37 (b). Although the mechanism of the sampling part is the same as the electrostatic sampler described in Chapter 5, the geometry of the parallel electrode was modified by adapting the vibration sampling system. The thickness and opening of the screen electrodes were 6 mm and $3 \times 3 \text{ mm}^2$, respectively, and the distance between the screen electrodes was fixed at 6 mm. A single-phase rectangular high voltage applied to the parallel electrodes was generated by a high-voltage power supply (HEOPT-5B20, Matsusada Precision) and a function generator. The particles agitated by the electrostatic part pass through the opening of electrodes and the captured particles are transported by the vibrating tube toward the collection box. The experimental setup without the electrostatic part is the same as that of the Type-A sampling system as shown in Figure 7.29.

Figure 7.38 (a) shows a photograph of vibration sampling system combined with the magnetic sampler, while Figure 7.38 (b) shows the diagram of the sampling part. The solenoid coil (wire turn: 1,000) is wound around the end of the acrylic tube. The inclination of the sampler and the distance from the sampler and particle were set to be 30° and 0 mm, respectively, as shown in Figure 7.38 (b). Pulse currents were supplied ten times to the solenoid coil (magneto-motive force: 5,000 AT, applied time: 40 ms, dead time: 500 ms). Then, the agitated particles were attracted inside the coil and transported by the vibrating tube to the

collection box. The experimental setup without the electromagnetic coil is the same as the Type-B vibration sampling system, as shown in Figure 7.30. In this experiment, the magnetic particle was used, and the detail was shown in Chapter 6.

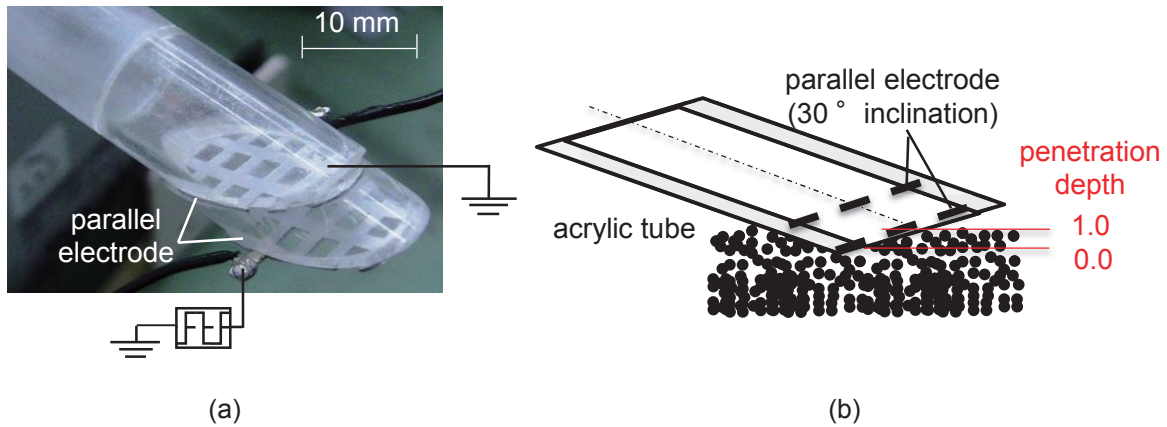


Figure 7.37 (a) Photograph of sampling part of vibration sampling system combined with electrostatic force, and (b) definition of penetration depth of pipe into the regolith layer.

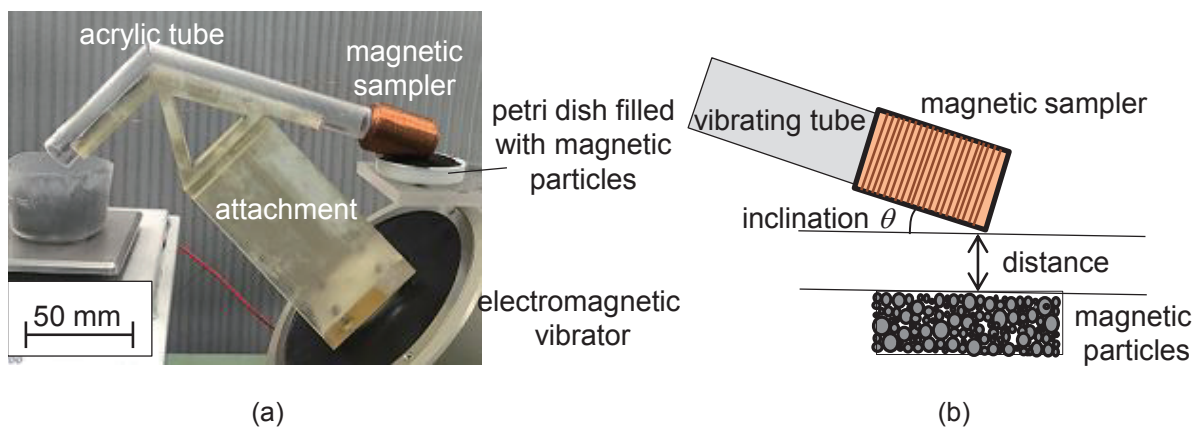


Figure 7.38 (a) Photograph of vibration sampling system combined with magnetic sampler, and (b) definition of inclination of the sampling part and distance between sampling part and particles surface.

7.5.2 Sampling and Transport Performance of Vibration System Combined with Electrostatic Sampler

Figure 7.39 (a) shows the weight of captured regolith plotted against the operating time when a high AC voltage was applied between the parallel screen electrodes. The start of the operating time was determined to be the moment when the particles reached the capsule. Some amount of regolith can be captured when the screen electrode is in contact with the regolith. However, the capture rate was much smaller than the transport rate. The total collection rate was capture controlled. Figure 7.39 (b) shows the effect of the applied voltage between the parallel screen electrodes. The capture rate increased with the increase in the applied voltage.

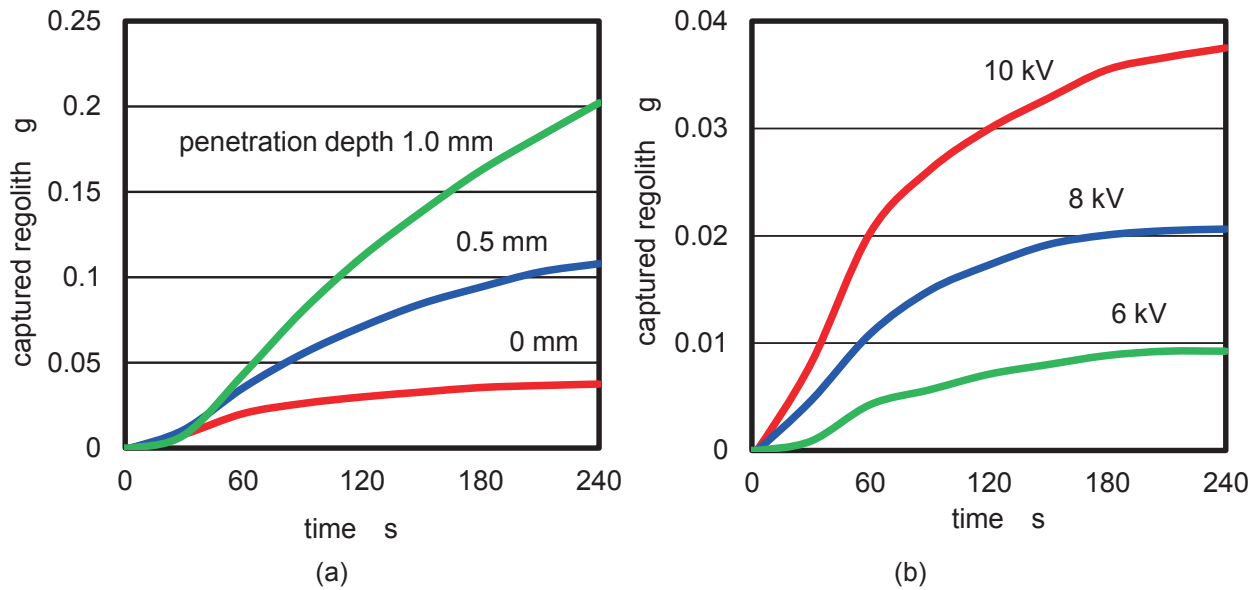


Figure 7.39 Weight of transported lunar regolith simulant in capsule plotted against operating time as (a) penetration depth of pipe into regolith and (b) applied voltage to part of electrostatic sampler are varied (vibration acceleration: $7.3\text{-}G_v$, vibration frequency: 90 Hz, vibration inclination: 35° , pipe inclination 15° , frequency of applied voltage: 1.0 Hz, (a) applied voltage: 10 kV_{p-p} , (b) penetration depth: 0 mm, in air and 1-G environment).

7.5.3 Sampling and Transport Performance of Vibration System Combined with Magnetic Sampler

Figure 7.40 (a) and (b) show the weight of captured magnetic particles plotted against the operating time when the magneto-motive force was applied and not applied, respectively, and when the vibration frequency was varied. Although the distance from the sampler and particle was set to be 0 mm, some particles were introduced into the pipe even though the magnetic sampler was not activated, as shown in Figure 7.40, because the vibration amplitude is comparably large at vibration frequencies of 30 Hz and 50 Hz, and the particles entered the pipe when the pipe reached the lowest position of vibration. At 70 Hz and 90 Hz frequencies, the particles could not be collected. When the magnetic sampler was activated, the total amounts of collected particles were increased in all conditions of vibration frequency.

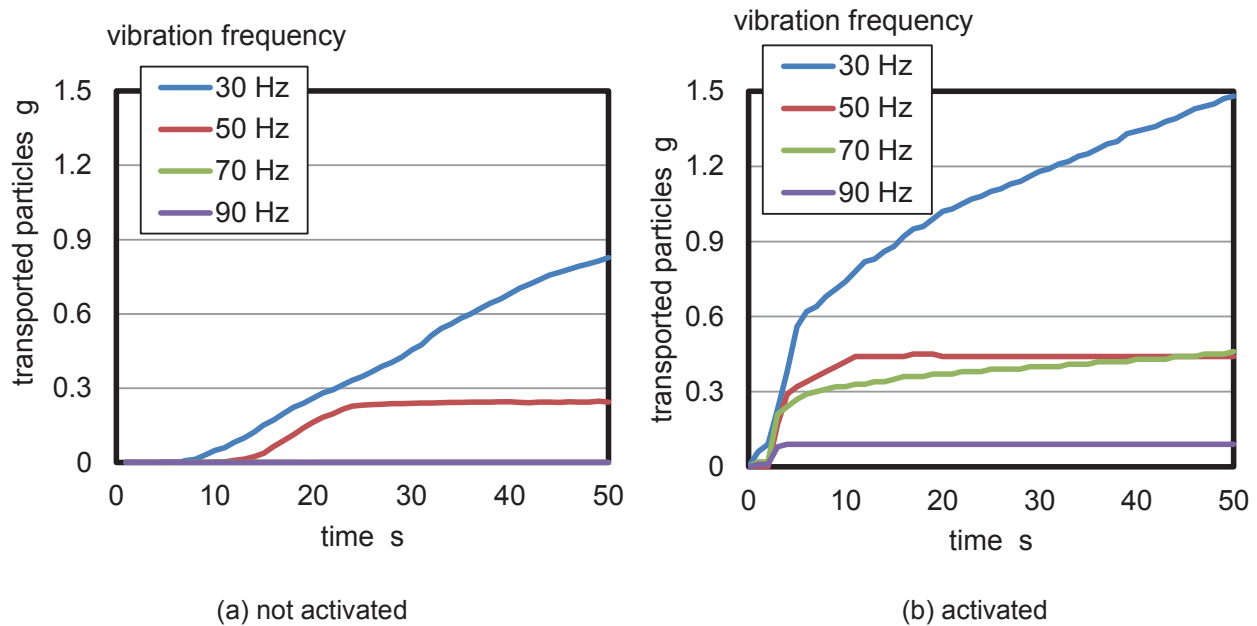


Figure.7.40 Weight of transported magnetic particles in capsule plotted against operating time as vibration frequency is varied by (a) not activating and (b) activating magnetic sampler (vibration acceleration: $3.0\text{-}G_v$, vibration inclination: 45° , pipe inclination 30° , distance between coil and particles: 0 mm, (b) magneto-motive force: 5,000 AT, (b) applied time: 40 ms, (b) dead time: 500 ms, (b) pulse times: 10, in air and 1-G environment).

7.6 Summary

To achieve reliable handling of large amounts of lunar and Martian regolith, a vibration transport system utilizing the DEA and an electromagnetic vibrator has been developed. Its performance was evaluated by simple model calculations and experiments. The insights achieved from the results are shown below.

1. The vibration transport and vibration sampling system can transport large amounts of lunar and Martian regolith particles. Two types of DEA and electromagnetic vibrators could be used as actuators. The particles are transported as they slip on the vibrated plate at low-vibration acceleration, or as they jump above the plate at large vibration acceleration.
2. High vibration acceleration and low vibration frequency are preferable for better system performance.
3. Large particles could be transported in the horizontal direction easier than small particles because the effect of inertial force increased with particle diameter.
4. The vibration sampling system could transport particles in the oblique direction in the Earth environment for a maximum inclination of approximately 45° .
5. The results of the simple model calculations agreed quantitatively well with the experimental results. The calculation predicted that the vibration transport performance and the vibration sampling system

performance will be improved in space environments.

6. The vibration sampling system could not collect particles that did not contact the vibrated parts. However, when the system is combined with the electrostatic sampler and magnetic sampler, it could collect particles without contacting them.

The vibration transport systems equipped with the DEA and electromagnetic vibrator do not require mechanical drives and have a high tolerance to dust contamination. In addition, the transport systems can be designed compactly and simply, making them suitable for space application. The transport systems are expected to be used for future exploration missions on the Moon and Mars.

Chapter 8 Conclusion

8.1 Discussion of Particle Dynamics in Space Environments

8.1.1 Effect of Gravitational Acceleration on Large Particles

As described in Chapters 3 and 5, particle charge density and the value of gravitational acceleration are key influences on the dynamics of particles affected by the Coulomb force. Therefore, the relationship between those factors is considered here. The balance between the Coulomb force and the gravitational force applied to i -th particle is represented by Equation (8.1).

$$\frac{4}{3}\pi R_i^3 \rho_{s,i} \rho_{c,i} \mathbf{E} = \frac{4}{3}\pi R_i^3 \rho_{s,i} \mathbf{g} \quad (8.1)$$

where R , ρ_s , ρ_c , \mathbf{E} , and \mathbf{g} are the particle radius, specific gravity of particle, charge density of particle, electrostatic field, and gravitational acceleration, respectively. Equation (8.1) is rearranged as Equation (8.2) to show that the minimum charge density required to move a particle is determined by the gravitational acceleration.

$$\rho_{c,i} = \frac{\mathbf{g}}{\mathbf{E}} \quad (8.2)$$

The relationship between gravitational acceleration and charge density was calculated using the external electrostatic field \mathbf{E} that was calculated using the finite difference method based on the calculation model, as shown in Figure 2.14. Figure 8.1 shows the calculated result.

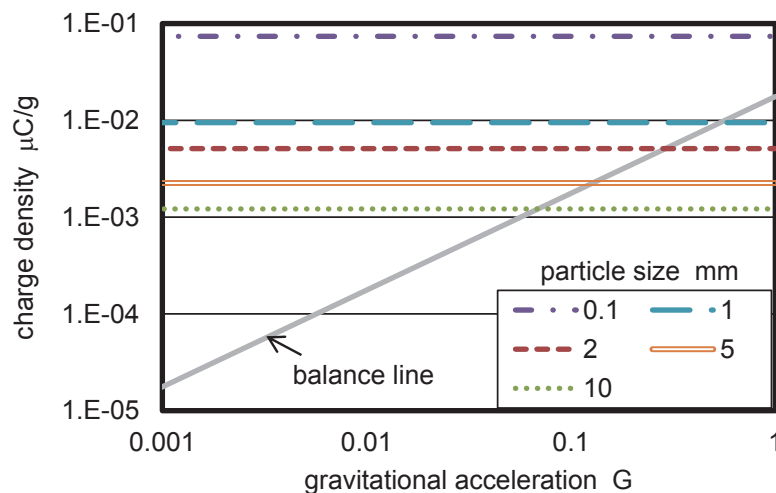


Figure 8.1 Balance between gravitational acceleration and charge density of a particle (Electrostatic field \mathbf{E} is calculated under condition shown in Figure 2.14). Measured charge densities of particles ranging from 100 μm to 10 mm in diameter are extracted from Figure 2.11 to compare with the balance. When the measured charge density is larger than the balance, the particle can be moved by using the Coulomb force.

The balance line in Figure 8.1 shows the minimum charge density needed to move particles in each condition of gravitational acceleration, and the density decreases with respect to the gravitational acceleration. As a reference, the measured charge densities of lunar regolith simulant ranging from 100 μm to 10 mm in diameter are shown in Figure 8.1. In the 1-G environment, because charge densities of the simulant particles smaller than several hundred micrometers are higher than the balance line, those particles can be moved by using the Coulomb force. The experimental results shown in Chapters 3 and 5 agree with the theoretical calculation results. In 0.01-G, the sampling of glass beads (2 mm in diameter) and rocks (4 mm in diameter) were performed experimentally in Chapter 5. The calculation result in Figure 8.1 agrees with the experimental results. From the results shown above, the relationship between the gravitational acceleration and the charge density can be determined.

The effect of gravitational acceleration on dielectrophoresis force and magnetic force was also considered. The balance between the dielectrophoresis force and the gravitational force applied to the i -th particle is represented by Equation (8.3).

$$\left(4\pi\varepsilon_0 \frac{\varepsilon_r - 1}{\varepsilon_r + 2} R_i^3 \mathbf{E} \cdot \nabla\right) \mathbf{E} = \frac{4}{3} \pi R_i^3 \rho_{s,i} \mathbf{g} \quad (8.3)$$

where ε_r and ε_0 are the relative permittivity of particle and permittivity of free space (8.85×10^{-12} F/m), respectively. Equation (8.3) is rearranged as Equation (8.4) to show that the minimum relative permittivity to move the particle can be deduced by the gravitational acceleration and the specific gravity of particles, if the electrostatic field is fixed.

$$\varepsilon_r = \frac{3\varepsilon_0 (\mathbf{E} \cdot \nabla) \mathbf{E} + 4\rho_{s,i} \mathbf{g}}{3\varepsilon_0 (\mathbf{E} \cdot \nabla) \mathbf{E} - 2\rho_{s,i} \mathbf{g}} \quad (8.4)$$

By similarity, the balance between the magnetic force and the gravitational force is represented by Equations (8.5) and (8.6).

$$\left(\frac{4\pi}{\mu_0} \frac{\mu_r - 1}{\mu_r + 2} R_i^3 \mathbf{B} \cdot \nabla\right) \mathbf{B} = \frac{4}{3} \pi R_i^3 \rho_{s,i} \mathbf{g} \quad (8.5)$$

$$\mu_r = \frac{3(\mathbf{B} \cdot \nabla) \mathbf{B} + 4\mu_0 \rho_{s,i} \mathbf{g}}{3(\mathbf{B} \cdot \nabla) \mathbf{B} - 2\mu_0 \rho_{s,i} \mathbf{g}} \quad (8.6)$$

where μ_r , μ_0 and \mathbf{B} are the relative magnetic permeability of the particle, the magnetic permeability of free space (1.25×10^{-6} H/m), and the magnetic flux density, respectively. The effects of the relative permittivity

and relative permeability were calculated using the external electrostatic field E and the magnetic field B , which were calculated using the finite difference method, considering the calculation models shown in Figures 2.14 and 2.16. Figure 8.2 shows the calculated results.

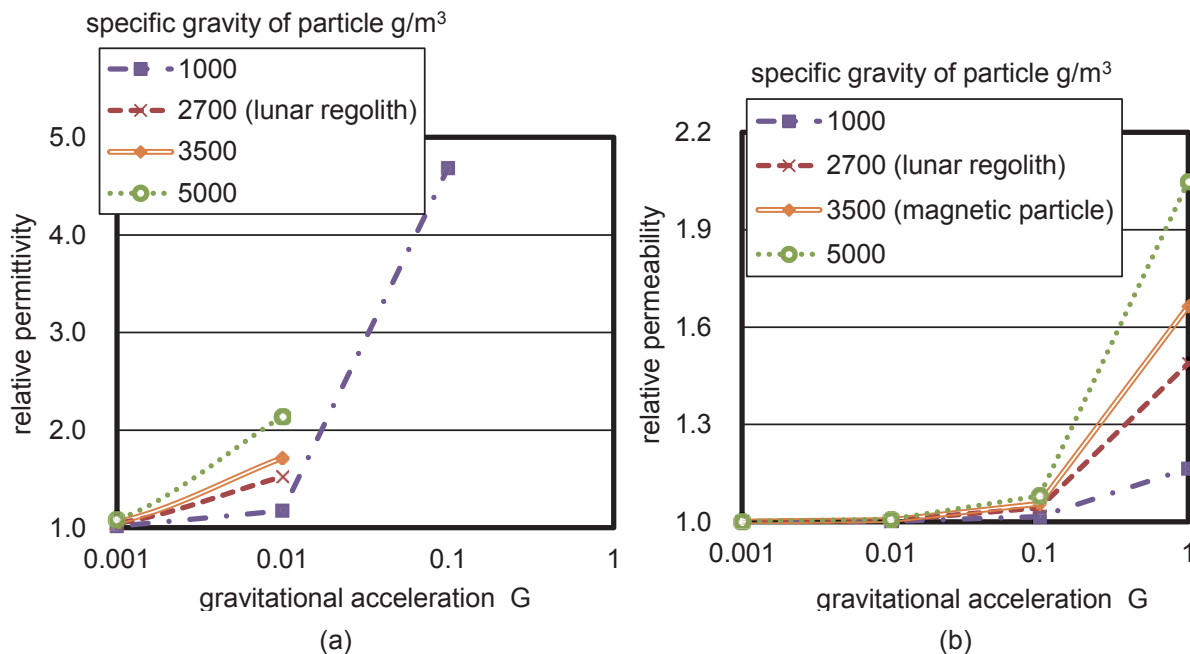


Figure 8.2 Balances between (a) dielectrophoresis force and gravitational force and (b) between magnetic force and gravitational force (Electrostatic field E and magnetic field B are calculated under conditions shown in Figures 2.14 and 2.16, respectively, and specific gravity of particle is set as parameter).

In Figure 8.2 (a), the dielectrophoresis force does not balance with the gravitational force in 1-G, and the force cannot be used to move particles in the condition. In addition, the minimum relative permittivity required to move particles decreases with respect to the gravitational acceleration and the specific gravity of the particle. In Chapter 5, the large particles, such as lunar regolith simulant, glass beads, and rocks, of which the relative permittivities are approximately 3.0, were affected by the dielectrophoresis force in 0.01-G, and the trend agrees with the calculation result. The minimum relative permittivity is close to 1.0 in conditions less than 0.001-G; therefore, the relative permittivity of the particle is not critical to successful agitation of particles by using the electrostatic force in a low-G environment. The conductivity of the particle is an important influence on the dielectrophoresis force in low-G, as described in section 5.4. Similar to the calculation result for the dielectrophoresis force, the minimum relative magnetic permeability required to move particles decreases with respect to the gravitational acceleration and the specific gravity, as shown in Figure 8.2 (b). Section 1.1.2 listed that the magnetic permeability of lunar regolith simulant is less than approximately 1.1; therefore, sampling of the simulant is difficult in 1-G. On the other hand, the relative permeability of the magnetic particle used in Chapter 6 is 4.0, and the sampling of the particles was successfully performed in 1.0-G. Actual lunar regolith has a relative permeability of approximately 1.3, and the sampling of that on the Moon and Mars is expected. In the micro-G environment, the relative permeability does not

need to be high for successful sampling, and the sampling of particles whose permeability is low is also expected. Although the electric and magnetic parameters, such as the applied voltage, electric current, and geometry of electrodes, are not optimized in Figures 8.1 and 8.2, the calculation results can be used to determine an applicable range of particle-handling technologies using the electrostatic and magnetic forces.

8.1.2 Dynamics of Small particles in Vacuum

As described in Chapter 4, air drag can be neglected in a vacuum, and the dynamics of small particles can be controlled easily by the electrostatic and magnetic forces in a vacuum. Figure 8.3 shows the balance between air drag, adhesion force, Coulomb force, and vibrational inertial force that are applied to a particle. The calculation conditions of air drag, adhesion force, and Coulomb force were the same as that shown in Figure 2.18. In addition, the summations of Coulomb force and vibrational inertial forces, as the vibration acceleration was varied from $2-G_v$ to $2,000-G_v$, are also shown in Figure 8.3. The vibration acceleration of $2-G_v$ is almost the same as that achieved by vibration transport system developed in Chapter 7. If the amplitude and frequency of the vibrated plate are varied as the vibration velocity is fixed, the vibration acceleration increases with the frequency, as shown in Table 8.1.

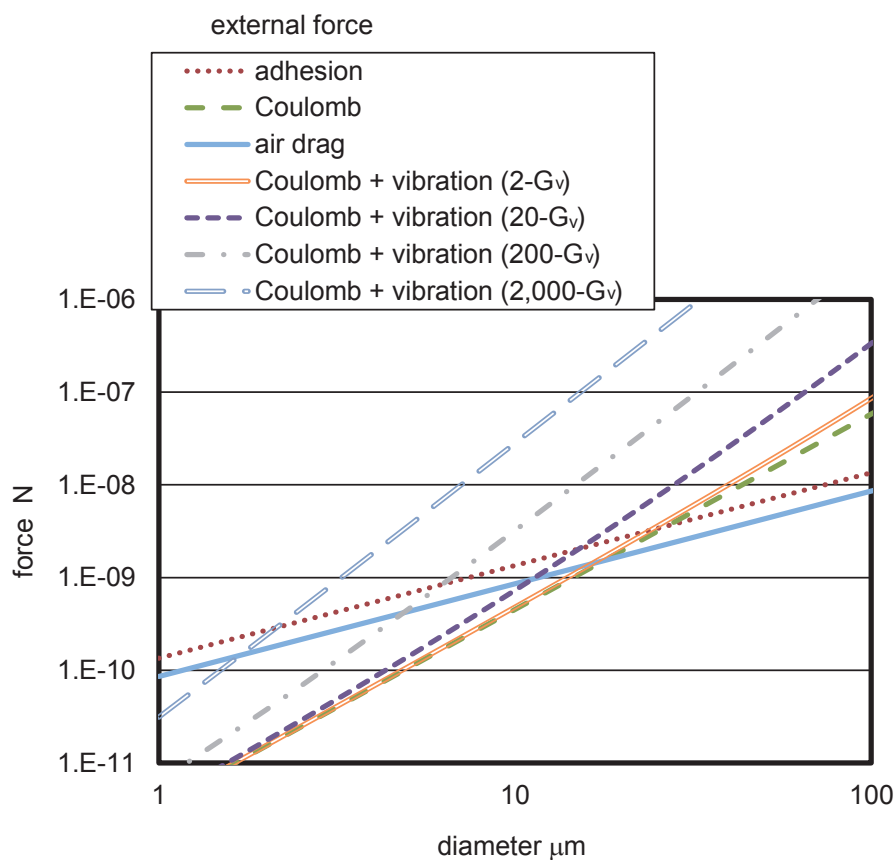


Figure 8.3 Forces acting on particle less than $100 \mu\text{m}$ in diameter (applied voltage: $10 \text{ kV}_{\text{p-p}}$, coefficient of adhesion force α : 0.00027 , specific gravity of particle: 2.7 g/cm^3 , relative permittivity ϵ_0 : 3.0 , gravitational acceleration: 9.8 m/s^2 , particle velocity: 0.5 m/s , viscosity coefficient: $1.82 \times 10^{-5} \text{ Pa}\cdot\text{s}$).

As shown in Figure 8.3, the dominant force on particles smaller than 10 μm is the adhesion force in a vacuum; therefore, mitigation of the adhesion force is important to control the particle dynamics in vacuum. As a countermeasure to the adhesion force, the vibrational inertial force can be combined with the electrostatic force. Although the vibration of 2- G_v acceleration cannot contribute to the mitigation of the adhesion force on small particles, the Coulomb force becomes dominant with respect to the acceleration of the combined vibration. The range of particles that can be moved by the Coulomb force expands with the range of vibration acceleration. In the condition of 2,000- G_v , the frequency is equal to 20 kHz, which is in the ultrasonic range, and particles that are approximately 2 μm in diameter can be moved by using ultrasonic vibration. From the results, the motions of small floating particles can be controlled using the electrostatic and magnetic forces, and the deposited small particles can be moved by the combination of the Coulomb force and ultrasonic vibration. In addition, vibration can be used to transport of particles independently, as shown in Chapter 7, as well as for the mitigation of adhesion force.

Table 8.1 Conditions of vibration transport system developed in Chapter 7 and other conditions that have same vibration speed.

Vibration acceleration G_v	Amplitude mm	Frequency Hz	Maximum velocity of vibrated plate mm/s
2 (Chapter 7)	1.2 (Chapter 7)	20 (Chapter 7)	24
20	0.12	200	24
200	0.012	2,000	24
2,000	0.0012	20,000	24

8.2 Summary of Dissertation

The mitigation and utilization of regolith particles on the Moon, Mars, and asteroids are critical to the success of future space exploration missions. It is necessary to develop regolith handling technologies that work effectively in the harsh environments of space. To that end, this research focused on building a fundamental theory for the dynamics of electromagnetic particles in space environments, and applying the theory to the development of particle handling technologies that utilize the electrostatic and magnetic forces suitable for space environments.

In Chapter 1, the background, necessity, and direction of this research were explained and compared with previous studies on particle handling technology. In particular, the variation in the balance between the external forces acting on a particle relative to its size is crucial on its dynamics, and this relationship in the space environment was set as the center of this research. In addition, handling technologies required for specific issues in exploration missions were introduced, such as the electrostatic dust shield system for manned and unmanned exploration on the Moon and Mars, the electrostatic size-sorting system for lunar and Martian ISRU, the electrostatic and magnetic samplers used for sample return missions on asteroids, and the vibration transport system for ISRU as well as for sample return.

In Chapter 2, the theoretical equations of external forces acting on the electromagnetic particle and

the theoretical model of particle motion were established. Based on the theoretical equations, the balance of the forces acting on a particle was evaluated, considering actual particle characteristics, including the mechanical, electrostatic, and magnetic properties of a lunar regolith particle. The evaluation asserts that particles ranging from 20 μm to 500 μm in diameter can be moved by the Coulomb force in a 1-G environment, and particles larger than 500 μm in diameter can be moved in a low-gravity environment similar to that on the Moon, Mars, and asteroids. The evaluation also indicated that the magnetic force can be used to move the particles in a low-gravity environment, and particles of large relative magnetic permeability can be moved in a 1-G environment. Particles smaller than 20 μm are significantly affected by the adhesion force and air drag, and it is expected that these particles can be handled easily by using the electrostatic and magnetic forces, owing to the absence of air drag in a vacuum. From the predictions, the handling technologies using the electrostatic and magnetic forces are expected to be useful in the space environment. Moreover, a numerical calculation using the modified DEM, which is critical for the completion of this research, was developed and the methodologies were explained, with reference to the abovementioned theoretical calculations. The calculation method can reduce the calculation load to 1/3,000 compared with the conventional DEM; this is one of the most important issues for the DEM. The developed method was used in later chapters.

In Chapter 3, to prevent lunar and Martian dust particles from intruding into mechanical gaps of extravehicular equipment, an electrostatic dust shield system was developed to achieve long-term exploration missions on the Moon and Mars. The performances of plate and wire type of electrostatic dust shields on the Earth, Moon, and Mars have been evaluated by conducting experiments and numerical calculations. The accuracy of the calculation method was confirmed by comparing the experimental results with those of the numerical calculations. From the results, it was confirmed that the electrostatic dust shield system could remove most of the particles that were about to intrude into the mechanical gap. The performance of the wire type was better than that of the plate type, and the shield rate reached approximately 95% for the wire type in experiments on the Earth. The electrostatic dust shield system worked well against heavily charged particles. The performance of the shield system will be improved in the lunar environment owing to the small gravitational force and the absence of air drag. If the particles are heavily charged, the shield system works effectively in the Martian environment. In addition, the power consumption of the shield system is extremely small, which is a big advantage of the system. In this chapter, the unique and unprecedented dust shield system was proposed, and the system is expected to be used in future lunar and Martian exploration missions.

In Chapter 4, an electrostatic size-sorting system was developed to obtain particles of lunar regolith smaller than 10 μm , and to synthesize the particles effectively in chemical processing for the extraction of astronaut's consumables and construction materials for exploration bases in ISRU missions. The size-sorting performance in air, vacuum, and Moon environments were evaluated by conducting experiments in a vacuum and by numerical calculations. It was confirmed that small particles had relatively large charges, compared with large particles, and the numerical calculations showed that small particles float higher than large particles in a vacuum, owing to the absence of air drag although the particles could not reach a high altitude in air. The demonstration of extracting particles smaller than 20 μm in diameter was experimentally performed in a

vacuum. From the results, the effect of the vacuum on the motion of electromagnetic particles was confirmed. In addition, the numerical calculation predicted that the size-sorting performance will be improved on the Moon, and the size-sorting system can be expected to extract particles smaller than 10 μm .

In Chapters 5 and 6, an electrostatic sampler and magnetic sampler were developed to achieve a reliable sampling of regolith particles from asteroids. The performance of the electrostatic sampler in a low-gravity environment were investigated by numerical calculations and by model experiments in 0.01-G reproduced by a parabolic flight of an aircraft. Although the sampling of lunar regolith particles did not succeed in 1-G, the sampler experimentally collected a substantial amount (~ 900 mg) containing small particles as well as particles larger than 0.5 mm in diameter in 0.01-G. The particles with conductivities exceeding $1.0 \times 10^{-8} \Omega^{-1}\text{m}^{-1}$ were significantly affected by the dielectrophoresis force; however, this force has negligible effects on particles with conductivities smaller than $1.0 \times 10^{-10} \Omega^{-1}\text{m}^{-1}$. The Coulomb force is the predominant force for the collected particles. In addition, the sampler could successfully collect glass beads 2 mm in diameter at 0.01-G and rocks 5 mm in diameter for gravitational acceleration below 0.001-G. In low gravity, although the electrostatic force creates particle bridges between electrodes owing to electric dipole moment, the sampling of particles that are not contained in the bridges was successful. The numerical calculation results agreed fairly well with the experiments in low gravity, and the results showed that the sampler performance is improved as the applied voltage is increased and the gravitational acceleration is decreased. From the results, the effect of the gravitational force on particles larger than 1 mm was clarified, and the feasibility of using the electrostatic sampler in negligible gravity was confirmed.

In Chapter 6, a magnetic sampler employing a coil gun mechanism was developed. The performance of the magnetic system in air and in a vacuum was experimentally performed, and that in low gravity was predicted in numerical calculations. The experimental results show that the electric current and the applied time to the coil mutually affect the sampler performance, and an optimum combination is a key factor for the sampling. The sampling was successful in the case of using plural pulses of electric current, and the dead time between each pulse should be set longer. The sampling also succeeded in cases even when the sampler is laid down and is not touching the particles. In addition, the interaction of magnetic particles created their chain and aggregation and contributed to the improvement of the sampler performance. Similar to the electrostatic systems, the vacuum and low gravity improve the performance. It is expected that the electrostatic and magnetic sampling can be utilized in future sample return missions.

Although the electrostatic system has some advantages, such as low-power consumption, easy control, no mechanical drives, and no contamination of impurities, the electrostatic force is small and the application is limited to the cleaning system of regolith particles, sampling system, and size-sorting systems, which do not need to move large amounts of particles. The magnetic system can be applied only to magnetic particles. For space exploration missions in which large amounts of particles have to be transported, regardless of the compositions, an additional particle handling system that has a high tolerance to dust contamination on the Moon and Mars was developed in this research. The system utilized a mechanism of vibration transport. In Chapter 7, two types of vibration transport systems were developed. First, the feasibility of vi-

bration transport was investigated by a simple model calculation of a single particle on a vibrating plate. Based on the calculation results, a unique vibration transport system that utilizes the DEA as the excitation source was developed. The transport performance in the horizontal direction was experimentally investigated. In addition, another vibration sampling and transport system was developed using an electromagnetic coil as the excitation actuator. In the development of the sampling and transport system, the transport performance in the oblique direction was investigated. Moreover, as an extension of the two vibration transport systems, the combination of the electrostatic sampler and magnetic sampler was investigated. From the calculation and experimental results, it was demonstrated that the vibration transport and vibration sampling system can transport large amounts of lunar and Martian regolith particles. The particles are transported as they slip on the vibrated plate at low vibration acceleration, or as they jump above the plate at large vibration acceleration. The large vibration acceleration and low frequency of vibration were preferable for better performance of the systems, and large particles could be transported in the horizontal direction easier than small particles because the effect of inertial force increased with particle diameter. The vibration sampling system could also transport particles in the oblique direction on the Earth as the maximum inclination was approximately 45° . In addition, the numerical calculation results indicated that the performance of the vibration transport and vibration sampling systems is improved in space environments. Moreover, although the vibration sampling system could not collect particles that did not contact the vibrating parts, the system that combined the electrostatic sampler and the magnetic sampler could collect particles without contact. As support to the electrostatic and magnetic systems, vibration transport systems that do not require mechanical drives and have high tolerance to dust contamination are expected to be used for future exploration missions on the Moon and Mars.

From results as shown in Chapters 3-7, the effect of the gravitational acceleration on large particles and the dynamics of small particles in vacuum were discussed, and the conditions of moving particles in space environments were introduced in Chapter 8. In conclusion, the basic dynamics of an electromagnetic particle in space environments could be clarified from the theoretical calculation and development processes of particle handling technologies using the electrostatic and magnetic forces. Moreover, the feasibility of the systems used for exploration missions on the Moon, Mars, and asteroids could be demonstrated in a vacuum and a low-gravity environment. It is expected that the performances of all systems will be improved in space environments, and the systems will contribute to future exploration missions.

8.3 Future Works

Although this dissertation focused on the effects of a vacuum and low gravity on the motion of electromagnetic particles, it is necessary to systematize the dynamics of particles. In particular, the effect of particle interactions with each other has not been sufficiently studied. As explained in Chapters 6 and 7, particle motion largely depends on the electrostatic and magnetic interactions in the space environment because the gravitational force and air drag are relatively small. The electrostatic and magnetic interactions are caused by elec-

trostatic and magnetic dipole moments generated in particles and the mechanisms are almost similar. Both investigations will complement each other, and an integrated theory will be developed in the future. In addition, the particle shape also affects the particle motions. The aggregation of particles was observed in Chapters 6 and 7, and the phenomenon would be caused by the mechanical interaction of particle shape. Moreover, the electrostatic and magnetic interactions would be affected by the mechanical interaction of each particle. The interactions have to be investigated together in the future, and the dynamics must be systematized.

Related to the particle shape, actual lunar and Martian regolith is slightly different from the simulant, as explained in section 1.1.2. Actual lunar regolith consists of agglutinate generated by the bombardments of micrometeorites, and its shape is more distorted than that of the simulant. In addition, actual regolith is rich in $np\text{-Fe}^0$, and it can affect the performance of the magnetic sampler, as described in Chapter 6. Martian regolith has not been sufficiently investigated, and the matching of the regolith and the simulant has to be considered. The particle characteristics significantly affect the particle dynamics and the performances of the electrostatic and magnetic handling technologies; thus, the effect of actual regolith has to be investigated.

In the case where electrostatic force is used, particle charge is one of the key factors used to handle particle motion, as described in Chapter 3. The charge is affected by the space environment, including radiation and irradiation, and the complex phenomenon of electrons, protons, and positively and negatively charged ions. The mechanism of the charging process for a particle in space has to be clarified and the unsteady effect of the charge state on particle dynamics must be considered.

Based on the insights on the effects shown above, actual designs of systems have to be considered and feasibility studies must be performed considering the harsh space environment. The electrostatic and magnetic handling technologies of particles will then be made worthy of being used for future space exploration missions. The insights will also be used for applications of the handling technologies in the Earth environment. The utilization of electrostatic force is attractive for the mitigations of air pollution, pollen scattering, and dust depositions of solar panels, glass of building materials, monitoring cameras. The electrostatic force is capable of autonomous cleaning for small particles without mechanical drives, frequent maintenances, and large power consumption. Moreover, the electrostatic cleaning of dust has adoptability to harsh environments similar to the space environment, such as in a desert, vacuum equipment, and dangerous places for human to access. In addition, industrial applications as well as the mitigation use of electrostatic and magnetic handling technologies are also expected. The transport of particles from one place to another is a fundamental process in many manufacturing fields, such as pharmaceutical, cosmetics, steel, and food industries. Although the electrostatic and magnetic handling technologies cannot move large amounts of particles, as similar to mechanical and pneumatic systems, those have advantages on precision manipulation of particles and prevention from contaminations. Applications of these technologies are expected to improve quality of products made of particles. As described above, insights about dynamics of electromagnetic particles will be used in the Earth as well as in space environments, and the handling technologies of particles using the electrostatic and magnetic forces have potentials to generate innovation in any fields.

Acknowledgments

The author would like to highlight his appreciation for all the support and supervision from Prof. H. Kawamoto (Waseda Univ.), who has supported the author's work as well as his daily life with kindness and generosity. This study could not have been established without the help from Prof. H. Kawamoto. The author would also like to thank Prof. J. Tomioka, Prof. E. Iwase, Prof. H. Okuno (Waseda Univ.), and Prof. T. Hashimoto (JAXA) for their comments and helpful discussions on this dissertation.

The parabolic flights for experiments in low-G and the experimental set-up for creating a vacuum environment were supplied by the Japan Aerospace Exploration Agency (JAXA). In addition, the author is grateful to Dr. T. Hoshino, Dr. S. Wakabayashi, Dr. S. Hosoda, and Dr. M. Sudo (JAXA) for their useful comments on experiments in vacuum, and also to K. Sakamoto, and S. Yoshihara (Japan Aerospace Technology Foundation) for their support in conducting the experiments.

The author is thankful to Dr. T. Nakayama, Dr. T. Ito, Dr. K. Tada (Fuji Xerox Co., Ltd.), Prof. T. Sugiura, his laboratory members (Keio Univ.), Prof. S. Umezu, his laboratory members (Waseda Univ.), and Dr. J. Agui, and his colleagues (National Aeronautics and Space Administration, NASA) for providing useful comments based on their expertise. In addition, the author received an opportunity to be a visiting researcher in Prof. G. T.-C. Chiu's laboratory at Purdue Univ., where he was able to obtain new insights during the visit. Therefore, the author would like to thank Prof. G. T.-C. Chiu, N. Bajaj, A. Kumra, J. R. Thomas, J. Wang, W. Chen, L. Ye, and K. Zheng for their comprehensive supports.

The author thanks T. Shibata, W. Suzuki, S. Watanabe, K. Toide, Y. Hashi, I. Tsushima, Y. Kainuma, A. Nishiyama, M. Ikeda, S. Kanda, K. Ashiba, H. Hoshino, H. Maezono, H. Suda, N. Tajima, K. Nogami, S. Inari, Y. Kadono, T. Kojima, A. Shigeta, Y. Haga, Y. Mimuro, K. Kodachi, R. Sawai, S. Fukuyama, R. Suzuki, T. Sakata, H. Teguri, M. Kato, H. Moroka, S. Kojima, R. Obata, N. Takeda, A. Haga, K. Hamazawa, and K. Ikuta (Waseda Univ.) for supporting and conducting experiments and numerical calculations,

A part of this work is supported by a Grant-in-Aid for Japan Society for the Promotion of Science Research Fellow Number 16J10635 and the Program for Leading Graduate Schools, "Graduate Program for Embodiment Informatics" of the Ministry of Education, Culture, Sports, Science and Technology.

Finally, I would like to express my most sincere thanks to my family for their ongoing and sacrificial support throughout my studies as well as my life, and the deepest gratitude to my wife, Yurina.

Acknowledgments to the Program of Embodiment Informatics

The author belongs to the Department of Applied Mechanics, from the Graduate School of Fundamental Science and Engineering in Waseda University, as well as the Program for Leading Graduate Schools, “Graduate Program for Embodiment Informatics, EI.”

What Is the Graduate Program for Embodiment Informatics?

The EI is a new scientific platform where not only graduate students, but also engineers, researchers, and entrepreneurs gather seeking to lead innovation centered on the Japanese “monozukuri” field which is a kind of manufacturing and mechanical engineering field that is well-regarded around the world while integrating it with other fields, and supporting it with informatics. This innovation would then be expected to create new technologies, to establish new bodies of knowledge, and also to create new businesses. The combination of different fields can create a frontier, which can be highlighted by the Japanese “monozukuri” field and also can be developed rapidly by means of the information and communication technologies. For example, a new surgery support system can be realized by combining precision robotics and knowledge of surgery with high-speed data processing human interfaces. In addition, deep space exploration can be further developed by an autonomous spacecraft that is realized using knowledge of propulsion engineering and planetary science, controlled by an artificial intelligent that can assess the spacecraft’s own condition to then generate adequate instructions to itself. The students in the EI program can obtain this new knowledge, and they are expected to become leaders and bring about innovation in each of their fields.

Learning Contents in Embodiment Informatics

Students in the EI program can acquire skills to generate two types of fusions. One is the fusion of technologies. Although each student has his/her own expertise, this expertise must be combined with the “monozukuri” and informatics in the EI. Therefore, students in this program must learn the basic knowledge regarding these subjects. In the conventional education system, students learn only one field, and they will gain expertise in one subject; however, a student in the EI program can successfully develop a wider insight gaining more expertise. Moreover, it is necessary to learn the ability to integrate advanced technologies in a broad range of fields. A mere combination of technologies can be easily achieved by anyone, but the inimitable and competitive technology can only be realized by talented individuals who have been educated in a comprehensive program.

The second fusion is about how to collaborate with others and how to combine the new technology with the conventional technology, as well as with the social system, all this in order to generate innovation. There is a limit to what one person as well as one technology can do, and changing the social system in a short period of time is impossible; therefore, it is necessary to attract the interest and support of others, as

well as to gradually adopt the technology with the current society. The leadership and forecast abilities to identify possible areas to create the stream of innovation are also required for students in the EI program.

Lessons Learned in Embodiment Informatics

The research field of the author centers on the dynamics of electromagnetic particles in space environments and its application for the development of particle-handling technologies using electrostatic and magnetic forces. This new field requires knowledge of the “monozukuri” field, including mechanical engineering, electromagnetics, aerospace engineering, and granular dynamics. Moreover, as frequent experiments in space environments are impossible because of the cost and preparation time, information technology, including programming, numerical simulation, and parallel computing, is critical to the effective progression of this research field. However, as only conducting numerical calculations may not be enough to validate the accuracy of calculation results, demonstrations in space environments, including low-G and vacuum environments, are important to compare with the numerical calculations. Therefore, a combination of the experiments performed on the Earth, the experiments performed in reproduced space environments, and numerical calculations, are all necessary. This research was aided by discussions with supervisors, internal and external experts (such as researchers in JAXA and NASA), and also professors in the field of information technology. The imagination needed to integrate the technology and to set the research objective was cultivated through the discussion process. This research proposal has been highly valued in related fields, and the author was accepted into the Research Fellowship for Young Scientists in the Japan Society for the Promotion of Science.

To realize the combination of the author’s research with informatics fields, the author, whose major is the mechanical engineering, has learned the basics of information technology in the EI program. Moreover, the class of parallel computing was planned and conducted with a professor in the program. From the experience of this class, the author was able to reduce the calculation load to approximately 1/3000 of the conventional method. As described above, the author was able to achieve wider insights and integration skills of technologies in this program.

Regarding to the strategy required to develop technology, the author gained leadership skills in this program. In his study, experiments in low-G and vacuum environments are necessary, but the equipment for these experiments is not affordable. Therefore, the author proposed that the parabolic flight of an aircraft to reproduce low-G to be shared with other research groups to decrease the cost. He also proposed the collaboration with JAXA who owns the vacuum chambers. The meeting with other groups and members in JAXA was set and the proposal to borrow the vacuum chamber in JAXA was created. Then, both experiments, which are a key in this dissertation, were realized. The leadership skill to involve others to get closer to the goal was achieved throughout the program. Moreover, the author visited various companies, universities, and space agencies across the world during the EI program and gave a lecture on the work of this dissertation.

The author did this to spread the developed technology to different research groups in order to evolve the stream of innovation. During this lecture, the experience in the Graduate School of Science and Engineering English for Science and Technology Program in U.C. Davis, that is one of the curriculums of the EI program, effectively worked to attract the interest of the researchers in those institutions. Effective presentation skills were developed in this English program to the extent in which the author got four awards. As a result of giving the lectures, collaborations with some research groups have been realized.

To become a person who can play an important role in any place as well as in any field, the author has experienced the process of planning and creating innovation not only in his own study, but also in another project that focused on the development of infrastructure in developing countries. In this project, the author and other members in the EI program visited Vietnam and Thailand to conduct field studies to find the latent needs of the railway systems in those countries. Moreover, they held meetings with persons in the industry, government, and academia fields not only in Japan, but also in Vietnam and Thailand. From the discussions and results of the field studies, new concepts for the railway systems for these countries were created, and the strategy to develop the railway was also able considered. The results were summarized in a research paper and the presentation of the work was performed in an international conference. The members in the program were able to get invaluable insights in the business and administrative fields from this experience.

Throughout the EI program, the author gained comprehensive skills to create innovation. The author would like to express his gratitude to the EI program and all the people in the program who supported the author's work and activities.

References

Chapter 1

- [1] Vaniman, D., et al., "Exploration, samples, and recent concepts of the Moon." *Lunar sourcebook* (1991), 5-26.
- [2] Racca, G. D., et al., "SMART-1 mission description and development status." *Planetary and space Science* **50**, 14 (2002), 1323-1337.
- [3] Kato, M., et al., "The Kaguya mission overview." *Space Science Reviews* **154**, 1-4 (2010), 3-19.
- [4] Li, C., et al., "The Chang'e 3 Mission Overview." *Space Science Reviews* **190**, 1-4 (2015), 85-101.
- [5] Goswami, J. N., Annadurai, M., "Chandrayaan-1: India's first planetary science mission to the moon." *Curr. Sci* **96**, 4 (2009), 486-491.
- [6] Paige, D. A., et al., "Diviner lunar radiometer observations of cold traps in the Moon's south polar region." *Science* **330**, 6003 (2010), 479-482.
- [7] Golombek, M. P., et al., "Overview of the Mars Pathfinder mission and assessment of landing site predictions." *Science* **278**, 5344 (1997), 1743-1748.
- [8] Soderblom, L. A., et al., "Soils of Eagle Crater and Meridiani Planum at the Opportunity rover landing site." *Science* **306**, 5702 (2004), 1723-1726.
- [9] Grotzinger, J. P., "Analysis of surface materials by the Curiosity Mars rover." *Science* **341**, 6153 (2013), 1475-1475.
- [10] Williams, R. M., et al., "Martian fluvial conglomerates at Gale crater." *Science* **340**, 6136 (2013), 1068-1072.
- [11] Veverka, J., et al. "The landing of the NEAR-Shoemaker spacecraft on asteroid 433 Eros." *Nature* **413**, 6854 (2001), 390-393.
- [12] Robinson, M. S., et al., "The nature of ponded deposits on Eros." *Nature* **413**, 6854 (2001), 396-400.
- [13] Yano, H., et al., "Touchdown of the Hayabusa spacecraft at the Muses Sea on Itokawa." *Science* **312**, 5778 (2006), 1350-1353.
- [14] Hörz, F., et al., "Impact features on Stardust: Implications for comet 81P/Wild 2 dust." *Science* **314**, 5806 (2006), 1716-1719.
- [15] Glassmeier, K., et al., "The Rosetta mission: flying towards the origin of the solar system." *Space Science Reviews* **128**, 1-4 (2007), 1-21.
- [16] Hand, E., "Touch and go." *Science* **345**, 6196 (2014), 504-505.
- [17] Tsuda, Y., et al., "System design of the Hayabusa 2-asteroid sample return mission to 1999 JU3." *Acta Astronautica* **91** (2013), 356-362.
- [18] Lauretta, D. S., OSIRIS-Rex Team., "An overview of the OSIRIS-REx asteroid sample return mission." *Lunar and Planetary Science Conference* **43** (2012), 2491.
- [19] Beshore, E., et al., "The OSIRIS-REx asteroid sample return mission." *2015 IEEE Aerospace Conference* (2015), 1-14.

- [20] Colwell, J. E., et al. "Lunar surface: Dust dynamics and regolith mechanics." *Reviews of Geophysics* **45**, (2007).
- [21] McKay, D. S., et al., "The lunar regolith." *Lunar sourcebook* (1991), 285-356.
- [22] Noguchi, T., et al., "Incipient space weathering observed on the surface of Itokawa dust particles." *Science* **333**, 6046 (2011), 1121-1125.
- [23] Nakamura, E., et al., "Space environment of an asteroid preserved on micrograins returned by the Hayabusa spacecraft." *Proceedings of the National Academy of Sciences* **109**, 11 (2012), E624-E629.
- [24] Tsuchiyama, A., et al., "Three-dimensional structure of Hayabusa samples: origin and evolution of Itokawa regolith." *Science* **333**, 6046 (2011), 1125-1128.
- [25] Shimizu Corporation, Lunar resource utilization <Lunar soil simulant> Shimizu leaflet (1997) (in Japanese).
- [26] Kanamori, H., et al., "Properties of lunar soil simulant manufactured in Japan." *Space* **98** (1998), 462-468.
- [27] Zeng, X., et al., "Geotechnical properties of JSC-1A lunar soil simulant." *Journal of Aerospace Engineering* **23**, 2 (2009), 111-116.
- [28] Iai, M., Ronaldo L., "Direct shear tests on JSC-1A lunar regolith simulant." *Journal of Aerospace Engineering* **24**, 4 (2010), 433-441.
- [29] Ray, C. S., et al., "JSC-1A lunar soil simulant: Characterization, glass formation, and selected glass properties." *Journal of Non-Crystalline Solids* **356**, 44 (2010), 2369-2374.
- [30] Ethridge, E. C., William, K., "Microwave Processing of Planetary Surfaces for the Extraction of Volatiles." *49th AIAA Aerospace Sciences Meeting Including the New Horizons Forum and Aerospace Exposition*, (2011), 612.
- [31] Carrier, W. D., Gary R. O., Wendell M., "Physical properties of the lunar surface." *Lunar sourcebook* (1991): 475-594.
- [32] Gast, P. W., et al., "The Apollo 15 lunar samples: A preliminary description." *Science* **175** (1972), 363-375.
- [33] Liu, Y., et al., "Unique properties of lunar impact glass: Nanophase metallic Fe synthesis." *American Mineralogist* **92**, 8-9 (2007), 1420-1427.
- [34] Allen, C. C., et al., "Martian soil simulant available for scientific, educational study." *Eos, Transactions American Geophysical Union* **79**, 34 (1998), 405-409.
- [35] Rover Team, "Characterization of the Martian surface deposits by the Mars Pathfinder rover, Sojourner." *Science* **278**, 5344 (1997), 1765-1768.
- [36] Rieder, R., et al., "The chemical composition of Martian soil and rocks returned by the mobile alpha proton X-ray spectrometer: Preliminary results from the X-ray mode." *Science* **278**, 5344 (1997), 1771-1774.
- [37] Goetz, W., et al., "The nature of Martian airborne dust. Indication of long-lasting dry periods on the surface of Mars." *LPI Contributions* **1353** (2007), 3104.
- [38] Goetz, W., et al., "Microscopic Views of Martian Soils and Evidence for Incipient Diagenesis." *LPI Contributions* **1791** (2014), 1443.

- [39] Wagner, S., "The Apollo experience lessons learned for constellation lunar dust management." *TP-2006-213726* (2006).
- [40] Wagner, S., "Asteroid, Lunar and Planetary Regolith Management A Layered Engineering Defense." *NASA Technical Report* (2014), 20140011751
- [41] Jaffe, L. D., "Blowing of lunar soil by Apollo 12: Surveyor 3 evidence." *Science* **171**, 3973 (1971), 798-799.
- [42] Grün, E. M., et al., "The lunar dust environment." *Planetary and Space Science* **59**, 14 (2011), 1672-1680.
- [43] Abbas, M. M., et al., "Lunar dust charging by photoelectric emissions." *Planetary and Space Science* **55**, 7 (2007), 953-965.
- [44] Abbas, M. M., et al., "Lunar dust grain charging by electron impact: complex role of secondary electron emissions in space environments." *The Astrophysical Journal* **718**, 2 (2010), 795.
- [45] McCoy, J. E., David, R. C., "Evidence for a high altitude distribution of lunar dust." *Lunar and Planetary Science Conference Proceedings B* (1974), 2991-3005.
- [46] Criswell, D. R., "Horizon-glow and the motion of lunar dust." *Photon and particle interactions with surfaces in space* (1973), 545-556.
- [47] Mazumder, M. K., et al., "Lunar and Martian dust dynamics." *IEEE Industry Applications Magazine* **16**, 4 (2010), 14-21.
- [48] Wagner, S., "An assessment of dust effects on planetary surface systems to support exploration requirements." *NASA Technical Report* (2004), 20080047665.
- [49] Gaier, J. R., "The effects of lunar dust on EVA systems during the Apollo missions." *NASA Technical Report* (2005), 20050160460.
- [50] Christoffersen, R., et al., "Lunar dust effects on spacesuit systems: insights from the Apollo spacesuits." *NASA Technical Report* (2008), 20090015239.
- [51] Thomas, P., Peter J. G., "Dust devils on Mars." *Science* **230**, 4722 (1985), 175-177.
- [52] Greeley, R., et al. "Active dust devils in Gusev crater, Mars: observations from the Mars exploration rover spirit." *Journal of Geophysical Research: Planets* **111**, E12 (2006).
- [53] Snyder, S. J., et al., "Triboelectric charging of dust and its relation to organic degradation on Mars." *Proceedings of the ESA Annual Meeting on Electrostatics* (2008).
- [54] Sternovsky, Z., et al., "Contact charging of lunar and Martian dust simulants." *Journal of Geophysical Research: Planets* **107**, E11 (2002).
- [55] Vaughan, A. F., et al., "Pancam and Microscopic Imager observations of dust on the Spirit Rover: Cleaning events, spectral properties, and aggregates." *International Journal of Mars Science and Exploration* **5** (2010), 129-145.
- [56] Anderson, R. C., et al. "Particle transport and distribution on the Mars Science Laboratory mission: Effects of triboelectric charging." *Icarus* **204**, 2 (2009), 545-557.
- [57] Taylor, L. A., et al. "The lunar dust problem: from liability to asset." *AIAA 1st Space Exploration Mission* (2005).

- [58] Sanders, G. B., William E. L., "Integration of In-Situ Resource Utilization into lunar/Mars exploration through field analogs." *Advances in Space Research* **47**, 1 (2011), 20-29.
- [59] Sanders, G. B., William E. L., "Progress made in lunar in situ resource utilization under NASA's exploration technology and development program." *Journal of Aerospace Engineering* **26**, 1 (2012), 5-17.
- [60] Platts, W. J., et al., "Prospecting for native metals in lunar polar craters." *Proceedings of the American Institute of Aeronautics and Astronautics 7th Symposium on Space Resource Utilization* **338** (2014), 1-13.
- [61] Crawford, I. A., "Lunar resources: A review." *Progress in Physical Geography*, (2015), 0309133314567585.
- [62] Allton, J. H. "Lunar Samples: Apollo Collection Tools, Curation Handling, Surveyor III and Soviet Luna Samples." *Lunar Regolith Simulant Workshop* (2009).
- [63] Klein, H. P., "The Viking mission and the search for life on Mars." *Reviews of Geophysics* **17**, 7 (1979), 1655-1662.
- [64] Zacny, K., et al., "Honeybee Robotics approach to technology development and infusion." *Aerospace Conference 2010* (2010), 1-7.
- [65] Anderson, R. C., et al., "Collecting samples in Gale Crater, Mars; an overview of the Mars Science Laboratory sample acquisition, sample processing and handling system." *Space Science Reviews* **170**, 1-4 (2012), 57-75.
- [66] Finzi, A. E., et al., "SD2—How to sample a comet." *Space science reviews* **128**, 1-4 (2007), 281-299.
- [67] Mueller, R. P., Ivan T., "Lunar regolith simulant feed system for a hydrogen reduction reactor system." *47th AIAA Aerospace Sciences Meeting* (2009).
- [68] Mueller, R. P., Paul, J. V. S., "A review of lunar regolith excavation robotic device prototypes." *Space* (2011).
- [69] Sullivan, T. A., et al., "Pneumatic conveying of materials at partial gravity." *Journal of Aerospace Engineering* **7**, 2 (1994), 199-208.
- [70] Zacny, K, et al., "Investigating the efficiency of pneumatic transfer of JSC-1a lunar regolith simulant in vacuum and lunar gravity during parabolic flights." *AIAA Space*, (2010).
- [71] Mantovani, J. G., Ivan I. T., "Planetary regolith delivery systems for ISRU." *Journal of Aerospace Engineering* **26**, 1 (2012), 169-175.
- [72] The Institute of Electrostatics Japan. "Electrostatics Handbook." Ohmsha (1981). (in Japanese)
- [73] Clements, J. S., et al., "Development of an electrostatic precipitator to remove Martian atmospheric dust from ISRU gas intakes during planetary exploration missions." *IEEE Transactions on Industry Applications* **49**, 6 (2013), 2388-2396.
- [74] Calle, C. I., et al. "An electrostatic precipitator system for the Martian environment." *Journal of Electrostatics* **71**, 3 (2013), 254-256.
- [75] The Imaging Society of Japan "Electrophotography - Process and Simulation -." Tokyo Denki University Press (2008). (in Japanese)

- [76] Kawamoto, H., Hiratsuka, T., "Statics and dynamics of carrier particles in two-component magnetic development system in electrophotography." *Journal of Imaging Science and Technology* **53**, 6 (2009), 60201-1.
- [77] Kawamoto, H., Adachi, M., "Numerical simulation and direct observation of dynamics of toner and carrier particles in electrophotographic two-component magnetic brush development system." *Journal of the Imaging Society of Japan* **52**, 6 (2013), 547-554.
- [78] Kawamura, J., et al. "Effect of toner charge on developing behavior in two-component electrophotographic system by discrete element method." *Journal of Imaging Science and Technology* **53**, 1 (2009), 10505-1.
- [79] Masuda, S. K., et al., "Confinement and transportation of charged aerosol clouds via electric curtain." *Electrical Engineering in Japan* **92**, 1 (1972), 43-52.
- [80] Masuda, S., Matsumoto, Y., "Theoretical characteristics of standing-wave electric curtains." *Electrical Engineering in Japan* **93**, 1 (1973): 71-77.
- [81] Moesner, F. M., Higuchi, T., "Devices for particle handling by an AC electric field." *Micro Electro Mechanical Systems 1995*, (1995), 66.
- [82] Kawamoto, H., Seki, K., "Mechanism on traveling-wave transport of particles." *NIP & Digital Fabrication Conference 2004*, 2 (2004), 1019-1026.
- [83] Mazumder, M., et al., "Characterization of electrodynamic screen performance for dust removal from solar panels and solar hydrogen generators." *IEEE Transactions on Industry Applications* **49**, 4 (2013), 1793-1800.
- [84] Horenstein, M. N., et al., "Predicting particle trajectories on an electrodynamic screen-theory and experiment." *Journal of Electrostatics* **71**, 3 (2013), 185-188.
- [85] Kawamoto, H., Shibata, T., "Electrostatic cleaning system for removal of sand from solar panels." *Journal of Electrostatics* **73** (2015), 65-70.
- [86] Sayyah, A., et al., "Energy yield loss caused by dust deposition on photovoltaic panels." *Solar Energy* **107** (2014), 576-604.
- [87] Guo, B., et al. "Effect of dust and weather conditions on photovoltaic performance in Doha, Qatar." *Smart Grid and Renewable Energy (SGRE)*, (2015), 1-6.
- [88] Adams, J. G., et al. "Lunar Dust Degradation Effects and Removal/prevention Concepts. Volume 1-Summary Final Report." *NASA-CR-93594, TR-792-7-207A* (1967).
- [89] Calle, C. I., et al. "Dust particle removal by electrostatic and dielectrophoretic forces with applications to NASA exploration missions." *Proc. ESA Annual Meeting on Electrostatics*, (2008).
- [90] Calle, C. I., et al. "Reduced gravity flight demonstration of the dust shield technology for optical systems." *2009 IEEE Aerospace conference*. (2009).
- [91] Calle, C. I., et al. "Active dust control and mitigation technology for lunar and Martian exploration." *Acta Astronautica* **69**, 11 (2011), 1082-1088.
- [92] Johansen, M. R., et al. "History and Flight Development of the Electrodynamic Dust Shield." *AIAA SPACE 2015 Conference and Exposition*, 2015.
- [93] Kawamoto, H., et al. "Mitigation of lunar dust on solar panels and optical elements utilizing electrostatic traveling-wave." *Journal of Electrostatics* **69**, 4 (2011), 370-379.

- [94] Afshar-Mohajer, N., et al., "Efficiency determination of an electrostatic lunar dust collector by discrete element method." *Journal of Applied Physics* **112**, 2 (2012), 023305.
- [95] Afshar-Mohajer, N., et al. "Design of an electrostatic lunar dust repeller for mitigating dust deposition and evaluation of its removal efficiency." *Journal of Aerosol Science* **69** (2014), 21-31.
- [96] Kawamoto, H., Hara, N., "Electrostatic cleaning system for removing lunar dust adhering to space suits." *Journal of Aerospace Engineering* **24**, 4 (2010), 442-444.
- [97] Kawamoto, H., Inoue, H., "Magnetic cleaning device for lunar dust adhering to spacesuits." *Journal of Aerospace Engineering* **25**, 1 (2011), 139-142.
- [98] Trigwell, S., et al. "The use of tribocharging in the electrostatic beneficiation of lunar simulant." *IEEE Transactions on Industry Applications* **45**, 3 (2009), 1060-1067.
- [99] Trigwell, S., et al. "Electrostatic Beneficiation of Lunar Regolith: Applications in In Situ Resource Utilization." *Journal of Aerospace Engineering* **26**, 1 (2012), 30-36.
- [100] Mironovs, V., Viba, J., "Elevator for Iron Powders." (2007). *European Congress and Exhibition on Powder Metallurgy. European PM Conference Proceedings; Shrewsbury* **2.1** (2007), 39-43.
- [101] Lapkovskis, V., et al. "Conveying of ferromagnetic powder materials by pulsed electromagnetic field." *In: Euro PM2011 – Tools for Improving PM: Modelling & Process Control, Spain, Barcelona* (2011), 253-258.
- [102] Lapkovskis, V., Mironovs, V., "Single-stage electromagnetic elevator modelling in FEMM software." *8th International DAAAM Baltic Conference* (2012), 321-325.
- [103] Mironovs, V., et al. "Applications of Pulsed Electromagnetic Fields in Powder Materials High Speed Forming." *6th International Conference on High Speed Forming*, (2014).
- [104] Andrews, J. A. "Coilgun structures." *IEEE transactions on magnetics* **29**, 1 (1993), 637-642.
- [105] Coşkun, I., et al. "Optimization of parameters acting on a projectile velocity within a four stage induction coil-gun." *Measurement* **43**, 10 (2010), 1656-1660.
- [106] Lee, S., et al. "Coil gun electromagnetic launcher (EML) system with multi-stage electromagnetic coils." *J. Magn* **18**, 4 (2013), 481-486.
- [107] Cundall, P. A., Strack, O. L., "A discrete numerical model for granular assemblies." *Geotechnique* **29**, 1 (1979), 47-65.
- [108] Tsuji, Y., et al., "Cluster patterns in circulating fluidized beds predicted by numerical simulation (discrete particle model versus two-fluid model)." *Powder Technology* **95**, 3 (1998), 254-264.
- [109] Hoomans, B. P. B., et al. "Experimental validation of granular dynamics simulations of gas-fluidized beds with homogenous in-flow conditions using positron emission particle tracking." *Powder Technology* **116**, 2 (2001), 166-177.
- [110] Deen, N. G., et al. "Review of discrete particle modeling of fluidized beds." *Chemical Engineering Science* **62**, 1 (2007), 28-44.
- [111] Matsushima, T., Saomoto, H., "Discrete element modeling for irregularly-shaped sand grains." *Proc. NUMGE2002: Numerical methods in geotechnical engineering, Mestat (ed.)* (2002), 239-246.
- [112] Matsushima, T., et al. "Discrete element simulation of an assembly of irregularly-shaped grains: Quantitative comparison with experiments." *16th ASCE Engineering Mechanics Conference* (2003).

- [113] Suzuki, M., et al., "Experimental study on a brush-type seal in air and in vacuum as a candidate for regolith seal applications." *Proc., 54th Space Sciences and Technology Conf.* (2010). (in Japanese)
- [114] Suzuki, et al., "Long-term experiments in vacuum on a brush-type seal as a candidate for regolith seal applications." *Mechanical Engineering Congress Japan 2011*, J192033 (2011). (in Japanese)
- [115] Suzuki, M., et al., "Study on Dust Seal for Activity on the Moon-Evaluation of Properties in Air-." *Proc., 52th Space Sciences and Technology Conf.* (2008). (in Japanese)
- [116] Delgado, I. R., Handschuh, M. J., "Preliminary assessment of seals for dust mitigation of mechanical components for lunar surface systems." *NASA Technical Report* (2010), 20100025844.
- [117] Herman, J., et al. "Dust-Tolerant Connector Development for Lunar Surface Systems." *2009 AIAA Space Conference Proceedings* (2009).
- [118] Taylor, L. A., et al. "Lunar mare soils: Space weathering and the major effects of surface-correlated nanophase Fe." *Journal of Geophysical Research: Planets* **106**, E11 (2001), 27985-27999.
- [119] Taylor, L. A., "Hot-pressed iron from lunar soil." *Space Resources Roundtable II*, **1**, (2000).
- [120] Taylor, L. A., Meek, T. T., "Microwave sintering of lunar soil: properties, theory, and practice." *Journal of Aerospace Engineering* **18**, 3 (2005), 188-196.
- [121] Wilkinson, A., "Size beneficiation of regolith for simplicity and efficiency." *Presentation at Planetary and Terrestrial Mining and Sciences Symposium (PTMSS)* (2011).
- [122] Kubota, T., et al. "Robotics technology for asteroid sample return mission MUSES-C." *The 6th International Symposium on Artificial Intelligence, Robotics and Automation in Space: A New Space Odyssey*, (2001).
- [123] Morishita, H., et al. "Study and evaluation experiments of adhesive based sampling system for the next minorbody exploration." *Space Engineering Conference 2010*, **19** (2011). (in Japanese)
- [124] Saiki, T., et al. "Small carry-on impactor of Hayabusa2 mission." *Acta Astronautica* **84** (2013), 227-236.
- [125] Matunaga, S., et al. "Result of micro-gravity experiment using parabolic flight for tethered recovery in tethered sampling method." *Transactions of The Japan Society For Aeronautical and Space Sciences, Space Technology Japan* **7 ists26** (2009), Pk_23-Pk_28.
- [126] Watanabe, T., et al. "Micro gravity experiment and 3 dimensional dynamic analysis of tethered sampler." *Transactions of the Japan Society for Aeronautical and Space Sciences, Space Technology Japan* **7 ists26**, (2009), Pk_17-Pk_22.
- [127] Bonitz, R., "The brush wheel sampler-A sampling device for small-body touch-and-go missions." *Aerospace Conference* (2012).
- [128] Clark, D. L., et al., "A novel approach to planetary regolith collection: the bucket drum soil excavator." *AIAA Space 2009 Conference & Exposition* **2**, 6. (2009).
- [129] Younse, P., et al. "Sample acquisition and caching using detachable scoops for Mars sample return." *2009 IEEE Aerospace conference* (2009).
- [130] Zacny, K., et al. "Asteroids: Anchoring and Sample Acquisition Approaches in Support of Science, Exploration, and In Situ Resource Utilization." Springer Berlin Heidelberg (2013), 287-343.

- [131] Zacny, K., et al. "Mars 2020 sample acquisition and caching technologies and architectures." *2014 IEEE Aerospace Conference* (2014).
- [132] Eimer, B. C., Taylor, L. A., "Lunar regolith, soil, and dust mass mover on the Moon." *Lunar and Planetary Science Conference* **38**, (2007).

Chapter 2

- [1] The Institute of Electrostatics Japan, *The handbook of electrostatics* (1998), pp.1193-1196, Ohmsha (in Japanese).
- [2] Abbas, M. M., et al., "Lunar dust charging by photoelectric emissions." *Planetary and Space Science* **55**, 7 (2007), 953-965.
- [3] Abbas, M. M., et al., "Lunar dust grain charging by electron impact: complex role of secondary electron emissions in space environments." *The Astrophysical Journal* **718**, 2 (2010), 795.
- [4] Sternovsky, Z, et al., "Contact charging of lunar and Martian dust simulants." *Journal of Geophysical Research: Planets* **107**, E11 (2002).
- [5] Schein, L. B., Czarnecki, W. S., "Proximity theory of toner adhesion." *Journal of Imaging Science and Technology* **48**, 5 (2004), 412-416.
- [6] The Imaging Society of Japan "Electrophotography - Process and Simulation -." Tokyo Denki University Press (2008). (in Japanese)
- [7] Jones, T. B., "Electromechanics of particles." Cambridge University Press (1975), 5-8.
- [8] Imura, H., "Study on Adhesion and Transfer of Toner Particles in Electrophotography Process." Waseda University (2013) (in Japanese. doctoral dissertation).
- [9] The Society of Powder Technology Japan, "Fundamental properties of powder." *Nikkan Kogyo Shimbun* (2005), 227-231, (in Japanese).
- [10] National Astronomical Observatory of Japan, "Chronological scientific tables." Maruzen (2008), 378 (in Japanese).
- [11] Munakata, T., "Note on Cunningham correction factor." *Journal of the Society of Powder Technology* **40** (1990), pp.91-97 (in Japanese).
- [12] Davies, C.N., "Definitive equations for the fluid resistance of spheres." *Proceedings of the Physical Society* **57**, 4 (1945), 259-270.
- [13] Komiya, M., "Wakariyasui shinkugijutsu." Ohmsha (2002), 9-12 (in Japanese).
- [14] Cundall, P. A., Otto DL S., "A discrete numerical model for granular assemblies." *Geotechnique* **29.1** (1979): 47-65.
- [15] Kawamoto, H., Adachi, M., "Numerical simulation and direct observation of dynamics of toner and carrier particles in electrophotographic two-component magnetic brush development system." *Journal of the Imaging Society of Japan* **52**, 6 (2013), 547-554.
- [16] Deen, N. G., et al. "Review of discrete particle modeling of fluidized beds." *Chemical Engineering Science* **62**, 1 (2007), 28-44.

- [17] Hoomans, B. P. B., et al. "Experimental validation of granular dynamics simulations of gas-fluidized beds with homogenous in-flow conditions using positron emission particle tracking." *Powder Technology* **116**, 2 (2001), 166-177.
- [18] Adachi, M., Kawamoto, H., "Electrostatic Sampler for Large Regolith Particles on Asteroids." *Journal of Aerospace Engineering* (2016) in press.
- [19] Adachi, M., Kawamoto, H., "Electrostatic dust shield system used for Lunar and Mars exploration equipment." *Trans. JSME* **81**, 821 (2015), 14-00224-14-00224 (in Japanese).
- [20] Allen, M. P., "Computer simulation of liquids." Oxford University Press (1987), 102-103.

Chapter 3

- [1] Gaier, J. R., "The effects of lunar dust on EVA systems during the Apollo missions." *NASA Technical Report* (2005), 20050160460.
- [2] Suzuki, M., et al., "Experimental study on a brush-type seal in air and in vacuum as a candidate for regolith seal applications." *Proc., 54th Space Sciences and Technology Conf.* (2010). (in Japanese)
- [3] Suzuki, et al., "Long-term experiments in vacuum on a brush-type seal as a candidate for regolith seal applications." *Mechanical Engineering Congress Japan 2011* (2011), J192033. (in Japanese)
- [4] Suzuki, M., et al., "Study on Dust Seal for Activity on the Moon-Evaluation of Properties in Air-." *Proc., 52th Space Sciences and Technology Conf.* (2008). (in Japanese)
- [5] Delgado, I. R., Handschuh, M. J., "Preliminary assessment of seals for dust mitigation of mechanical components for lunar surface systems." *NASA Technical Report* (2010), 20100025844.
- [6] Herman, J., et al. "Dust-Tolerant Connector Development for Lunar Surface Systems." *2009 AIAA Space Conference Proceedings* (2009).
- [7] Adachi, M., Kawamoto, H., "Electrostatic dust shield system used for Lunar and Mars exploration equipment." *Trans. JSME* **81**, 821 (2015), 14-00224 (in Japanese).
- [8] Rover Team, "Characterization of the Martian surface deposits by the Mars Pathfinder rover, Sojourner." *Science* **278**, 5344 (1997), 1765-1768.

Chapter 4

- [1] Sanders, G. B., Larson, W. E., "Progress made in lunar in situ resource utilization under NASA's exploration technology and development program." *Journal of Aerospace Engineering* **26**, 1 (2012), 5-17.
- [2] Taylor, L. A., et al., "Lunar mare soils: Space weathering and the major effects of surface-correlated nanophase Fe." *Journal of Geophysical Research: Planets* **106**, E11 (2001), 27985-27999.
- [3] Taylor, L. A., Meek, T. T., "Microwave sintering of lunar soil: properties, theory, and practice." *Journal of Aerospace Engineering* **18**, 3 (2005), 188-196.
- [4] Berggren, M., et al. "Lunar soil particle separator." *Proc., 49th AIAA Aerospace Sciences Meeting* (2011).

- [5] Wilkinson, A., "Size beneficiation of regolith for simplicity and efficiency." *Presentation at Planetary and Terrestrial Mining and Sciences Symposium (PTMSS)*, (2011).
- [6] Wentworth, S. J., et al., "Sieving the Finest Fractions of Lunar Soils." *Lunar and Planetary Science Conference* **26** (1995).
- [7] Masuda, S., et al., "Confinement and transportation of charged aerosol clouds via electric curtain." *Electrical Engineering in Japan* **92**, 1 (1972), 43-52.
- [8] Masuda, S., Matsumoto, Y., "Theoretical characteristics of standing-wave electric curtains." *Electrical Engineering in Japan* **93**, 1 (1973), 71-77.
- [9] Adachi, M., et al., "Particle-Size Sorting System of Lunar Regolith Using Electrostatic Traveling Wave." *Proceedings of the 2016 Electrostatics Joint Conference*, (2016), B5.

Chapter 5

- [1] Kubota, T., et al. "Robotics technology for asteroid sample return mission MUSES-C." *The 6th International Symposium on Artificial Intelligence, Robotics and Automation in Space: A New Space Odyssey* (2001), AS016.
- [2] Saiki, T., et al. "Small carry-on impactor of Hayabusa2 mission." *Acta Astronautica* **84** (2013), 227-236. (in Japanese)
- [3] Morishita, H., et al. "Study and evaluation experiments of adhesive based sampling system for the next minorbody exploration." *Space Engineering Conference 2010*, **19**, (2011).
- [4] Matunaga, S., et al. "Result of micro-gravity experiment using parabolic flight for tethered recovery in tethered sampling method." *Transactions of The Japan Society For Aeronautical and Space Sciences, Space Technology Japan 7 ists26* (2009), Pk_23-Pk_28.
- [5] Watanabe, T., et al. "Micro gravity experiment and 3 dimensional dynamic analysis of tethered sampler." *Transactions of the Japan Society for Aeronautical and Space Sciences, Space Technology Japan 7 ists26* (2009), Pk_17-Pk_22.
- [6] Bonitz, R., "The brush wheel sampler-A sampling device for small-body touch-and-go missions." *Aerospace Conference 2012* (2012).
- [7] Clark, D. L., et al., "A novel approach to planetary regolith collection: the bucket drum soil excavator." *AIAA Space 2009 Conference & Exposition* **2**, 6, (2009).
- [8] Younse, P., et al. "Sample acquisition and caching using detachable scoops for Mars sample return." *2009 IEEE Aerospace conference*, (2009).
- [9] Zacny, K., et al. "Asteroids: Anchoring and Sample Acquisition Approaches in Support of Science, Exploration, and In Situ Resource Utilization." Springer Berlin Heidelberg (2013) 287-343.
- [10] Beshore, E., et al. "The OSIRIS-REx asteroid sample return mission." *2015 IEEE Aerospace Conference*, (2015).
- [11] Hajime, Y., et al. "Touchdown of the Hayabusa spacecraft at the Muses Sea on Itokawa." *Science* **312**, 5778 (2006), 1350-1353.
- [12] Veverka, J., et al. "The landing of the NEAR-Shoemaker spacecraft on asteroid 433 Eros." *Nature* **413**, 6854 (2001), 390-393.

- [13] Adachi, M., et al., "Sampling of Regolith on Asteroids Using Electrostatic Force." *J. Aerospace Engineering* **29**, 4 (2016), 04015081-1-9.
- [14] Adachi, M., et al., "Electrostatic Sampler for Large Regolith Particles on Asteroids." *J. Aerospace Engineering* (in press) (2016).
- [15] Scheeres, D. J., et al. "Scaling forces to asteroid surfaces: The role of cohesion." *Icarus* **210**, 2 (2010), 968-984.

Chapter 6

- [1] McKay, D. S., et al. "The lunar regolith." Lunar sourcebook (1991), 285-356.
- [2] Noguchi, T., et al. "Incipient space weathering observed on the surface of Itokawa dust particles." *Science* **333**, 6046 (2011), 1121-1125.
- [3] Goetz, W., et al. "The nature of Martian airborne dust. Indication of long-lasting dry periods on the surface of Mars." *LPI Contributions* **1353** (2007), 3104.
- [4] Andrews, J. A. "Coilgun structures." *IEEE transactions on magnetics* **29**, 1 (1993), 637-642.
- [5] Coşkun, I., et al. "Optimization of parameters acting on a projectile velocity within a four stage induction coil-gun." *Measurement* **43**, 10 (2010), 1656-1660.
- [6] Lee, S., et al. "Coil gun electromagnetic launcher (EML) system with multi-stage electromagnetic coils." *J. Magn.* **18**, 4 (2013), 481-486.
- [7] Adachi, M., et al., "Sampling of Regolith from Asteroids Utilizing Magnetic Force." *AIAA SciTech2015* (2016), (AIAA 2016-0718).

Chapter 7

- [1] Eimer, B. C., Taylor, L. A., "Lunar regolith, soil, and dust mass mover on the Moon." *Lunar and Planetary Science Conference* **38**, (2007).
- [2] Mantovani, J. G., Townsend, I. I., "Planetary regolith delivery systems for ISRU." *Journal of Aerospace Engineering* **26**, 1 (2012), 169-175.
- [3] Pelrine, R., et al. "High-speed electrically actuated elastomers with strain greater than 100%." *Science* **287**, 5454 (2000), 836-839.
- [4] Pelrine, R., et al. "High-field deformation of elastomeric dielectrics for actuators." *Materials Science and Engineering C* **11**, 2 (2000), 89-100.
- [5] Pei, Q., et al. "Multiple-degrees-of-freedom electroelastomer roll actuators." *Smart Materials and Structures* **13**, 5 (2004), N86.
- [6] Plante, J., et al., "A road to practical dielectric elastomer actuators based robotics and mechatronics: discrete actuation." *The 14th International Symposium on: Smart Structures and Materials & Nondestructive Evaluation and Health Monitoring*, (2007).
- [7] Rosset, S. Shea, H. R., "Flexible and stretchable electrodes for dielectric elastomer actuators." *Applied Physics A* **110**, 2 (2013), 281-307.

- [8] Carpi, F., et al., "Folded dielectric elastomer actuators." *Smart Materials and Structures* **16**, 2 (2007), S300.
- [9] Adachi, M., et al., "Transport of Regolith Utilizing Dielectric Elastomer Actuator for In-Situ Resource Utilization on Moon and Mars," *30th ISTS: International Symposium on Space Technology and Science*, Kobe (2015), 2015-k-26.
- [10] Kawamoto, H., et al., "Utilizing Electrostatic Force and Mechanical Vibration to Obtain Regolith Sample from the Moon and Mars," *J. Aerospace Engineering* **29**, 1 (2016), 04015031-1-6.
- [11] Kanamori, H., et al. "Properties of lunar soil simulant manufactured in Japan." *Space* **98** (1998), 462-468.
- [12] Gaier, J. R., "The effects of lunar dust on EVA systems during the Apollo missions." *NASA Technical Report* (2005), 20050160460.

Research Achievements

Peer Reviewed Journal Papers

- [1] 安達, 川本, "月・火星探査機器用の静電防塵機構", 日本機械学会論文集, Vol. **81**, No. 821 (2015). [M. Adachi and H. Kawamoto, "Electrostatic dust shield system used for Lunar and Mars exploration equipment," *Transactions of the JSME* (in Japanese), Vol. **81**, No. 821 (2015).]
- [2] Kawamoto, H., Shigeta, A., and Adachi, M., "Utilizing Electrostatic Force and Mechanical Vibration to Obtain Regolith Sample from the Moon and Mars," *J. Aerospace Engineering*, Vol. **29**, Issue 1 (2016) 04015031-1-6.
- [3] Adachi, M., Maezono, H., and Kawamoto, H., "Sampling of Regolith on Asteroids Using Electrostatic Force," *J. Aerospace Engineering*, Vol. **29**, Issue 4 (2016) pp.04015081-1-9.
- [4] Kawamoto, H., Megumi, K., and Masato, A., "Electrostatic Transport of Regolith Particles for Sample Return Mission from Asteroids." *J. Electrostatics*, Vol. **84** (2016) pp.42-47
- [5] Adachi, M., Kojima, T., and Kawamoto, H., "Electrostatic Sampler for Large Regolith Particles on Asteroids," *J. Aerospace Engineering* (in press).

Invited Review Paper

- [1] Kawamoto, H., and Adachi, M., "Numerical Simulation and Direct Observation of Dynamics of Toner and Carrier Particles in Electrographic Two-Component Magnetic Brush Development System," *Journal of the Imaging Society of Japan*, Vol. **52**, No. 6 (2013) pp.547-554.

Proceedings of International Conferences

- [1] Kawamoto, H., and Adachi, M., "Electrostatic Particle-Size Classification of Lunar Regolith for In-Situ Resource Utilization," *AIAA SciTech 2014*, National Harbor, MD (2014-1).
- [2] Kawamoto, H., Shigeta, A., and Adachi, M., "Sampling of Regolith on Moon and Mars Utilizing Electrostatic Force and Mechanical Vibration," *14th ASCE International Conference on Engineering, Science, Construction and Operations in Challenging Environments: Earth and Space 2014*, St. Louis, Missouri (2014-10) pp.247- 255.
- [3] Adachi, M., Maezono, H., Ashiba, K., Hashi, Y., and Kawamoto, H., "Sampling of Regolith from Asteroids Utilizing Electrostatic Force," *14th ASCE International Conference on Engineering, Science, Construction and Operations in Challenging Environments: Earth and Space 2014*, St. Louis, Missouri (2014-10) pp.266-273.
- [4] Kawamoto, H., Adachi, M., and Shigeta, A., "Sampling of Regolith on the Moon and Mars Utilizing Electrostatic Force, Magnetic Force and Mechanical Vibration," *11th Low-Cost Planetary Missions Conference (LCPM-11)*, Berlin (2015-6) pp.57.
- [5] Adachi, M., and Kawamoto, H., "Sampling of Regolith on Asteroids Utilizing Electrostatic Force," *11th Low- Cost Planetary Missions Conference (LCPM-11)*, Berlin (2015-6) pp.69.

- [6] Adachi, M., Aguirre, G. D., Sasaki, T., Tsumura, R., Koshi, T., and Mori, K., "Novel Social Innovation Concept Based on the Viewpoint of the Infrastructure User," *2015 IEEE Twelfth International Symposium on Autonomous Decentralized Systems*, pp.295-300, (2015-3).
- [7] Adachi, M., Kojima, T., and Kawamoto, H., (Student Paper Competition Award) "Electrostatic Sampler for Collecting Large Regolith Particles on Asteroids," *Proc. ESA Annual Meeting on Electrostatics 2015*, I2 (2015-6).
- [8] Adachi, M., Nogami, K., and Kawamoto, H., "Transport of Regolith Utilizing Dielectric Elastomer Actuator for In-Situ Resource Utilization on Moon and Mars," *30th ISTS: International Symposium on Space Technology and Science*, Kobe (2015-7) 2015-k-26.
- [9] Adachi, M., Kojima, K., and Kawamoto, H., "Dynamics of Particles Agitated by the Electrostatic Sampler in Low Gravity Environment," *The Joint Conference of 6th International Symposium on Physical Sciences in Space*, Kyoto (2015-9).
- [10] Adachi, M., Kato, M., Fukuyama, S., Shigeta, A., and Kawamoto, H., "Sampling of Regolith from Asteroids Utilizing Magnetic Force," *AIAA SciTech2015*, AIAA 2016-0718, San Diego (2016-1).
- [11] Kawamoto, H., Kato, M., and Adachi, M., "Electrostatic Transport of Regolith Particles for Sample Return Mission from Asteroids" *Proceedings of the 2016 Electrostatics Joint Conference*, B3, Purdue University (2016-6).
- [12] Adachi, M., Moroka, H., Kawamoto, H., Wakabayashi, S., and Hoshino, T., (Student Paper Competition Award 1st place), "Particle-Size Sorting System of Lunar Regolith Using Electrostatic Traveling Wave," *Proceedings of the 2016 Electrostatics Joint Conference*, B5, Purdue University (2016-6).

Proceedings in Domestic Conferences (in Japanese)

- [1] 安達, 川本, "電子写真の2成分磁気ブラシ現像系における磁気ブラシと感光体の接触状態が画質に及ぼす影響", *Imaging Conference JAPAN 2012 Fall Meeting*, 京都 (2012-11) pp.5-8.
- [2] 安達, 川本, "電子写真の二成分磁気ブラシ現像システムにおける粒子挙動のシミュレーション", *機械学会 IIP2013 情報・知能・精密機器部門講演会*, 東京 (2013-3) pp.220-223.
- [3] 安達, 川本, 前園, "静電力を利用した粉体のハンドリング技術に関するシミュレーション", *Dynamics and Design Conference 2014, D&D2014*, 上智大学 (2014-9) pp.91.
- [4] 前園, 安達, 川本, "交流電界中の誘電泳動力を考慮した小惑星における静電粒子採取機構のシミュレーション", *日本機械学会第23回スペース・エンジニアリング・コンファレンス [SEC'14]* (2014-12).
- [5] 野上, 上遠野, 三室, 安達, 川本, "誘電アクチュエータを利用した月土壌の振動搬送システム", *日本機械学会第23回スペース・エンジニアリング・コンファレンス [SEC'14]* (2014-12).
- [6] 須田, 葉賀, 安達, 川本, "静電力を利用した月レゴリス分級機構の開発", *日本機械学会第23回スペース・エンジニアリング・コンファレンス [SEC'14]* (2014-12).
- [7] 田島, 沢井, 稲荷, 西山, 安達, 川本, "帯電したルナレゴリスに対する静電防塵機構の性能評価", *日本機械学会第23回スペース・エンジニアリング・コンファレンス [SEC'14]* (2014-12).

- [8] 繁田, 小太刀, 福山, 安達, 川本, "磁気力と振動を用いた月・火星土壌のサンプリングシステム", 第 27 回「電磁力関連のダイナミクス」シンポジウム SEAD27, 長崎 (2015-5) pp.211-216.
- [9] 小島, 前園, 坂田, 安達, 川本, "交流電界を利用した小惑星からの粒子採取システム", 第 27 回「電磁力関連のダイナミクス」シンポジウム SEAD27, 長崎 (2015-5) pp.217-222.
- [10] 川本, 安達, "月極域探査ミッション: レゴリスの静電分級", 第 59 回宇宙科学技術連合講演会, 鹿児島 (2015-10) 1D15.
- [11] 小畑, 芳賀, 小太刀, 繁田, 安達, 川本, 星野, 若林, "磁気力を用いた月・火星試料の採取機構", 第 24 回スペース・エンジニアリング・コンファレンス [SEC'15], 琴平 (2015-12) A01.
- [12] 濱澤, 上遠野, 三室, 生田, 安達, 川本, "誘電アクチュエータを用いた月レゴリスの振動搬送", 第 28 回「電磁力関連のダイナミクス」シンポジウム SEAD28, 慶応大学 (2016-5) pp.442-447.
- [13] 加藤, 武田, 小島, 福山, 安達, 川本, "静電力や磁気力を利用した小惑星上のレゴリスのサンプリング", 第 28 回「電磁力関連のダイナミクス」シンポジウム SEAD28, 慶応大学 (2016-5) pp.448-453.
- [14] 諸岡, 葉賀, 鈴木, 安達, 川本, "月レゴリスの静電分級", 第 28 回「電磁力関連のダイナミクス」シンポジウム SEAD28, 慶応大学 (2016-5) pp.506-511.
- [15] 小嶋, 稲荷, 手操, 安達, 川本, "火星環境における電気集塵", 日本機械学会 2016 年度年次大会, 九州大学 (2016.9) G1900105.
- [16] 安達, 野崎, 諸岡, 川本, "進行波電界を利用した月レゴリスの分級機構", 第 40 回静電気学会全国大会, 群馬大学 (2016.9) 29pA-1.

Awards

- [1] Outstanding Presentation Award, Graduate School of Science and Engineering English for Science and Technology Program in U.C. Davis, Davis, CA. (2014-9)
- [2] Student Paper Competition Award, 2015 Annual Meeting of the Electrostatics Society of America, Pomona, CA (2015-6).
- [3] Student Paper Competition Award 1st place, 2016 Electrostatics Joint Conference, West Lafayette, IN (2016-6).
- [4] トレック・宍戸・HRSB 賞, 静電気学会 (2016-9).

